

https://dspace.org/

A study of the Ni-Pt-Ru and Co-Pt-Ru systems.

Glaner, Lizelle.

2011-10-11
http://hdl.handle.net/10539/10537

Downloaded from a DSpace repository. https://dspace.org/

A Study of the Ni-Pt-Ru and Co-Pt-Ru Systems

Lizelle Glaner

A dissertation submitted to the Faculty of Engineering and the Build Environment, University of the Witwatersrand, in fulfilment of the requirements for the degree of Master of Science in Engineering.

Johannesburg, 2009.

DECLARATION

I, Lizelle Glaner, declare that this dissertation is my own work except where otherwise acknowledged. It is being submitted for the degree of Master of Science in Engineering at the University of the Witwatersrand, Johannesburg. It has not been submitted previously at this, or any other university of any degree or examination.

L Glaner
SIGNATURE

2/6/2010
DATE

ABSTRACT

The solidification projections and 1000°C isothermal sections of the Ni-Pt-Ru and Co-Pt-Ru systems were determined by characterising alloys of different using SEM and XRD on arc-melted as-cast and annealed samples. Hardness measurements were undertaken and the hardness indentations were also used to determine the preliminary toughness of the samples.

The solidification projection of the Ni-Pt-Ru system showed that the (Ni,Pt) solvus retreats to the Pt corner in the ternary wherever (Ru) formed where it was not expected and a third phase appeared after heat treatment on a locus from ~Ni_{20}: Pt_{30}: Ru_{50} to ~Ni_{10}: Pt_{50}: Ru_{40}. A possible miscibility gap in the (Ni,Pt) phase was found in Alloy LG 10. Alloys LG 1 underwent the ordering after heat treatment. The other alloys softened after annealing. Reasonable toughness was exhibited by all the alloys because of the fcc phase that occur in all of them. The Co-Pt-Ru system showed that the $\alpha \rightarrow \varepsilon$ transformation that took place in two of the component binaries was stabilised in the ternary system, in both the as-cast and annealed alloys. The L + (Ru) $\rightarrow$ fcc (Co,Pt) peritectic reaction was demonstrated by many of the annealed alloys. During heat treatment (Ru) precipitates formed and this indicated that the fcc (Co,Pt) solvus was sloping and retreating towards lower Ru contents at lower temperatures. The hardnesses of the alloys did not change very much after heat treatment, with the exception of Alloys LG 11 and LG 15. Alloy LG 11 showed ordering and Alloy LG 15 showed a significant decrease in hardness due to the coarsening of the microstructure. The toughness remained reasonable for al the alloys as a result of the presence of the fcc phase in all of them.

ACKNOWLEDGEMENTS

I would like to thank the following people for their contribution and assistance:

- My supervisor, Prof. Lesley Cornish for her endless patients, expertise and assistance.
- Dr. Alistair Douglas for the encouragement to do this degree.
- Dr. Lesley Chown for her encouragement and the endless advice, encouragement and all the cups of coffee.
- Mrs. Iris Klingbiel for her friendship throughout the last five years.
- MINTEK for granting me their opportunity and financial assistance.
- The PDI for the platinum used in this investigation and support for the project.
- The Wits DST/NRF Centre of Excellence in Strong Materials.
- My wonderful family, Ralph, Kirsten and Marco. This one is for you guys.
- God, because your grace has always been enough for me.

Table of Contents

Declaration ii

Abstract iii

Acknowledgements iv

List of Figures vi

List of Tables xvii

1. Introduction 1

1.1 Rational for the project 1

1.2 Reasons for interest in the Ni-Pt-Ru and Co-Pt-Ru Systems 3

1.3 Benefits that could arise from the investigation (SA, PDI and CSIR) 3

2. Literature Review 5

2.1 Introduction 5

2.2 General Platinum Alloys 5

2.2.1 Autocatalysts 5

2.2.2 Jewellery 5

2.2.3 Electrical 6

2.2.4 Chemical Industry 6

2.2.4.1 Petroleum 6

2.2.4.2 Fuel Cells 6

2.2.5 Glass Industry 7

2.3 Ni-Pt-Ru (Nickel-Platinum-Ruthenium) 7

2.3.1 Binary Ni-Pt system 7

2.3.2 Binary Pt-Ru system 9

2.3.3 Binary Ni-Ru system 11

2.4 Co-Pt-Ru (Cobalt-Platinum-Ruthenium) 13

2.4.1 Binary Co-Pt system 13

2.4.2 Binary Co-Ru system 16

3. Experimental Procedure 18

3.1 Sample Manufacture 18

3.2 Metallography 19

3.3 Characterisation **20**
3.3.1 Scanning Electron microscopy (SEM) and Energy Dispersive Spectrometry (EDS) **20**
3.3.2 XRD **20**
3.4 Mechanical Properties **20**
3.4.1 Hardness and Toughness **20**

4. Results **22**
4.1 Ni-Pt-Ru System **22**
4.1.1 As-cast Alloys **22**
4.1.2 Alloys after Heat Treatment at 1000°C for 1000 hours and water quench **52**
4.1.3 Ordering Heat Treatment at 500°C **80**
4.2 Co-Pt-Ru System **83**
4.2.1 As-cast Alloys **83**
4.2.2 Alloys after Heat Treatment at 1000°C for 1000 hours and water quench **125**
4.2.3 Ordering Heat Treatment at 500°C **160**
4.3 Mechanical Properties **166**
4.3.1 Ni-Pt-Ru Hardness and Toughness **166**
4.3.2 Co-Pt-Ru Hardness and Toughness **175**

5. Discussion **183**
5.1 Solidification Projection of the Ni-Pt-Ru System **183**
5.2 Isothermal Sections of the Ni-Pt-Ru System **183**
5.3 Solidification Projection of the Co-Pt-Ru System **186**
5.4 Isothermal Section of the Co-Pt-Ru System **187**
5.5 Mechanical Properties of the Ni-Pt-Ru System **189**
5.6 Mechanical Properties of the Co-Pt-Ru System **190**

6. Conclusions **191**

7. Recommendations **192**

8. References **193**

9. Abstract: Papers published during the course of this study **197**

List of Figures

Figure 2.1. Binary Ni-Pt equilibrium phase diagram [1990Mas]. 7

Figure 2.2. Binary Pt-Ru equilibrium phase diagram [1990Mas]. 10

Figure 2.3. Calculated Pt-Ru phase diagram [2007Wat]. 10

Figure 2.4. Binary Ni-Ru equilibrium phase diagram [1990Mas]. 12

Figure 2.5. Binary Co-Pt equilibrium phase diagram [1990Mas]. 14

Figure 2.6. Calculated Co-Pt phase diagram [2001Oik]. 14

Figure 2.7. The total Gibbs energy G_m of the Fcc phase at 400°C with reference to Co and Pt in the Co-Pt system. The dashed line shows the Gibbs energy curve without the magnetic contribution term ${}^{mag}G_m$ [2001Oik]. 15

Figure 2.8. Binary Co-Ru equilibrium phase diagram [1990Mas]. 17

Figure 3.1. Compositions of nominal Ni-Pt-Ru alloys (at.%). 18

Figure 3.2. Compositions of nominal Co-Pt-Ru alloys (at.%). 19

Figure 4.1. BEI of LG 1 (Nominal $Ni_{47.5}$:$Pt_{47.5}$:Ru_5) showing single phase (Ni,Pt) with unmelted Pt and Ru (scale bar = 600μm). 22

Figure 4.2. XRD spectrum of LG 1 (Nominal $Ni_{47.5}$:$Pt_{47.5}$:Ru_5) in the as-cast condition. 23

Figure 4.3. EDS analyses of LG 1 (Nominal $Ni_{47.5}$:$Pt_{47.5}$:Ru_5) in the as-cast condition (at.%). 24

Figure 4.4. BEI of LG 2 (Nominal Ni_{10}:Pt_{23}:Ru_{67}) showing (Ni,Pt) of two different composition contrasts in the as-cast condition (scale bar = 500μm). 25

Figure 4.5. XRD spectrum of LG 2 (Nominal Ni_{10}:Pt_{23}:Ru_{67}) in the as-cast condition. 26

Figure 4.6. EDS analyses of LG 2 (Nominal Ni_{10}:Pt_{23}:Ru_{67}) in the as-cast condition (at.%). 27

Figure 4.7. BEI of LG 3 (Nominal Ni_{20}:Pt_{20}:Ru_{60}) showing two different composition contrasts in the as-cast condition (scale bar = 700μm). 28

Figure 4.8. XRD spectrum of LG 3 (Nominal Ni_{20}:Pt_{20}:Ru_{60}) in the as-cast condition. 29

Figure 4.9. EDS analyses of LG 3 (Nominal Ni_{20}:Pt_{20}:Ru_{60}) in the as-cast condition (at.%). 30

Figure 4.10. BEI of LG 4 (Nominal $Ni_{35}:Pt_{13}:Ru_{52}$) with dark, irregular (Ru) dendrites and light (Ni,Pt) cored matrix in the as-cast condition (scale bar = 24μm). 31
Figure 4.11. XRD spectrum of LG 4 (Nominal $Ni_{35}:Pt_{13}:Ru_{52}$) in the as-cast condition. 32
Figure 4.12. EDS analyses of LG 4 (Nominal $Ni_{35}:Pt_{13}:Ru_{52}$) in the as-cast condition (at.%). 33
Figure 4.13. BEI of LG 5 (Nominal $Ni_{50}:Pt_{5}:Ru_{45}$) with light, (Ru) dendrites and dark, cored (Ni,Pt) matrix in the as-cast condition (scale bar = 24μm). 34
Figure 4.14. XRD spectrum of LG 5 (Nominal $Ni_{50}:Pt_{5}:Ru_{45}$) in the as-cast condition. 35
Figure 4.15. EDS analyses of LG 5 (Nominal $Ni_{50}:Pt_{5}:Ru_{45}$) in the as-cast condition (at.%). 36
Figure 4.16 BEI of LG 6 (Nominal $Ni_{60}:Pt_{5}:Ru_{35}$) with light, (Ru) dendrites and cored, dark (Ni,Pt) matrix in the as-cast (scale bar = 50μm). 37
Figure 4.17: XRD spectrum of LG 6 (Nominal $Ni_{60}:Pt_{5}:Ru_{35}$) in the as-cast condition. 38
Figure 4.18. EDS analyses of LG 6 (Nominal $Ni_{60}:Pt_{5}:Ru_{35}$) in the as-cast condition (at.%). 39
Figure 4.19. BEI of LG 7 (Nominal $Ni_{45}:Pt_{25}:Ru_{30}$) showing (Ni,Pt) in the as-cast condition with some precipitates (scalebar = 16 μm). 40
Figure 4.20. XRD spectrum of LG 7 (Nominal $Ni_{45}:Pt_{25}:Ru_{30}$) in the as-cast condition. 41
Figure 4.21. EDS analyses of LG 7 (Nominal $Ni_{45}:Pt_{25}:Ru_{30}$) in the as-cast condition (at.%). 42
Figure 4.22. BEI of LG 8 (Nominal $Ni_{35}:Pt_{25}:Ru_{35}$), in the as-cast condition showing (scale bar = 120μm). 43
Figure 4.23. XRD spectrum of LG 8 (Nominal $Ni_{35}:Pt_{25}:Ru_{35}$) in the as-cast condition. 44
Figure 4.24. EDS analyses of LG 8 (Nominal $Ni_{35}:Pt_{25}:Ru_{35}$) in the as-cast condition (at.%). 45
Figure 4.25. BEI of LG 9 (Nominal $Ni_{25}:Pt_{45}:Ru_{30}$) showing (Ni,Pt) matrix (scale bar = 40μm) in the as-cast condition. 46

Figure 4.26. XRD spectrum of LG 9 (Nominal $Ni_{25}:Pt_{45}:Ru_{30}$) in the as-cast condition. 47
Figure 4.27. EDS analyses of LG 9 (Nominal $Ni_{25}:Pt_{45}:Ru_{30}$) in the as-cast condition (at.%). 48
Figure 4.28. BEI of LG 10 (Nominal $Ni_{15}:Pt_{55}:Ru_{30}$) in the as-cast condition, showing a matrix with different contrasts (scale bar = 40μm). 49
Figure 4.29. XRD spectrum of LG 10 (Nominal $Ni_{15}:Pt_{55}:Ru_{30}$) in the as-cast condition. 50
Figure 4.30. EDS analyses of LG 10 (Nominal $Ni_{15}:Pt_{55}:Ru_{30}$) in the as-cast condition (at.%). 51
Figure 4.31: BEI of LG 2 (Nominal $Ni_{10}:Pt_{23}:Ru_{67}$) after heat treatment and water quench showing (Ni,Pt) (light), with coring and (Ru) needles (scale bar = 24μm). 52
Figure 4.32. XRD scan of LG 2 (Nominal $Ni_{10}:Pt_{23}:Ru_{67}$) after heat treatment and water quench. 54
Figure 4.33. EDS analyses of LG 2 (Nominal $Ni_{10}:Pt_{23}:Ru_{67}$) after heat treatment and water quench (at.%). 55
Figure 4.34: BSE image of LG 3 (Nominal $Ni_{20}:Pt_{20}:Ru_{60}$) after heat treatment and water quench showing (Ni,Pt) (light) with (Ru) needles (dark) (scale bar = 16μm). 56
Figure 4.35: XRD spectrum of LG 3 (Nominal $Ni_{20}:Pt_{20}:Ru_{60}$) after heat treatment and water quench. 57
Figure 4.36: EDS analyses of LG 3 (Nominal $Ni_{20}:Pt_{20}:Ru_{60}$) after heat treatment and water quench (at.%). 58
Figure 4.37: BEI of LG 4 (Nominal $Ni_{35}:Pt_{13}:Ru_{52}$) after heat treatment and water quench showing (Ni,Pt) (light) and (Ru) (dark) (scale bar = 17μm). 59
Figure 4.38: XRD spectrum of LG 4 (Nominal $Ni_{35}:Pt_{13}:Ru_{52}$) after heat treatment and water quench. 60
Figure 4.39: EDS analyses of LG 4 (Nominal $Ni_{35}:Pt_{13}:Ru_{52}$) after heat treatment and water quench (at.%). 61
Figure 4.40. BEI of LG 5 (Nominal $Ni_{50}:Pt_{5}:Ru_{45}$) after heat treatment and water quench showing light (Ru) dendrites and dark (Ni,Pt) matrix, (scale bar = 24μm). 62
Figure 4.41: XRD scan of LG 5 (Nominal $Ni_{50}:Pt_{5}:Ru_{45}$) after

heat treatment and water quench. 63
Figure 4.42: EDS analyses of LG 5 (Nominal $Ni_{50}:Pt_5:Ru_{45}$) after heat treatment and water quench (at.%). 64
Figure 4.43: BEI of LG 6 (Nominal $Ni_{60}:Pt_5:Ru_{35}$) after heat treatment and water quench showing (Ru) (light) and (Ni,Pt) (dark) (scale bar = 16μm). 65
Figure 4.44: XRD scan of LG 6 (Nominal $Ni_{60}:Pt_5:Ru_{35}$) after heat treatment and water quench. 66
Figure 4.45: EDS analyses of LG 6 (Nominal $Ni_{60}:Pt_5:Ru_{35}$) after heat treatment and water quench (at.%). 67
Figure 4.46: Microstructure of LG 7 (Nominal $Ni_{45}:Pt_{25}:Ru_{30}$) after heat treatment. (The micron markers are 100 and 30μm respectively.) 68
Figure 4.47: XRD spectrum LG 7 (Nominal $Ni_{45}:Pt_{25}:Ru_{30}$) after heat treatment and water quench. 69
Figure 4.48: EDS analyses of LG 7 (Nominal $Ni_{45}:Pt_{25}:Ru_{30}$) after heat treatment (at.%). 70
Figure 4.49: BEI showing the microstructure of LG 8 (Nominal $Ni_{35}:Pt_{25}:Ru_{35}$) after heat treatment and water quench. The micron markers are 100 and 30μm respectively. 71
Figure 4.50: XRD spectrum of LG 8 (Nominal $Ni_{35}:Pt_{25}:Ru_{35}$) after heat treatment and water quench. 72
Figure 4.51: EDS analyses of LG 8 (Nominal $Ni_{35}:Pt_{25}:Ru_{35}$) after heat treatment and water quench (at.%). 73
Figure 4.52: BEI of LG 9 (Nominal $Ni_{25}:Pt_{45}:Ru_{30}$) showing a cored single-phase after heat treatment and water quench (micron marker = 90μm). 74
Figure 4.53: XRD scan of LG 9 (Nominal $Ni_{25}:Pt_{45}:Ru_{30}$) after heat treatment and water quench. 75
Figure 4.54: EDS analyses of LG 9 (Nominal $Ni_{25}:Pt_{45}:Ru_{30}$) after heat treatment and water quench (at.%). 76
Figure 4.55: BEI of the microstructure of LG 10 (Nominal $Ni_{15}:Pt_{55}:Ru_{30}$) after heat treatment and water quench (micron markers =220μm). 77
Figure 4.56: XRD scan of LG 10 (Nominal $Ni_{15}:Pt_{55}:Ru_{30}$) after heat treatment at 1000°C for 1000 hours and water quench. 78
Figure 4.57: EDS analyses of LG 10 (Nominal $Ni_{15}:Pt_{55}:Ru_{30}$) after heat treatment and water quench (at.%). 79

Figure 4.58. BEI of LG 1 (Nominal $Ni_{47.5}$:$Pt_{47.5}$:Ru_5) after ordering heat treatment and water quench (micron markers =40μm). 80
Figure 4.59: XRD spectrum of LG 1 (Nominal $Ni_{47.5}$:$Pt_{47.5}$:Ru_5) after ordering heat treatment at 500°C for a 1000 hours. 81
Figure 4.60: EDS analyses of LG 1 (Nominal $Ni_{47.5}$:$Pt_{47.5}$:Ru_5) ordering heat treatment at 500°C for a 1000 hours (at.%). 82
Figure 4.61. BEI of LG 11 (Nominal Co_{40}:Pt_{50}:Ru_{10}) in the as-cast condition showing a single-phase matrix. 83
Figure 4.62. XRD spectrum of LG 11 (Nominal Co_{40}:Pt_{50}:Ru_{10}) in the as-cast condition showing a comparison with both a) fcc Co and b) Pt peaks. 84
Figure 4.63. XRD spectrum of LG 11 (Nominal Co_{40}:Pt_{50}:Ru_{10}) in the as-cast condition showing the a) fcc Co and b) Pt peaks after shifting. 85
Figure 4.64. XRD spectrum of LG 11 (Nominal Co_{40}:Pt_{50}:Ru_{10}) in the as-cast condition, with both shifted fcc Co and Pt peaks overlaid. 86
Figure 4.65. EDS analyses of LG 11 (Nominal Co_{40}:Pt_{50}:Ru_{10}) in the as-cast condition (at.%). 87
Figure 4.66. BEI of LG 12 (Nominal Co_{15}:Pt_{75}:Ru_{10}) in the as-cast condition, showing the grey matrix. 88
Figure 4.67. XRD spectrum of LG 12 (Nominal Co_{15}:Pt_{75}:Ru_{10}) in the as-cast condition, with the Pt peaks overlaid. 89
Figure 4.68. EDS analyses of LG 12 (Nominal Co_{15}:Pt_{75}:Ru_{10}) in the as-cast condition (at.%). 90
Figure 4.69. BEI of LG 13 (nominal Co_{90}:Pt_5:Ru_5) in the as-cast condition showing a grey matrix 91
Figure 4.70. XRD spectrum of LG 13 (nominal Co_{90}:Pt_5:Ru_5) in the as-cast condition showing a comparison with both a) fcc Co and b) hcp εCo peaks. 92
Figure 4.71. XRD spectrum of LG 13 (nominal Co_{90}:Pt_5:Ru_5) in the as-cast condition showing the a) fcc Co and b) hcp εCo peaks after shifting. 93
Figure 4.72. XRD spectrum of LG 13 (nominal Co_{90}:Pt_5:Ru_5) in the as-cast condition, with the shifted fcc Co and hcp εCo peaks overlaid. 94
Figure 4.73. EDS analyses of LG 13 (nominal Co_{90}:Pt_5:Ru_5) in the as-cast condition (at.%). 95
Figure 4.74. BEI of LG 14 (nominal Co_{80}:Pt_{10}:Ru_{10}) in the as-cast condition showing a cored matrix. 96

Figure 4.75. XRD spectrum of LG 14 (nominal $Co_{80}:Pt_{10}:Ru_{10}$) in the as-cast condition showing a comparison with hexagonal hcp εCo. 97
Figure 4.76. XRD spectrum of LG 14 nominal ($Co_{80}:Pt_{10}:Ru_{10}$) in the as-cast condition, showing the shifted peak matches for hcp ε Co. 98
Figure 4.77. EDS analyses of LG 14 nominal ($Co_{80}:Pt_{10}:Ru_{10}$) in the as-cast condition (at.%). 99
Figure 4.88. BEI of LG 15 (nominal $Co_{30}:Pt_{20}:Ru_{50}$) in the as-cast condition showing dark, (Ru) dendrites in a lighter, fcc(Co,Pt) matrix. 100
Figure 4.79. XRD spectrum of LG 15 (nominal $Co_{30}:Pt_{20}:Ru_{50}$) in the as-cast condition showing a comparison with a) Pt and b) Ru. 101
Figure 4.80. XRD spectrum of LG 15 (nominal $Co_{30}:Pt_{20}:Ru_{50}$) in the as-cast condition showing the a) Pt and b) Ru peaks after shifting. 102
Figure 4.81. XRD spectrum of LG 15 (nominal $Co_{30}:Pt_{20}:Ru_{50}$) in the as-cast condition, with both Pt and Ru peaks overlaid. 103
Figure 4.82. EDS analyses of LG 15 (nominal $Co_{30}:Pt_{20}:Ru_{50}$) in the as-cast condition (at.%). 104
Figure 4.83. LG 16 (Nominal $Co_{60}:Pt_{20}:Ru_{20}$) in the as-cast condition showing a single phase structure. 105
Figure 4.84. XRD spectrum of LG 16 (Nominal $Co_{60}:Pt_{20}:Ru_{20}$) in the as-cast condition showing a comparison with a) εCo and b) Pt. 106
Figure 4.85. XRD spectrum of LG 16 (Nominal $Co_{60}:Pt_{20}:Ru_{20}$)in the as-cast condition showing a comparison with a) εCo and b) Pt after shifting. 107
Figure 4.86. *XRD spectrum of LG 16 (Nominal $Co_{60}:Pt_{20}:Ru_{20}$) in the as-cast condition with both ε Co and Pt overlaid.* 108
Figure 4.87. EDS analysis of LG 16 (Nominal $Co_{60}:Pt_{20}:Ru_{20}$) in the as-cast condition (at.%). 109
Figure 4.88. BEI of LG 17 (Nominal $Co_{10}:Pt_{30}:Ru_{60}$) in the as-cast condition showing dark (Ru) and fcc (Co,Pt) light phase. 110
Figure 4.89. XRD spectrum of LG 17 (Nominal $Co_{10}:Pt_{30}:Ru_{60}$) in the as-cast condition showing a comparison with a) Pt and b) Ru. 111
Figure 4.90. XRD spectrum of LG 17 (Nominal $Co_{10}:Pt_{30}:Ru_{60}$) in the as-cast condition showing a comparison with a) Pt and b) Ru after shifting. 112
Figure 4.91. XRD spectrum of LG 17 (Nominal $Co_{10}:Pt_{30}:Ru_{60}$) in the as-cast condition with both Ru and Pt overlaid.Figure 4.92. EDS analyses of

LG 17 (Nominal $Co_{10}:Pt_{30}:Ru_{60}$) in the as-cast condition (at.%). *113*
Figure 4.92. EDS analyses of LG 17 (Nominal $Co_{10}:Pt_{30}:Ru_{60}$) in the as-cast condition (at.%). *114*
Figure 4.93. LG 18 (Nominal $Co_{20}:Pt_{30}:Ru_{50}$) in the as-cast condition showing dark (Ru) and light fcc fcc(Co,Pt) phase. *115*
Figure 4.94. XRD spectrum of LG 18 (Nominal $Co_{20}:Pt_{30}:Ru_{50}$) in the as-cast condition showing a comparison with a) Pt and b) Ru. *116*
Figure 4.95. XRD spectrum of LG 18 (Nominal $Co_{20}:Pt_{30}:Ru_{50}$) in the as-cast condition showing a comparison with a) Pt and b) Ru after shifting. *117*
Figure 4.96. XRD spectrum of LG 18 (Nominal $Co_{20}:Pt_{30}:Ru_{50}$) in the as-cast condition with both Ru and Pt overlaid. 118
Figure 4.97. EDS analyses of LG 18 (Nominal $Co_{20}:Pt_{30}:Ru_{50}$) in the as-cast condition (at.%). *119*
Figure 4.98. BEI of LG 19 (Nominal $Co_{50}:Pt_{20}:Ru_{30}$) in the as-cast condition showing dark (Ru) and light fcc(Co,Pt). *120*
Figure 4.99. XRD spectrum of LG 19 (Nominal $Co_{50}:Pt_{20}:Ru_{30}$) in the as-cast condition showing a comparison with a) Ru and b) Pt. *121*
Figure 4.100. XRD spectrum of LG 19 (Nominal $Co_{50}:Pt_{20}:Ru_{30}$) in the as-cast condition showing a comparison with a) Ru and b) Pt after shifting. *122*
Figure 4.101. XRD spectrum of LG 19 (Nominal $Co_{50}:Pt_{20}:Ru_{30}$) in the as-cast condition with both Ru and Pt overlaid. *123*
Figure 4.102. EDS analyses of LG 19 (Nominal $Co_{50}:Pt_{20}:Ru_{30}$) in the as-cast condition (at.%). *124*
Figure 4.103. BEI of LG13 (Nominal $Co_{90}:Pt_{5}:Ru_{5}$) in the heat treated and water quenched condition showing an apparent single phase matrix. *125*
Figure 4.104. XRD spectrum of LG13 (Nominal $Co_{90}:Pt_{5}:Ru_{5}$) in the heat treated condition showing a comparison with a) Pt and b) εCo. *126*
Figure 4.105. XRD spectrum of LG13 (Nominal $Co_{90}:Pt_{5}:Ru_{5}$) in the heat treated condition showing a comparison with a) Pt and b) εCo after shifting. *127*
Figure 4.106. XRD spectrum of LG13 (Nominal $Co_{90}:Pt_{5}:Ru_{5}$) in the heat treated condition with both εCo and Pt overlaid. *128*
Figure 4.107. EDS analyses of LG13 (Nominal $Co_{90}:Pt_{5}:Ru_{5}$) in the heat treated condition (at.%). *129*
Figure 4.108. BEI of LG 14 (Nominal $Co_{80}:Pt_{10}:Ru_{10}$) in the heat treated and

water quenched condition showing a grey matrix containing
ε(Co) and fcc(Co,Pt) *130*
Figure 4.109. XRD spectrum of LG14 (Nominal $Co_{80}:Pt_{10}:Ru_{10}$*) in the heat treated condition showing a comparison with a) Pt and b)* εCo. *131*
Figure 4.110. XRD spectrum of LG14 (Nominal $Co_{80}:Pt_{10}:Ru_{10}$*) in the heat treated condition showing a comparison with a) Pt and b) εCo after shifting.* *132*
Figure 4.111. XRD spectrum of LG 14 (Nominal $Co_{80}:Pt_{10}:Ru_{10}$*) in the heat treated condition with both* εCo *and Pt overlaid.* *133*
Figure 4.112. EDS analyses of LG 14 (Nominal $Co_{80}:Pt_{10}:Ru_{10}$*) in the heat treated condition (at.%).* *134*
Figure 4.113. BEI of LG 15 (Nominal $Co_{30}:Pt_{20}:Ru_{50}$*) in the heat treated condition showing light matrix fcc(Co,Pt) with dark second phase (Ru).* *135*
Figure 4.114. XRD spectrum of LG 15 (Nominal $Co_{30}:Pt_{20}:Ru_{50}$*) in the heat treated condition showing a comparison with a) Pt and b) Ru.* *136*
Figure 4.115. XRD spectrum of LG 15 (Nominal $Co_{30}:Pt_{20}:Ru_{50}$*) in the heat treated condition showing a comparison with a) Pt and b) Ru after shifting.* *137*
Figure 4.116. XRD spectrum of LG 15 (Nominal $Co_{30}:Pt_{20}:Ru_{50}$*) in the heat treated condition with both Ru and Pt overlaid.* *138*
Figure 4.117. EDS analyses of LG 15 (nominal $Co_{30}:Pt_{20}:Ru_{50}$*) in the heat treated condition (at.%).* *139*
Figure 4.118. BEI of LG 16 (Nominal $Co_{60}:Pt_{20}:Ru_{20}$ *) heat treated condition showing a dark second phase (Ru) in a light matrix fcc(Co,Pt).* *140*
Figure 4.119. XRD spectrum of LG16 (Nominal $Co_{60}:Pt_{20}:Ru_{20}$*) in the heat treated condition showing a comparison with a) Pt and b) Ru.* *141*
Figure 4.120. XRD spectrum of LG 16 (Nominal $Co_{60}:Pt_{20}:Ru_{20}$*) in the heat treated condition showing a comparison with a) Pt and b) Ru after shifting.* *142*
Figure 4.121. XRD spectrum of LG 16 (Nominal $Co_{60}:Pt_{20}:Ru_{20}$*) in the heat treated condition with both Pt and Ru overlaid.* *143*
Figure 4.122. EDS analyses of LG 16 (Nominal $Co_{60}:Pt_{20}:Ru_{20}$*) in the heat treated condition (at.%).* *144*
Figure 4.123. BEI of LG 17 (Nominal $Co_{10}:Pt_{30}:Ru_{60}$*) heat treated condition showing a dark second phase (Ru) in a light matrix fcc(Co,Pt) and dark Ru needles.* *145*

Figure 4.124. XRD spectrum of LG 17 (Co_{60}:Pt_{20}:Ru_{20}) in the heat treated condition showing a comparison with a) Pt and b) Ru. 146
Figure 4.125. XRD spectrum of LG 17 (Co_{60}:Pt_{20}:Ru_{20}) in the heat treated condition showing a comparison with a) Pt and b) Ru after shifting. 147
Figure 4.126. XRD spectrum of LG 17 (Co_{60}:Pt_{20}:Ru_{20}) in the heat treat condition with both Pt and Ru overlaid. 148
Figure 4.127. EDS analyses of LG 17 (Co_{60}:Pt_{20}:Ru_{20}) in the heat treated condition (at.%). 149
Figure 4.128. BEI of LG 18 (Nominal Co_{20}:Pt_{30}:Ru_{50}) heat treated condition showing the mixed dendrites containing a mixture of (Ru) and fcc(Co,Pt) in a light matrix fcc(Co,Pt) with dark (Ru) needles. 150
Figure 4.129. XRD spectrum of LG 18 (Nominal Co_{20}:Pt_{30}:Ru_{50}) in the heat treated condition showing a comparison with a) Pt and b) Ru. 151
Figure 4.130. XRD spectrum of LG 18 (Nominal Co_{20}:Pt_{30}:Ru_{50}) in the heat treated condition showing a comparison with a) Pt and b) Ru. 152
Figure 4.131. XRD spectrum of LG 18 (Nominal Co_{20}:Pt_{30}:Ru_{50}) in the heat treat condition with both Pt and Ru overlaid. 153
Figure 4.132. EDS analyses of LG 18 (Nominal Co_{20}:Pt_{30}:Ru_{50}) in the heat treated condition (at.%). 154
Figure 4.133. BEI of LG 19 (Nominal Co_{50}:Pt_{20}:Ru_{30}) heat treated condition showing a dark second phase (Ru) in a light matrix fcc(Co,Pt) and dark (Ru) needles. 155
Figure 4.134. XRD spectrum of LG 19 (Co_{50}:Pt_{20}:Ru_{30}) in the heat treated condition showing a comparison with a) Pt and b) Ru. 156
Figure 4.135. XRD spectrum of LG 19 (Co_{50}:Pt_{20}:Ru_{30}) in the heat treated condition showing a comparison with a) Pt and b) Ru after shifting. 157
Figure 4.136. XRD spectrum of LG 19 (Nominal Co_{50}:Pt_{20}:Ru_{30}) in the heat treat condition with both Pt and Ru overlaid. 158
Figure 4.137. EDS analyses of LG 19 (Nominal Co_{50}:Pt_{20}:Ru_{30}) in the heat treated condition (at.%). 159
Figure 4.138. BEI of LG 11 (Nominal Co_{40}:Pt_{50}:Ru_{10}) after ordering heat treatment and water quench. 160
Figure 4.139. XRD spectrum of LG 11 (Nominal Co_{40}:Pt_{50}:Ru_{10}) in the heat treated condition showing a comparison with CoPt. 161

Figure 4.140. EDS analyses of LG 11 (Nominal Co_{40}:Pt_{50}:Ru_{10}) in the heat treated condition (at.%). 162
Figure 4.141. BEI of LG 12 (Nominal Co_{15}:Pt_{75}:Ru_{10}) after ordering heat treatment and water quench. 163
Figure 4.142. XRD spectrum of LG 12 (Nominal Co_{15}:Pt_{75}:Ru_{10}) in the as-cast condition with the Pt peaks overlaid. 164
Figure 4.143. EDS analyses of LG 12 (Nominal Co_{15}:Pt_{75}:Ru_{10}) in the heat treated condition (at.%). 165
Figure 4.144. Hardness (HV_{10}) values of the as-cast Ni-Pt-Ru alloys superposed on the solidification projection. 167
Figure 4.145. Hardness (HV_{10}) values of the heat treated Ni-Pt-Ru alloys superposed on the 1000°C isothermal section. 168
Figure 4.146. Micrographs of the hardness indentations in the Ni-Pt-Ru alloys (as-cast), showing the mode of slip. 169
Figure 4.147. Mode of slip of the as-cast Ni-Pt-Ru alloys superposed on the solidification projection. 170
Figure 4.148. Micrographs of the hardness indentations in the heat treated Ni-Pt-Ru alloys, showing the mode of slip. 171
Figure 4.149. Mode of slip of the heat treated Ni-Pt-Ru alloys superposed on the 1000°C isothermal section. 172
Figure 4.150. Hardness values (HV_{10}) of the as-cast Co-Pt-Ru alloys superposed on the solidification projection. 175
Figure 4.151. Vickers Hardness (HV_{10}) values for the heat treated Co-Pt-Ru alloys superposed on the 1000°C isothermal section. 176
Figure 4.152. Micrographs of the hardness indentations in the as-cast Co-Pt-Ru alloys showing the mode of slip. 178
Figure 4.153. Mode of slip of the as-cast Co-Pt-Ru alloys superposed on the solidification projection. 179
Figure 4.154. Micrographs of the hardness indentations in the heat treated Co-Pt-Ru alloys showing the mode of slip. 180
Figure 4.155. Slip modes for the heat treated Co-Pt-Ru alloys superposed on the 1000°C isothermal section. 181
Figure 5.1. Solidification projection for the Ni-Pt-Ru system. 184
Figure 5.2. 1000°C isothermal section of the Ni-Pt-Ru system. 186

Figure 5.3. Solidification projection of the Co-Pt-Ru system. *187*
Figure 5.4. 1000°C Isothermal section for the Co-Pt-Ru system. *189*

List of Tables

Table 2.1. Solid phases in the Ni-Pt binary phase diagram. *8*
Table 2.2. Invariant equilibria for the Ni-Pt binary phase diagram. *9*
Table 2.3. Solid phases in the Pt-Ru binary phase diagram. *11*
Table 2.4. Invariant equilibrium for the Pt-Ru binary phase diagram. *11*
Table 2.5. Solid phases in the Ni-Ru binary phase diagram. *12*

Table 2.6. Invariant equilibrium for the Ru-Ni binary phase diagram. 12
Table 2.7. Solid phases in the Co-Pt binary phase diagram 15
Table 2.8. Invariant Equilibria for the Co-Pt binary phase diagram. 16
Table 2.9. Solid phases in the Co-Ru binary phase diagram. 17
Table 2.10. Invariant equilibrium for the Co-Ru binary phase diagram. 17

Table 4.1. EDS analyses of LG 1 (Nominal $Ni_{47.5}$:$Pt_{47.5}$:Ru_5) in the as-cast condition. 22
Table 4.2. EDS analyses of LG 2 (Nominal Ni_{10}:Pt_{23}:Ru_{67}) in the as-cast condition. 25
Table 4.3. EDS analyses of LG 3 (Nominal Ni_{20}:Pt_{20}:Ru_{60}) in the as-cast condition. 28
Table 4.4. EDS analyses of LG 4 (Nominal Ni_{35}:Pt_{13}:Ru_{52}) in the as-cast condition. 31
Table 4.5. EDS analyses of LG 5 (Nominal Ni_{50}:Pt_5:Ru_{45}) in the as-cast condition. 34
Table 4.6. EDS analyses of LG 6 (Nominal Ni_{60}:Pt_5:Ru_{35}) in the as-cast condition. 37
Table 4.7. EDS analyses of LG 7 (Nominal Ni_{45}:Pt_{25}:Ru_{30}) in the as-cast condition. 40
Table 4.8. EDS analyses of LG 8 (Nominal Ni_{35}:Pt_{25}:Ru_{35}) in the as-cast condition. 43
Table 4.9. EDS analyses of LG 9 (Nominal Ni_{25}:Pt_{45}:Ru_{30}) in the as-cast condition. 46
Table 4.10. EDS analyses of LG 10 (Nominal Ni_{15}:Pt_{55}:Ru_{30}) in the as-cast condition. 49
Table 4.11. EDS analyses of LG 2 (Nominal Ni_{10}:Pt_{23}:Ru_{67}) in the annealed condition. 53
Table 4.12: EDS analyses of LG 3 (Nominal Ni_{20}:Pt_{20}:Ru_{60}) in the annealed condition. 56
Table 4.13: EDS analyses of LG 4 (Nominal Ni_{35}:Pt_{13}:Ru_{52}) in the annealed condition. 59
Table 4.14. EDS analyses of LG 5 (Nominal Ni_{50}:Pt_5:Ru_{45}) after heat treatment and a water quench. 62
Table 4.15: EDS analyses of LG 6 (Nominal Ni_{60}:Pt_5:Ru_{35}) after heat treatment and water quench. 65
Table 4.16: EDS analyses of LG 7 (Nominal Ni_{45}:Pt_{25}:Ru_{30}) after heat treatment and water quench. 68
Table 4.17: EDS analyses of LG 8 (Nominal Ni_{35}:Pt_{25}:Ru_{35}) after heat treatment and water quench. 71
Table 4.18. EDS analyses of LG 9 (Nominal Ni_{25}:Pt_{45}:Ru_{30}) after heat treatment and water quench. 74
Table 4.19: EDS analyses of LG 10 (Nominal Ni_{15}:Pt_{55}:Ru_{30}) after heat treatment and water quench. 77
Table 4.20. EDS analyses of LG 1 (Nominal $Ni_{47.5}$:$Pt_{47.5}$:Ru_5) after ordering heat treatment. 80
Table 4.21. EDS analyses of LG 11 (Nominal Co_{40}:Pt_{50}:Ru_{10}) in the as-cast condition (at.%). 83

Table 4.22. Unidentified peaks in the as-cast condition. 87
Table 4.23. EDS analyses of LG 12 (Nominal $Co_{15}:Pt_{75}:Ru_{10}$) in the as-cast condition (at.%). 88
Table 4.24. Unidentified peaks in the as-cast condition. 90
Table 4.25. EDS analyses of LG13 (nominal $Co_{90}:Pt_{5}:Ru_{5}$) in the as-cast condition (at.%). 91
Table 4.26. Unidentified peaks in the as-cast condition. 95
Table 4.27. EDS analyses of LG 14 (nominal $Co_{80}:Pt_{10}:Ru_{10}$) in the as-cast condition (at.%). 96
Table 4.28. Unidentified peaks in the as-cast condition. 99
Table 4.29 EDS analyses of LG 15 (nominal $Co_{30}:Pt_{20}:Ru_{50}$) in the as-cast condition (at.%). 100
Table 4.30. Unidentified peaks in the as-cast condition. 104
Table 4.31. Analyses LG 16 (Nominal $Co_{60}:Pt_{20}:Ru_{20}$) in the as-cast condition (at.%). 105
Table 4.32. Unidentified peaks in the as-cast condition. 109
Table 4.33. EDS analyses LG 17 (Nominal $Co_{10}:Pt_{30}:Ru_{60}$) in the as-cast condition (at.%). 110
Table 4.34. Unidentified peaks in the as-cast condition. 114
Table 4.35. Analyses LG 18 (Nominal $Co_{20}:Pt_{30}:Ru_{50}$) in the as-cast condition (at.%). 115
Table 4.36. Unidentified peaks in the as-cast condition. 119
Table 4.37. EDS analyses LG 19 (Nominal $Co_{50}:Pt_{20}:Ru_{30}$) in the as-cast condition (at.%). 120
Table 4.38. Analyses of LG13 (Nominal $Co_{90}:Pt_{5}:Ru_{5}$) in the heat treated condition (at.%). 125
Table 4.39. Unidentified peaks formed after heat treatment. 129
Table 4.40. Analyses of LG14 (Nominal $Co_{80}:Pt_{10}:Ru_{10}$) in the heat treated condition (at.%). 130
Table 4.41. Unidentified peaks formed after heat treatment. 134
Table 4.42. EDS analyses of LG15 (Nominal $Co_{30}:Pt_{20}:Ru_{50}$) in the heat treated condition (at.%). 135
Table 4.43 Unidentified peaks formed after heat treatment. 139
Table 4.44. EDS analyses of LG16 (Nominal $Co_{60}:Pt_{20}:Ru_{20}$) in the

heat treated condition (at.%). 140
Table 4.45. Unidentified peaks formed after heat treatment. 144
Table 4.45. EDS analyses of LG 17 (Co_{60}:Pt_{20}:Ru_{20}) in the heat treated condition (at.%). 145
Table 4.46. Unidentified peaks formed after heat treatment. 149
Table 4.47. EDS analyses of LG18 (Nominal Co_{20}:Pt_{30}:Ru_{50}) in the heat treated condition (at.%). 150
Table 4.48. Unidentified peaks formed after heat treatment. 154
Table 4.49. EDS analyses of LG19 (Co_{50}:Pt_{20}:Ru_{30}) in the heat treated condition (at.%). 155
Table 4.50. Unidentified peaks formed after heat treatment. 159
Table 4.51. EDS analyses of LG 11 (Nominal Co_{40}:Pt_{50}:Ru_{10}) after ordering heat treatment. 160
Table 4.52. Unidentified peaks formed after heat treatment. 162
Table 4.53. EDS analyses of LG 12 (Nominal Co_{15}:Pt_{75}:Ru_{10}) after ordering heat treatment (at.%). 163
Table 4.54. Unidentified peaks formed after heat treatment. 165
Table 4.55. Hardness values of the as-cast Ni-Pt-Ru alloys. 166
Table 4.56. Hardness values of the heat treated Ni-Pt-Ru alloys. 168
Table 4.57. Comparison of as-cast and heat treated hardness values. 173
Table 4.58. Hardness values and phase proportions of the as-cast Co-Pt-Ru alloys. 176
Table 4.59. Hardness values of the heat treated Co-Pt-Ru alloys. 177
Table 4.60. Hardness values of the as-cast Co-Pt-Ru alloys. 182

1. INTRODUCTION

1.1 Rationale for the project

Superalloys were developed for use at elevated temperatures where high yield stresses and high resistance to environmental attack are essential. Various superalloys are in use of which the nickel-based superalloys (NBSAs) are the most sophisticated and widely used. However, NBSAs have almost reached their temperature limits for operation in high temperature applications (e.g. turbine engines), because these operating temperatures are close to the melting point of the NBSAs. Thus, the need for materials with increased operational temperatures is apparent. Higher operating temperatures mean improved fuel efficiency, reduced pollution and greater thrust-to-mass ratios, which in turn leads to greater economical and environmental benefits [1987Sim]. Alloying additions and new processing techniques allow some of these alloys to be used at about 1100°C (~90% of their melting temperatures). Oxidation resistance of the alloys also places a limit on the maximum operational temperature. When NBSAs are exposed to an oxidizing environment, they form an aluminium oxide film to protect the underlying metal. Interdiffusion occurs at elevated temperatures between the coating and the substrate metal that alters the properties of both materials, rendering the oxide film less effective against further oxidation. [1987Sim, 1999Cle, 2001Süs, 2006Mal].

The high temperature strength of NBSAs arise mainly from the hardening of a γ matrix by cuboidal γ′ precipitates ($Ni_3(Al,Ti)$), although there are other phases present, such as grain boundary γ′, carbides, borides and T.C.P.-type (topologically close packed) phases. The matrix is a nickel-rich austenitic f.c.c. solid solution. NBSAs also contain several other alloying elements that benefit the γ′ phase:

- Nb, Ta combine with Ni to form intermetallic γ precipitates;
- Mo, W, Cr, Ta provide solid solution strengthening to the γ matrix;
- Co raises the γ′-solvus temperature (too much Cr lowers it);
- B, C form grain boundary phases;
- Cr, Mo, Ta, Hf strengthen the grain boundary phases;
- Al, Cr form oxides for oxidation protection;
- Cr, Ti enhances the hot corrosion resistance of NBSAs [1985Don].

An analogue of a nickel-based superalloy has been conceived [2000Wol], developed and optimised at Mintek and at the University of the Witwatersrand (Wits) [2001Hil, 2002Hil, 2002Süs1, 2004Cor, 2006Cor]. The superalloy is based on platinum, because of its higher melting point and chemical and structural similarity to nickel, which allows the presence of the γ/γ′ microstructure. The most optimum alloy to date is Pt_{84}:Al_{11}:Cr_2:Ru_3 (at.%) [2001Hil], although more work is in progress [2008Sho]. The advantage of this superalloy is that it has a higher melting point and exceptional environmental resistance at high temperatures [2004Cor, 2003Gla, 2002Süs1, 2002Cor]. The higher environmental resistance arises from the formation of a thin scale on the surface of the alloys. The combination of Pt, Al and Ru has a significantly improved effect on the hot corrosion resistance of alloys containing the three elements [2006Mal].

As well as the practical work, a Thermo-Calc™ thermodynamic database is being developed at Mintek and Wits. Thermo-Calc™ uses phase diagram information as well as thermodynamic data for the modelling of phases in simple and higher order alloys. This reduces experimental work and is also a tool to facilitate alloy development. In Thermo-Calc™, the Parrot module is being used to optimise coefficients and to extend the databases based on the data available in the SGTE group [1985Sun, 1991Din]. Results from this phase diagram work will be input to Thermo-Calc™ for optimization at a later stage.

Additionally, Pt is useful in strengthening the coatings on existing NBSAs [1996New]. Pt-modified aluminide coatings on nickel-based superalloys have been used for over a decade. A fundamental understanding of this mechanism and the degradation mechanism of these coatings is needed to optimise the Pt-modified alumina coatings. This will make the application of the coatings more cost effective and promote the use of it in other applications. Ruthenium additions are also beneficial to the coatings on NBSAs. Ru forms a solid solution with Pt [1990Mas, 1990ASM] and has a strengthening effect in the bulk form. It has been reported that the strengthening effect increases the tensile strength by a factor of 2-4 at low temperatures [1978Sav] and Ru additions decrease the creep rate at temperatures up to 1300°C by two orders of magnitude [1981Usi, 2004Hyu].

Although Pt-Al-Cr and Pt-Al-Ru alloys are very strong, they can be formed by heat treatment and hot rolling [2002Süs2]. It has been shown that Co additions increase the room temperature ductility of these alloys [2003Cho]. The motivation behind Co additions to Pt-Al-Cr-Ru alloys is

to facilitate the manufacturing process, and by possibly utilising thinner cross-sections, provide a lighter, more affordable high temperature Pt-based alloy.

Between 10-15 wt% cobalt in NBSAs provides solid solution strengthening and decreases the solubility of aluminium. This increases the volume fraction of γ′ precipitate in the γ matrix [2004Key]. Cobalt, with its slightly higher melting point, also increases the temperature range of nickel-based superalloys.

1.2 Reasons for interest in the Ni-Pt-Ru and Co-Pt-Ru systems

Ni-Pt-Ru system

The Pt-Ni-Ru system is one system that was studied here to understand and optimise the coatings and bulk material with both Pt and Ru additions. The binary systems are well known [1990Mas], but no literature on the ternary was found. The Pt-Ru and Ru-Ni binary phase diagrams are simple peritectic systems, whereas the Ni-Pt binary is a continuous solid solution with some ordering [1990Mas]. The ternary is expected to contain a simple peritectic, with the ordering extending into the ternary system from the Ni-Pt binary. The extent of the phases in the ternary and extent of the ordering needs to be established.

Co-Pt-Ru system

The Pt-Co system has some ordering in the continuous solid solution, whereas Co-Ru and Pt-Ru systems are simple peritectic systems [1990Mas]. No literature on the ternary was found. The extents of all the phases into the ternary need to be investigated. Additionally, the system needs to be checked for ternary phases, which might be deleterious to the properties.

1.3 Benefits that could arise from the investigation (SA, PDI and CSIR)

South Africa is the largest producer of platinum group metals (PGMs) in the world and traditionally exports most of its platinum without adding much value. If more value-addition was done in South Africa, there would be more profit and job creation, which would help the South Africa economy grow.

The Platinum Development Initiative (PDI) was a project between the three major platinum producers (Angloplat, Lonmin and Implats) and Mintek to perform research into new industrial uses for platinum between 1998 and 2007.

A project called the "Platinum Beneficiation Initiative" was run by a CSIR-based consortium, in which Mintek was a member, funded by the Innovation Fund between 2004 and 2006. Part of this project aimed to "Develop a fundamental understanding of Pt-aluminide crystal structures and bonding mechanisms of Pt-based coatings to nickel-based superalloy substrates through ab initio considerations to advance mechanical modeling methods, based on fundamental experimental research" [2004nml]. The current work was initiated within that project.

2. Literature Review

2.1 Introduction

Pt-based alloys are being developed to possibly replace nickel-based superalloys (NBSAs). Pt-based alloys have a similar microstructure to that of the NBSAs and consist of a Pt-based matrix with ~Pt_3Al precipitates. Pt-based alloys are more chemically inert than NBSAs because of the high Pt content and Pt is more noble than Ni. The melting point is also higher and the Pt-based alloys can be used in environments which require exceptional environmental resistance at higher temperatures [2001Süs3].

2.2 General Platinum Alloys

2.2.1 Autocatalysts

The largest portion of platinum produced is used by the autocatalysts industry [2008Pla]. A catalytic converter is installed in the exhaust line of a vehicle. The converter contains a fine honeycomb structure that is coated with a catalyst. The most common catalysts are the heterogeneous type where pure platinum (and other PGMs) are placed on a support. The support consists of a single metal oxide or a combination of different oxides; examples are Pt/SiO_2, $Pt/CoO_x/SiO_2$ and $Pt/MnO_x/SiO_2$ [2008Pla, 2003Twi].

Exhaust gases from vehicles contain pollutants such as CO, NO_x gases, hydrocarbons and particulates. Autocatalysts convert approximately 90% of these pollutants to CO_2, N_2 and water vapour and 30-40% of the particulates to CO_2 and water vapour. A large proportion of all vehicles sold annually are fitted with catalytic converters. The consumption of platinum in autocatalysts is increasing as more vehicles are sold annually and governments are introducing stricter emission control standards through lower limits [1981Diw, 1988Sea, 1999Twi].

2.2.2 Jewellery

The platinum jewellery industry is the second largest consumer of Pt in the world. Most jewellery alloys consist of 95 wt% Pt and they are usually alloyed with other PGMs like Ru or Cu. The alloying additions are made to optimise the workability and wear resistance of the alloys. The main attraction of platinum as a jewellery alloy is its strength and resistance to tarnishing. These qualities allow for designs beyond the scope of gold alloys. Platinum

jewellery is also perceived to have a more modern style by young people in the East and Europe. In North America its appeal as bridal jewellery is also growing rapidly [2008Pla].

2.2.3 Electrical

Palladium is mostly used for electronic components but platinum is used in sensors. Platinum wire is used in sensors detecting CO, NO_x and O_2 concentrations in several different applications. Oxygen sensors are used in engine control systems to optimise the air to fuel ratio and in vehicle inspection and maintenance systems [1997Mil]. Carbon monoxide and NO_x sensors are used in the climate control systems of vehicles. These detect CO and NO_x concentrations inside the vehicle and adjust the ventilation system accordingly and these sensors are also part of certain specialised autocatalysts to minimise emission levels to the atmosphere. Air-mass flow sensors are placed at the cylinders in engines to measure the airflow to each cylinder. A fine platinum wire coated with explosives can be found in sensors in air bags to facilitate the release of the air bag in the event of an accident. Platinum wire containing CO detectors are situated in homes and industrial buildings as a safety feature. Platinum wire, foil and discs are present in medical detectors for the analyses of blood gases [1993Lei].

2.2.4 Chemical Industry

2.2.4.1 Petroleum

Platinum catalysts are being used in the upgrading of low octane petroleum to high-quality products and in converting petrochemical feedstock to plastics, synthetic rubber and polyester fibres [1957Cur].

2.2.4.2 Fuel cells

Fuel cells use platinum catalysts to produce electricity by combining hydrogen and oxygen. Fuel cells need no recharging and will run indefinitely when supplied with fuel and can be use to supply electrical power to industrial plants, to mobile phone and laptop computers. They can also be a replacement for internal combustion engines in vehicles. The replacement of conventional power stations and internal combustion engines will lead to a significant reduction in environmentally harmful emissions (CO, NO_x and CO_2). However, the largest obstacle is the cost of commercialisation of this method of electricity production. It is also difficult to up-scale the process successfully.

2.2.5 Glass Industry

Platinum and its alloys are widely used in the glass production industry because these materials react very slowly with glass, oxidise or form scale at the melting temperatures of the different minerals that glass contains (up to 1700°C). The largest proportion of platinum is used in the manufacture of reinforcement fibre (glass fibre). The molten glass is poured in a platinum alloy container with precisely shaped holes through which the fibres are drawn. The molten glass is stirred using components made out of pure Pt, Pt-Ru, Pt-Ru DPH and Pt-Rh-Au alloys. Liquid crystal displays (LCDs), for use in digital watches and laptops require high quality glass (0.5mm thickness) and is the most intensive user of platinum. In these instances pure Pt or Pt-5%Au DPH alloys are used. Rhodium oxides can form when the molten glass is in contact with the Rh-containing alloy and so contaminate the glass. Cathode ray tubes (CRTs), previously used as television and computer screens, optical and ophthalmic glasses are manufactured using platinum and rhodium alloys in the melting, conditioning and forming phases [1975Loe,1965Sel].

2.3 Ni – Pt - Ru (Nickel – Platinum - Ruthenium)

There are no data available on the Ni-Pt-Ru system. However, there are a few articles on the three binary systems.

2.3.1 Binary Ni-Pt system

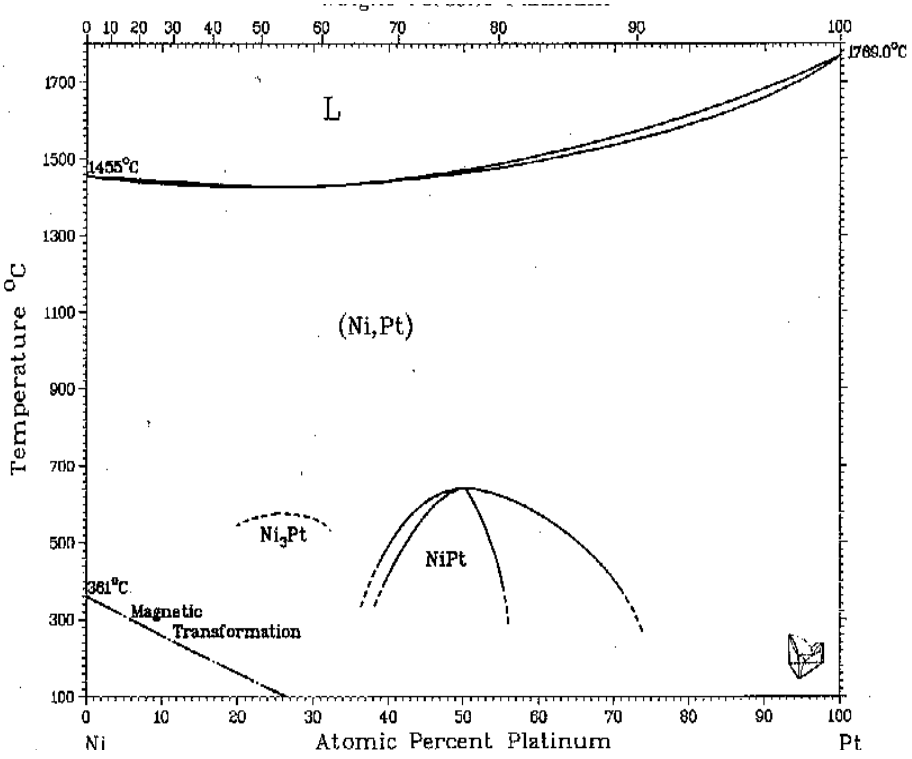


Figure 2.1. Binary Ni-Pt equilibrium phase diagram [1990Mas].

The most recent data available in the literature on the Ni-Pt phase diagram is by Nash [1991Nas1] in Figure 2.1. The phase diagram is unchanged from the diagram given by Hansen [1958Han]. Table 2.1 shows the solid fcc phases occurring in the Ni-Pt system shown in Figure 2.1. There are four phases known: (Ni,Pt), Ni_3Pt and NiPt and $NiPt_3$. Although this is a mainly solid solution phase diagram, there are three ordered phase regions that can be found at ~ 21-31 at.% Pt (Ni_3Pt), at ~ 40-50 at.% Pt (NiPt) and at ~ 65-74 at.% Pt ($NiPt_3$). According to Orani *et al*. [1953Ora], the disordering temperature of a Ni_3Pt is ~ 580°C and it has the Cu_3Au ($L1_2$)-type structure [1958Han]. NiPt, at the equiatomic composition, has a disordering temperature of ~ 645°C and has a tetragonal CuAu ($L1_0$) structure [1958Han]. $NiPt_3$ has a congruent formation temperature that is slightly lower than that of Ni_3Pt [1985Dah]. The phase equilibria are shown in Table 2.2. The system was determined through X-ray diffraction and microscopy [1978Ste]. Activities of Ni in the system were determined using electrical measurements [1931Kur], e.m.f. measurements [1965Sch] and the torsion-effusion vapour-pressure technique [1970Wal].

Table 2.1. Solid phases in the Ni-Pt binary phase diagram.

Phase/ Temperature Range (°C)	**Pearson Symbol/ Space Group/ Prototype**	**Lattice Parameters (nm)**	**References**
(Ni,Pt)	*cF*4 $Fm\bar{3}m$ Cu	a = 0.29233 – 0.35240	[1991Nas1]
Ni_3Pt	*cP*4 $Pm\bar{3}m$ $AuCu_3$	-	[1991Nas1]
NiPt	*TP*4 *P*4/*mmm* AuCu	a = 0.3873 c = 0.3589	[1991Nas1]
$NiPt_3$	-	-	[1985Dah]

Table 2.2. Invariant equilibria for the Ni-Pt binary phase diagram.

Reaction	T (°C)	Type	Phase	Ni at.%	Pt at.%
(Ni,Pt) → Ni_3Pt	~ 500 - 620	Ordering	(Ni,Pt) Ni_3Pt	21 - 31	69 - 79
(Ni,Pt) → NiPt	~ 400 - 645	Ordering	(Ni,Pt) NiPt	40 - 55 at 400°C	45 - 60 at 400°C
(Ni,Pt) → $NiPt_3$		Ordering	(Ni,Pt) $NiPt_3$	20 - 40	60 - 80

2.3.2 Binary Pt-Ru system

The latest available information on the Pt-Ru binary phase diagram, shown in Figure 2.2, by Massalski [1990Mas] is redrawn from Hutchinson [1972Hut]. Watson *et al.* [2007Wat] calculated a phase diagram using Pandat and optimisation using WinPhaD that is shown in Figure 2.3. They used data obtained by Hutchinson [1972Hut] for the Pandat calculations. It shows a very shallow eutectic reaction but has a reasonable fit with the phase boundaries for the two-phase field ((Ru) + (Pt)) of the experimental phase diagram in Figure 2.2. The solid phases of the Pt-Ru system are shown in Table 2.3. At 1000°C, the solubility of Ru in Pt is ~62 at.% and it increases to 70 at.% at 1900°C. The solubility of Pt in Ru at 1000°C is 20 at.% and there is very little increase in solubility as the temperature rises. Above ~2000°C, the solidus and liquidus lines are tentative. There is no intermediate phases present, so it is assumed that the system is a simple peritectic. The phase equilibrium is shown in Table 2.4.

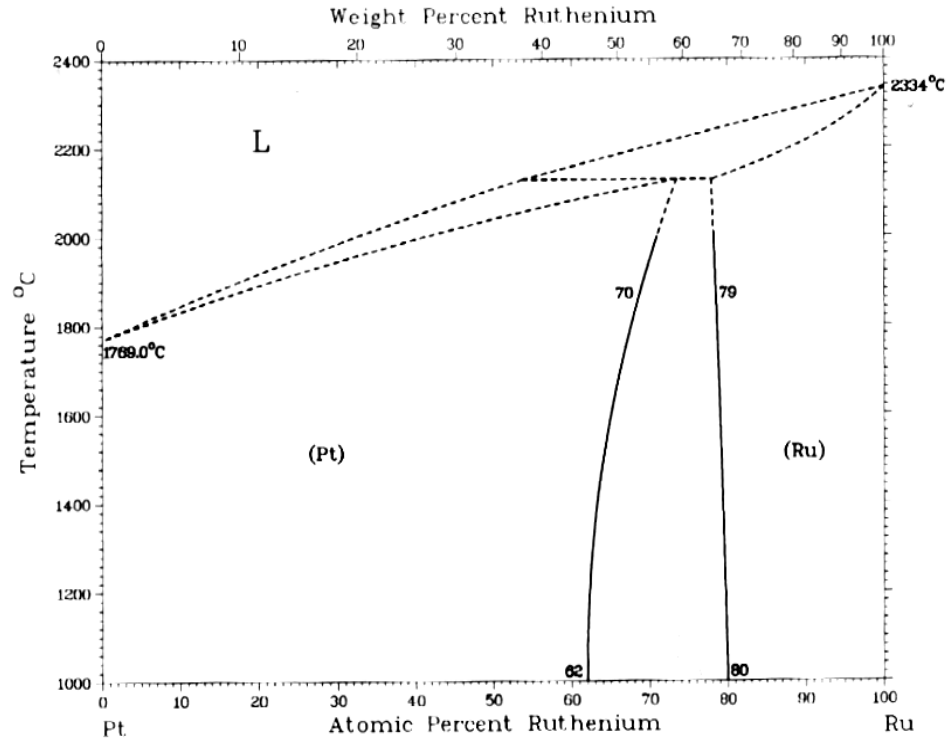


Figure 2.2. Binary Pt-Ru equilibrium phase diagram [1990Mas].

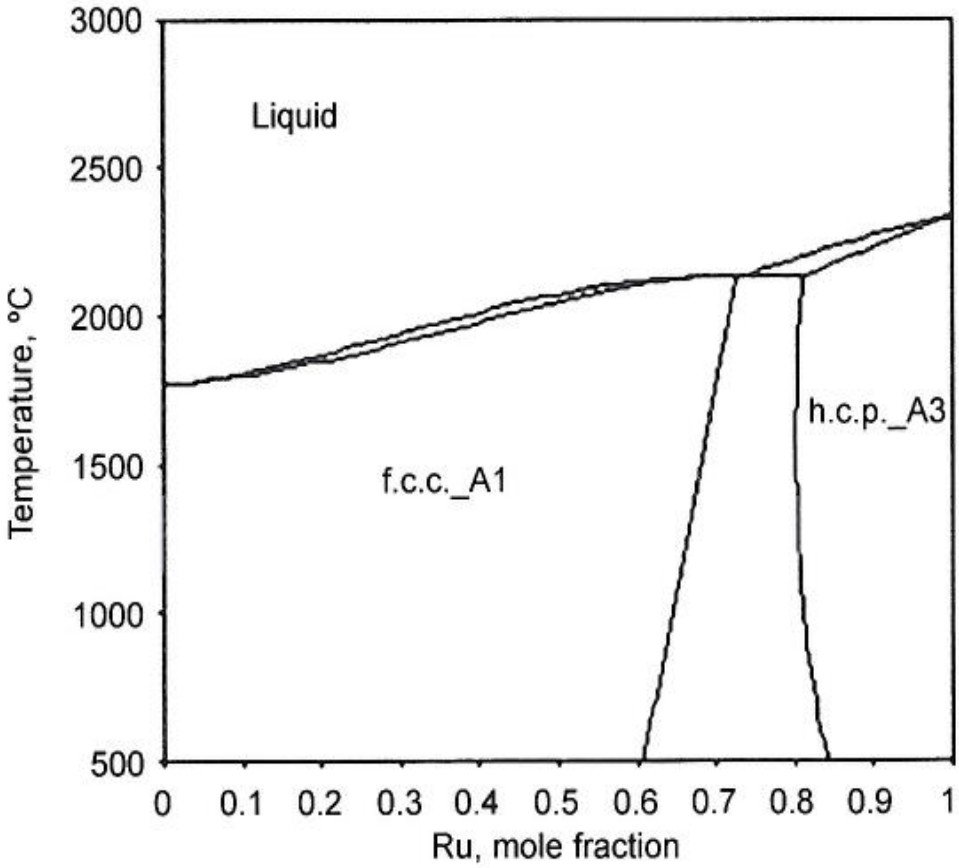


Figure 2.3. Calculated Pt-Ru phase diagram [2007Wat].

Table 2.3. Solid phases in the Pt-Ru binary phase diagram.

Phase	Pearson Symbol/ Space Group/Prototype	Lattice Parameters (nm)	References
(Pt)	*cF*4 $Fm\bar{3}m$ Cu	$a = 3.82$	[2005ICD]
(Ru)	*hP*2 $P6_3/mmc$ Mg	$a = 2.7$ $c = 4.275$	[2005ICD]

Table 2.4. Invariant equilibrium for the Pt-Ru binary phase diagram.

Reaction	T (°C)	Type	Phase	Pt at.%	Ru at.%
L + (Ru) → (Pt)	~ 2100°C	Peritectic	L (Pt) (Ru)	47 27 21	53 73 79

2.3.3 The binary Ni-Ru phase diagram

The Ni-Ru system (Figure 2.4) is also a simple peritectic system according to Nash [1991Nas2], with the peritectic temperature at 1550°C and at 34.5 – 50 at.% Ru. The peritectic liquid composition at 1550°C is 27 at.% Ru and experimental data is available up to 50 at.% Ru, after which the liquidus is extrapolated to the melting point of Ru at 2334°C [1991Nas2]. The solidus line was also experimentally determined up to ~70 at.% Ru and is extrapolated to the Ru melting point. The solid phases are shown in Table 2.5. The (Ni) and (Ru) phases are wide at high temperatures at high temperatures and become narrower as the (Ni) + (Ru) phase field increases in width with lowering temperatures. Nash reported on Ni-Ru alloys in the range of 30-40 at.% Ru that were melt spun and a metastable phase, and η (tetragonal) was synthesised [1991Nas2]. The phase boundaries have been determined through thermal analysis and microscopy [1961Rau, 1964Kor, 1937Mar, 1979Var]. The phase equilibrium is shown in Table 2.6.

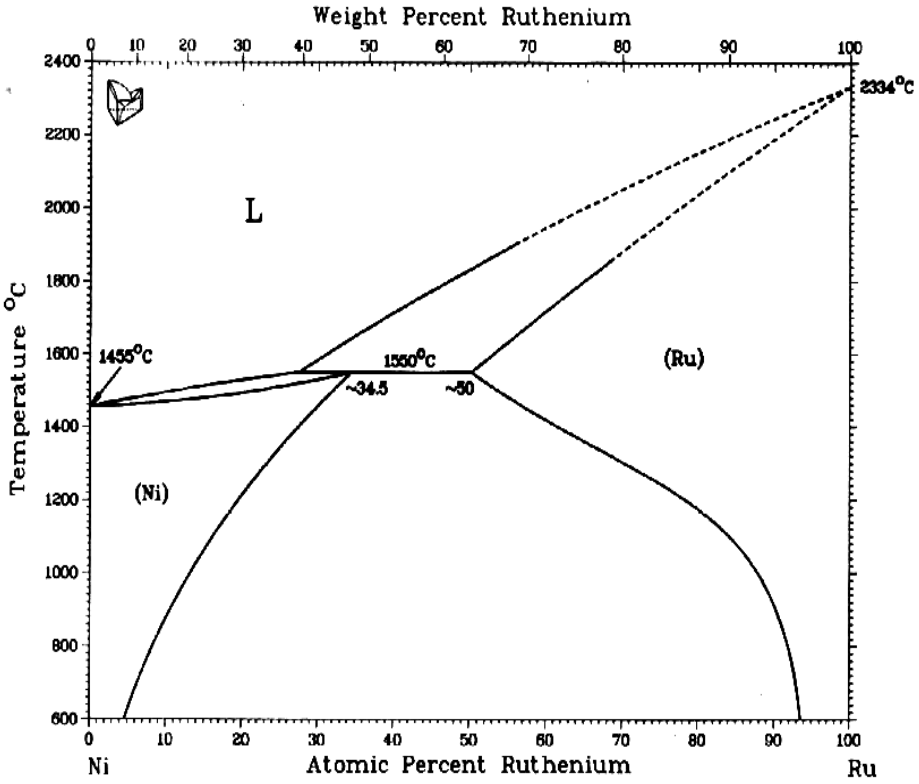


Figure 2.4. Binary Ni-Ru equilibrium phase diagram [1990Mas].

Table 2.5. Solid phases in the Ni-Ru binary phase diagram.

Phase	**Pearson Symbol/Space Group/Prototype**	**Lattice Parameters (nm)**	**References**
(Ni)	*cF*4 $Fm\bar{3}m$ Cu	a = 0.3524	[1991Nas2]
(Ru)	*hP*2 $P6_3/mmc$ Mg	a = 0.27053 c = 0.42814	[1991Nas2]
η		a = 0.45106 c = 0.362016	[1991Nas2]

Table 2.6. Invariant equilibrium for the Ru-Ni binary phase diagram.

Reaction	**T (°C)**	**Type**	**Phase**	**Ni (at.%)**	**Ru (at.%)**
L + (Ru) → (Ni)	1500	Peritectic	L	72	28
			(Ru)	65.5	34.5
			(Ni)	50	50

2.4 Co – Pt - Ru (Cobalt – Platinum - Ruthenium)

There are no data available on the ternary phase diagram for the Co-Pt-Ru system, except what was produced during the course of this work. However, there are data on the three binary systems: Pt-Ru, Co-Pt and Co-Ru. The Pt-Ru system was described in the Ni-Pt-Ru section.

2.4.1 Binary Co-Pt system

The Co-Pt system is shown in Figure 2.5 [1952Kos] and the calculated phase diagram is shown in Figure 2.6 [2001Oik]. The binary diagram was established through thermal analysis [1933Nem, 1940Geb]. Although this is mainly a solid solution phase diagram, there are five reported phases that form below 1000°C: (αCo,Pt); two ordered phases (Co_3Pt and CoPt); (αCo) and (εCo) that forms through a martensitic transformation. The magnetic transformation line starts at 1121°C (100 at.% Co), and it continues down to ~88 at.% Co at room temperature. The influence that the magnetic ordering in the Co-Pt system has on the total Gibbs energy G_m of the FCC phase of Co-Pt system at 400°C is shown in Figure 2.7. The Co-Pt system has a negative enthalpy and the FCC phase is chemically miscible (dashed line, Figure 2.7). Thus, Pt addition to Co gradually decreases the Curie temperature and the magnetic moment. The result is that no magnetically induced phase separation occurs [2001Oik], and according to Oikawa *et al.* the calculated phase diagram is in good accordance the experimental system.

The Pearson symbol, space group, prototype and lattice parameters are also shown in Table 2.7. Table 2.8 gives the invariant equilibria for the different Co-Pt phases that form. The first ordered region, forming CoPt, found in the range 41-75 at.% Pt, occurs from 825°C and the second, forming Co_3Pt, at 75 at.% Pt, occurs from ~750°C [1958Han]. CoPt and Co_3Pt have AuCu ($L1_0$) and $AuCu_3$ ($L1_2$) structures, respectively [1958Han]. Zhao described the (αCo) $\rightarrow$ (εCo) transformation as a martensitic transformation [1999Zha]. The transformation starts at 422°C in pure cobalt and reaches a maximum at ~575°C and ~8 at. % Pt, after which it decreases again. The binary diagram was established through thermal analysis [1933Nem, 1940Geb, 1951New, 1952Gei].

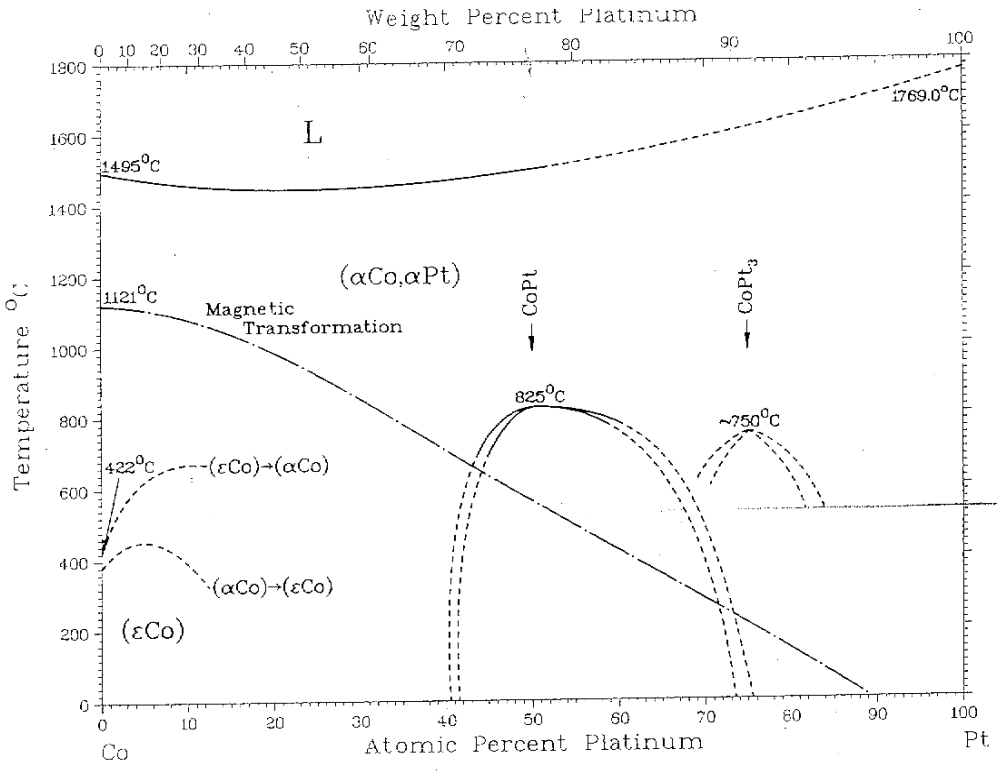


Figure 2.5. Binary Co-Pt equilibrium phase diagram [1990Mas].

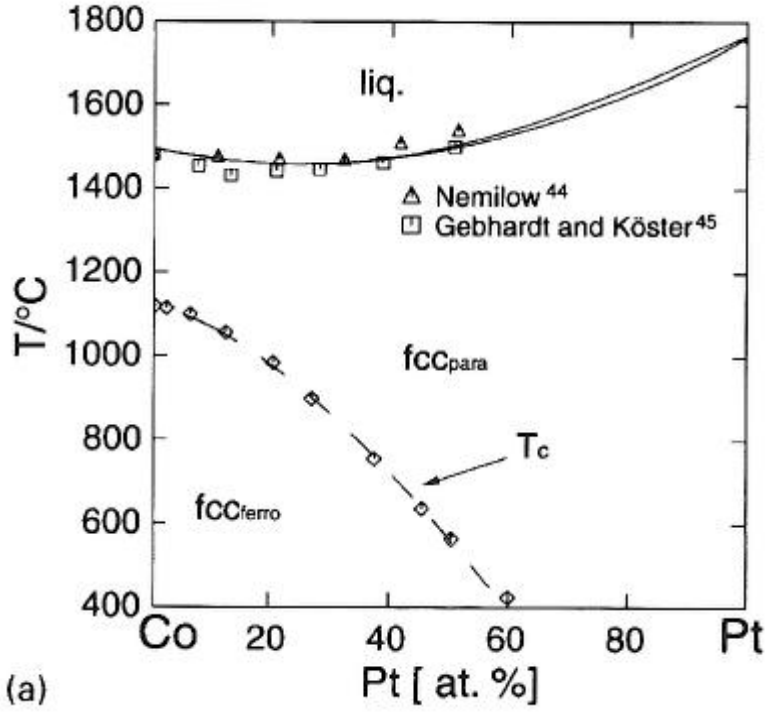


Figure 2.6. Calculated Co-Pt phase diagram [2001Oik].

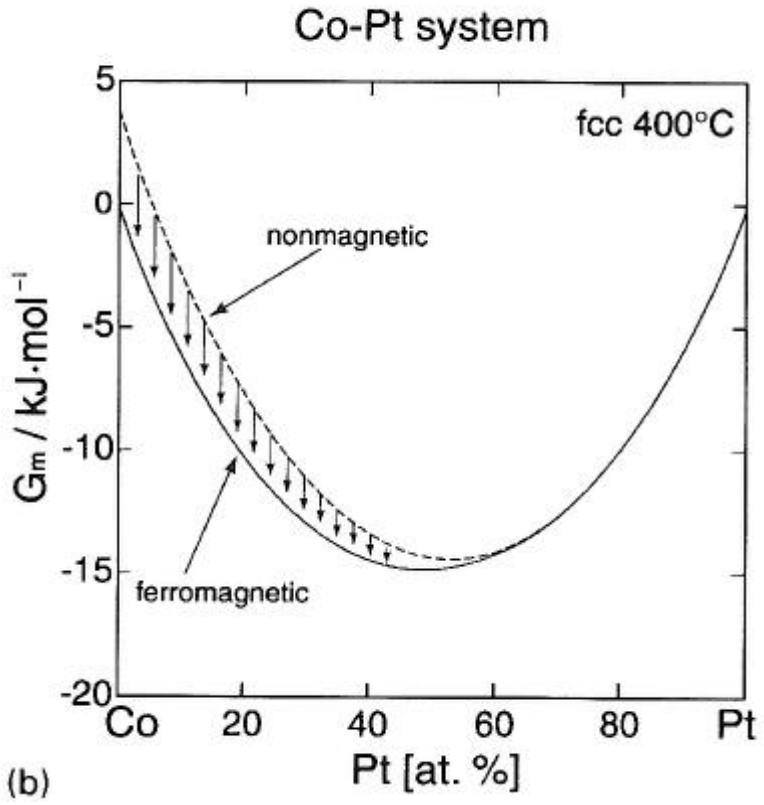


Figure 2.7. The total Gibbs energy G_m of the Fcc phase at 400°C with reference to Co and Pt in the Co-Pt system. The dashed line shows the Gibbs energy curve without the magnetic contribution term ${}^{mag}G_m$ [2001Oik].

Table 2.7. Solid phases in the Co-Pt binary phase diagram

Phase	**Pearson Symbol/ Space Group/ Prototype**	**Lattice Parameters (nm)**	**References**
(αCo,Pt)	*cF*4 $Fm\bar{3}m$ Cu	a = 3.829	At 70 at.% Pt [1958Han]
(εCo)	*cP*2 $P6_3/mmc$ Mg	a = 2.514 c = 4.105	[2005ICD]
CoPt	*tP*4 *P*4/*mmm* AuCu	a = 3.793 c = 3.675 c/a = 0.969	[1958Han]
$CoPt_3$	*cP*4 $Pm\bar{3}m$ $AuCu_3$	a = 3.831A	At 70 at.% Pt [1958Han]

Table 2.8. Invariant Equilibria for the Co-Pt binary phase diagram.

Reaction	**T (°C)**	**Type**	**Phases**	**Co**	**Pt**
(αCo,Pt)→ (εCo)	422°C	Martensitic	(αCo,Pt) (εCo)	76 – 100 above 422°	0 – 14 above 422°
(αCo,Pt)→ CoPt	825°C	Ordering	(αCo,Pt) CoPt	~ 26 – 58 at RT	~ 42 – 74 at RT
(αCo,Pt) → $CoPt_3$	~750°C	Ordering	(αCo,Pt) $CoPt_3$	25 at ~750°C	75 at ~750°C

2.4.2 The binary Co-Ru phase diagram

The Co-Ru phase diagram (Figure 2.6) is a peritectic system with the lines extrapolated above 1200°C. There is a minimum in the liquidus temperature at ~90 at.% Ru. The phase field where (αCo) and (εCo,Ru) are found is wide and stretches from ~16 at.% to 34 at.% Ru at ~1500°C. The phase field where L and (Co,Ru) co-exists is also assumed to be wide. There are lines representing the Curie temperature of (αCo) and (εCo). The line starts at 100 at.% Co (1121°C) and drops down to ~35 at.% Ru. The Pearson symbol, space group, prototype and lattice parameters are shown in Table 2.9. The invariant equilibrium is shown in Table 2.10. The reaction is L + (εCo,Ru)→ (αCo). There is a minimum in the (αCo) liquidus which occurs at ~10 at.% Ru and just above 1400°C.

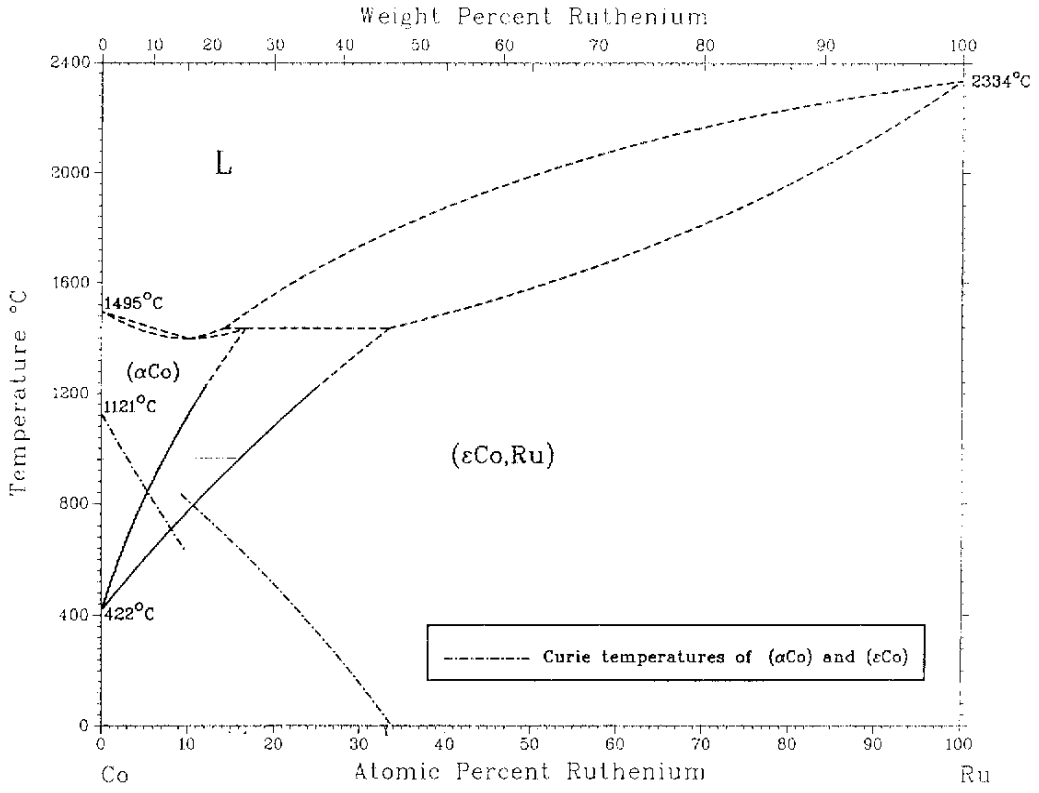


Figure 2.8. Binary Co-Ru equilibrium phase diagram [1990Mas].

Table 2.9. Solid phases in the Co-Ru binary phase diagram.

Phase	Pearson Symbol/ Space Group/Prototype	Lattice Parameters (Å)	Comments
(αCo)	*cF*4 $Fm\bar{3}m$ Cu	a = 3.5447	[1990Mas] [2005ICD]
(εCo,Ru)	*hP*2 $P6_3/mmc$ Mg	a = 2.6 c = 4.165	[1990Mas] [2005ICD]

Table 2.10. Invariant equilibrium for the Co-Ru binary phase diagram.

Reaction	T (°C)	Type	Phase	Co at.%	Ru at.%
L + (αCo,Ru) → (αCo)	~1450	Peritectic	L (αCo,Ru) (αCo)	86 85 67	14 15 33

3. EXPERIMENTAL PROCEDURE

3.1 Sample Manufacture

The nominal Ni-Pt-Ru alloys are shown in Figure 3.1 and the nominal Co-Pt-Ru alloys are shown in Figure 3.2. In each case, the phase boundaries within the ternaries were guessed. The alloys for the two ternary systems were chosen to determine the extent of the two-phase field and to establish how far the binary ordering extends into the ternary system. Some of the alloys were chosen subsequently to determine the deflection of the phase boundaries that was observed in this investigation.

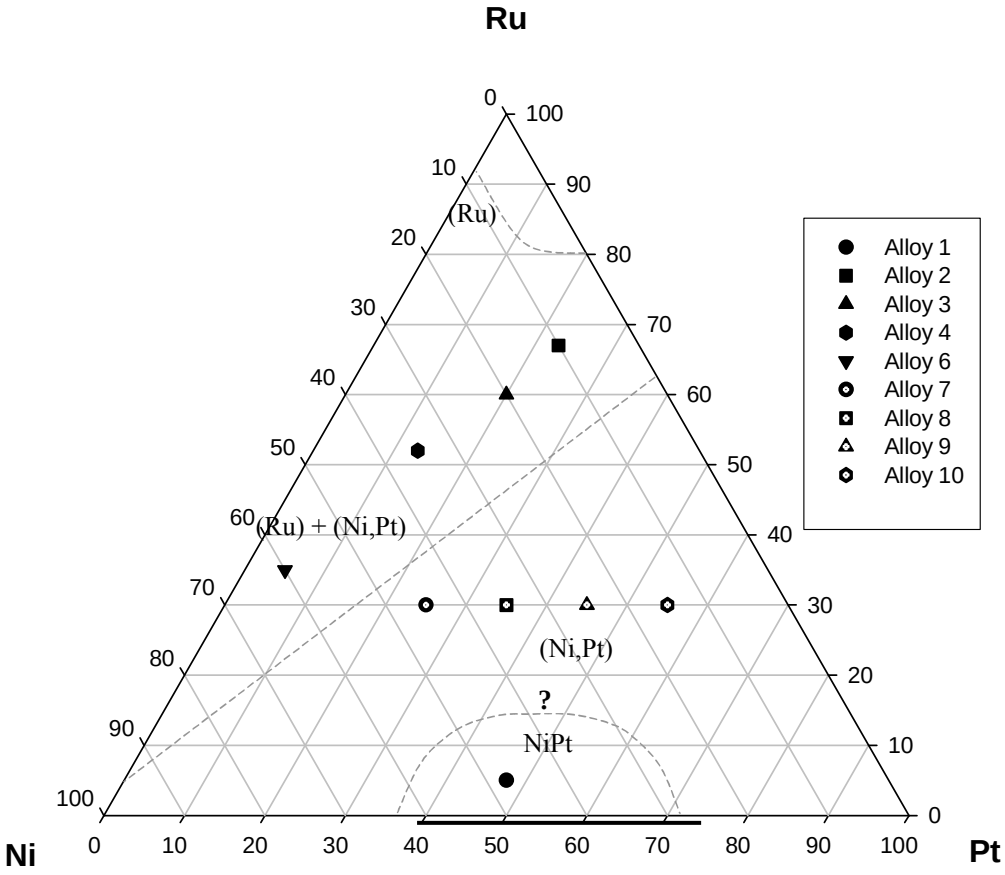


Figure 3.1. Compositions of nominal Ni-Pt-Ru alloys (at.%).

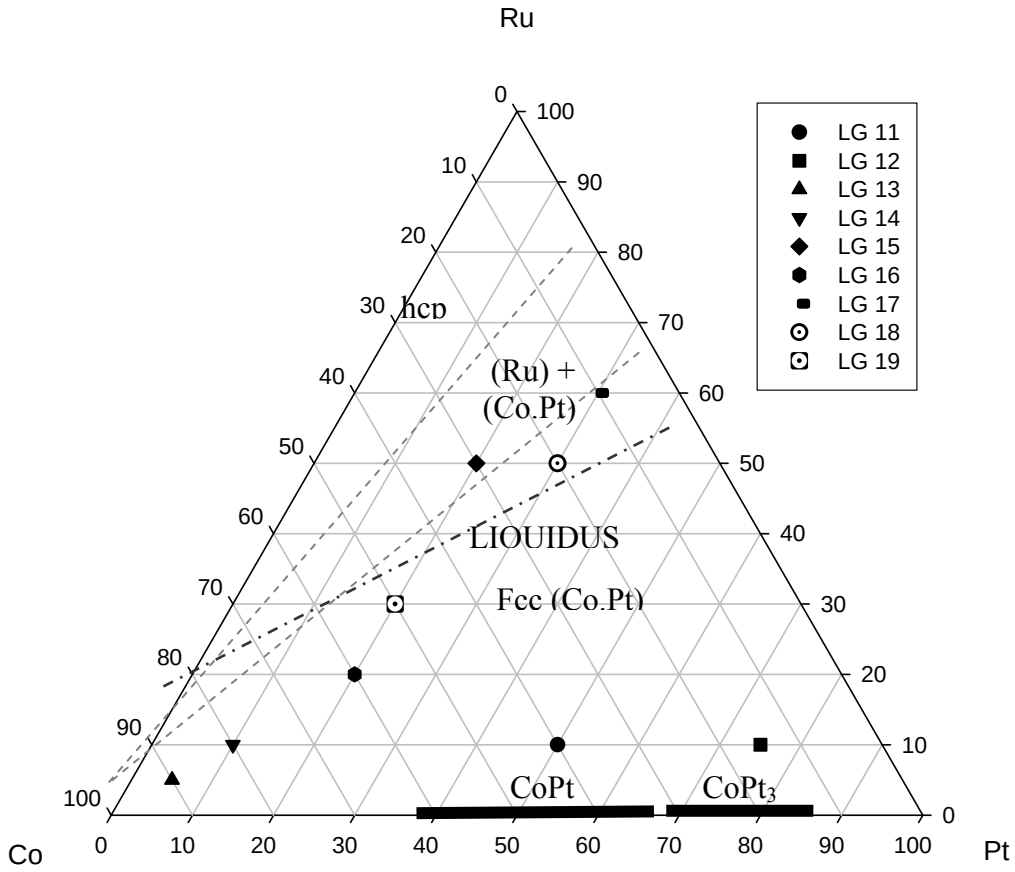


Figure 3.2. Compositions of nominal Co-Pt-Ru alloys (at.%).

The different source metals in the alloys were chemically pure (at least 99.9 wt%). The component metals for each 2g button were weighed out and arc-melted under a protective argon atmosphere on a copper hearth, using titanium as an oxygen getter. The samples were melted three times to make them as homogeneous as possible. The samples were cut in half with a Struers Secotom-10® cutting wheel. One half of each sample was left in the as-cast condition and the other half was heat treated at 1000°C for 1000 hours, except for the alloys that were prepared for checking the extent of ordering in the ternary systems. These samples were heat treated at 500°C for 1000 hours.

3.2 Metallography

The samples were all mounted and ground flat using 380, 800 and 1200 grit SiC paper. Polishing was done to a 1μm surface finish using a diamond suspension. No etching was done as all the imaging was performed in back-scattered electron mode on the scanning electron microscope. This was possible because the average atomic number of each different phase differed significantly. The higher the average atomic number of the phase, the lighter it appears

in the image in backscattered electron mode. Low average atomic numbers thus corresponded to darker areas on the image.

The phase proportions were determined using a 16 square grid. The grid was placed over the micrographs and the corners what were overlaid by a specific phase were counted and a percentage was calculated [1988Exn]. Five different counts were made for each micrograph and a statistical error was determined. In each case this was 5% or less.

3.3 Characterisation

3.3.1 Scanning Electron Microscopy (SEM) and Energy Dispersive Spectrometry (EDS

The microstructures and compositions were examined on two different SEMs:

- JEOL JSM-840® scanning electron microscope (SEM) using a Tracor Northern® EDS system with Vantage software. Images of the microstructure were taken in the back-scattered electron imaging (BEI) mode. A Si p-n junction (divided annular type) was used as a BSE detector.
- FEI Nova NanoSEM® using an EDAX EDS system. Images of the microstructure were taken in the back-scattered electron imaging (BEI) mode. The detector is a solid state BSE detector.

The EDS analyses were all normalised.

3.3.2 XRD

X-ray diffraction (XRD) analyses were done on the polished samples in both as-cast and heat treated conditions. A Siemens D500 Kristalloflex with Mo Kα radiation using Diffrac Plus® software was used. The peaks were compared against peaks of known and expected phases in the database [2005ICD].

3.4 Mechanical Properties

3.4.1 Hardness and Toughness

Hardness can be used as a preliminary assessment of the mechanical properties of an alloy [1991Fle]. The hardness can give an indication of the strength and the toughness can be assessed by examining the hardness indentations. The appearance of the material around the indentations can be classified using the following:

- Cracks show that the alloy will be brittle;
- Planar slip and twinning shows a tougher alloy where the dislocation movement are accommodated in certain slip systems only; and
- Wavy slip indicates good resistance to cracking and that dislocation movement are accommodated in several slip systems.

The hardness measurements were performed on a Vickers (Ltd) Hardness Tester using a 10kg load. Five indentations were made on each alloy and an average hardness value was obtained. Micrographs of the hardness indentations were taken on an Olympus Vanox-T light microscope connected to a JVC TK138E Colour Video Camera.

4. RESULTS

4.1 Ni-Pt-Ru SYSTEM

4.1.1 As-Cast Alloys

LG 1 (Nominal $Ni_{47.5}$:$Pt_{47.5}$:Ru_5)

The targeted composition for Alloy 1 (Nominal $Ni_{47.5}$:$Pt_{47.5}$:Ru_5), (Figure 4.1) place it near the ordered region on the Ni-Pt phase diagram. The alloy is single-phase and the XRD spectrum (Figure 4.2) identified the alloy as the (Pt,Ni) solid solution since the peaks were between the pure Pt and pure Ni lines. The spectrum is clear and shows a high signal to background ratio with a good match for Ni and Pt peaks once they were shifted. The light and dark lumps are unmelted Pt and Ru respectively. The EDS phase analyses is shown in Table 4.1 and the actual composition is plotted in Figure 4.3.

The solidification sequence for the alloy is: $L \rightarrow$ (Ni,Pt).

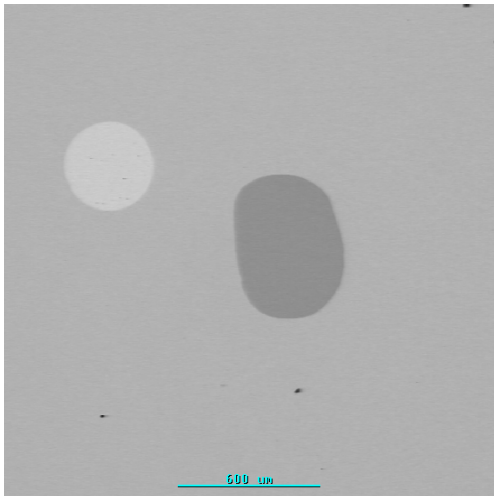


Figure 4.1. BEI of LG 1 (Nominal $Ni_{47.5}$:$Pt_{47.5}$:Ru_5) showing single phase (Ni,Pt) with unmelted Pt (light) and Ru (dark) (scale bar = 600μm).

Table 4.1. EDS analyses of LG 1 (Nominal $Ni_{47.5}$:$Pt_{47.5}$:Ru_5) in the as-cast condition.

Phase description	Ni (at.%)	Pt (at.%)	Ru (at.%)	Phase
Overall	47.7 ± 0.3	47.7 ± 0.2	4.6 ± 0.2	(Ni,Pt)

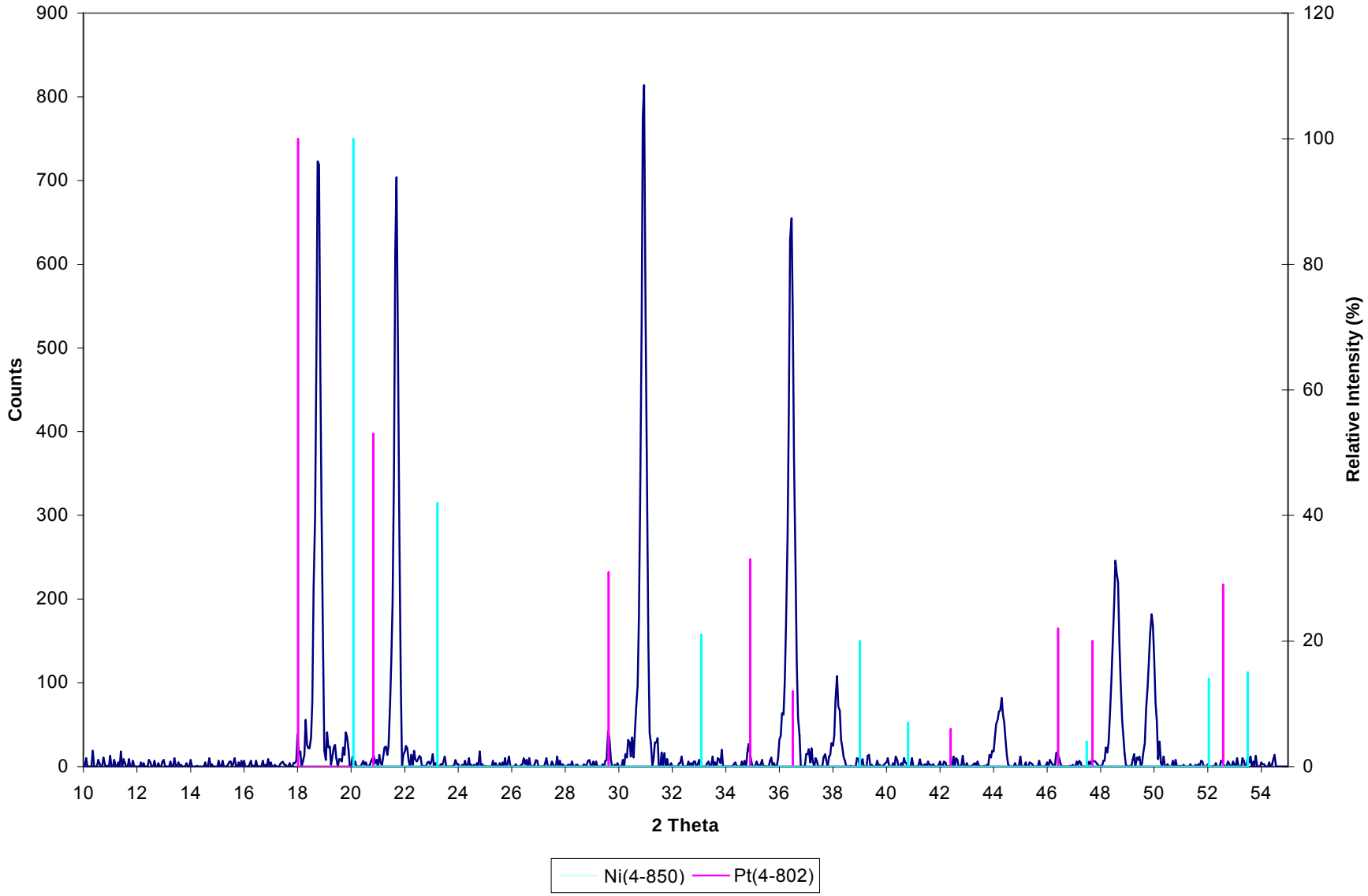


Figure 4.2. XRD spectrum of LG 1 (Nominal $Ni_{47.5}$:$Pt_{47.5}$:Ru_5) in the as-cast condition.

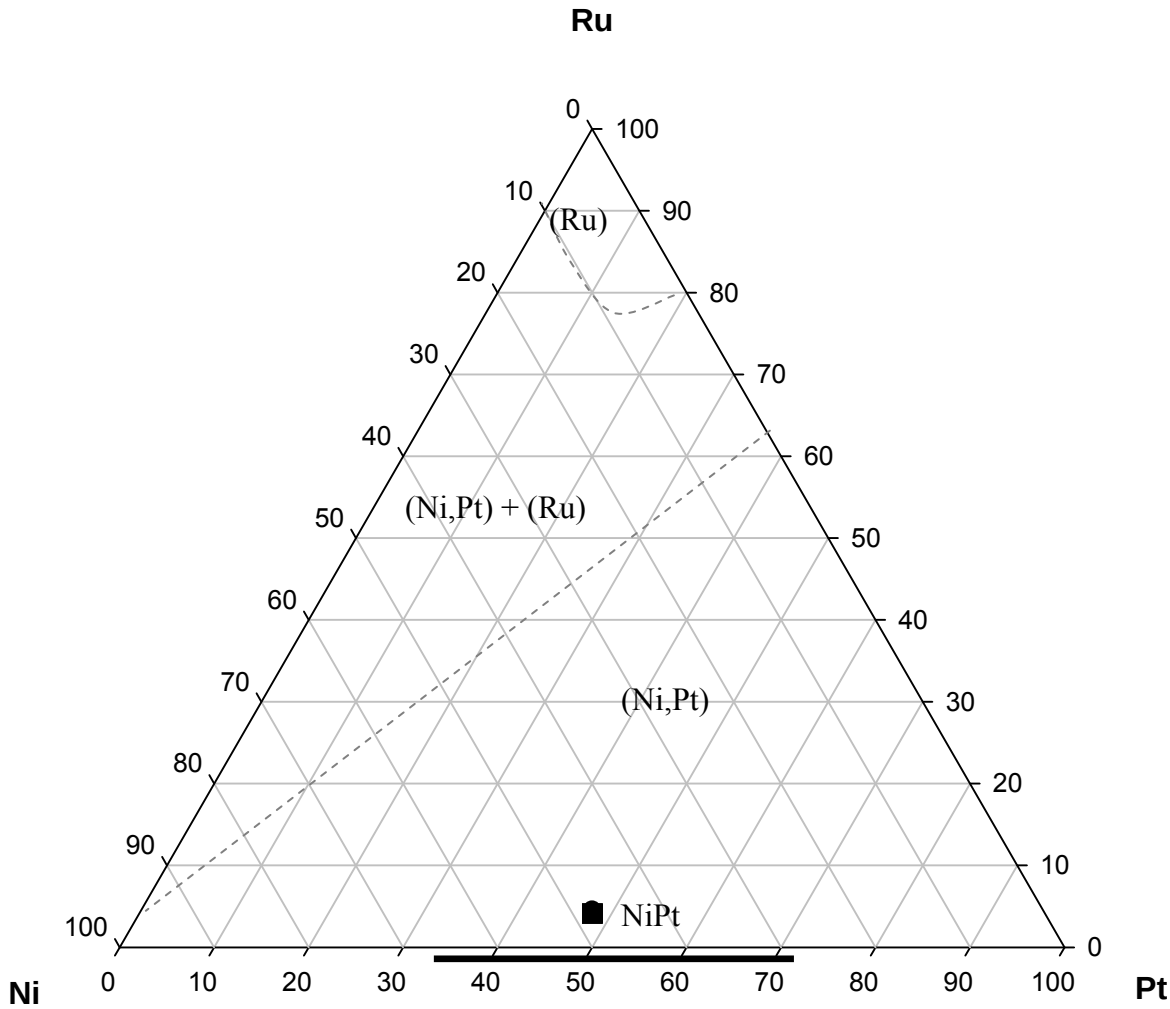


Figure 4.3. EDS analyses of LG 1 (Nominal $Ni_{47.5}$:$Pt_{47.5}$:Ru_5) in the as-cast condition (at.%).

LG 2 (Nominal Ni_{10}:Pt_{23}:Ru_{67})

LG 2 (Nominal Ni_{10}:Pt_{23}:Ru_{67}) had un-melted Ru and apparently comprised two phases of different contrasts in the center of the sample, although both were in the Ru-rich (Ni,Pt) solid solution area (Figure 4.4). This was confirmed by XRD (Figure 4.5), and the spectrum shows a high signal to background ratio. There is an unidentified peak at $2\theta \approx 12°$, which is too far from the plasticine peak identified on other samples. The EDS analyses are shown in Table 4.2 and plotted in Figure 4.6. The overall composition does not lie on the tie-line between the two different compositional contrasted areas, showing that a phase had been missed.

The solidification sequence for the alloy is: $L \rightarrow$ (Ni,Pt).

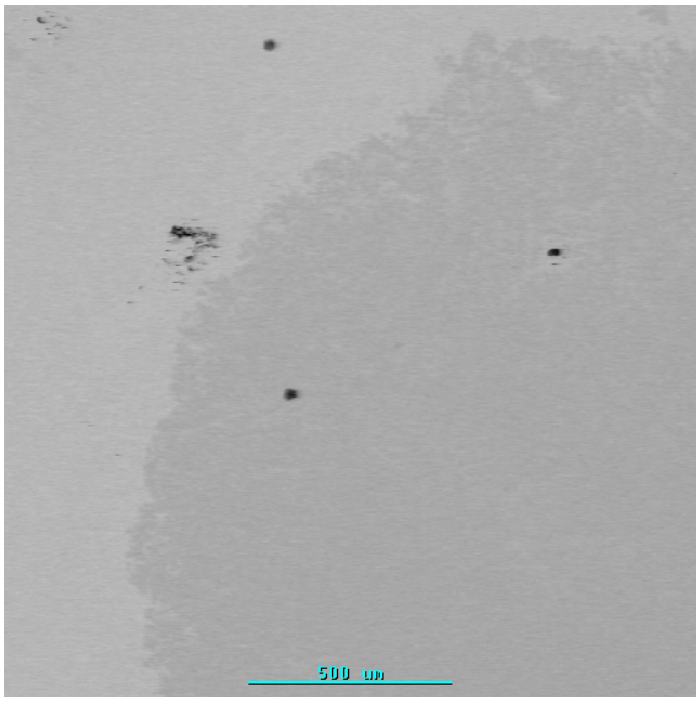


Figure 4.4. BEI of LG 2 (Nominal Ni_{10}:Pt_{23}:Ru_{67}) showing (Ni,Pt) of two different composition contrasts in the as-cast condition (scale bar = 500μm).

Table 4.2. EDS analyses of LG 2 (Nominal Ni_{10}:Pt_{23}:Ru_{67}) in the as-cast condition.

Phase description	Ni (at.%)	Pt (at.%)	Ru (at.%)	Phase
Overall	12.3 ± 0.6	36.6 ± 0.8	51.1 ± 1.3	-
Dark	21.4 ± 0.5	34.4 ± 0.4	44.2 ± 0.8	(Ni,Pt)
Light	21.3 ± 0.9	54.5 ± 0.6	24.2 ± 0.7	(Ni,Pt)

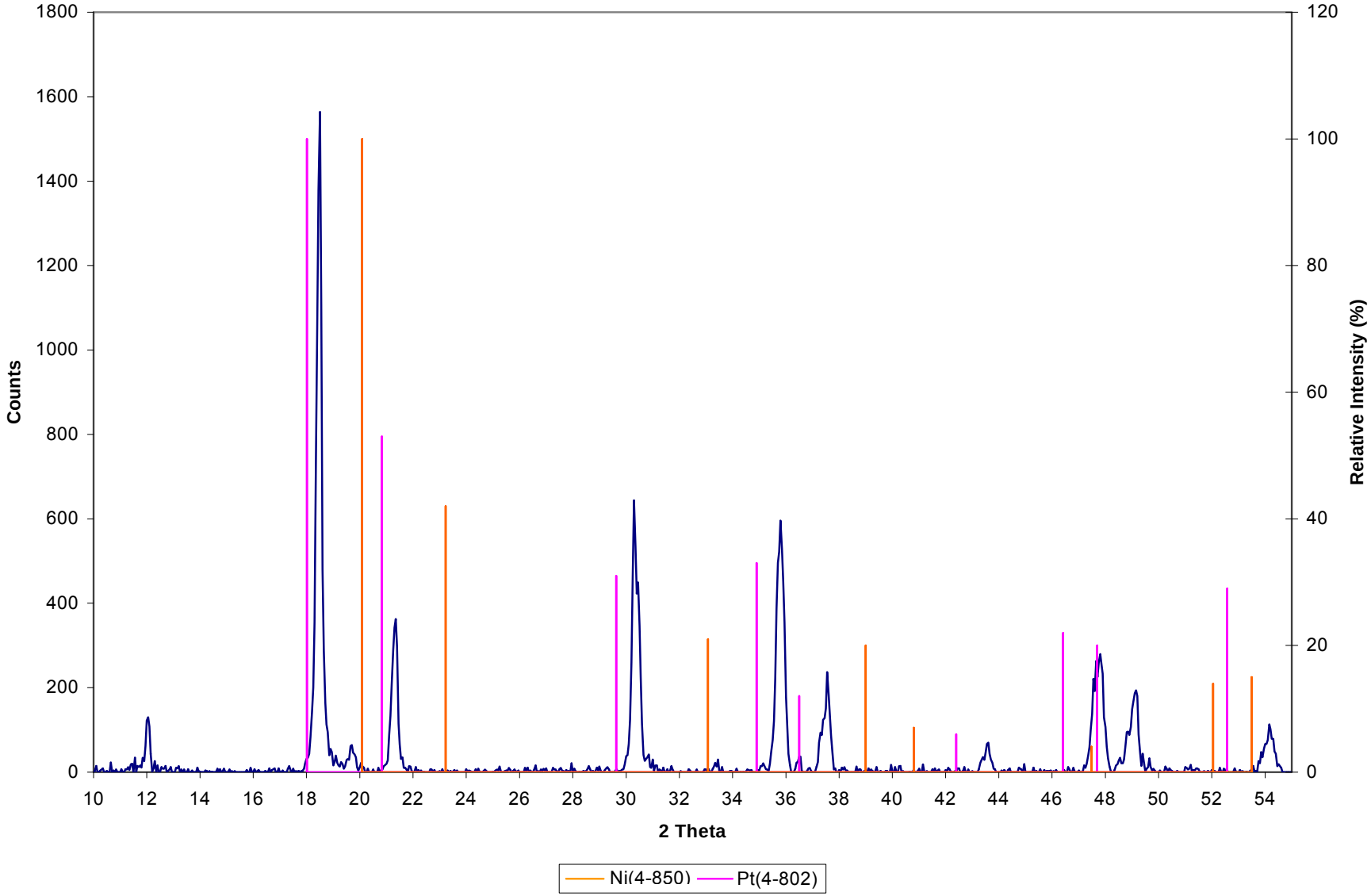


Figure 4.5. XRD spectrum of LG 2 (Nominal Ni_{10}:Pt_{23}:Ru_{67}) in the as-cast condition.

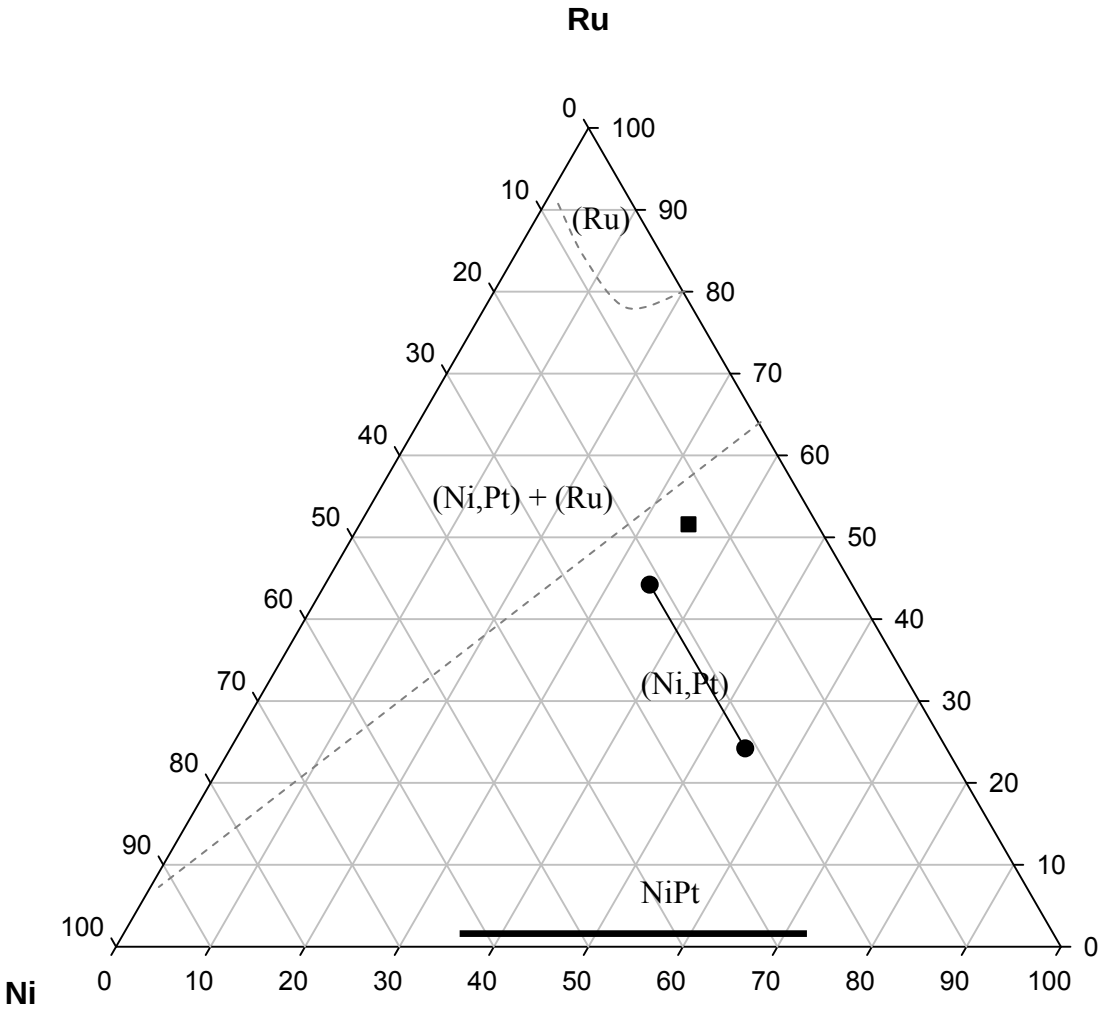


Figure 4.6. EDS analyses of LG 2 (Nominal Ni_{10}:Pt_{23}:Ru_{67}) in the as-cast condition (at.%).

LG 3 (Nominal Ni_{20}:Pt_{20}:Ru_{60})

LG 3 (Nominal Ni_{20}:Pt_{20}:Ru_{60}) is single phase and lies in the Ru-rich (Ni,Pt) solid solution area. The microstructure is shown in Figure 4.7 and two different compositional contrasts can be seen. The XRD spectrum is shown in Figure 4.8 and has a high signal to background ratio and is a good match for (Ni,P) and (Ru). The EDS analyses are given in Table 4.3 and are plotted in Figure 4.9. The overall composition of the alloy did not lie near the tie-line between the compositions of the different contrasted areas and was at a higher Ru content, suggesting that a phase had been missed.

The solidification sequence for the alloy is: $L \rightarrow$ (Ni,Pt).

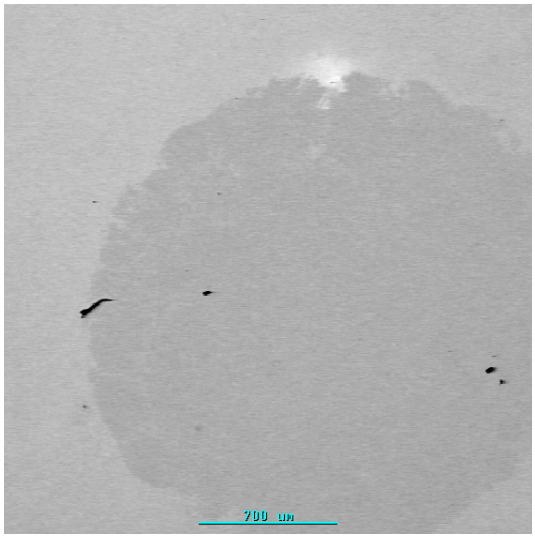


Figure 4.7. BEI of LG 3 (Nominal Ni_{20}:Pt_{20}:Ru_{60}) showing two different composition contrasts, both of the (Ni,Pt) phase, but with different atomic weights in the as-cast condition (scale bar = 700μm).

Table 4.3. EDS analyses of LG 3 (Nominal Ni_{20}:Pt_{20}:Ru_{60}) in the as-cast condition.

Phase description	Ni (at.%)	Pt (at.%)	Ru (at.%)	Phase
Overall	28.2 ± 0.4	30.4 ± 0.9	41.4 ± 0.2	-
Dark	26.1 ± 0.6	47.4 ± 0.5	26.5 ± 0.9	(Ni,Pt)
Light	34.6 ± 0.4	33.5 ± 0.8	31.9 ± 0.5	(Ni,Pt)

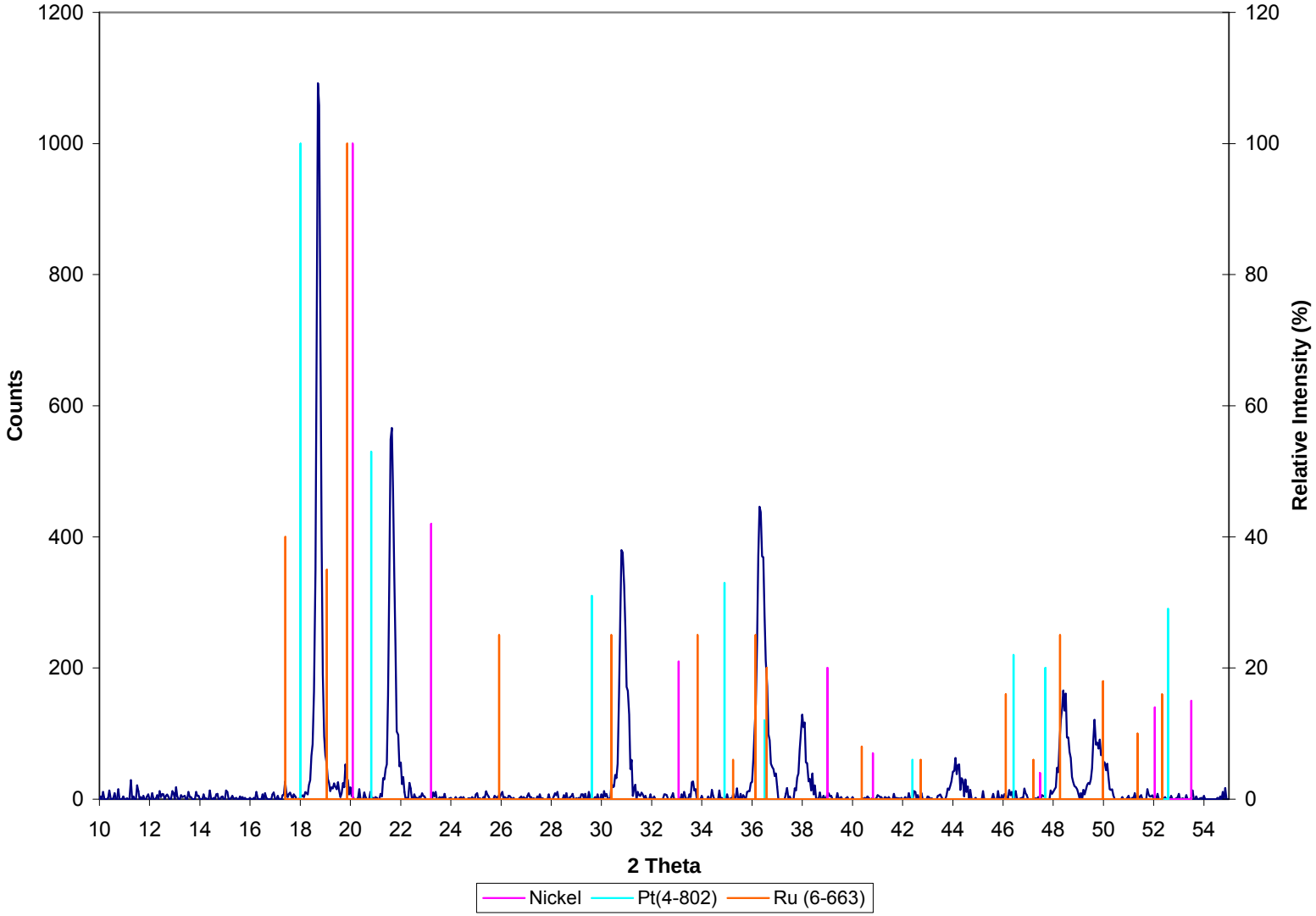


Figure 4.8. XRD spectrum of LG 3 (Nominal Ni_{20}:Pt_{20}:Ru_{60}) in the as-cast condition.

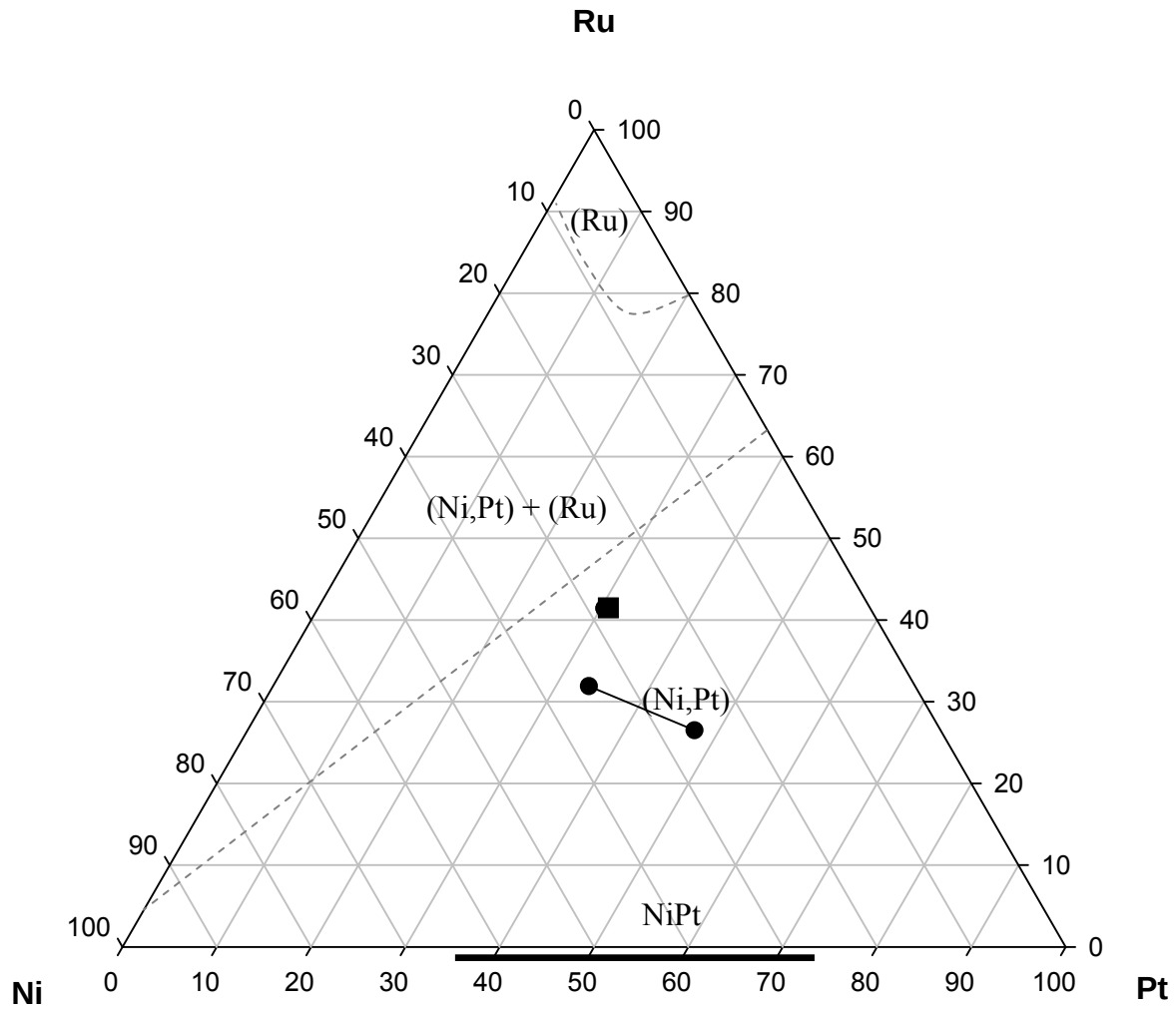


Figure 4.9. EDS analyses of LG 3 (Nominal Ni_{20}:Pt_{20}:Ru_{60}) in the as-cast condition (at.%).

LG 4 (Nominal Ni_{35}:Pt_{13}:Ru_{52})

The microstructure of LG 4 (Nominal Ni_{35}:Pt_{13}:Ru_{52}) is shown in Figure 4.10. It consists of a light grey, cored matrix with dark irregular dendrites. The dendrites were identified as consisting of (Ru) and the matrix of (Ni,Pt). The irregular dendrites confirm a peritectic formation of the matrix. The XRD spectrum is shown in Figure 4.11 and shows a high signal to background ratio. The peaks matched (Ni) with a shift and (Ru) where no shift was made. The EDS analyses is given in Table 4.4 and the actual compositions are plotted in Figure 4.12, with the overall composition lying on the tie-line between the two phases.

The solidification sequence for the alloy is as follows:

$$L \rightarrow (Ru);$$

$$L + (Ru) \rightarrow (Ni,Pt).$$

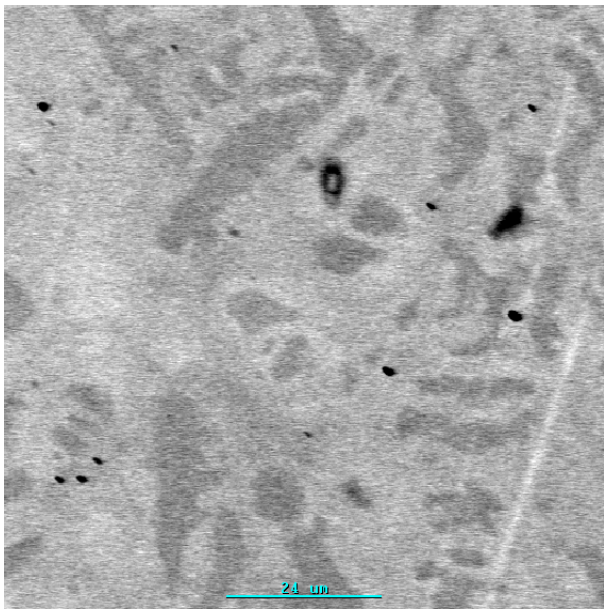


Figure 4.10. BEI of LG 4 (Nominal Ni_{35}:Pt_{13}:Ru_{52}) with dark, irregular (Ru) dendrites and light (Ni,Pt) cored matrix in the as-cast condition (scale bar = 24μm).

Table 4.4. EDS analyses of LG 4 (Nominal Ni_{35}:Pt_{13}:Ru_{52}) in the as-cast condition.

Phase description	Ni (at.%)	Pt (at.%)	Ru (at.%)	Phase	Proportions (%)
Overall	44.0 ± 1.3	16.1 ± 1.5	39.9 ± 0.5	-	-
Light phase	59.1 ± 1.6	20.4 ± 2.0	20.5 ± 1.3	(Ni,Pt)	60%
Dark phase	23.8 ± 1.0	9.9 ± 1.1	66.3 ± 0.9	(Ru)	40%

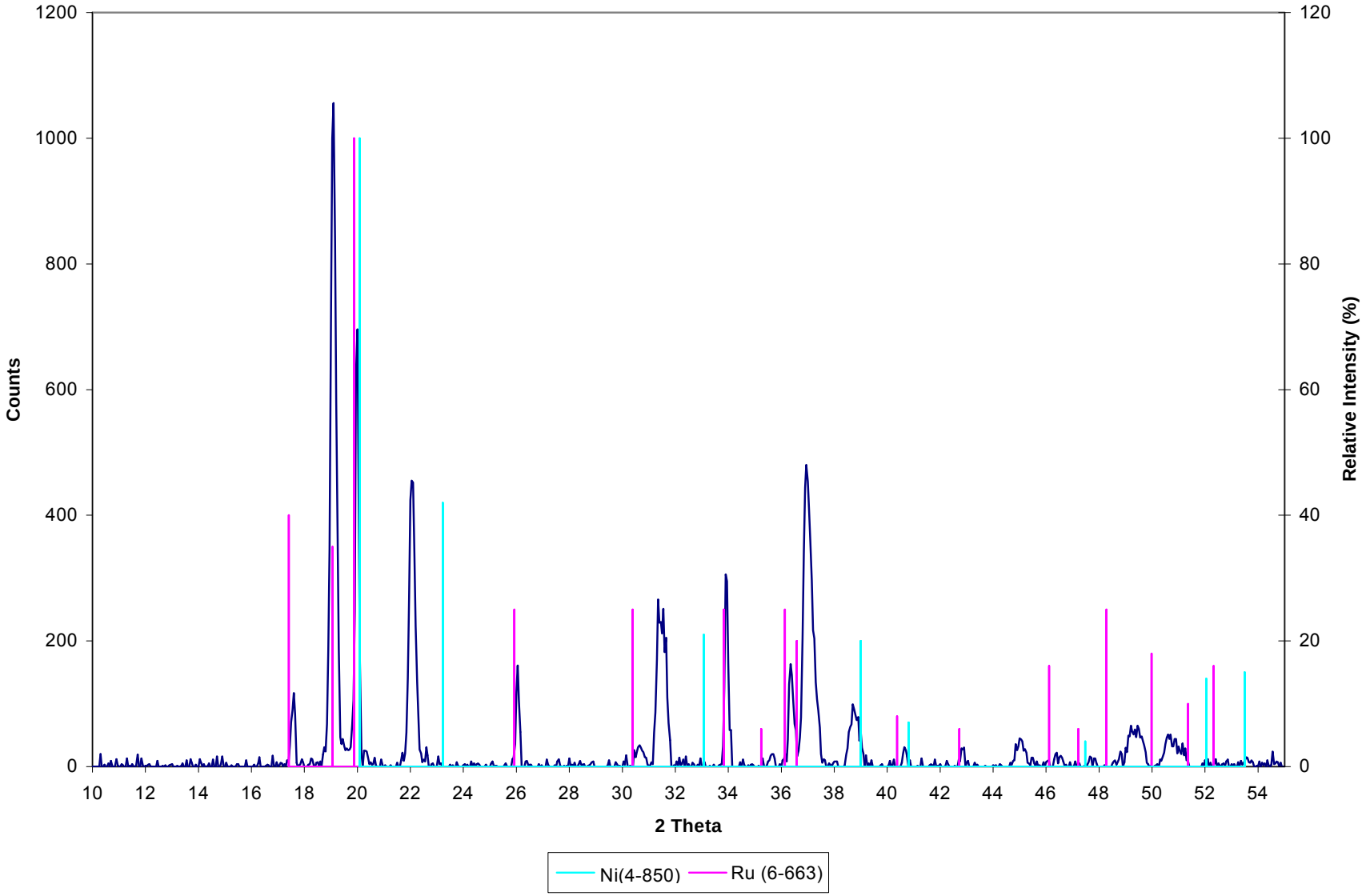


Figure 4.11. XRD spectrum of LG 4 (Nominal Ni_{35}:Pt_{13}:Ru_{52}) in the as-cast condition.

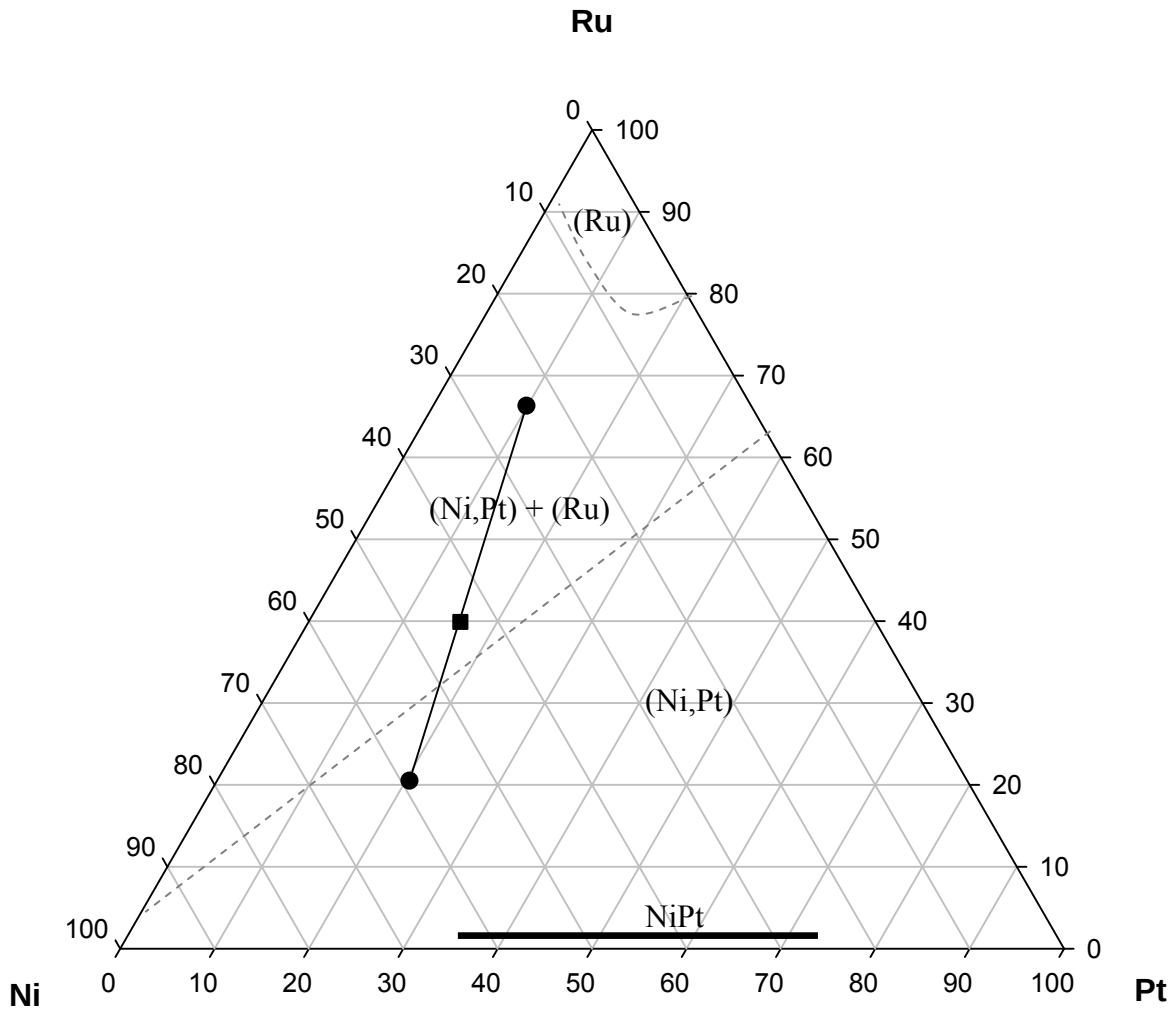


Figure 4.12. EDS analyses of LG 4 (Nominal Ni_{35}:Pt_{13}:Ru_{52}) in the as-cast condition (at.%).

LG 5 (Nominal Ni_{50}:Pt_5:Ru_{45})

LG 5 (Nominal Ni_{50}:Pt_5:Ru_{45}) consists of (Ru) dendrites in a cored, (Ni,Pt) matrix (Figure 4.13). The dendrites in this alloy is less irregular than in the previous alloy and are also lighter in contrast here, whereas those before were darker. The XRD spectrum in Figure 4.14 shows a good match with (Ru) and (Ni,Pt) with a shift, and has a high signal to background ratio. The EDS analyses are shown in Table 4.5 and the actual compositions are plotted in Figure 4.15. The overall compositions were on the tie-line between the two phases and the compositions of the coring in the dark matrix were lying on top of each other.

The solidification sequence for the alloy is as follows:

$$L \rightarrow (Ru);$$

$$L + (Ru) \rightarrow (Ni,Pt).$$

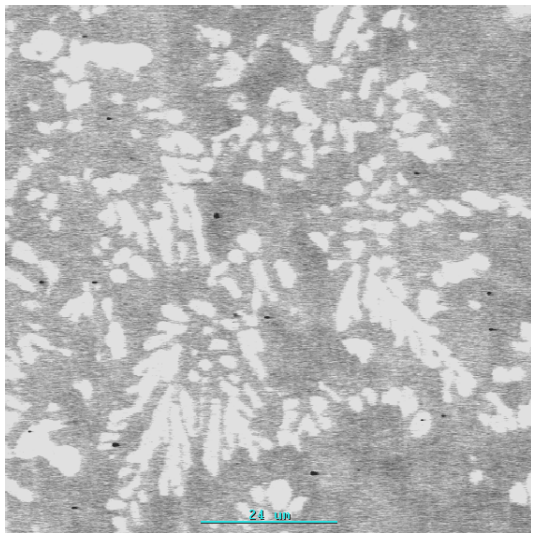


Figure 4.13. BEI of LG 5 (Nominal Ni_{50}:Pt_5:Ru_{45}) with light, (Ru) dendrites and dark, cored (Ni,Pt) matrix in the as-cast condition (scale bar = 24μm).

Table 4.5. EDS analyses of LG 5 (Nominal Ni_{50}:Pt_5:Ru_{45}) in the as-cast condition.

Phase description	Ni (at.%)	Pt (at.%)	Ru (at.%)	Phase	Proportions (%)
Overall	62.2 ± 0.3	5.9 ± 0.7	31.9 ± 2.0	-	-
Light phase	38.0 ± 0.3	3.3 ± 0.8	58.7 ± 0.3	(Ru)	40%
Dark phase (light coring)	69.6 ± 0.5	7.1 ± 1.2	23.3 ± 0.8	(Ni,Pt)	40%
Dark phase (dark coring)	69.3 ± 0.6	7.0 ± 0.2	23.7 ± 0.5	(Ni,Pt)	20%

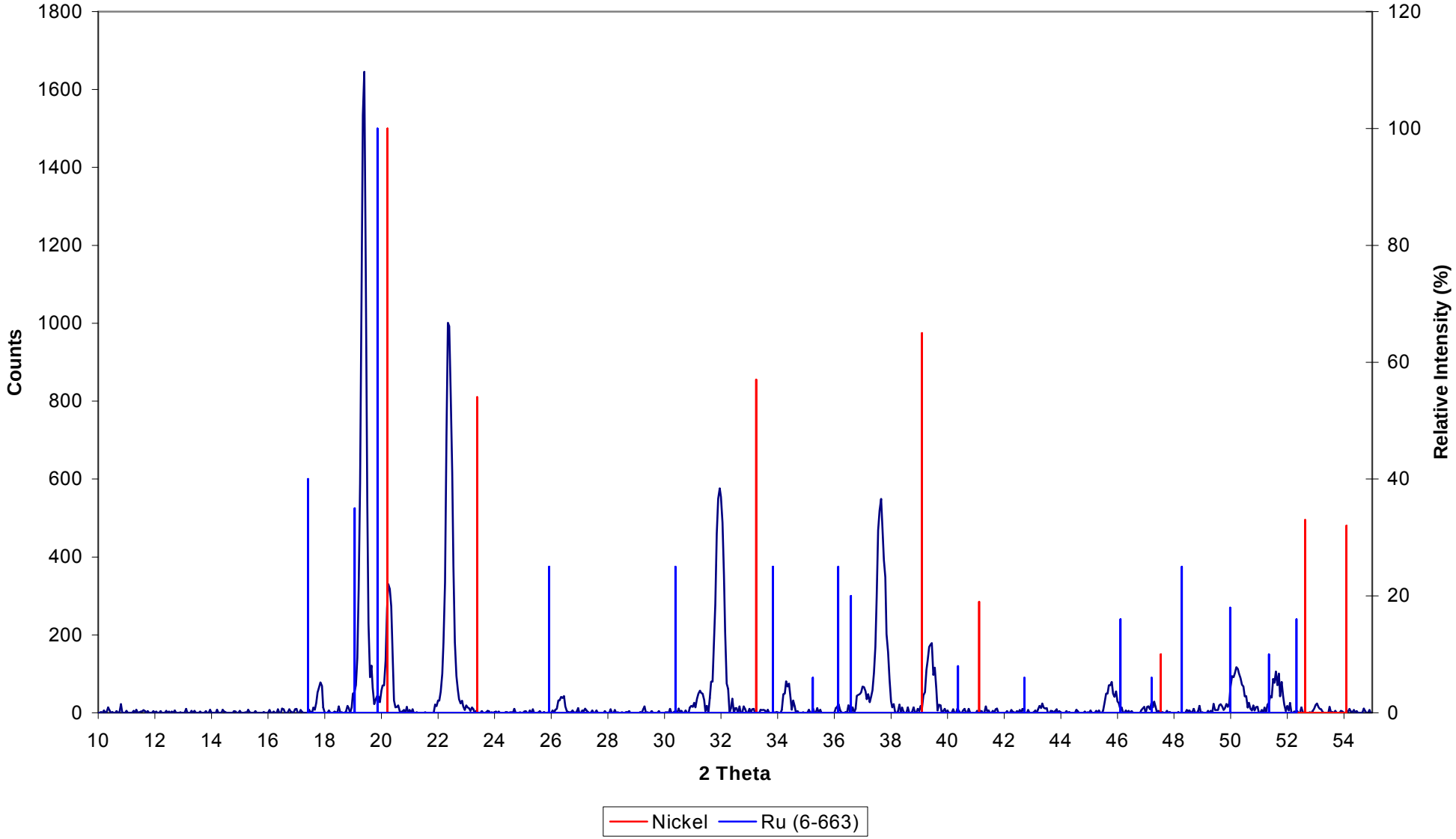


Figure 4.14. XRD spectrum of LG 5 (Nominal Ni_{50}:Pt_5:Ru_{45}) in the as-cast condition.

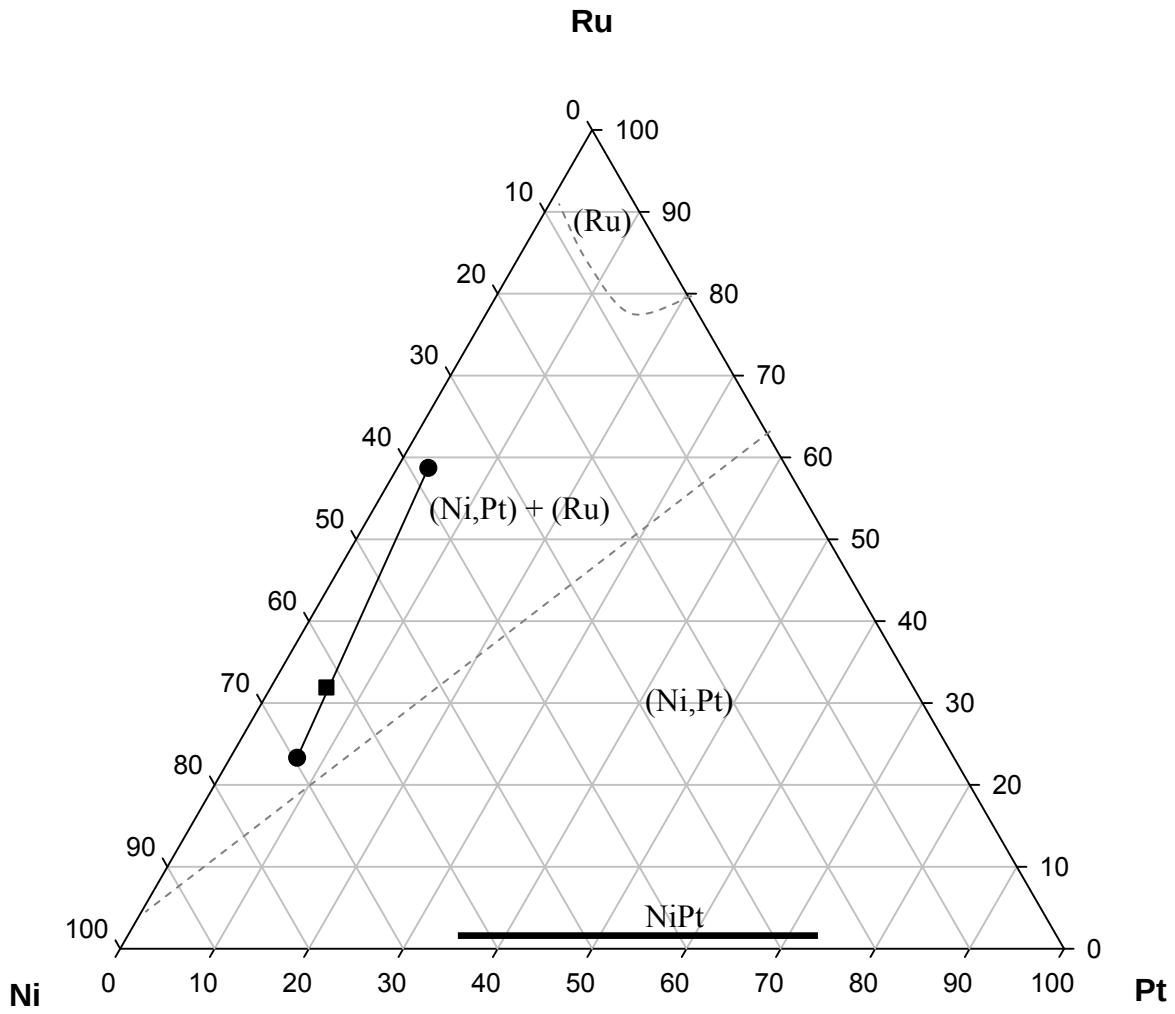


Figure 4.15. EDS analyses of LG 5 (Nominal Ni_{50}:Pt_5:Ru_{45}) in the as-cast condition (at.%).

LG 6 (Nominal Ni_{60}:Pt_5:Ru_{35})

The microstructure of LG 6 (Nominal Ni_{60}:Pt_5:Ru_{35}) consists of white (Ru) dendrites in a dark, cored (Ni,Pt) matrix (Figure 4.16). The dendrites in the alloy are also less irregular than that of LG 4. The phases were confirmed by XRD and the spectrum is shown in Figure 4.17 although the peaks had shifted with respect to the pure elements. The spectrum shows a high signal to background ratio. There were some minor unidentified peaks at $2\theta \approx 20°$, 23°, 26° and 31°. The EDS analyses are shown in Table 4.6 and the actual compositions are plotted in Figure 4.18 showing that the overall composition was on the tie-line of the component phases.

The solidification sequence for the alloy is as follows:

$$L \rightarrow (Ru);$$

$$L + (Ru) \rightarrow (Ni,Pt).$$

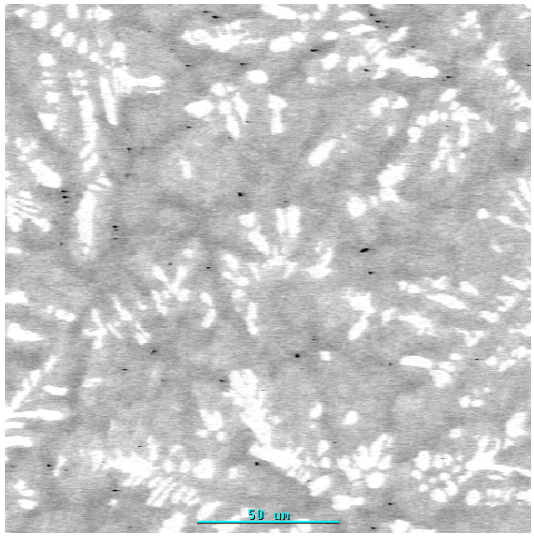


Figure 4.16 BEI of LG 6 (Nominal Ni_{60}:Pt_5:Ru_{35}) with light, (Ru) dendrites and cored, dark (Ni,Pt) matrix in the as-cast (scale bar = 50μm).

Table 4.6. EDS analyses of LG 6 (Nominal Ni_{60}:Pt_5:Ru_{35}) in the as-cast condition.

Phase description	Ni (at.%)	Pt (at.%)	Ru (at.%)	Phase	Proportions (%)
Overall	66.0 ± 0.5	5.4 ± 0.1	28.6 ± 1.0	-	-
Light phase	46.1 ± 0.6	3.2 ± 0.2	50.7 ± 0.6	(Ru)	24%
Dark phase (light coring)	73.9 ± 0.4	6.5 ± 0.9	19.6 ± 0.6	(Ni,Pt)	8%
Dark phase (dark coring)	78.8 ± 0.6	7.2 ± 0.5	14.0 ± 0.3	(Ni,Pt)	68%

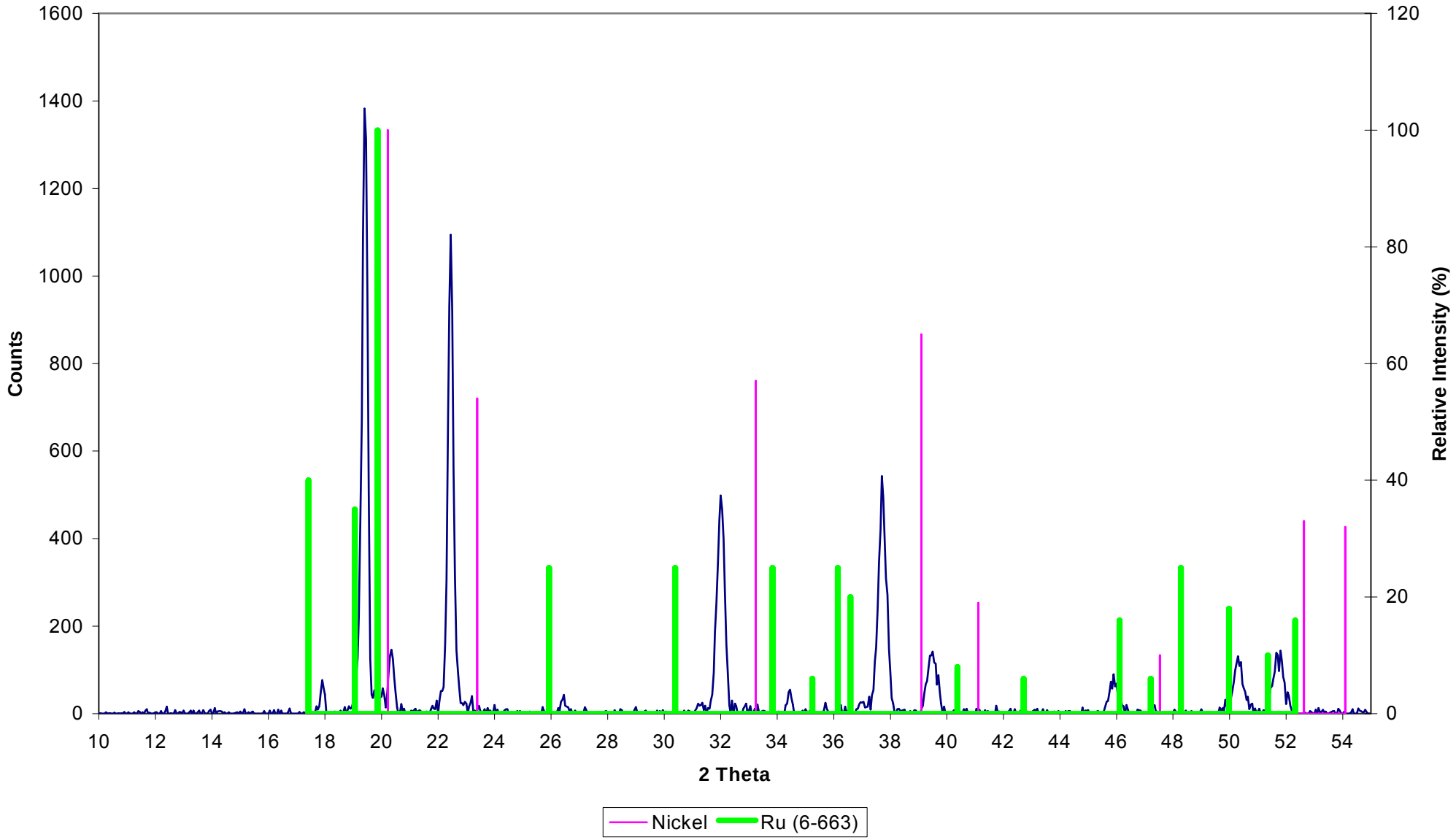


Figure 4.17: XRD spectrum of LG 6 (Nominal Ni_{60}:Pt_5:Ru_{35}) in the as-cast condition.

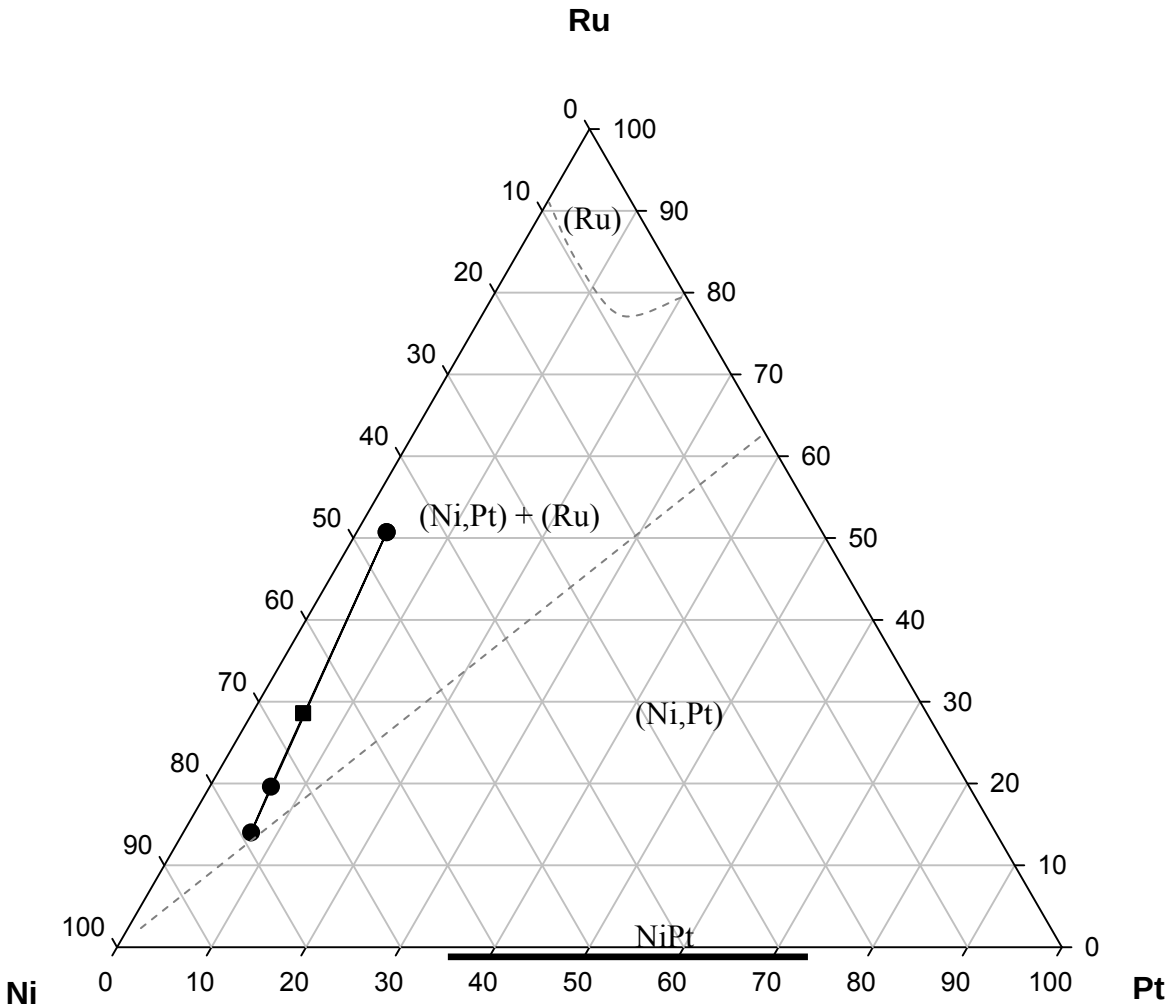


Figure 4.18. EDS analyses of LG 6 (Nominal Ni_{60}:Pt_5:Ru_{35}) in the as-cast condition (at.%).

LG 7 (Nominal Ni_{45}:Pt_{25}:Ru_{30})

LG 7 (Nominal Ni_{45}:Pt_{25}:Ru_{30}) appears to be a single-phase alloy with, barely discernable, small dark particles and the microstructure is shown in Figure 4.19. The matrix is identified as (Ni,Pt) and the XRD spectrum can be seen in Figure 4.20. However, Ru peaks have also been identified in the XRD spectrum. The (Ru) phase could be due to solid state precipitates (too small for EDS analyses) formed during cooling after solidification. The XRD spectrum shows a high signal to background ratio. The EDS analyses are given in Table 4.7 and the actual compositions are plotted in Figure 4.21.

The solidification sequence for the alloy is as follows:

$$L \rightarrow (Ni,Pt);$$

$$L + (Ni,Pt) \rightarrow (Ru).$$

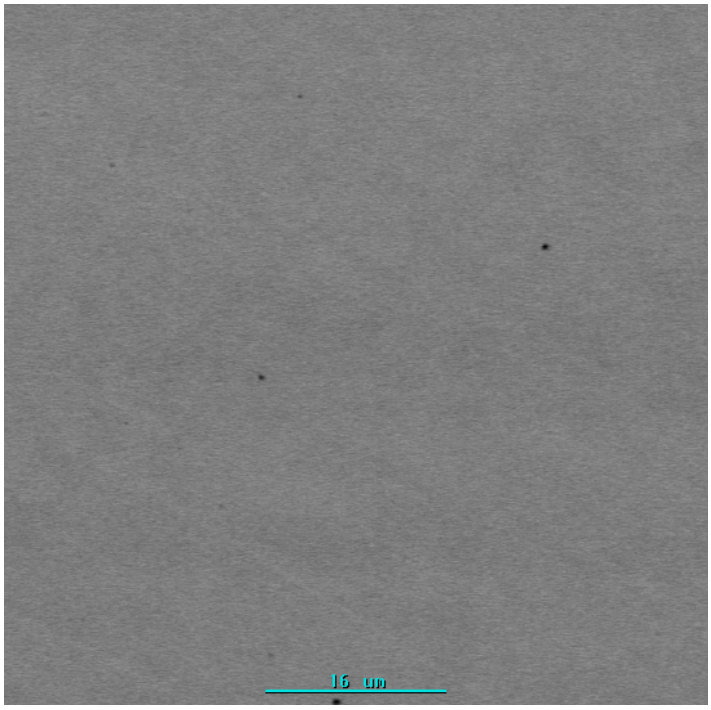


Figure 4.19. BEI of LG 7 (Nominal Ni_{45}:Pt_{25}:Ru_{30}) showing (Ni,Pt) in the as-cast condition with some pores (scale bar = 16 µm).

Table 4.7. EDS analyses of LG 7 (Nominal Ni_{45}:Pt_{25}:Ru_{30}) in the as-cast condition.

Phase description	Ni (at.%)	Pt (at.%)	Ru (at.%)	Phase
Overall	34.4 ± 0.1	21.4 ± 0.3	44.2 ± 0.2	(Ni,Pt)

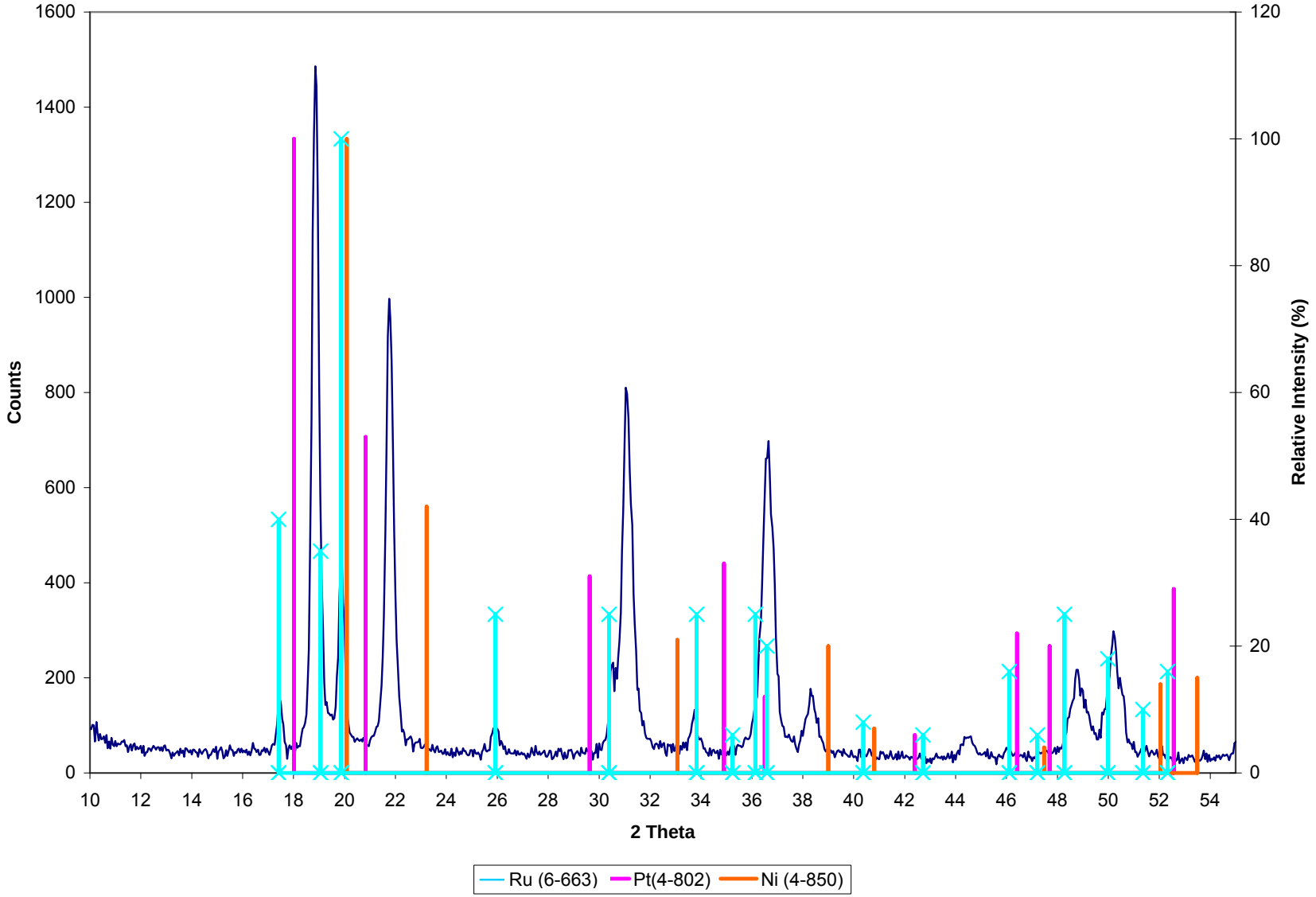


Figure 4.20. XRD spectrum of LG 7 (Nominal Ni_{45}:Pt_{25}:Ru_{30}) in the as-cast condition.

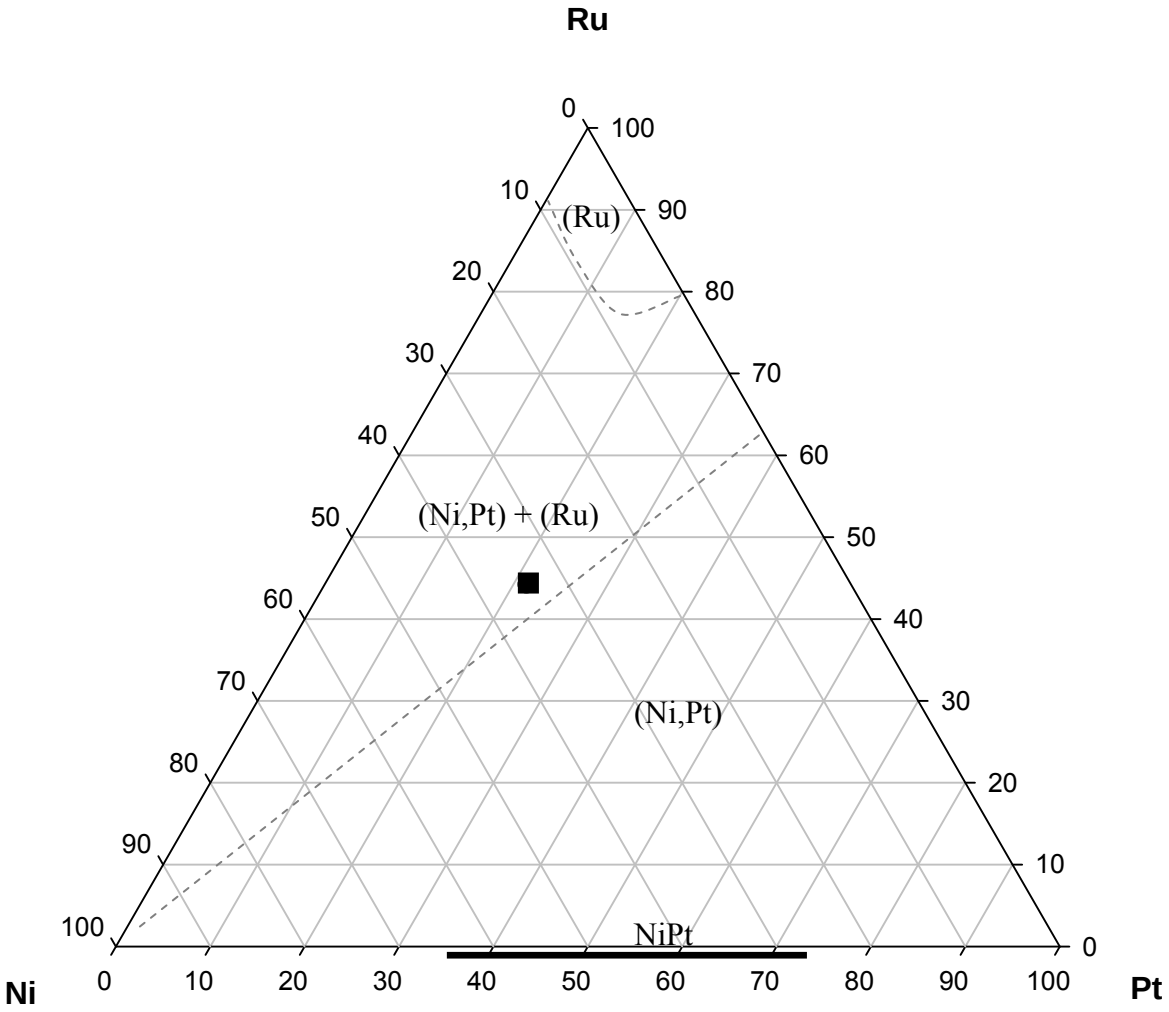


Figure 4.21. EDS analyses of LG 7 (Nominal Ni_{45}:Pt_{25}:Ru_{30}) in the as-cast condition (at.%).

LG 8 (Nominal Ni_{35}:Pt_{35}:Ru_{30})

The microstructure of LG 8 (Nominal Ni_{35}:Pt_{35}:Ru_{30}) (Figure 4.22) appears to be two-phase, with lighter dendrites in a darker matrix. The phases were confirmed by XRD (Figure 4.23) with larger (Ni,Pt) peaks, and also small Ru peaks. Some shift in the peaks was noticed. It is not clear how the (Ru) formed but it must have been on solidification because it is located at the edges of the dendrites (the edges of the dendrites are lighter compared to the rest of the dendrite, indicating a higher atomic mass). The spectrum shows a high signal to background ratio and the EDS analyses are shown in Table 4.8 with the actual compositions plotted in Figure 4.24. The overall did not lie on the tie-line between the phases.

The solidification sequence for the alloy is as follows:

$$L \rightarrow (Ni,Pt);$$

$$L \rightarrow (Ru).$$

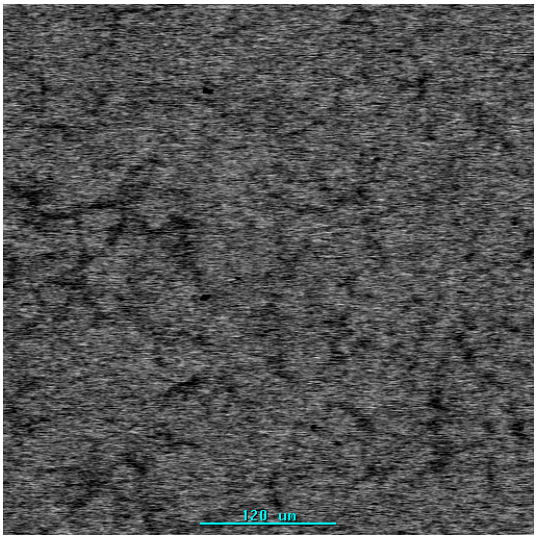


Figure 4.22. BEI of LG 8 (Nominal Ni_{35}:Pt_{35}:Ru_{30}), in the as-cast condition showing small (Ru) regions inside the cored (Ni,Pt) dendrites (scale bar = 120μm).

Table 4.8. EDS analyses of LG 8 (Nominal Ni_{35}:Pt_{35}:Ru_{30}) in the as-cast condition.

Phase description	Ni (at.%)	Pt (at.%)	Ru (at.%)	Phase	Proportions (%)
Overall	36.1 ± 0.6	37.2 ± 0.5	26.7 ± 0.8	-	-
Dark	55.0 ± 3.9	39.0 ± 1.1	6.0 ± 2.8	(Ni,Pt)	28%
Light	39.2 ± 7.1	38.9 ± 1.9	21.9 ± 8.9	(Ni,Pt)	72%

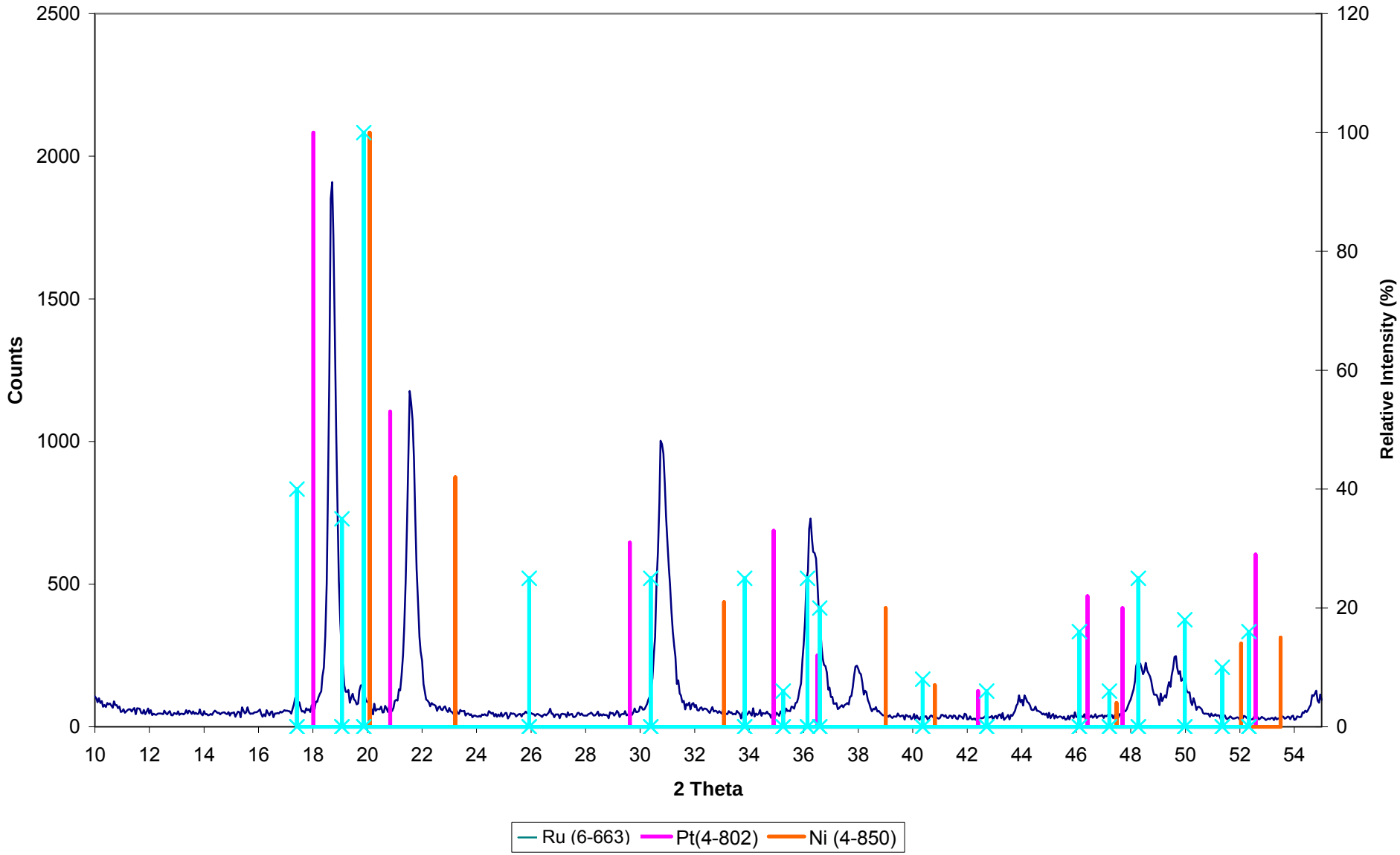


Figure 4.23. XRD spectrum of LG 8 (Nominal Ni_{35}:Pt_{35}:Ru_{30}) in the as-cast condition.

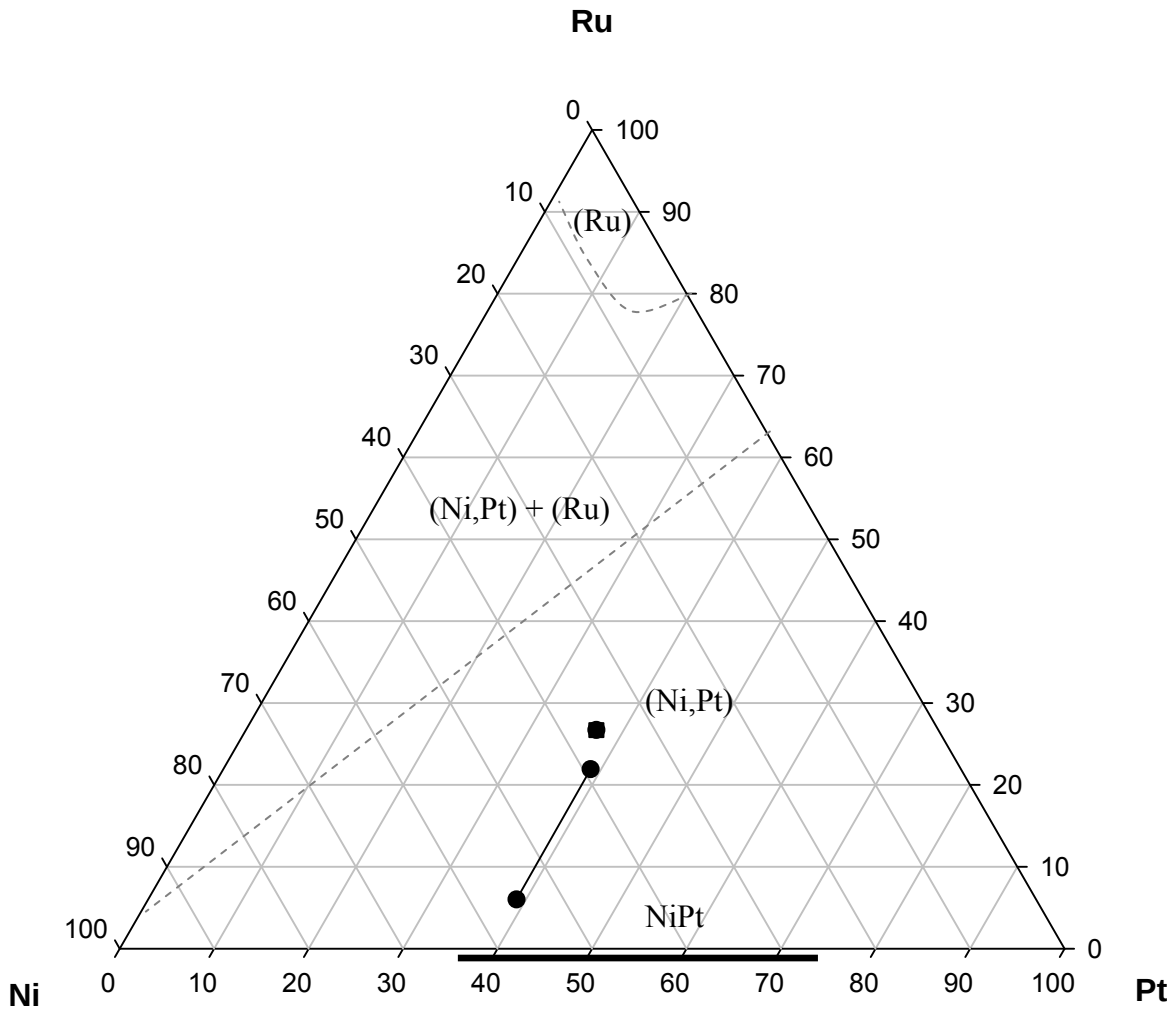


Figure 4.24. EDS analyses of LG 8 (Nominal Ni_{35}:Pt_{35}:Ru_{30}) in the as-cast condition (at.%).

LG 9 (Nominal Ni_{25}:Pt_{45}:Ru_{30})

The microstructure of LG 9 (Nominal Ni_{25}:Pt_{45}:Ru_{30}) appears to be a two-phase alloy (Figure 4.25) with dark dendrites in a light matrix. The XRD spectrum in Figure 4.26 confirmed that the alloy mainly consists of (Ni,Pt). However some of the Ru peaks are present in the spectrum. This might be due to solid state precipitation of Ru from (Ni,Pt). The spectrum shows a high signal to background ratio. The EDS analyses are shown in Table 4.9 and the actual compositions plotted in Figure 4.27. The overall composition lies just under the tie-line between the phases.

The solidification sequence for the alloy is as follows:

$$L \rightarrow (Ni,Pt);$$

$$L \rightarrow (Ru).$$

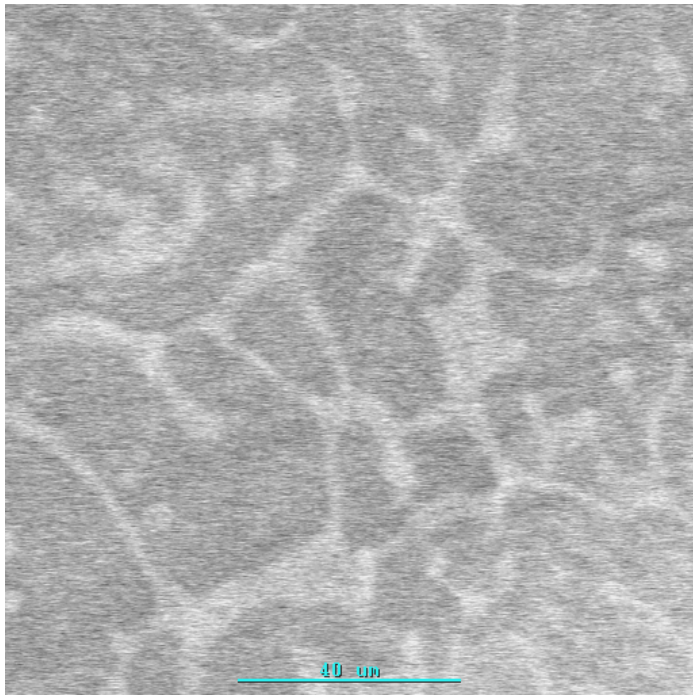


Figure 4.25. BEI of LG 9 (Nominal Ni_{25}:Pt_{45}:Ru_{30}) showing light (Ni,Pt) matrix and dark (Ru) dendrites (scale bar = 40μm) in the as-cast condition.

Table 4.9. EDS analyses of LG 9 (Nominal Ni_{25}:Pt_{45}:Ru_{30}) in the as-cast condition.

Phase description	Ni (at.%)	Pt (at.%)	Ru (at.%)	Phase	Proportions (%)
Overall	24.0 ± 0.6	46.0 ± 0.5	30.0 ± 0.5	-	-
Light	23.3 ± 8.4	45.3 ± 4.8	31.4 ± 5.1	(Ni,Pt)	32%
Dark	13.4 ± 0.6	39.2 ± 0.2	47.4 ± 0.8	(Ru)	68%

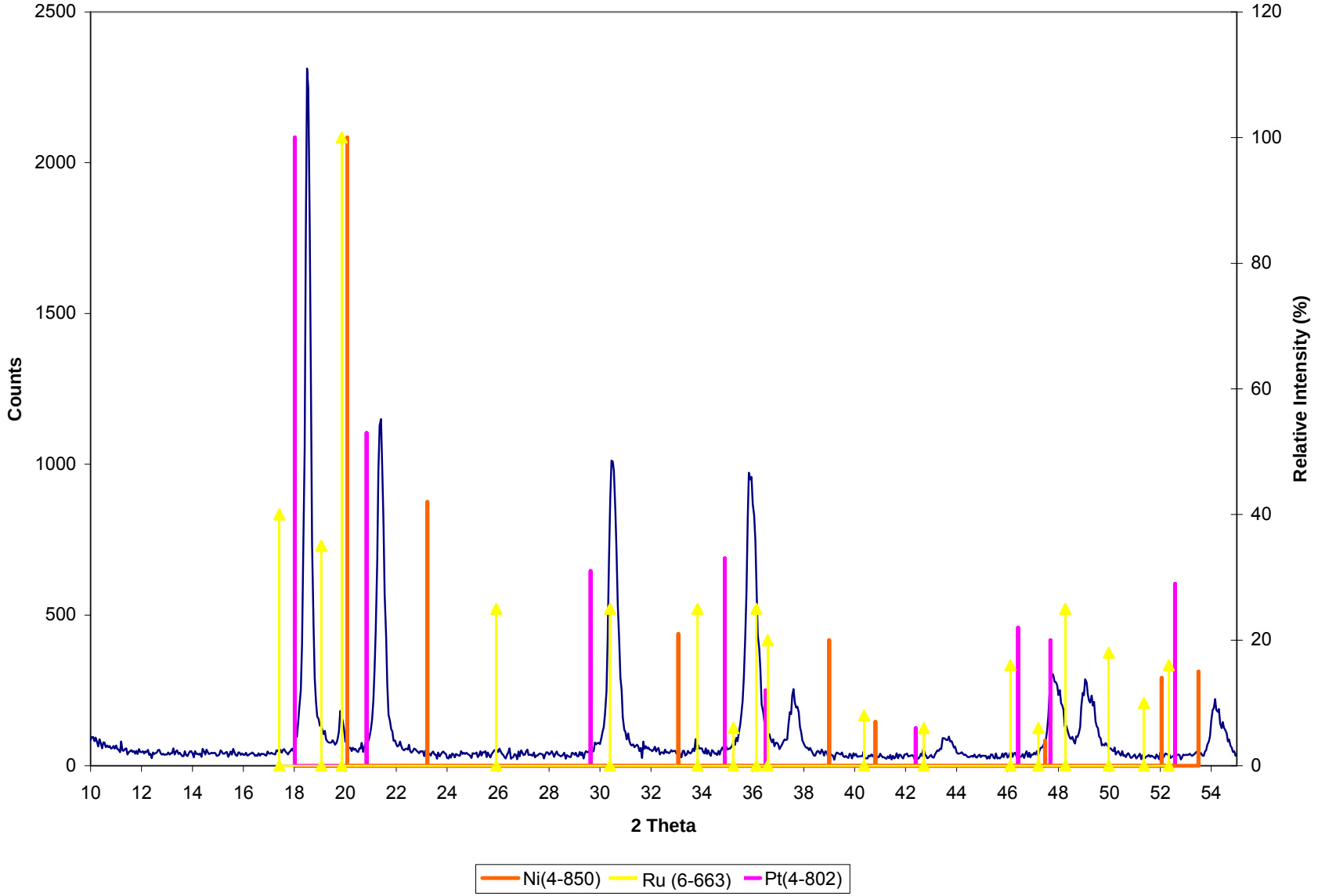


Figure 4.26. XRD spectrum of LG 9 (Nominal Ni_{25}:Pt_{45}:Ru_{30}) in the as-cast condition.

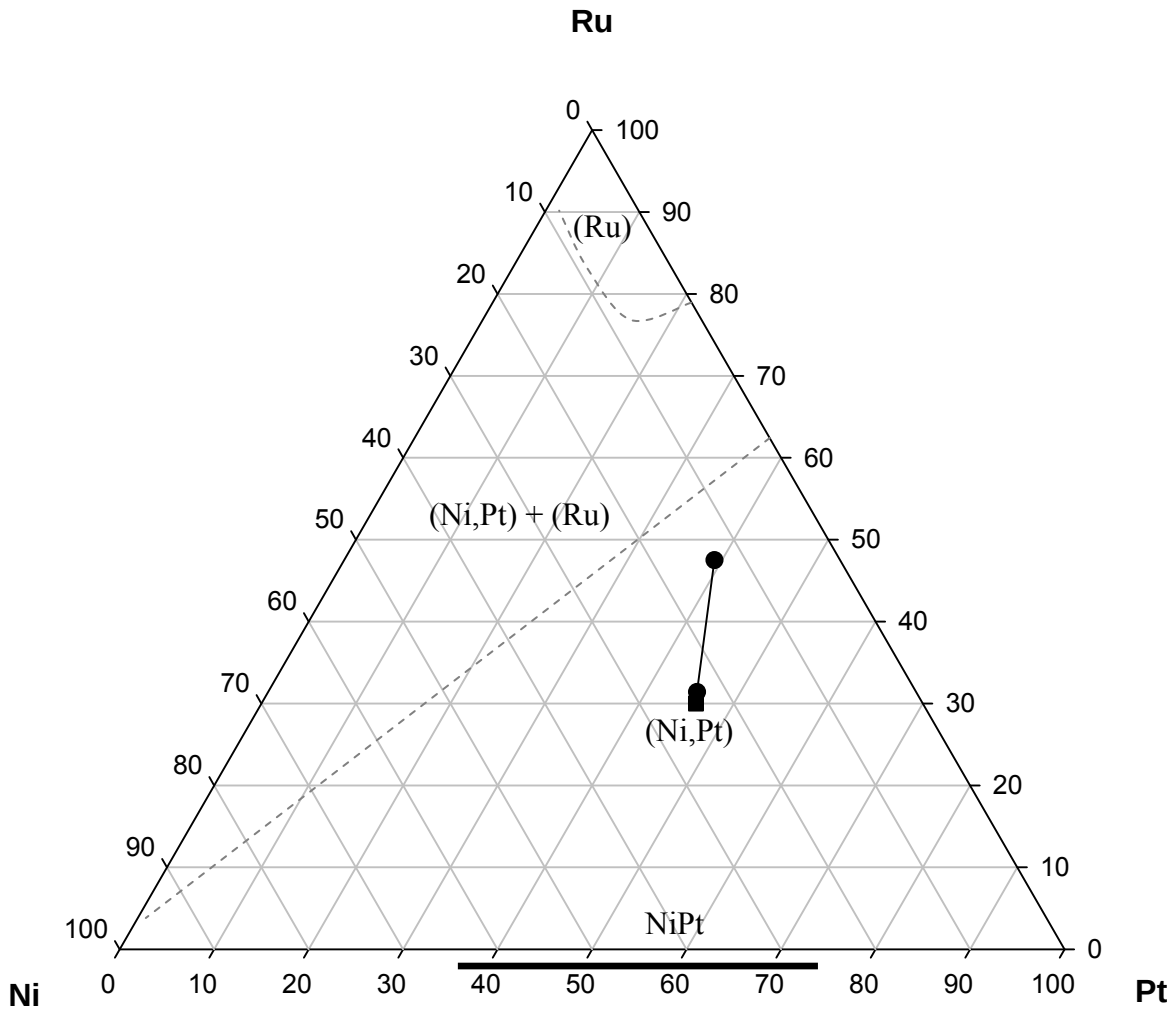


Figure 4.27. EDS analyses of LG 9 (Nominal Ni_{25}:Pt_{45}:Ru_{30}) in the as-cast condition (at.%).

LG 10 (Nominal Ni_{15}:Pt_{55}:Ru_{30})

LG 10 (Nominal Ni_{15}:Pt_{55}:Ru_{30}) appeared to be a two-phase alloy consisting of a cored dark and light phase (Figure 4.28). The XRD spectrum in Figure 4.29 confirmed that this is a single phase consisting of (Ni,Pt). No Ru peaks were present in the XRD spectrum, as in the previous alloys. The spectrum shows a high signal to background ratio. The EDS analyses are given in Table 4.10 and the actual compositions are plotted in Figure 4.30. It can be seen that a phase is missing, because the overall analysis does not lie on the tie-line joining the two phases.

The solidification sequence for the alloy is as follows:

$$L \rightarrow (Ni,Pt).$$

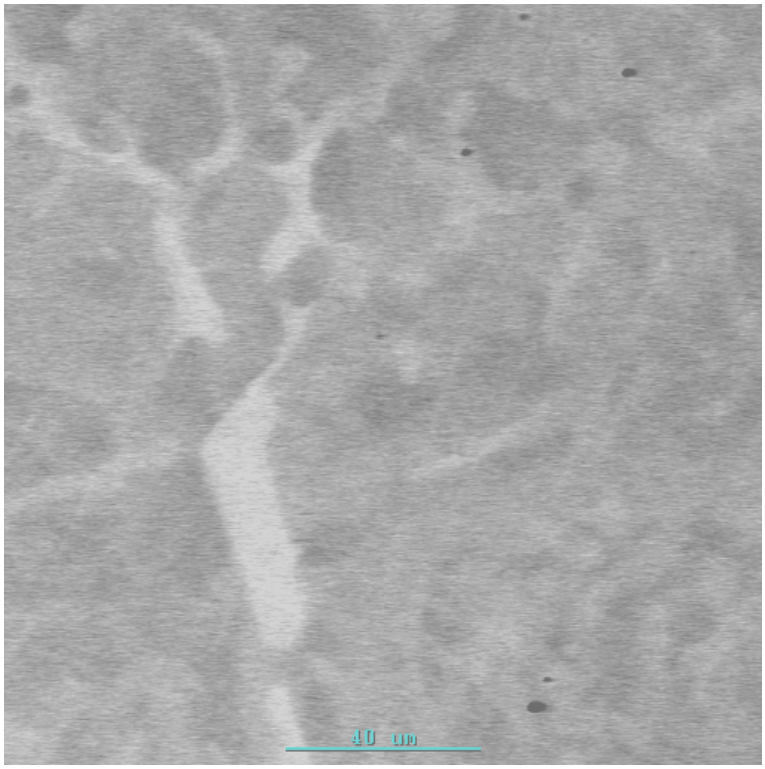


Figure 4.28. BEI of LG 10 (Nominal Ni_{15}:Pt_{55}:Ru_{30}) in the as-cast condition, showing a matrix with different contrasts of (Ni,Pt) (scale bar = 40μm).

Table 4.10. EDS analyses of LG 10 (Nominal Ni_{15}:Pt_{55}:Ru_{30}) in the as-cast condition.

Phase description	Ni (at.%)	Pt (at.%)	Ru (at.%)	Phase	Proportions (%)
Overall	16.9 ± 0.3	44.0 ± 0.3	39.1 ± 0.3	-	-
Light	15.5 ± 1.1	58.5 ± 4.3	26.0 ± 5.0	(Ni,Pt)	16%
Dark	10.8 ± 4.6	52.6 ± 1.2	36.6 ± 8.0	(Ni,Pt)	84%

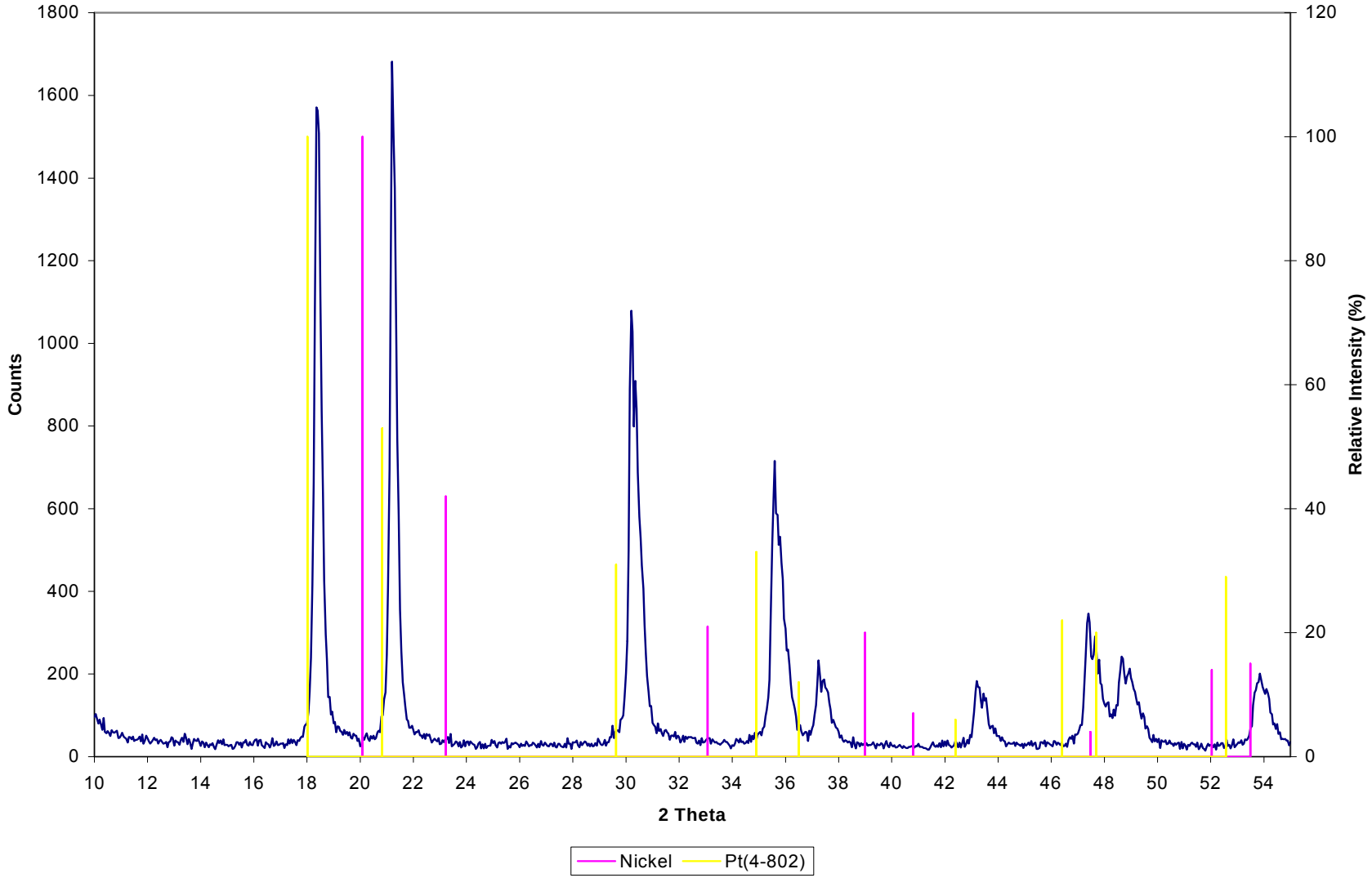


Figure 4.29. XRD spectrum of LG 10 (Nominal Ni_{15}:Pt_{55}:Ru_{30}) in the as-cast condition.

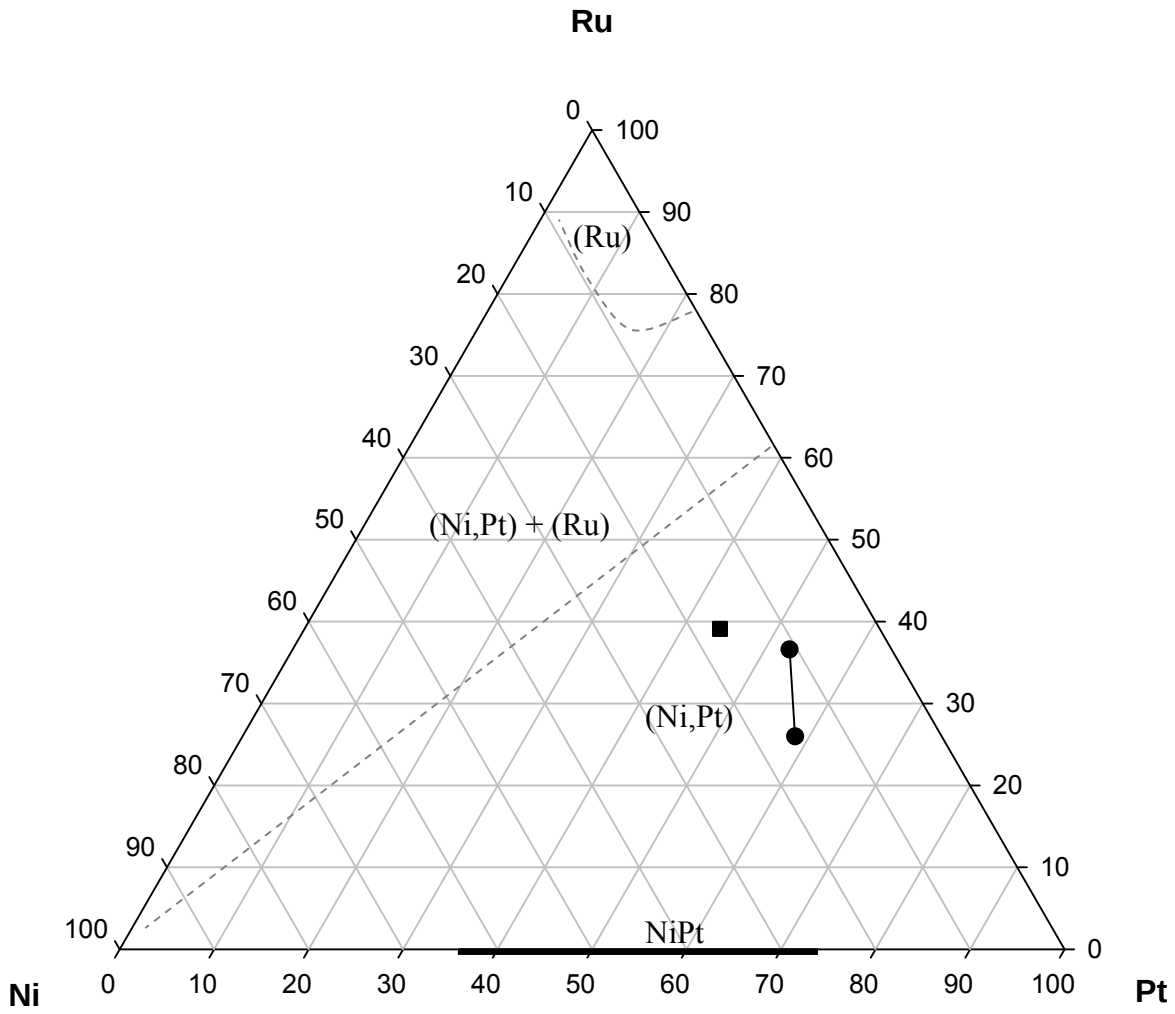


Figure 4.30. *EDS analyses of LG 10 (Nominal Ni_{15}:Pt_{55}:Ru_{30}) in the as-cast condition (at.%) (● =phases and ■= overall.*

4.1.2 Alloys after Heat Treatment at 1000°C for 1000 hours and water quench

LG 2 (Nominal Ni_{10}:Pt_{23}:Ru_{67})

After annealing the alloy for 1000 hours at 1000°C, the microstructure of LG 2 (Nominal Ni_{10}:Pt_{23}:Ru_{67}) changed from being single phase to an apparent three-phase alloy (Figure 4.31). The overall composition had also changed significantly, suggesting that the unmelted Ru, previously seen, dissolved and was incorporated fully in the sample. The main structures present were the (Ni,Pt), (Ru) and what could be an oxide that formed during heat treatment in air, according to XRD (Figure 4.32). The spectrum was much more complicated than before annealing (Figure 4.5) where a single-phase solid solution of Ni and Pt were identified, once the peaks were shifted. After annealing the (Ru) and nickel oxide peaks were present. The oxide was formed during the heat treatment of the alloy and was found on the outer surface of the sample. The needles were the darkest phase. Its identity is most likely to be (Ru). The lightest contrast phase should be (Ni,Pt) and the medium phase is either a new phase or a modulation of the local composition caused by the precipitation of (Ru), thus a depletion of Ru. The EDS analyses are given in Table 4.11 and the actual compositions are plotted in Figure 4.33. The overall analyses are very near the tie-line which is within acceptable error. The EDS analyses were all normalised and if oxygen was present, it would not be shown in the results. The phase proportions are given in Table 4.11.

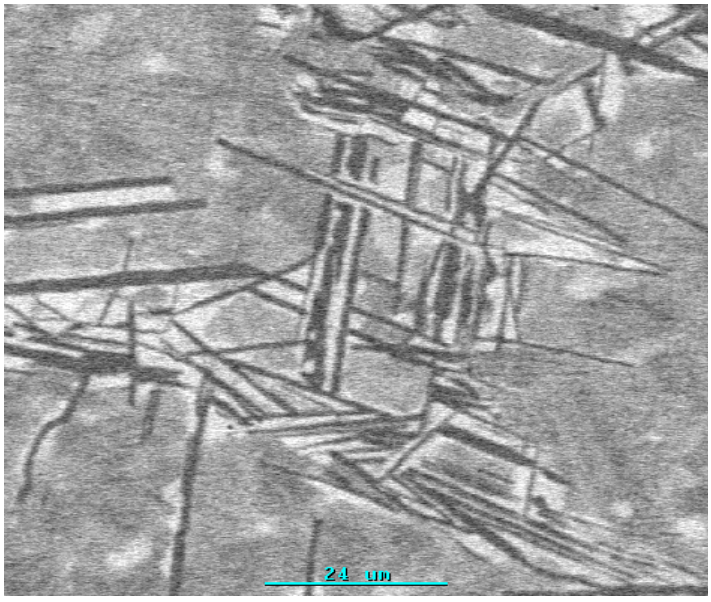


Figure 4.31: BEI of LG 2 (Nominal Ni_{10}:Pt_{23}:Ru_{67}) after heat treatment and water quench showing (Ni,Pt) (light), with coring and dark (Ru) needles (scale bar = 24µm).

Table 4.11. EDS analyses of LG 2 (Nominal $Ni_{10}:Pt_{23}:Ru_{67}$) in the annealed condition.

Phase description	Ni (at.%)	Pt (at.%)	Ru (at.%)	Phase	Proportion (%)
Overall	10.0 ± 0.3	27.8 ± 0.5	62.2 ± 0.9	-	-
Light Phase	18.3 ± 1.3	38.4 ± 1.2	43.3 ± 1.9	(Ni,Pt)	40%
Medium Phase	12.0 ± 0.6	29.1 ± 0.8	58.9 ± 0.7	(Ru)	32%
Dark Phase	3.5 ± 1.0	15.3 ± 0.9	81.2 ± 1.4	(Ru)	28%

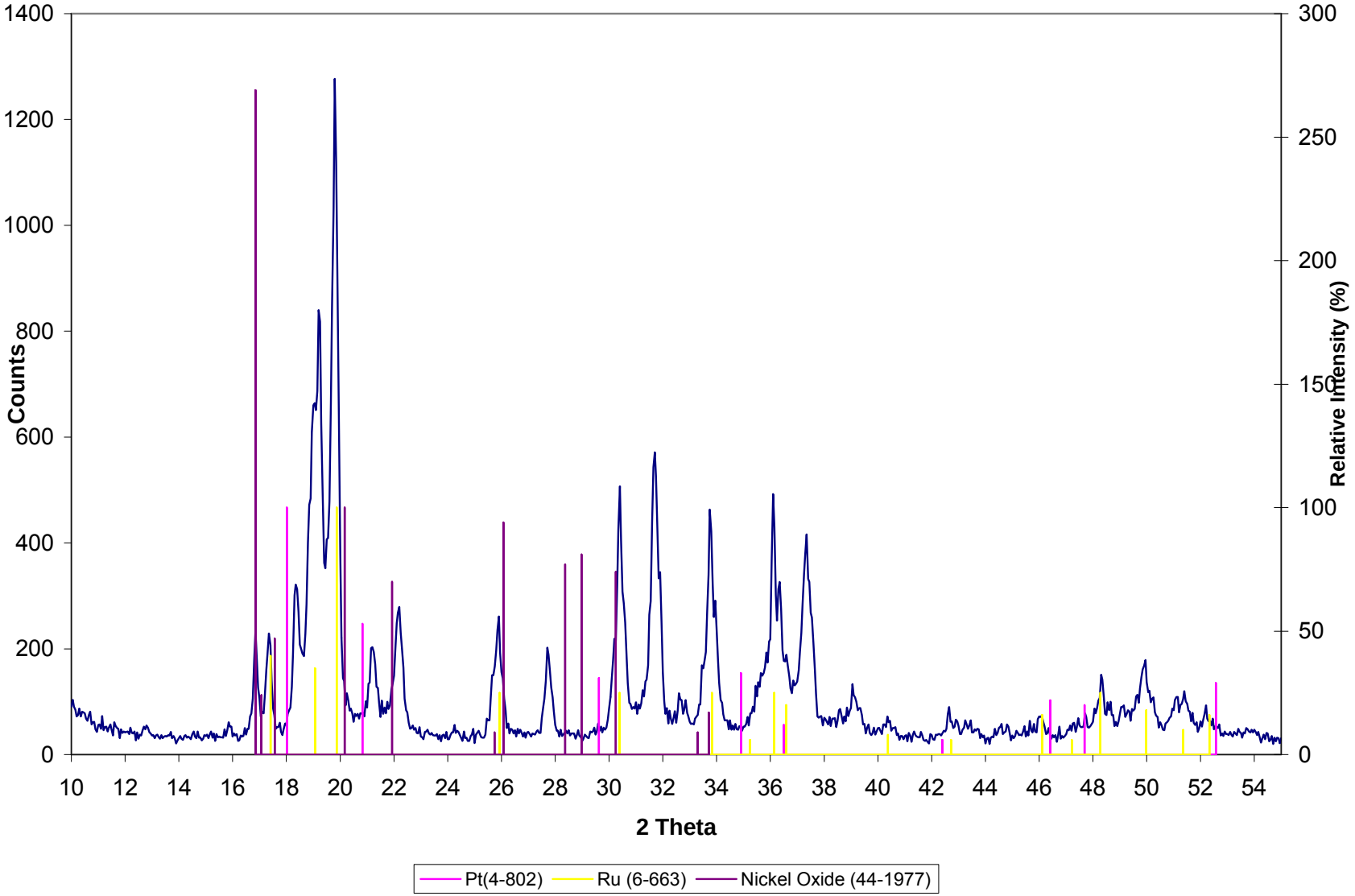


Figure 4.32. XRD scan of LG 2 (Nominal $Ni_{10}:Pt_{23}:Ru_{67}$) after heat treatment and water quench.

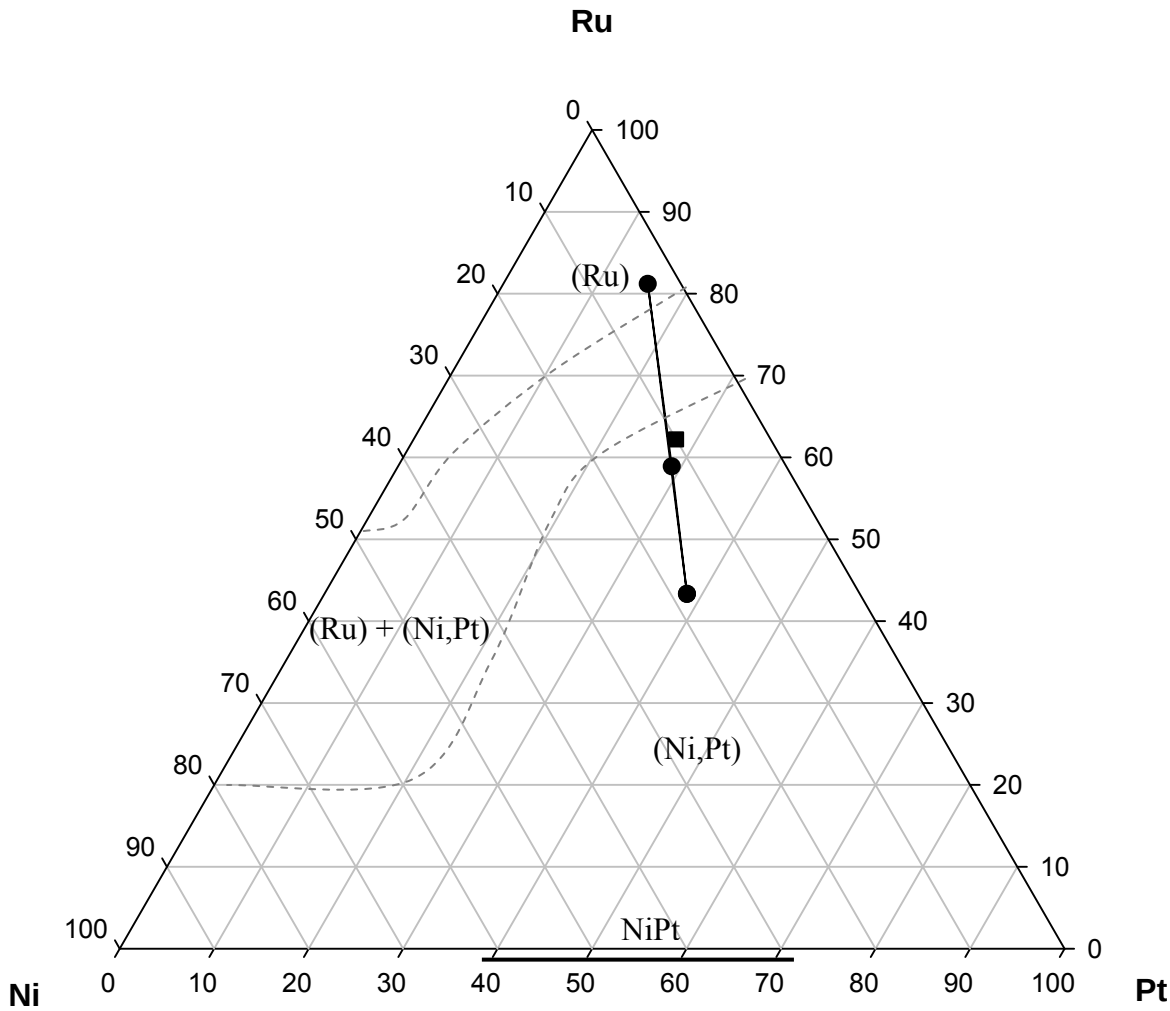


Figure 4.33. EDS analyses of LG 2 (Nominal Ni_{10}:Pt_{23}:Ru_{67}) after heat treatment and water quench (at.%).

LG 3 (Nominal Ni_{20}:Pt_{20}:Ru_{60})

LG 3 (Nominal Ni_{20}:Pt_{20}:Ru_{60}) changed after heat treatment and water quenching, from a single-phased alloy to what seems like a three-phase alloy (Figure 4.34). The medium phase consisted of fine dark (Ru) needles in a lighter (Ni,Pt) matrix. The overall composition had changed; thus some homogenisation had occurred (since there was no sign of the unmelted Ru). According to the XRD scan (Figure 4.35), the main structures present were (Ni,Pt), (Ru) and NiO when the peaks were shifted. Again, the XRD pattern had become more complex after heat treatment than in the as-cast state (Figure 4.8), but compared to the XRD spectrum from LG 2, the spectrum contains fewer peaks. However, the lightest contrast phases could both have been (Ni,Pt), with the local differences caused by the precipitation of the (Ru) needles. The EDS analyses are shown in Table 4.12 and the actual compositions are plotted in Figure 4.36. The sample might contain some oxygen in the form of a metal oxide (which formed on the surface of the sample during heat treatment), thus the overall composition lies outside the composition triangle. The phase proportions are shown in Table 4.12.

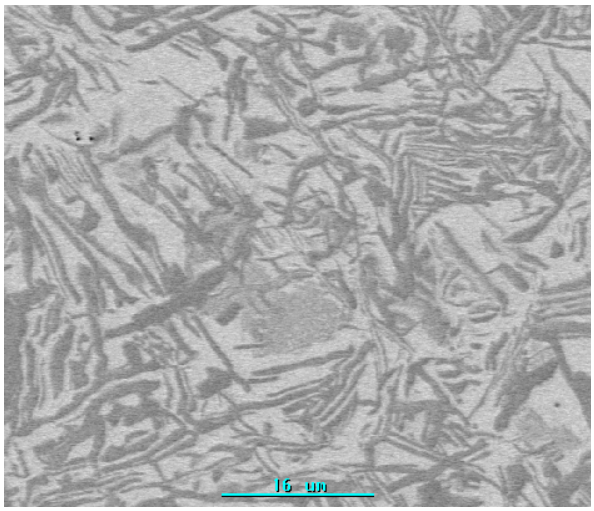


Figure 4.34: BSE image of LG 3 (Nominal Ni_{20}:Pt_{20}:Ru_{60}) after heat treatment and water quench showing (Ni,Pt) (light) with (Ru) needles (dark) and the medium contrast regions are fine needles (scale bar = 16μm).

Table 4.12: EDS analyses of LG 3 (Nominal Ni_{20}:Pt_{20}:Ru_{60}) in the annealed condition.

Phase description	Ni (at.%)	Pt (at.%)	Ru (at.%)	Phase	Proportion (%)
Overall	26.4 ± 0.6	20.8 ± 0.2	52.8 ± 0.8	-	-
Light Phase	42.8 ± 0.5	42.1 ± 0.6	15.1 ± 0.4	(Ni,Pt)	20%
Medium Phase	14.1 ± 0.5	36.0 ± 0.9	49.9 ± 0.7	(Ni,Pt), (Ru)	16%
Dark Phase	7.2 ± 0.9	13.2 ± 1.1	79.6 ± 0.8	(Ru)	64%

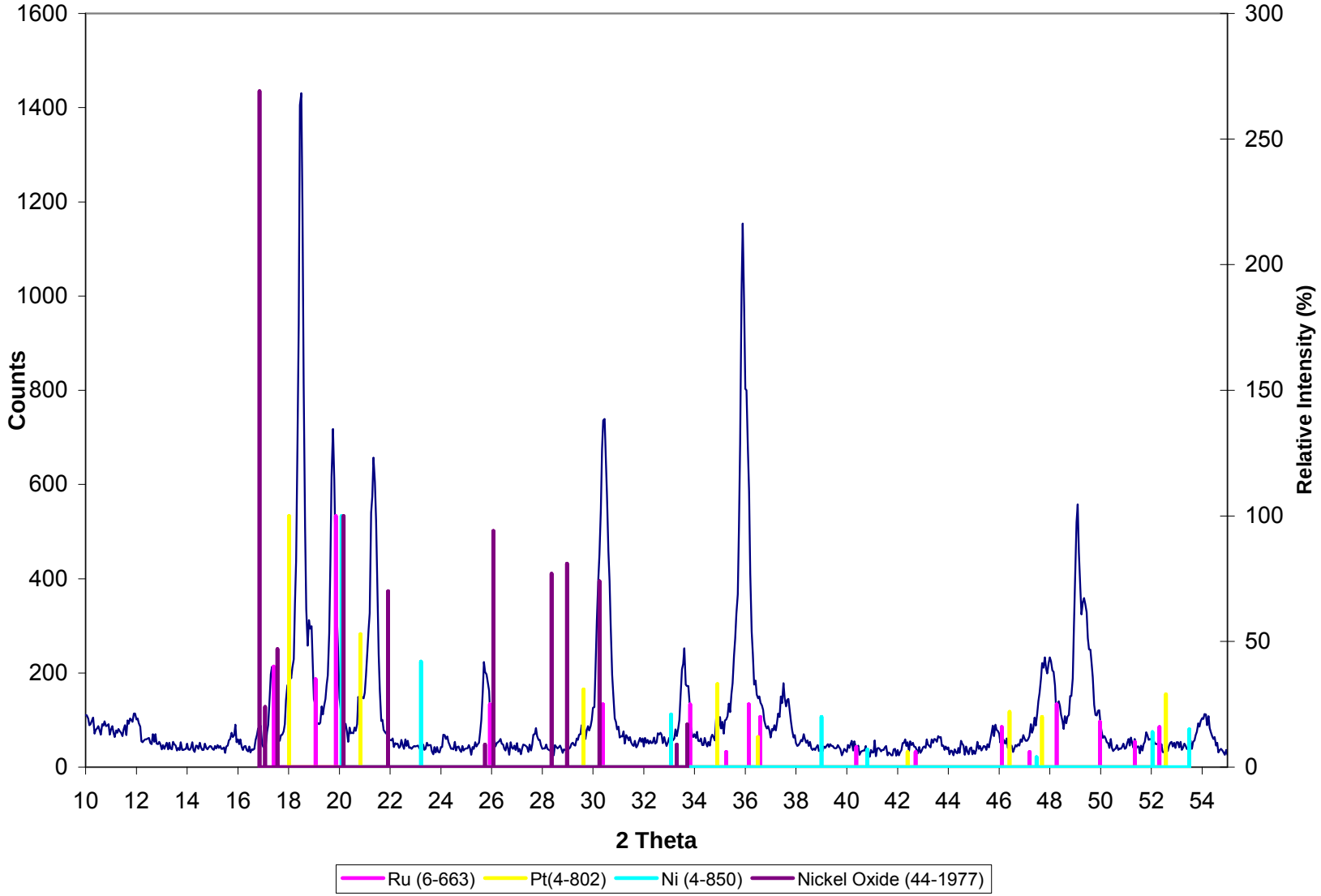


Figure 4.35: XRD spectrum of LG 3 (Nominal Ni_{20}:Pt_{20}:Ru_{60}) after heat treatment and water quench.

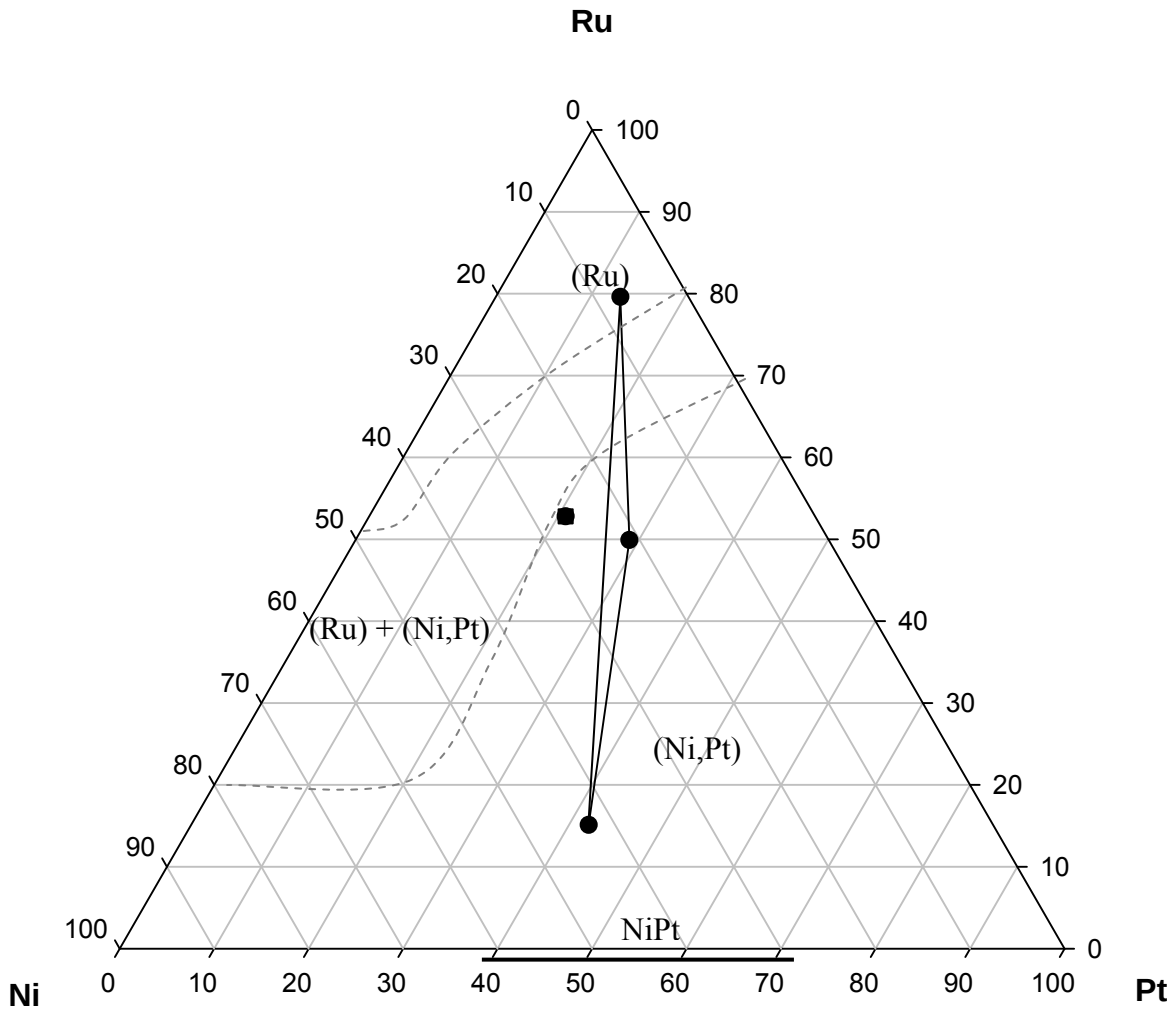


Figure 4.36: EDS analyses of LG 3 (Nominal Ni_{20}:Pt_{20}:Ru_{60}) after heat treatment and water quench (at.%).

LG 4 (Nominal Ni_{35}:Pt_{13}:Ru_{52})

In LG 4 (Nominal Ni_{35}:Pt_{13}:Ru_{52}), the proportions of the different phases that were present in the as-cast state changed after annealing the alloy for 1000 hours at 1000°C (Figure 4.37). The overall composition had changed after annealing, which was strange considering that no unmelted (Ru) had been observed before. However, before metallographic sample preparation, a layer of Ni-oxide was visible on the surface. The black spots visible in Figure 4.37 could be remnants of this oxide layer. These spots were too small to analyse correctly. The three main phases present are (Ni,Pt), (Ru) and NiO according to XRD (Figure 4.38), after shifting the peaks. The oxide formed during heat treatment and was mainly found on the outside surface of the sample. On comparing the as-cast (Figure 4.11) and heat-treated results (Figure 4.38), some peaks seemed to grow and others seemed to shrink. Once again, the XRD spectrum was more complex, suggesting more than two phases are present. However, microstructurally, the third phase was more difficult to resolve than in LG 2 (Nominal Ni_{10}:Pt_{23}:Ru_{67}) and LG 3 (Nominal Ni_{20}:Pt_{20}:Ru_{60}). The EDS analyses are shown in Table 4.13 and the actual composition is plotted in Figure 4.39. The overall composition lies away from the composition line and could be the result of the presence of oxygen as a metal oxide or due to another phase that was missed. The effect of precipitation in both phases skews the positions of the overall on the tie line in Figure 4.39. The EDS analyses were all normalised and if oxygen was present, it would not be shown in the results. The phase proportions are shown in Table 4.13.

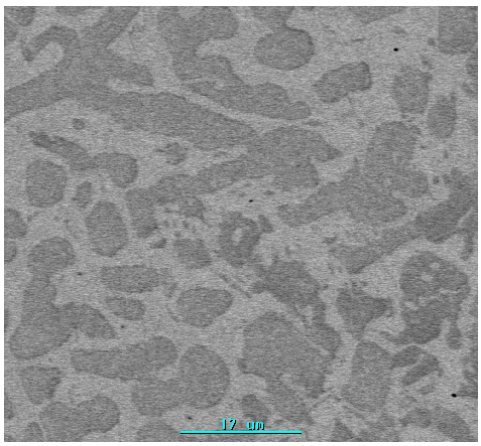


Figure 4.37: BEI of LG 4 (Nominal Ni_{35}:Pt_{13}:Ru_{52}) after heat treatment and water quench showing (Ni,Pt) (light) and (Ru) (dark) (scale bar = 17μm).

Table 4.13: EDS analyses of LG 4 (Nominal Ni_{35}:Pt_{13}:Ru_{52}) in the annealed condition.

Phase description	Ni (at.%)	Pt (at.%)	Ru (at.%)	Phase	Proportion (%)
Overall	28.8 ± 0.1	16.2 ± 0.4	55.0 ± 0.2	-	-
Light Phase	61.8 ± 0.3	27.3 ± 0.6	10.9 ± 0.9	(Ni,Pt)	56%
Dark Phase	16.5 ± 0.6	7.0 ± 0.5	76.5 ± 0.5	(Ru)	44%

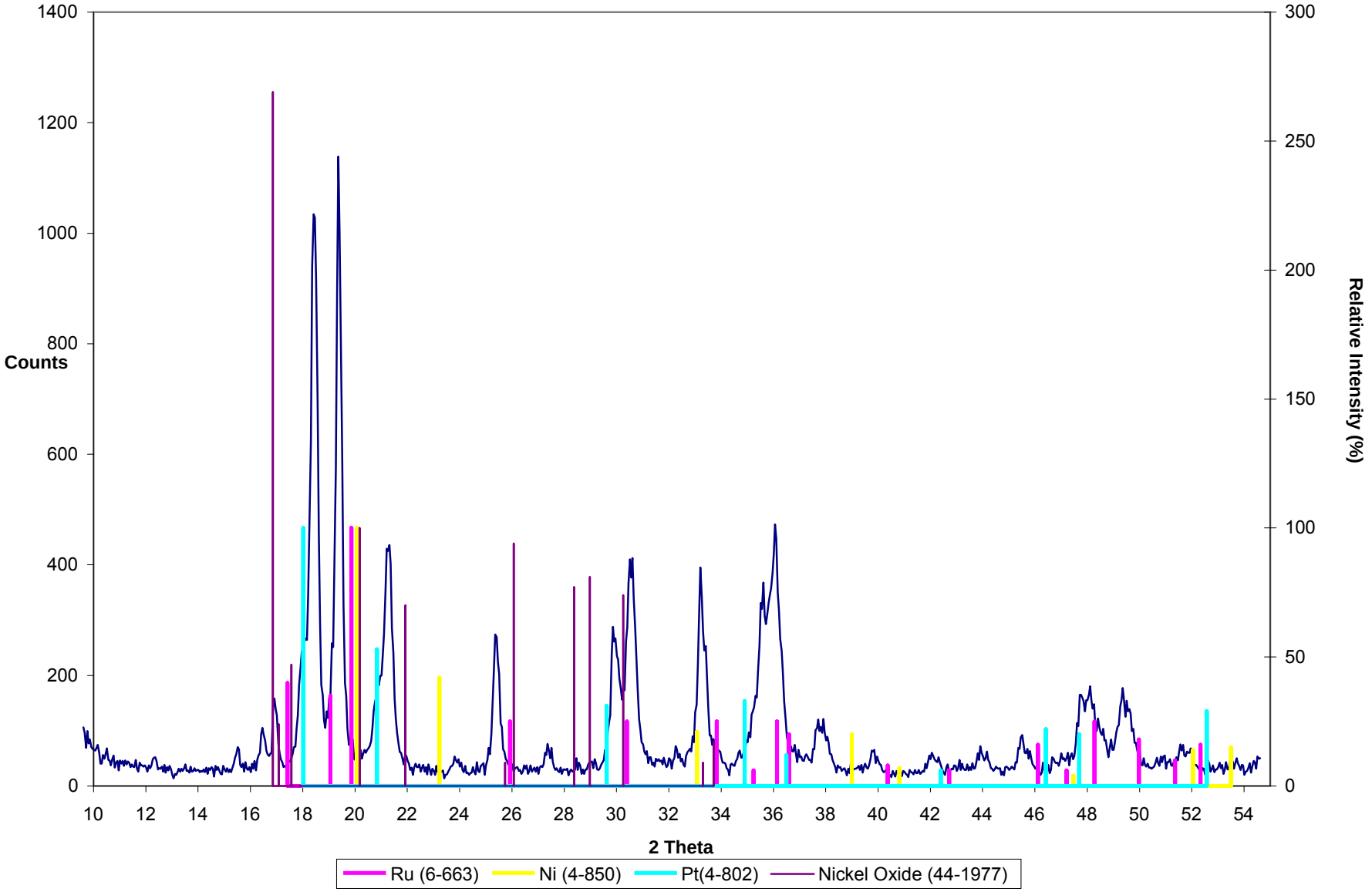


Figure 4.38: XRD spectrum of LG 4 (Nominal Ni_{35}:Pt_{13}:Ru_{52}) after heat treatment and water quench.

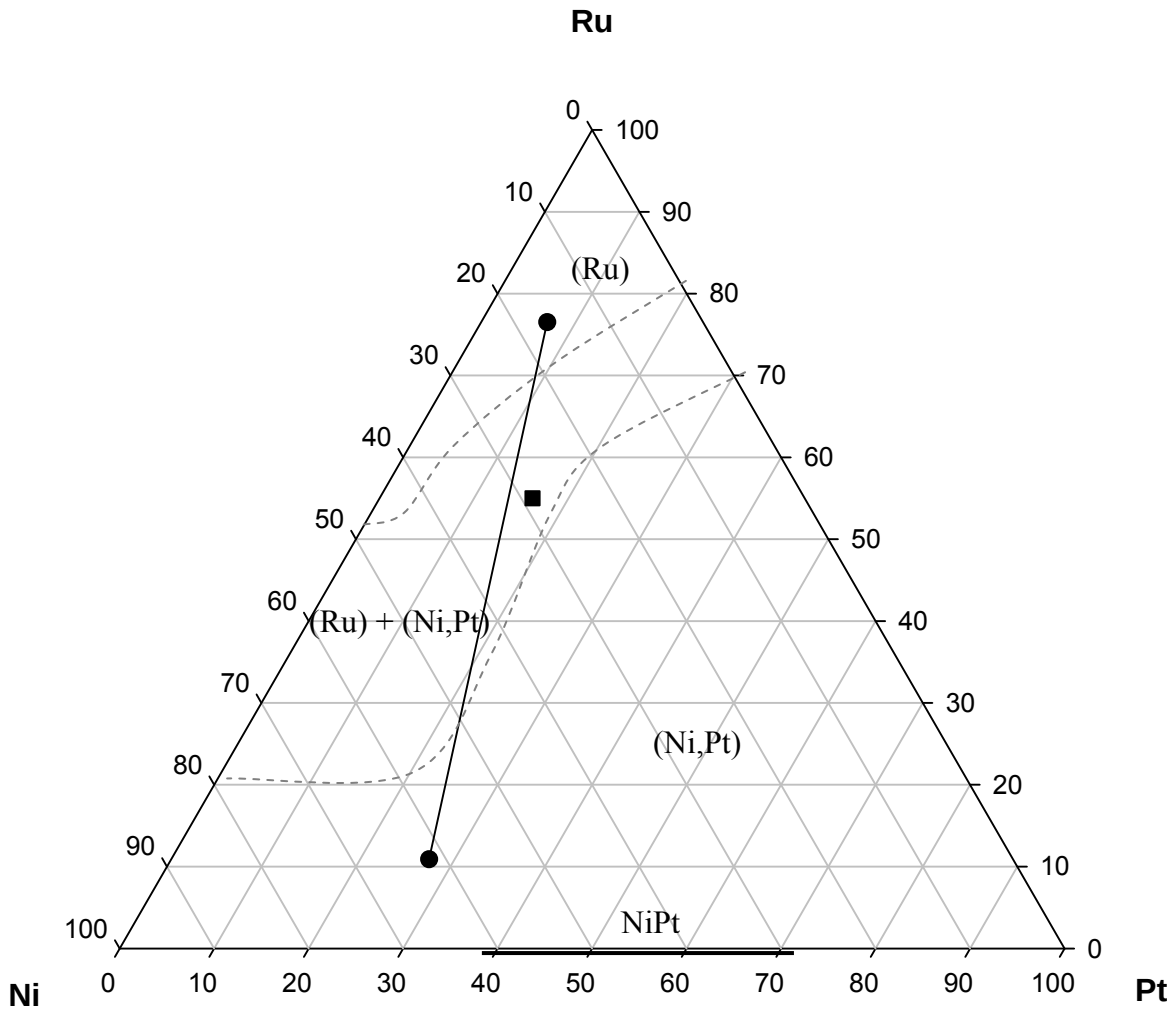


Figure 4.39: EDS analyses of LG 4 (Nominal Ni_{35}:Pt_{13}:Ru_{52}) after heat treatment and water quench (at.%).

LG 5 (Nominal $Ni_{50}:Pt_5:Ru_{45}$)

The phase proportions in Alloy LG 5 (Nominal $Ni_{50}:Pt_5:Ru_{45}$) changed after heat treating the alloy for 1000 hours at 1000°C (Figure 4.40) and the dendrites were more decomposed, giving a lower proportion of (Ru) dendrites. There was also no trace of coring in the (Ni,Pt). There are some dark spots that are pores. The two main structures present were the (Ni,Pt) and the (Ru), according to XRD (Figure 4.41), once the peaks are shifted. The (Ru) peaks seem to have grown, and the (Ni,Pt) seem to have shrunk, and NiO peaks appeared after the heat treatment. A black pores lay mostly within the light (Ru) phase. The EDS analyses are shown in Table 4.14 and are plotted in Figure 4.42. The overall composition lies very close to the compositional triangle and is within experimental error. The EDS analyses were all normalised and if oxygen was present, it would not be shown in the results. The phase proportions are shown in Table 4.14, 4% being holes.

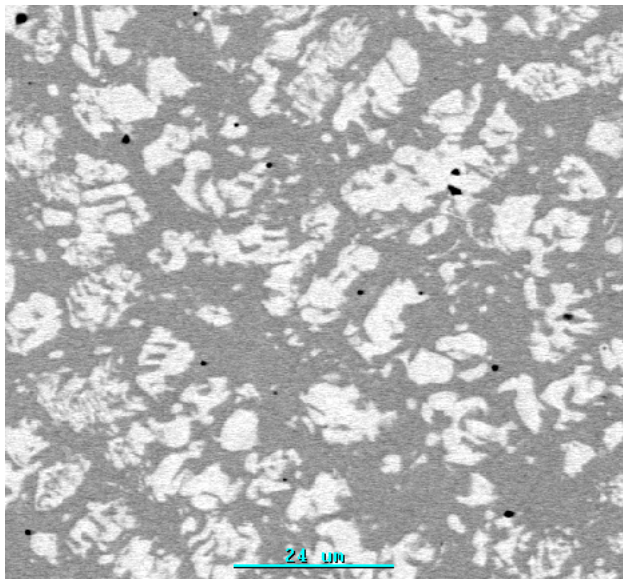


Figure 4.40. BEI of LG 5 (Nominal $Ni_{50}:Pt_5:Ru_{45}$) after heat treatment and water quench showing light (Ru) dendrites and dark (Ni,Pt) matrix and pores (scale bar = 24µm).

Table 4.14. EDS analyses of LG 5 (Nominal $Ni_{50}:Pt_5:Ru_{45}$) after heat treatment and a water quench.

Phase description	Ni (at.%)	Pt (at.%)	Ru (at.%)	Phase	Proportions
Overall	54.3 ± 0.3	7.2 ± 0.3	38.5 ± 0.4	-	-
Light Phase	11.4 ± 0.8	0.8 ± 0.4	87.8 ± 0.6	(Ru)	36%
Dark Phase	77.9 ± 0.6	9.1 ± 0.5	13.0 ± 0.6	(Ni,Pt)	60%

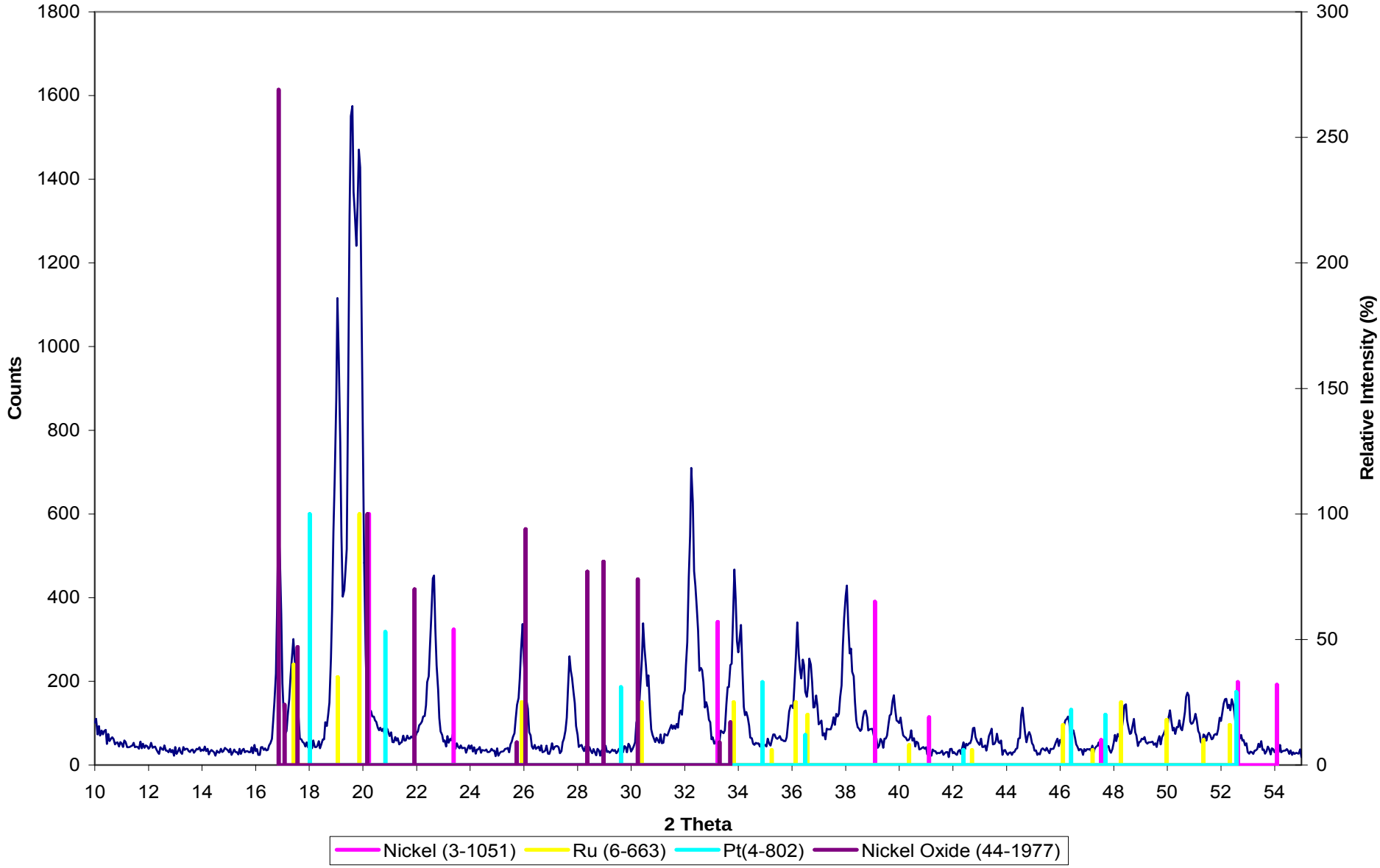


Figure 4.41: XRD scan of LG 5 (Nominal $Ni_{50}:Pt_5:Ru_{45}$) after heat treatment and water quench.

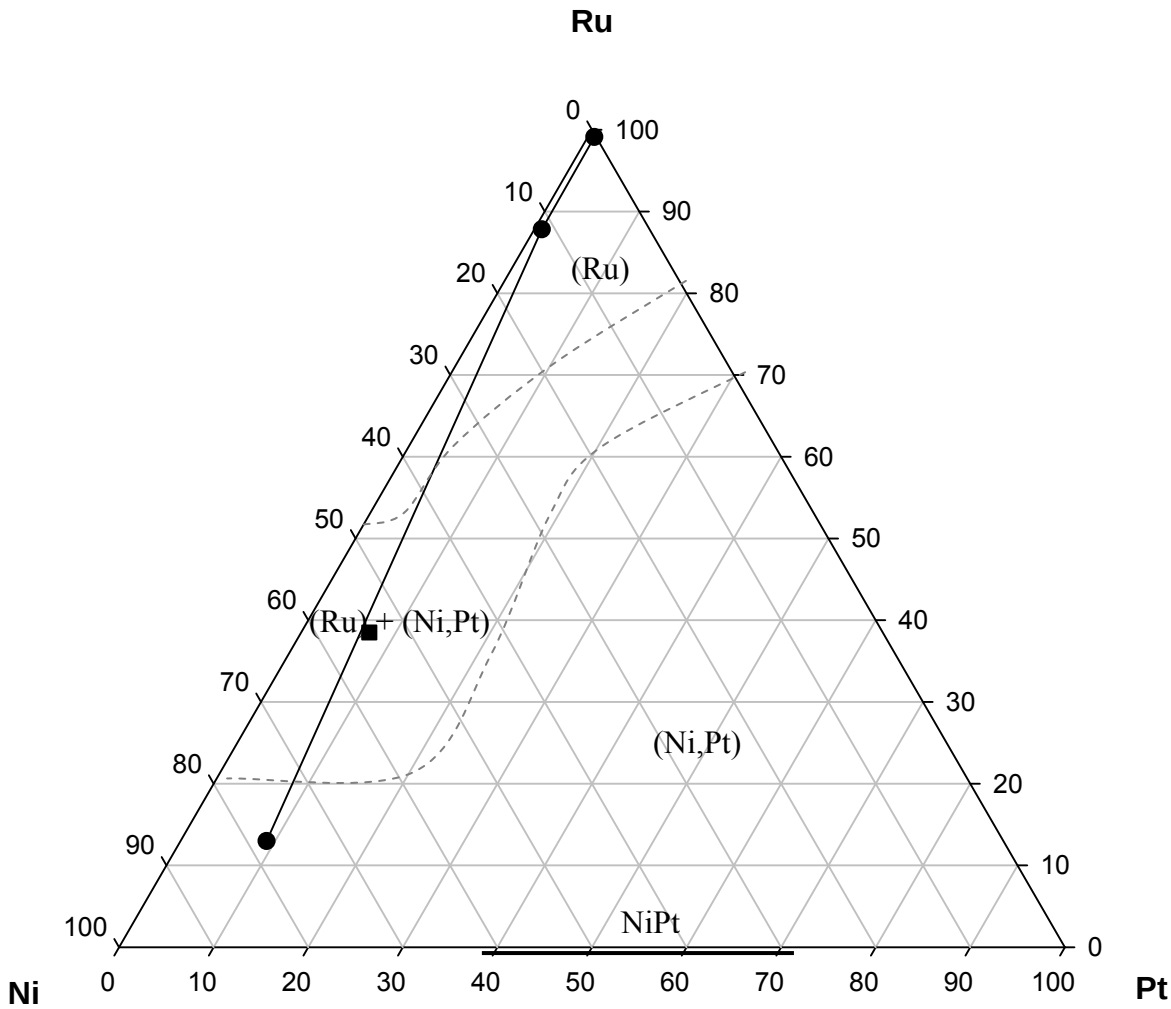


Figure 4.42: EDS analyses of LG 5 (Nominal Ni_{50}:Pt_5:Ru_{45}) after heat treatment and water quench (at.%).

LG 6 (Nominal $Ni_{60}:Pt_5:Ru_{35}$)

The phase proportions in LG 6 (Nominal $Ni_{60}:Pt_5:Ru_{35}$) had changed less after heat treatment (Figure 4.43) than in the other alloys. However, the (Ru) phase had become more rounded and the coring in (Ni,Pt) had disappeared. XRD identified the two main structures as (Ni,Pt) and (Ru) and some of the peaks were identified as NiO (Figure 4.44) as compared to the XRD spectrum for the as-cast sample in Figure 4.17. The peaks have shifted due to the solid solution of the elements in each other. The Ru peaks became more prominent and the (Ni,Pt) peaks became smaller after annealing. The spectrum showed a high signal to background ratio. The EDS analyses are shown in Table 4.15 and the compositions are plotted in Figure 4.45. The overall composition lies right on the tie-line between the two phases.

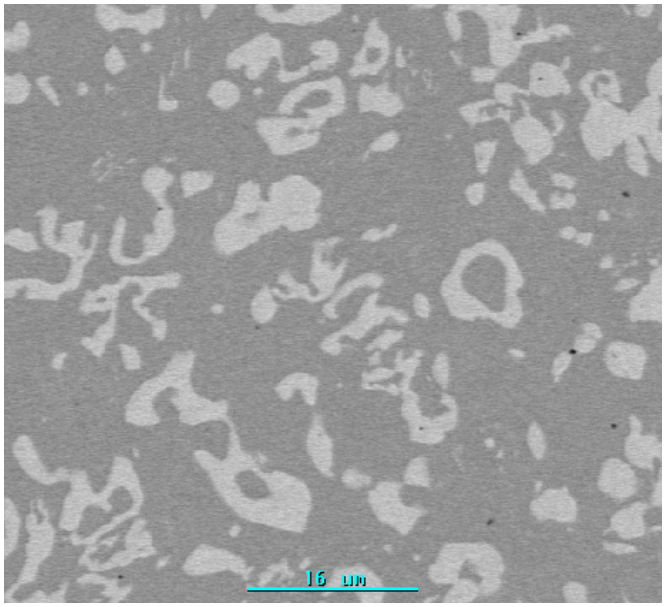


Figure 4.43: BEI of LG 6 (Nominal $Ni_{60}:Pt_5:Ru_{35}$) after heat treatment and water quench showing (Ru) (light) and (Ni,Pt) (dark) (scale bar = 16µm).

Table 4.15: EDS analyses of LG 6 (Nominal $Ni_{60}:Pt_5:Ru_{35}$) after heat treatment and water quench.

Phase description	Ni (at.%)	Pt (at.%)	Ru (at.%)	Phase	Proportions (%)
Overall	62.8 ± 0.6	5.4 ± 0.9	31.8 ± 0.3	-	-
Light Phase	12.1 ± 0.3	0.6 ± 0.5	87.3 ± 0.6	(Ru)	28%
Dark Phase	79.8 ± 0.2	7.4 ± 0.7	12.8 ± 0.4	(Ni,Pt)	72%

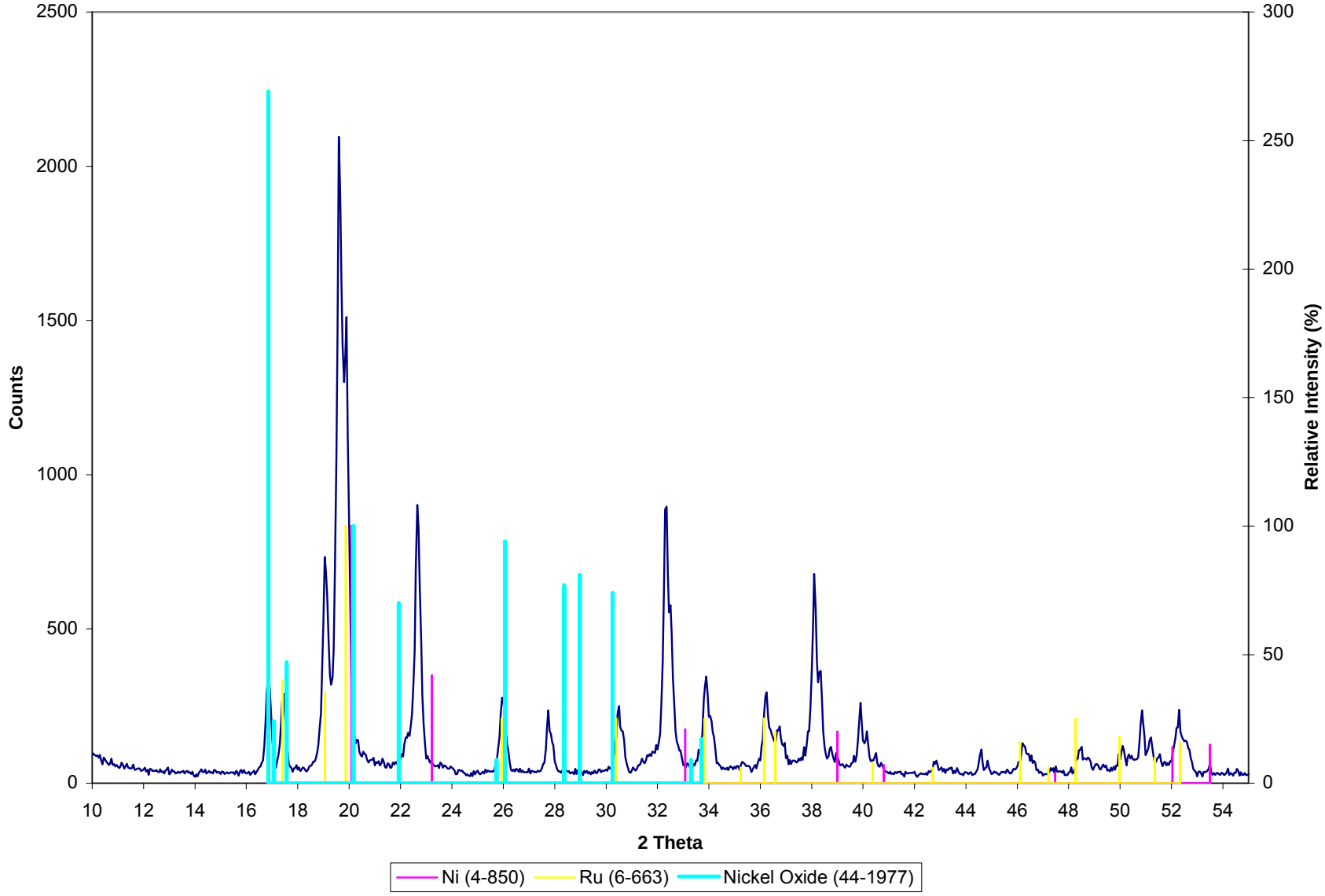


Figure 4.44: XRD scan of LG 6 (Nominal Ni_{60}:Pt_5:Ru_{35}) after heat treatment and water quench.

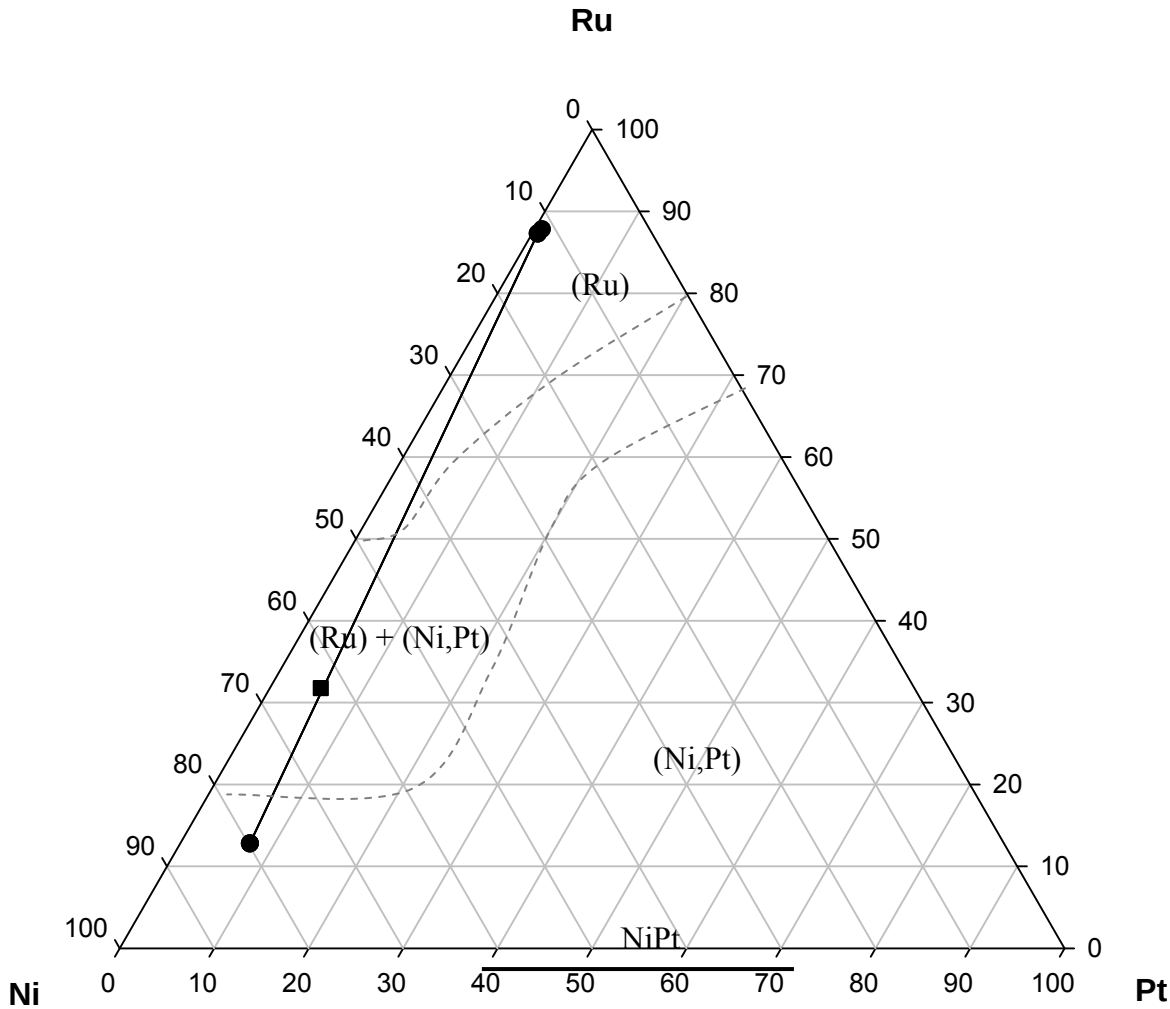
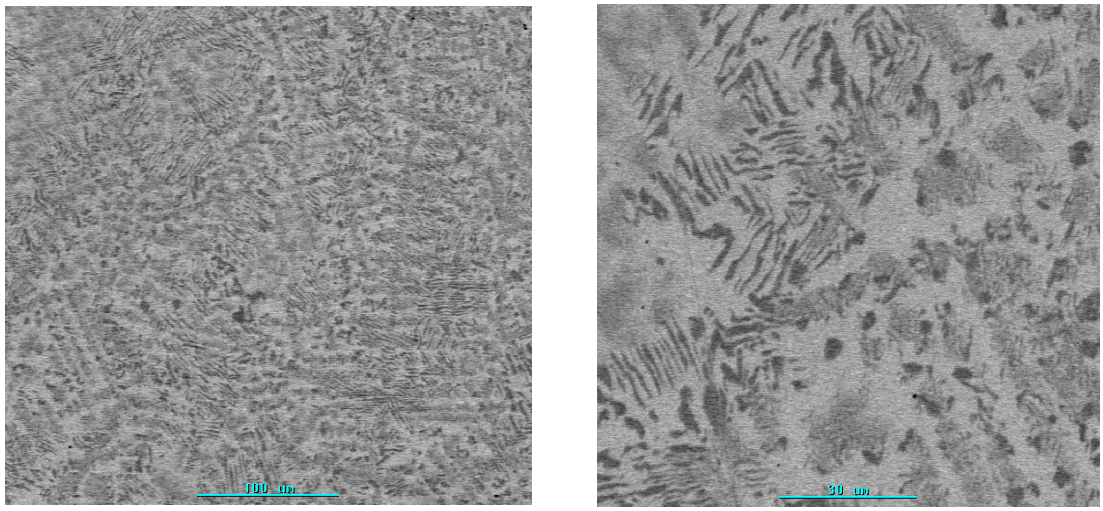


Figure 4.45: EDS analyses of LG 6 (Nominal $Ni_{60}:Pt_5:Ru_{35}$) after heat treatment and water quench (at.%).

LG 7 (Nominal Ni_{45}:Pt_{25}:Ru_{30})

LG 7 (Nominal Ni_{45}:Pt_{25}:Ru_{30}) shows three phases (Figure 4.46). The black phase is a newly-precipitated phase that was too small to be analysed by EDS. Figure 4.47 shows the XRD spectrum of LG 7 (Nominal Ni_{45}:Pt_{25}:Ru_{30}) in the heat treated state. The XRD spectrum for the as-cast sample in Figure 4.20 shows a single-phase and from this it can be ascertained that LG 7 (Nominal Ni_{45}:Pt_{25}:Ru_{30}) is a single phase alloy before heat treatment. It is likely that the needles were (Ru) according to the XRD spectrum (Figure 4.47). More peaks are visible after heat treatment, and those are identified to be NiO (after shifting the peaks). The light phase is the (Ni,Pt) and the dark phase is the (Ru). The EDS analyses are shown in Table 4.16 and the actual compositions are plotted in Figure 4.48. The EDS analyses were all normalised and if oxygen was present, it would not be shown in the results. The phase proportions are shown in Table 4.16.



a b

Figure 4.46: Microstructure of LG 7 (Nominal Ni_{45}:Pt_{25}:Ru_{30}) after heat treatment containing a light (Ru) matrix, dark regions consisting of fine (Ni,Pt) needles and black (Ni,Pt) precipitates. (The micron markers are 100 and 30μm respectively.)

Table 4.16: EDS analyses of LG 7 (Nominal Ni_{45}:Pt_{25}:Ru_{30}) after heat treatment and water quench.

Phase description	Pt (at.%)	Ru (at.%)	Ni (at.%)	Phase	Proportions (%)
Overall	25.5 ± 4.0	36.1 ± 1.9	38.4 ± 5.8	-	-
Light Phase	32.2 ± 1.1	11.9 ± 4.4	55.9 ± 3.5	(Ru)	40%
Dark Phase	7.4 ± 0.4	84.8 ± 1.1	7.8 ± 0.7	(Ni,Pt)	28%
Black Phase	4.1 ± 0.9	93.5 ± 1.1	2.4 ± 0.6	(Ni,Pt)	32%

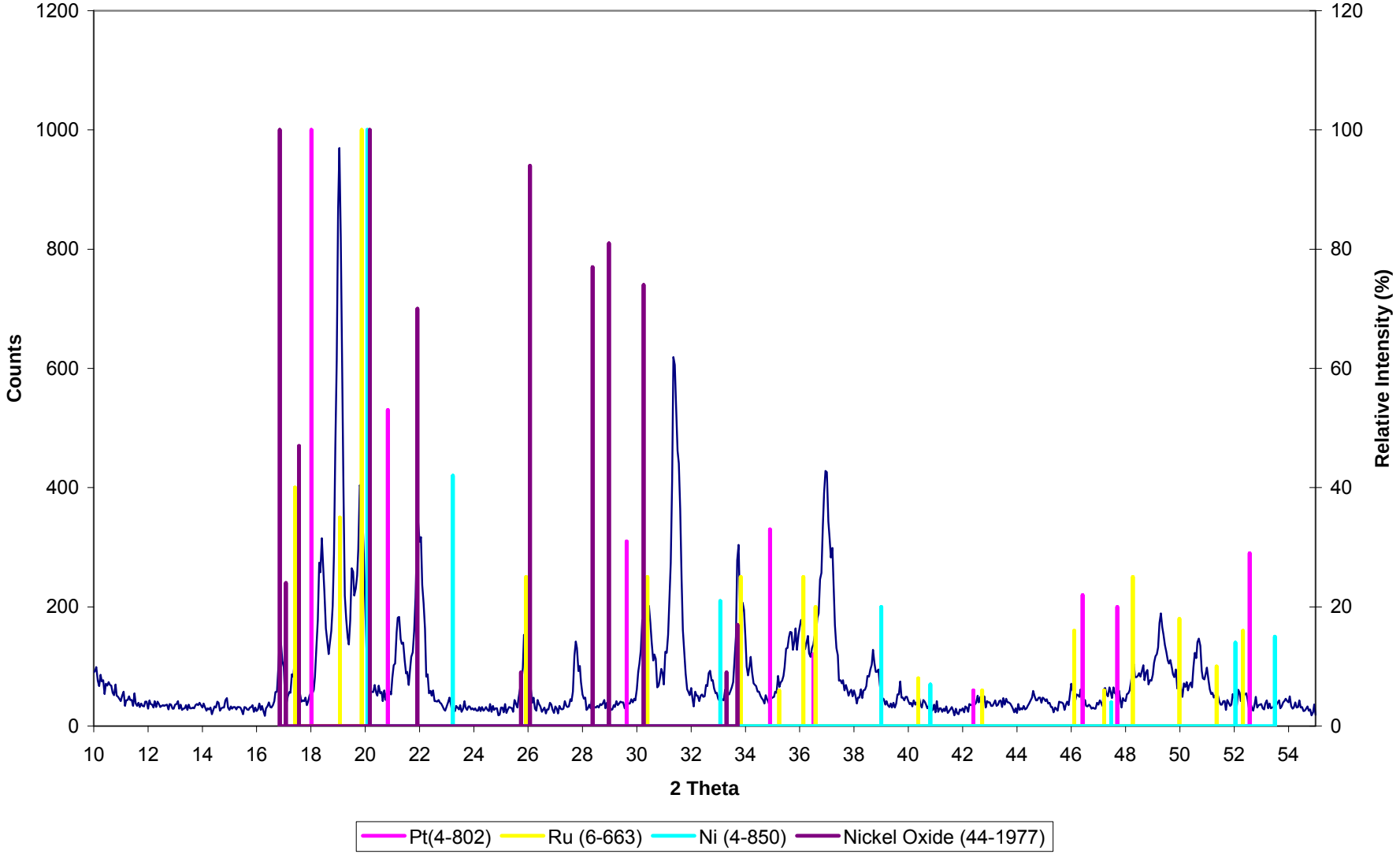


Figure 4.47: XRD spectrum LG 7 (Nominal Ni_{45}:Pt_{25}:Ru_{30}) after heat treatment and water quench.

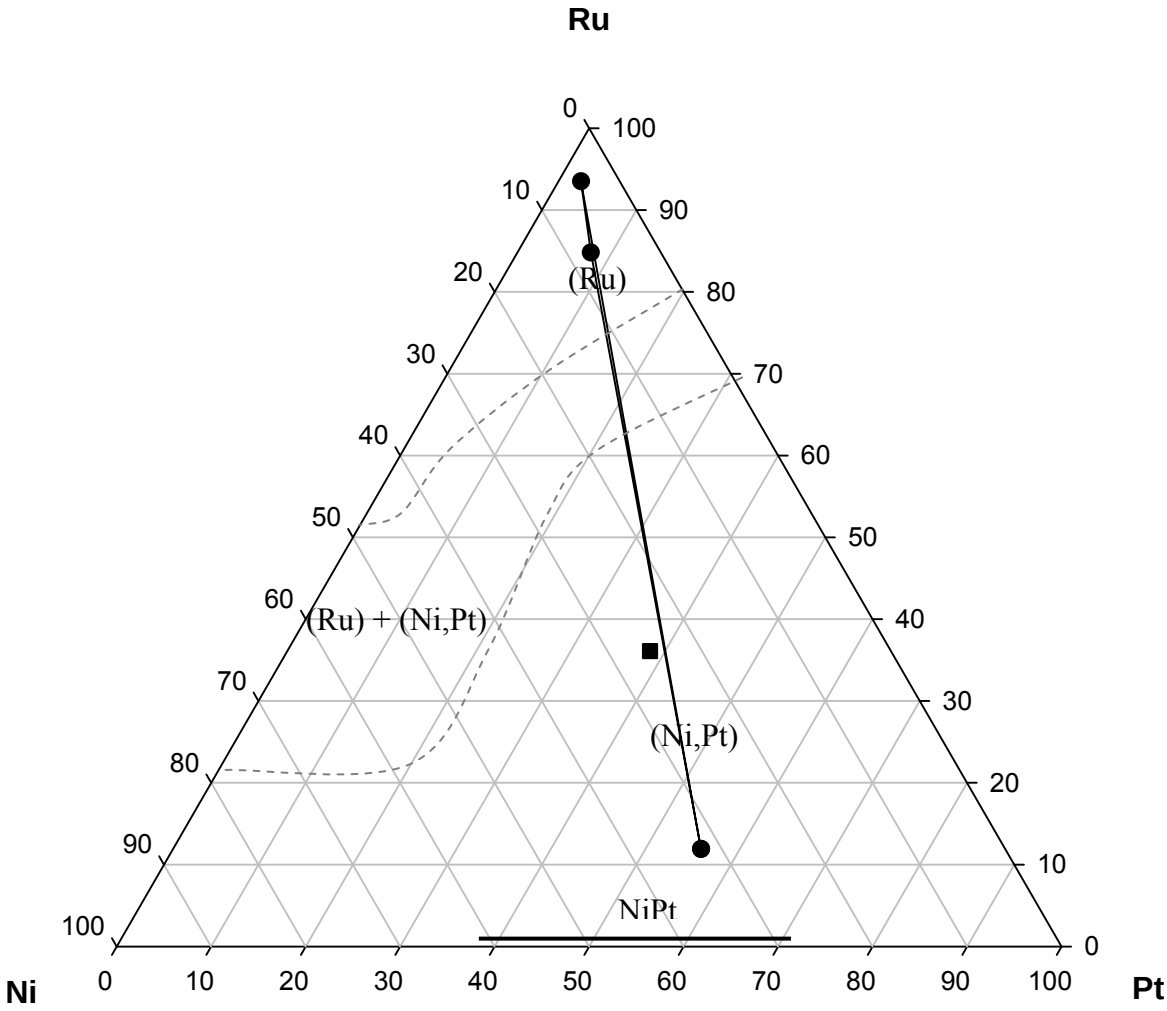
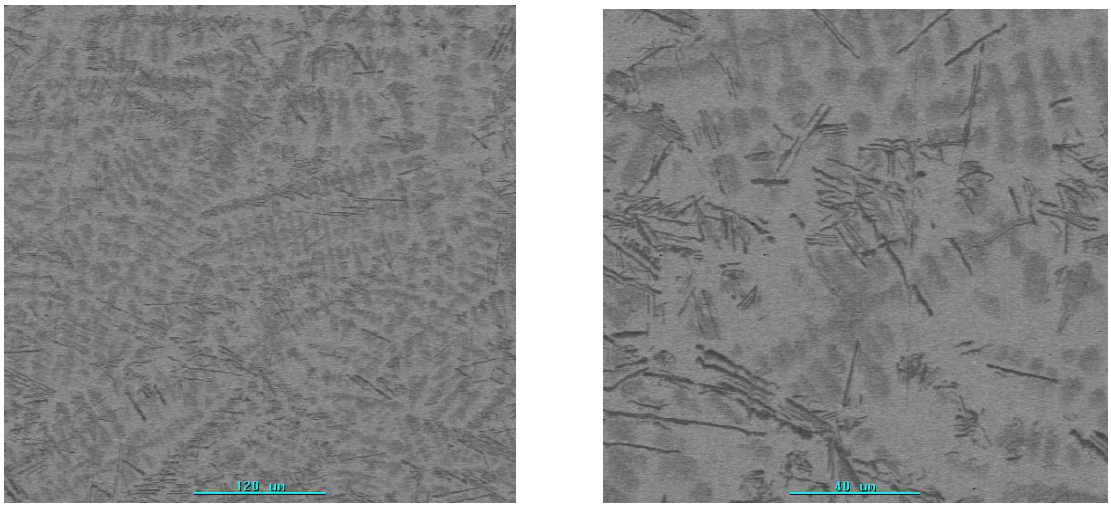


Figure 4.48: EDS analyses of LG 7 (Nominal Ni_{45}:Pt_{25}:Ru_{30}) after heat treatment (at.%).

LG 8 (Nominal Ni_{35}:Pt_{35}:Ru_{30})

LG 8 (Nominal Ni_{35}:Pt_{35}:Ru_{30}) was very similar to LG 7. It had three phases: dark, newly precipitated, Ru-rich (Ru) needles and light (Ni,Pt), and medium (Ru) phases. The microstructure is shown is Figure 4.49. Figure 4.49a is at a lower magnification to show the appearance of the dendrites. The XRD spectrum of the as-cast sample is shown in Figure 4.23 and shows that LG 8 (Nominal Ni_{35}:Pt_{35}:Ru_{30}) is single phase before heat treatment. After heat treatment, the (Ni,Pt) peaks have grown and that there are more peaks on the XRD spectrum which have been identified as NiO, once the peaks were shifted. The peak at $2\theta \approx 13°$ is from the plasticine that the sample was mounted in. The light phase is (Ni,Pt) and the medium phase is (Ru). The EDS analyses are shown in Table 4.17 and the actual compositions are plotted is Figure 4.51. The EDS analyses were all normalised. The phase proportions are shown in table 4.17.



a b

Figure 4.49: BEI showing the microstructure of LG 8 (Nominal Ni_{35}:Pt_{35}:Ru_{30}) after heat treatment and water quench containing a light (Ru) matrix, dark regions consisting of fine (Ni,Pt) needles and black (Ni,Pt) precipitates. The micron markers are 100 and 30μm respectively.

Table 4.17: EDS analyses of LG 8 (Nominal Ni_{35}:Pt_{35}:Ru_{30}) after heat treatment and water quench.

Phase description	Pt (at.%)	Ru (at.%)	Ni (at.%)	Phase	Proportions (%)
Overall	34.2 ± 1.7	35.1 ± 1.4	30.7 ± 1.2	-	-
Light Phase	41.9 ± 0.1	13.5 ± 0.2	44.6 ± 0.1	(Ru)	44%
Medium Phase	27.5 ± 1.7	51.1 ± 2.2	21.4 ± 1.3	(Ni,Pt)	28%
Dark Phase	5.6 ± 2.9	91.0 ± 3.0	3.4 ± 2.6	(Ni,Pt)	28%

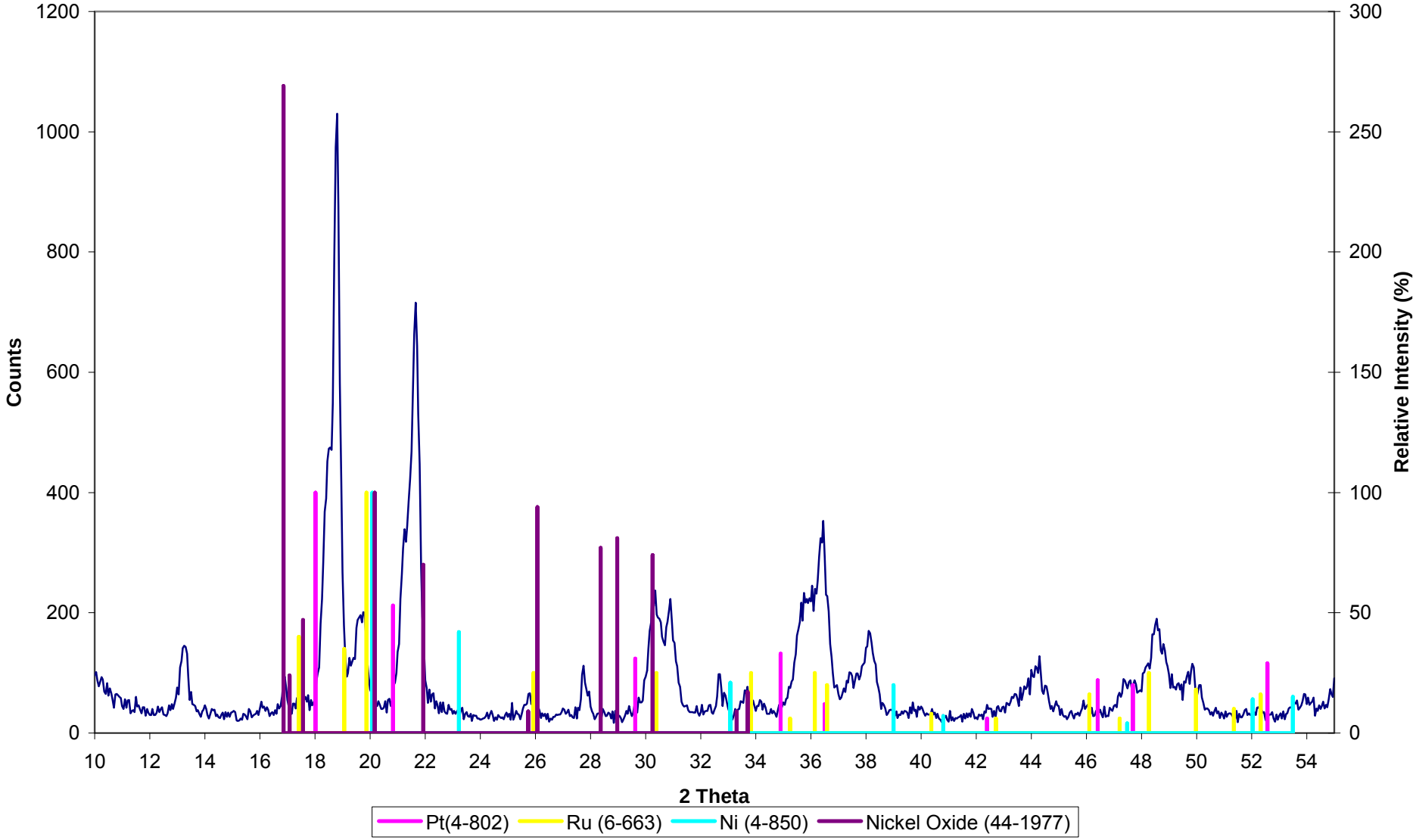


Figure 4.50: XRD spectrum of LG 8 (Nominal Ni_{35}:Pt_{35}:Ru_{30}) after heat treatment and water quench.

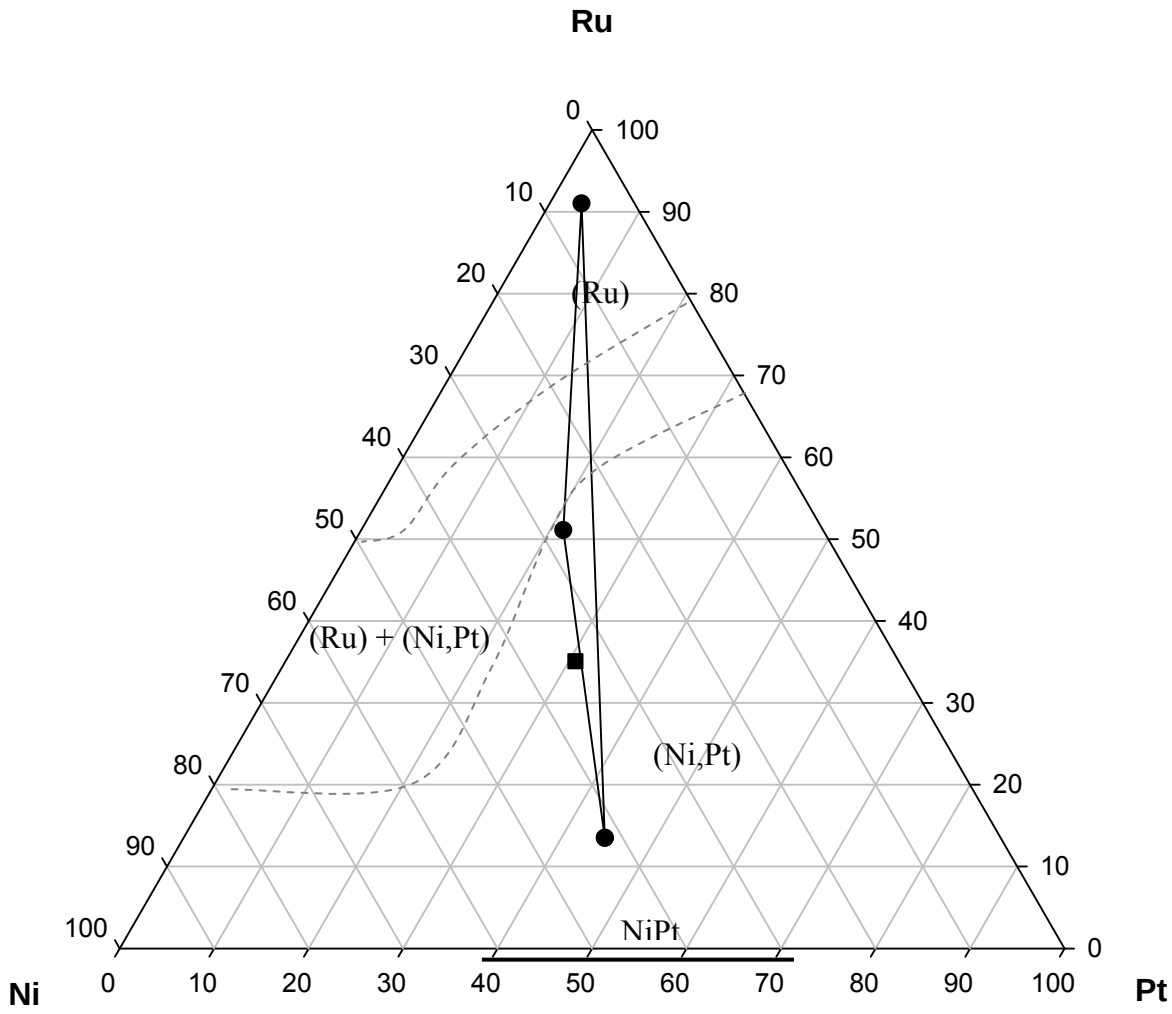


Figure 4.51: EDS analyses of LG 8 (Nominal Ni_{35}:Pt_{35}:Ru_{30}) after heat treatment and water quench (at.%).

LG 9 (Nominal Ni_{25}:Pt_{45}:Ru_{30})

LG 9 (Nominal Ni_{25}:Pt_{45}:Ru_{30}) was a single phase alloy in the as-cast condition and did not change much after heat treatment. The microstructure of LG 9 after heat treatment is shown in Figure 4.52 coring is still visible. The XRD spectrum (Figure 4.26) of the as-cast sample shows (Ni,Pt) with a small amount of Ru present. The XRD spectrum (Figure 4.53) of the heat treated sample shows the same peaks, but in different proportions. There are peaks that have appeared after heat treatment that correspond to (Ru), after shifting of the peaks. The shift was due to large amounts of Ni and Pt in solution. The peak at $2\theta \approx 13°$ is from the plasticine holding the sample. The EDS analyses are shown in Table 4.18 and the compositions are plotted in Figure 4.54. The phase proportions are shown in Table 4.18.

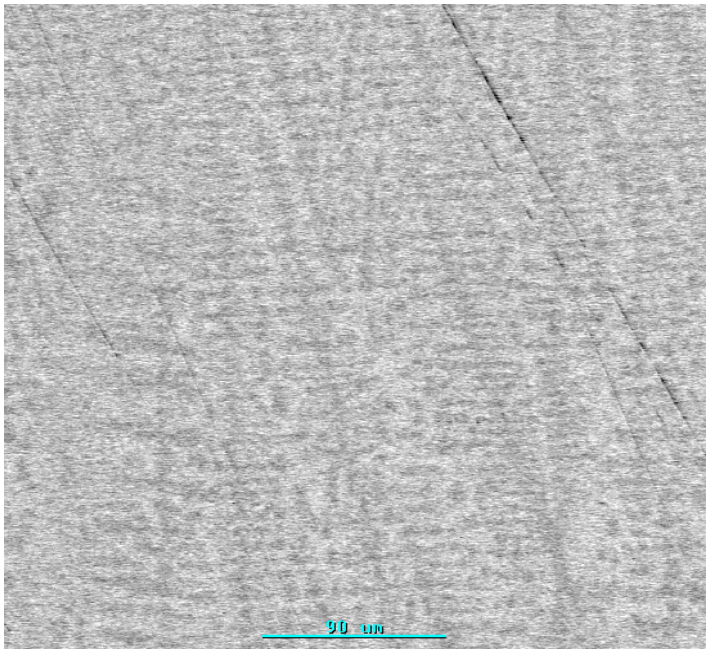


Figure 4.52: BEI of LG 9 (Nominal Ni_{25}:Pt_{45}:Ru_{30}) showing a cored single-phase after heat treatment and water quench containing a light (Ru) matrix, dark (Ni,Pt) dendrites. (micron marker = 90μm).

Table 4.18. EDS analyses of LG 9 (Nominal Ni_{25}:Pt_{45}:Ru_{30}) after heat treatment and water quench.

Phase description	Pt (at.%)	Ru (at.%)	Ni (at.%)	Phase	Proportions
Overall	46.5 ± 2.0	29.9 ± 2.0	23.6 ± 3.4	-	-
Light Phase	49.6 ± 1.2	16.6 ± 4.0	33.8 ± 3.0	(Ru)	55%
Dark Phase	40.6 ± 0.3	43.5 ± 1.2	15.9 ± 1.2	(Ni,Pt)	45%

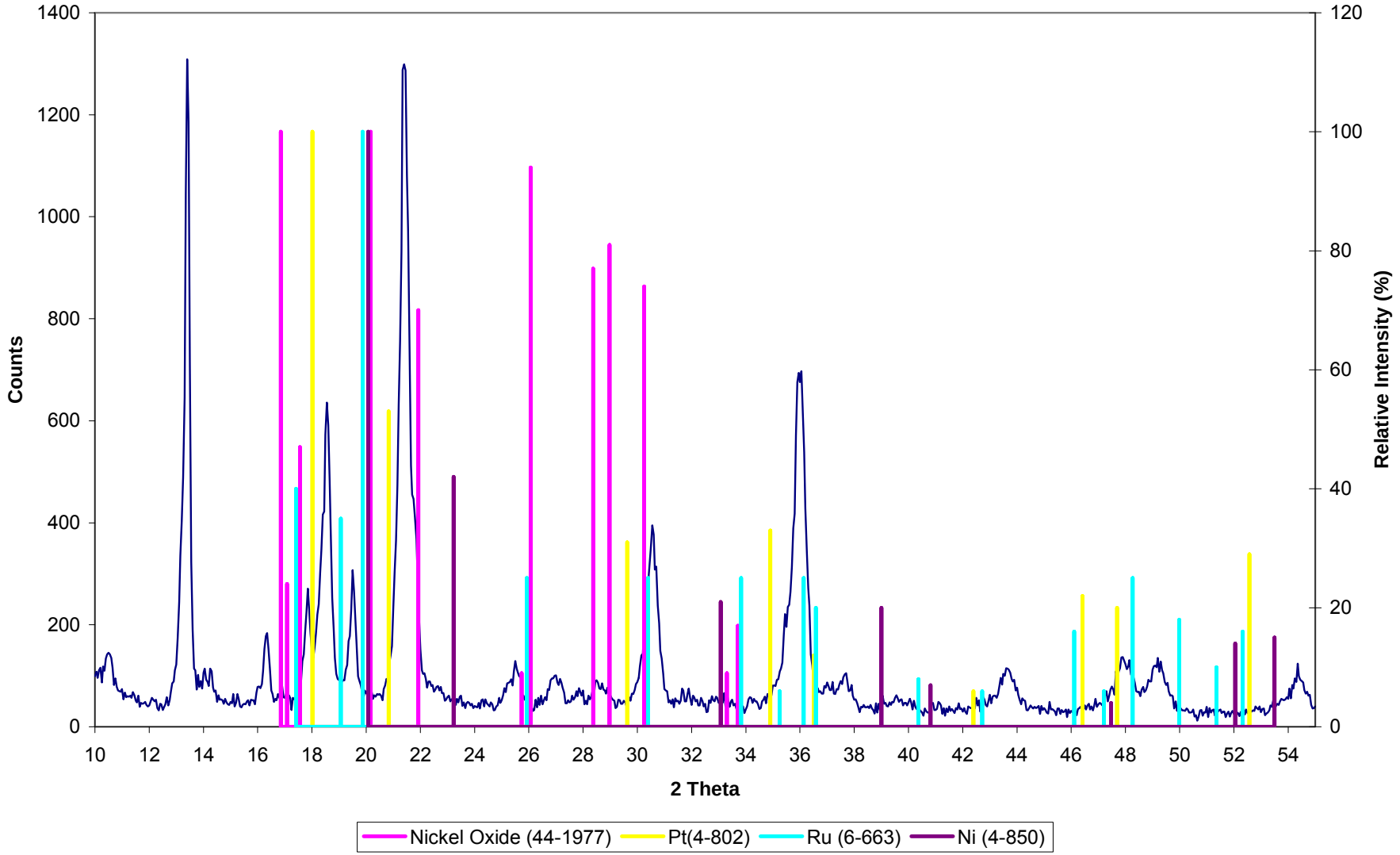


Figure 4.53: XRD scan of LG 9 (Nominal Ni_{25}:Pt_{45}:Ru_{30}) after heat treatment and water quench.

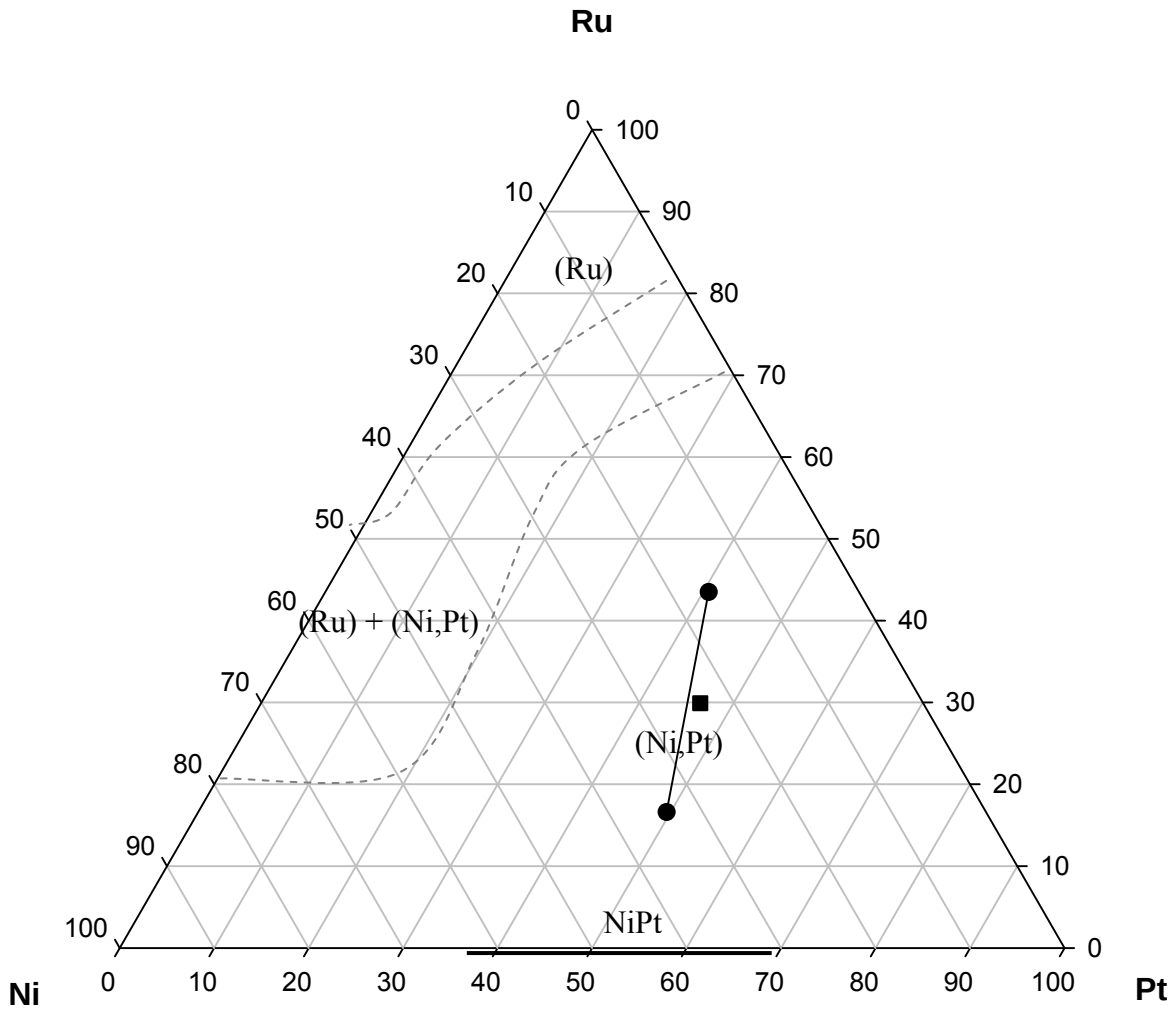


Figure 4.54: EDS analyses of LG 9 (Nominal Ni_{25}:Pt_{45}:Ru_{30}) after heat treatment and water quench (at.%).

LG 10 (Nominal Ni_{15}:Pt_{55}:Ru_{30})

LG 10 (Nominal Ni_{15}:Pt_{55}:Ru_{30}) is similar to LG 9 (Nominal Ni_{25}:Pt_{45}:Ru_{30}). The microstructure of the heat treated sample is shown in Figure 4.55 (single phase with coring). The XRD spectra of the as-cast and heat treated samples show a good fit after shifting and are shown in Figures 4.29 and 4.56 and show a single phase (Ni,Pt), since all the peaks are the same and the alloy lies in the (Ni,Pt) phase field. The EDS analyses are shown in Table 4.19 and the compositions are plotted in Figure 4.57.

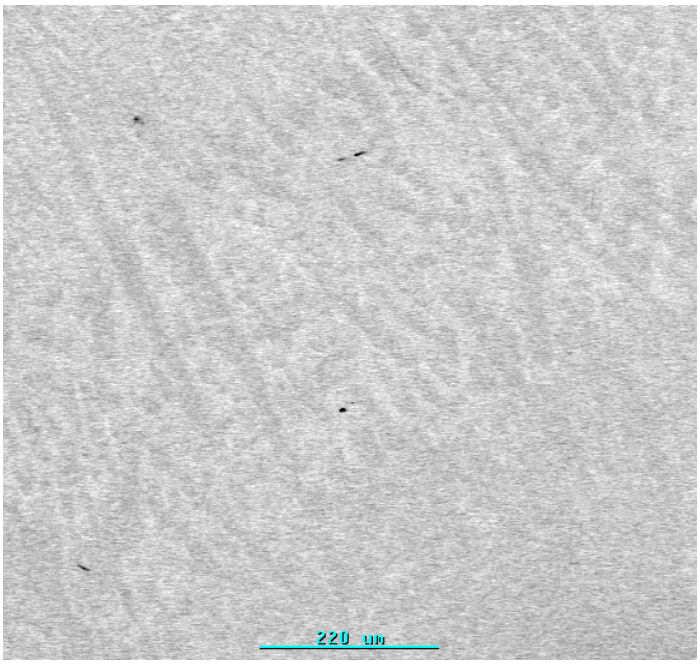


Figure 4.55: BEI of the microstructure of LG 10 (Nominal Ni_{15}:Pt_{55}:Ru_{30}) after heat treatment and water quench, consisting of different contrast regions of (Ni,Pt), (micron markers =220μm).

Table 4.19: EDS analyses of LG 10 (Nominal Ni_{15}:Pt_{55}:Ru_{30}) after heat treatment and water quench.

Phase description	Pt (at.%)	Ru (at.%)	Ni (at.%)	Phase	Proportions
Overall	55.9 ± 1.2	29.1 ± 1.7	15.0 ± 0.7	-	-
Light Phase	60.8 ± 2.9	17.1 ± 6.3	22.1 ± 3.5	(Ni,Pt)	30%
Dark Phase	53.6 ± 0.5	38.5 ± 1.6	7.9 ± 1.2	(Ni,Pt)	70%

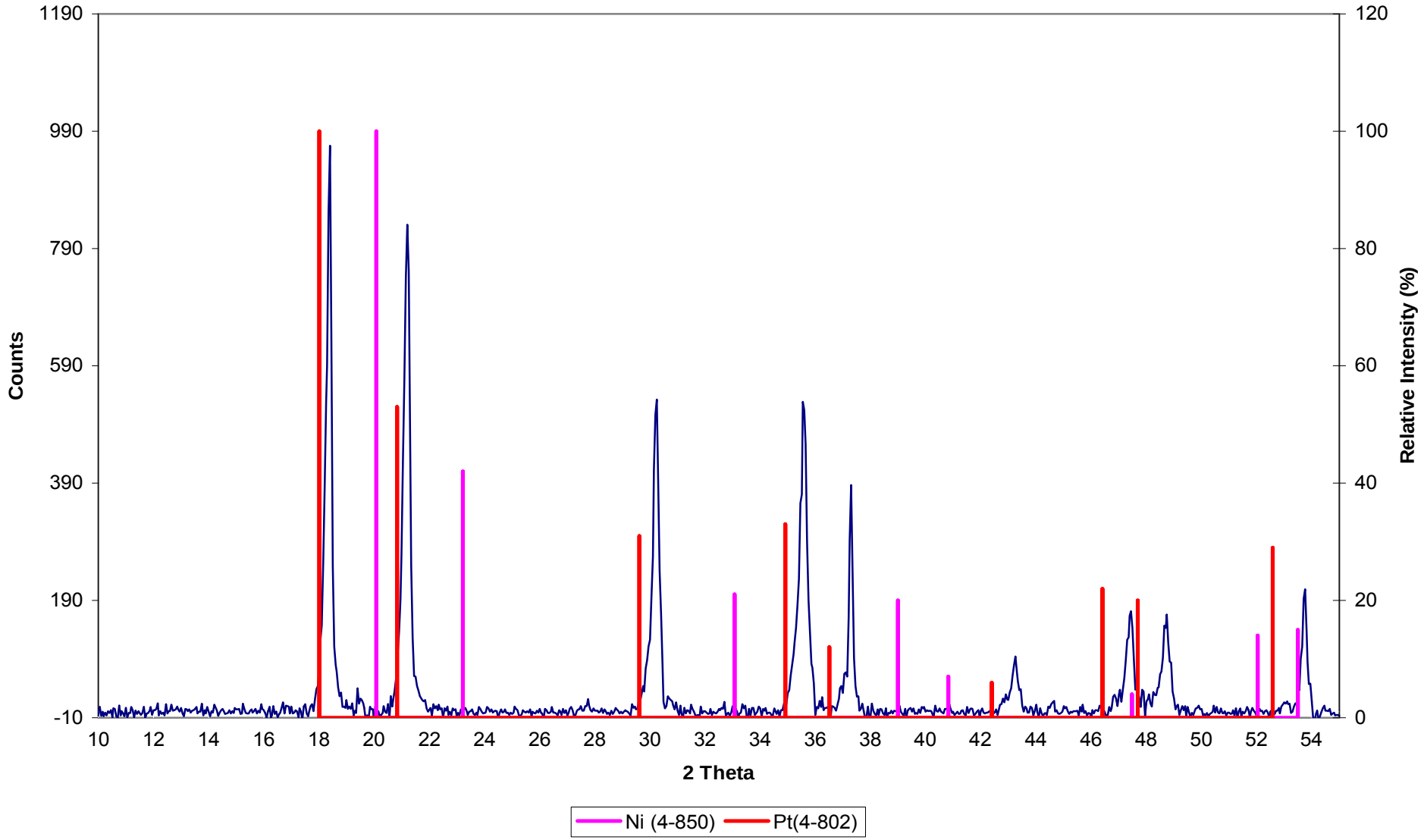


Figure 4.56: XRD scan of LG 10 (Nominal Ni_{15}:Pt_{55}:Ru_{30}) after heat treatment at 1000°C for 1000 hours and water quench.

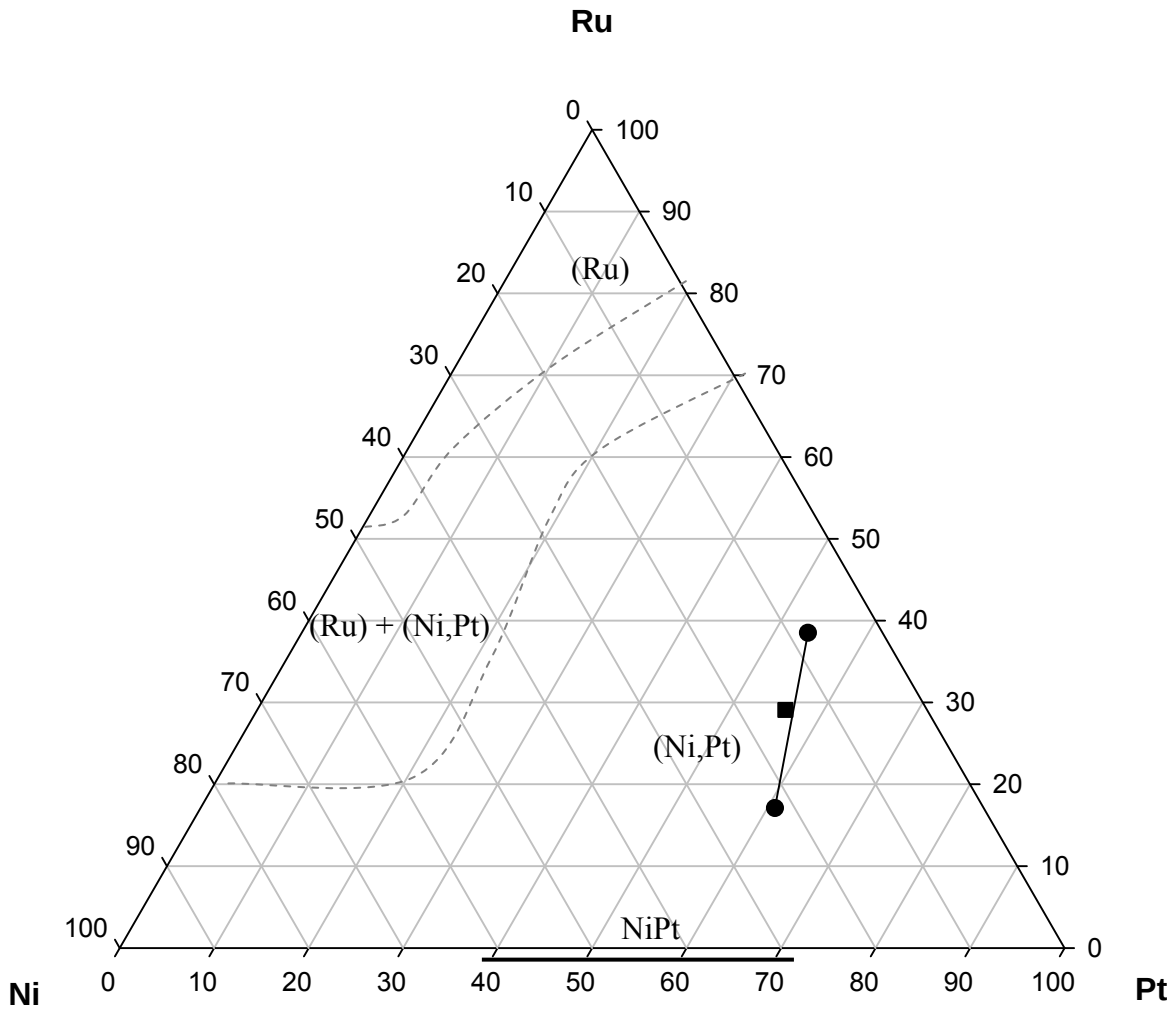


Figure 4.57: EDS analyses of LG 10 (Nominal Ni_{15}:Pt_{55}:Ru_{30}) after heat treatment and water quench (at.%).

4.1.3 Ordering Heat Treatment at 500°C

LG 1 (Nominal $Ni_{47.5}$:$Pt_{47.5}$:Ru_5)

LG 1 (Nominal $Ni_{47.5}$:$Pt_{47.5}$:Ru_5) experienced some changes after the heat treatment at 500°C to promote ordering, as shown by the peaks in the XRD spectra of the as-cast and heat treated samples (Figures 4.2 and 4.59). Some peaks are larger and a few are smaller (Figure 4.59) compared to the as-cast sample (Figure 4.2) which could be expected from a change in texture on annealing. Ordering has occurred, because there is an increase in the number of peaks, showing that some superlattice peaks are appearing. The peaks in Figure 4.59 correspond to the ordered phase NiPt. Only one peak at $2\theta \approx 19.5°$ has not been identified. The EDS analyses are shown in Table 4.20 and are plotted in Figure 4.60.

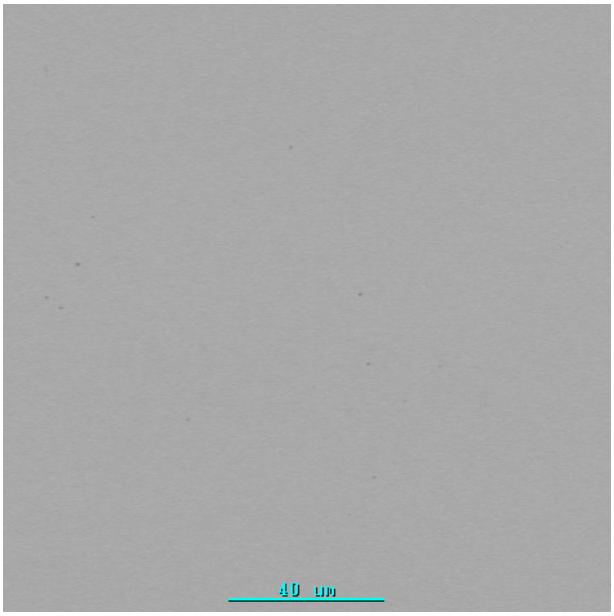


Figure 4.58. BEI of LG 1 (Nominal $Ni_{47.5}$:$Pt_{47.5}$:Ru_5) after ordering heat treatment and water quench consisting of single phase (Ni,Pt), (micron markers =40μm).

Table 4.20. EDS analyses of LG 1 (Nominal $Ni_{47.5}$:$Pt_{47.5}$:Ru_5) after ordering heat treatment.

Phase description	Ni (at.%)	Pt (at.%)	Ru (at.%)	Phase
Overall	45.3 ± 0.6	49.5 ± 0.4	5.2 ± 0.3	(Ni,Pt)

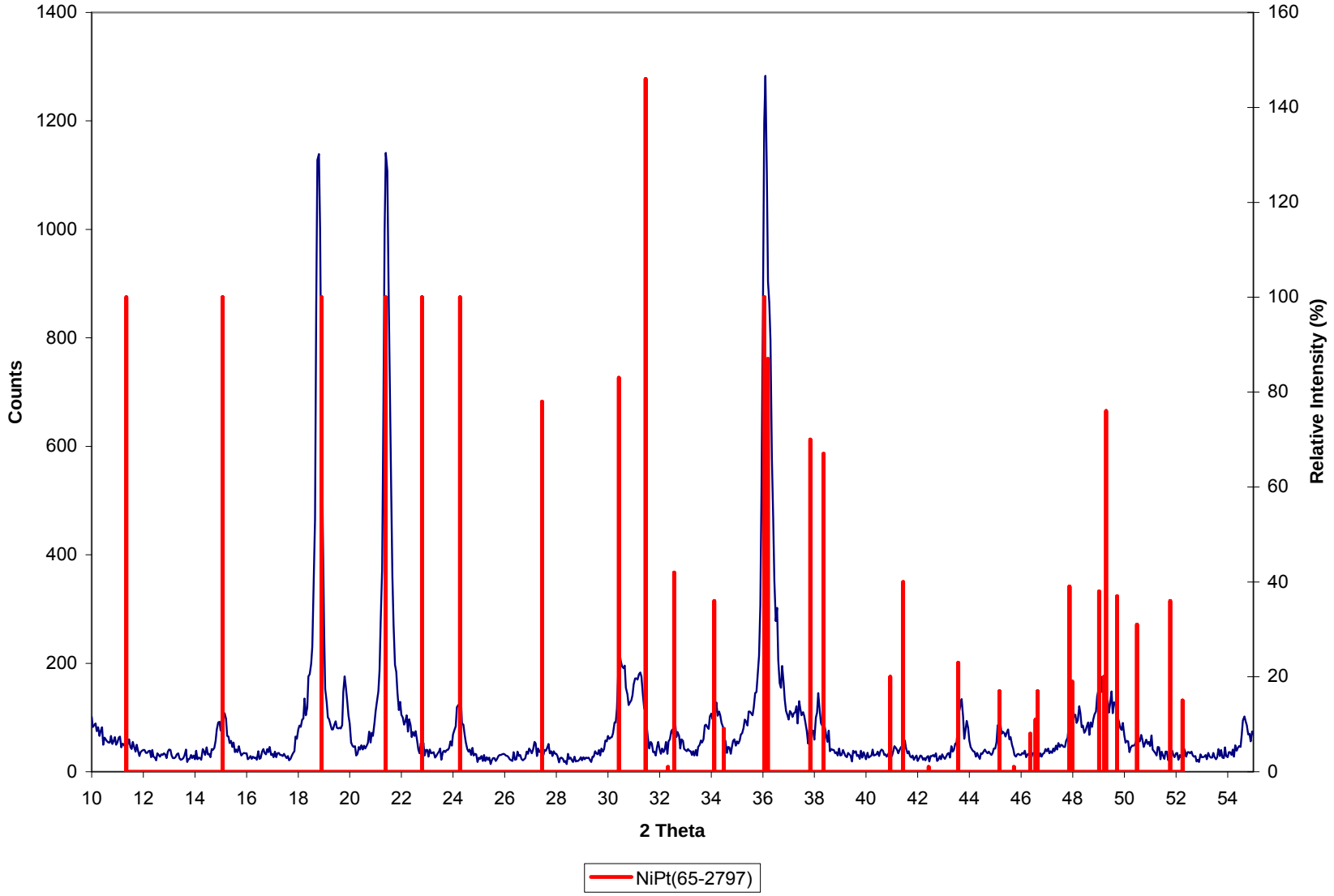


Figure 4.59: XRD spectrum of LG 1 (Nominal $Ni_{47.5}$:$Pt_{47.5}$:Ru_5) after ordering heat treatment at 500°C for a 1000 hours.

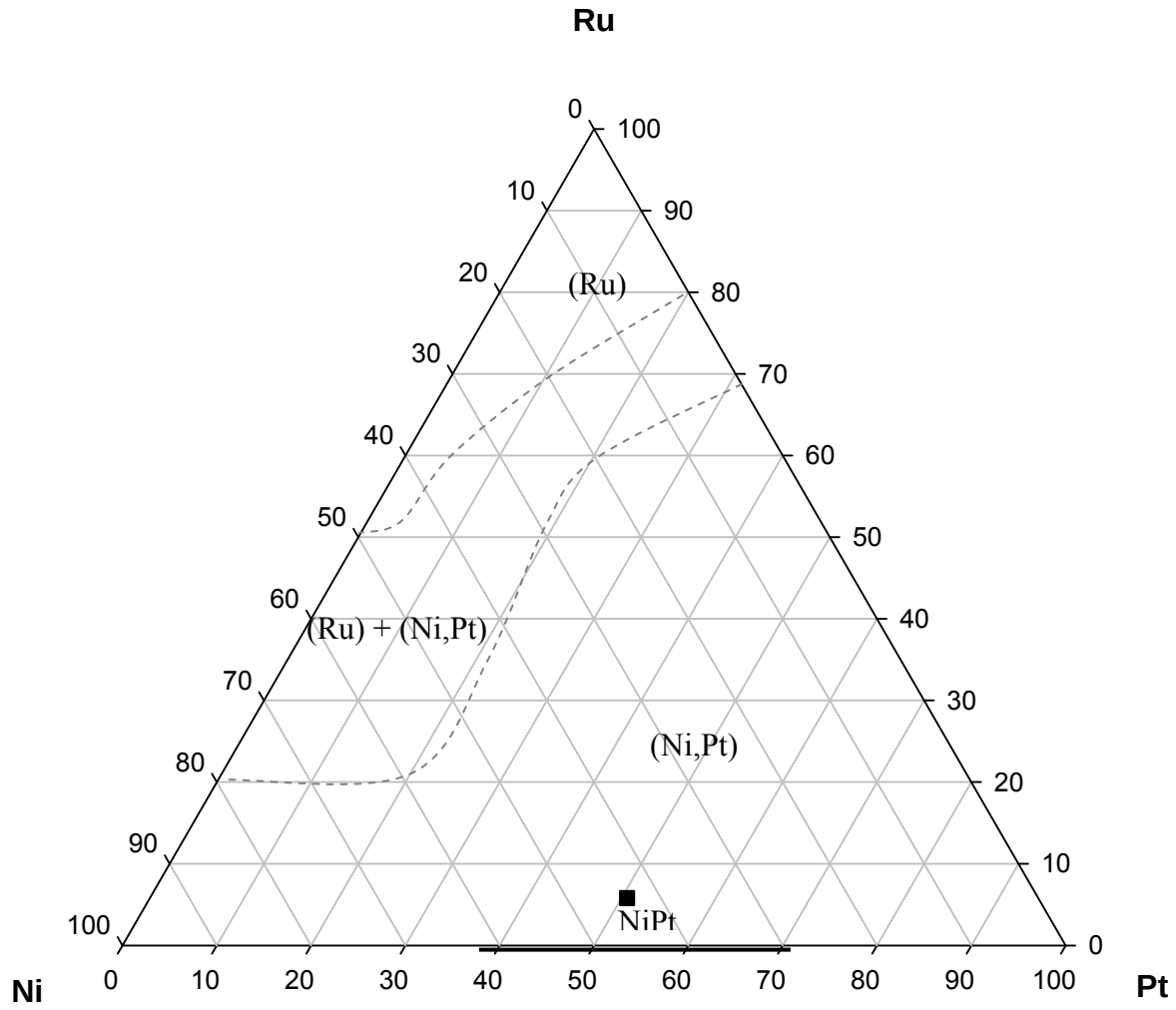


Figure 4.60: EDS analyses of LG 1 (Nominal $Ni_{47.5}$:$Pt_{47.5}$:Ru_5) ordering heat treatment at 500°C for a 1000 hours (at.%).

4.2 Co-Pt-Ru System

4.2.1 As-cast alloys

LG 11 (Nominal Co_{40}:Pt_{50}:Ru_{10})

The composition of alloy LG 11 (Nominal Co_{40}:Pt_{50}:Ru_{10}) was chosen to be close to the CoPt ordered region in the adjacent Co-Pt binary to test the extent of ordering into the ternary diagram. The microstructure (Figure 4.61) consisted of a grey matrix without any visible second phase although a difference in contrast consistent with coring is visible. A very good XRD spectrum was obtained for the alloy, showing a high signal to background ratio with neat, narrow peaks. Although there are significant shifts in the peaks, the XRD spectra in Figure 4.62 a) and b) show a possible fit for both fcc Co and Pt peaks, indicating a single phase. The Co peaks were shifted to the left and the Pt peaks were shifted to the right to match the spectrum as shown in Figure 4.63 a) and b) and are shown together on the spectrum in Figure 4.64. The alloy consists of (αCo,Pt) as shown by the XRD results. There are some small peaks shown in Table 4.22 that could not be identified. No peaks were found for the ordered phase, but this is expected in the as-cast condition. Table 4.21 gives the EDS phase analyses for the nominal Co_{40}:Pt_{50}:Ru_{10} alloy in the as-cast condition and the actual compositions are plotted in Figure 4.65.

The solidification sequence for the alloy is: $L \rightarrow$ fcc(Co,Pt).

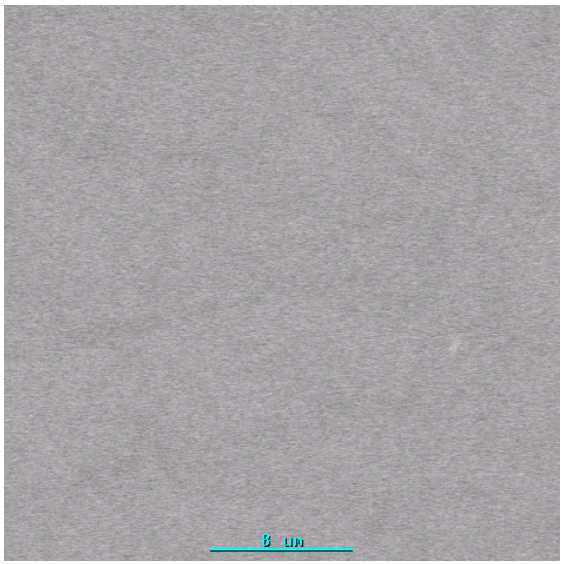
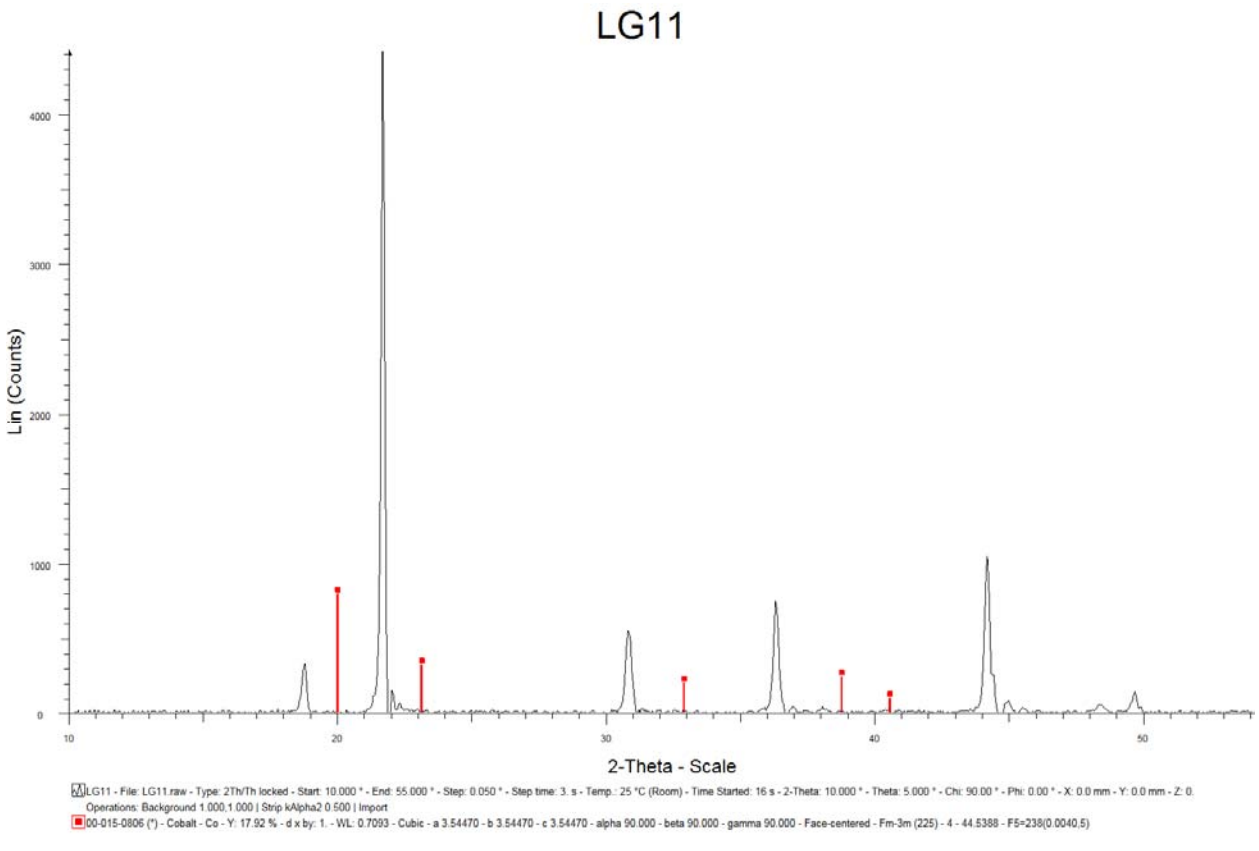


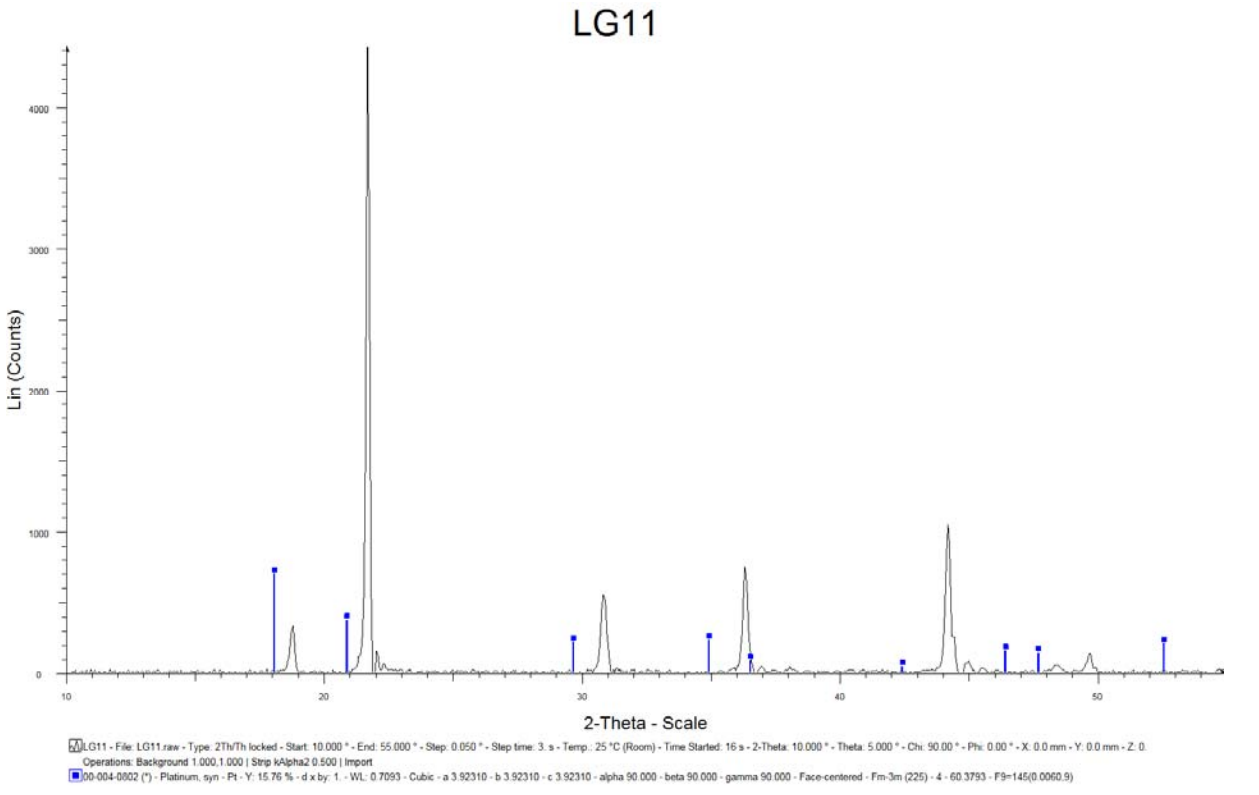
Figure 4.61. BEI of LG 11 (Nominal Co_{40}:Pt_{50}:Ru_{10}) in the as-cast condition showing a single-phase (Co,Pt) matrix.

Table 4.21. EDS analyses of LG 11 (Nominal Co_{40}:Pt_{50}:Ru_{10}) in the as-cast condition (at.%).

Phase description	Pt (at.%)	Ru (at.%)	Co (at.%)	Phase	Phase Proportion (%)
Overall	44.8 ± 0.2	8.9 ± 0.4	46.3 ± 0.2	fcc(Co,Pt)	~100 fcc(Co,Pt)

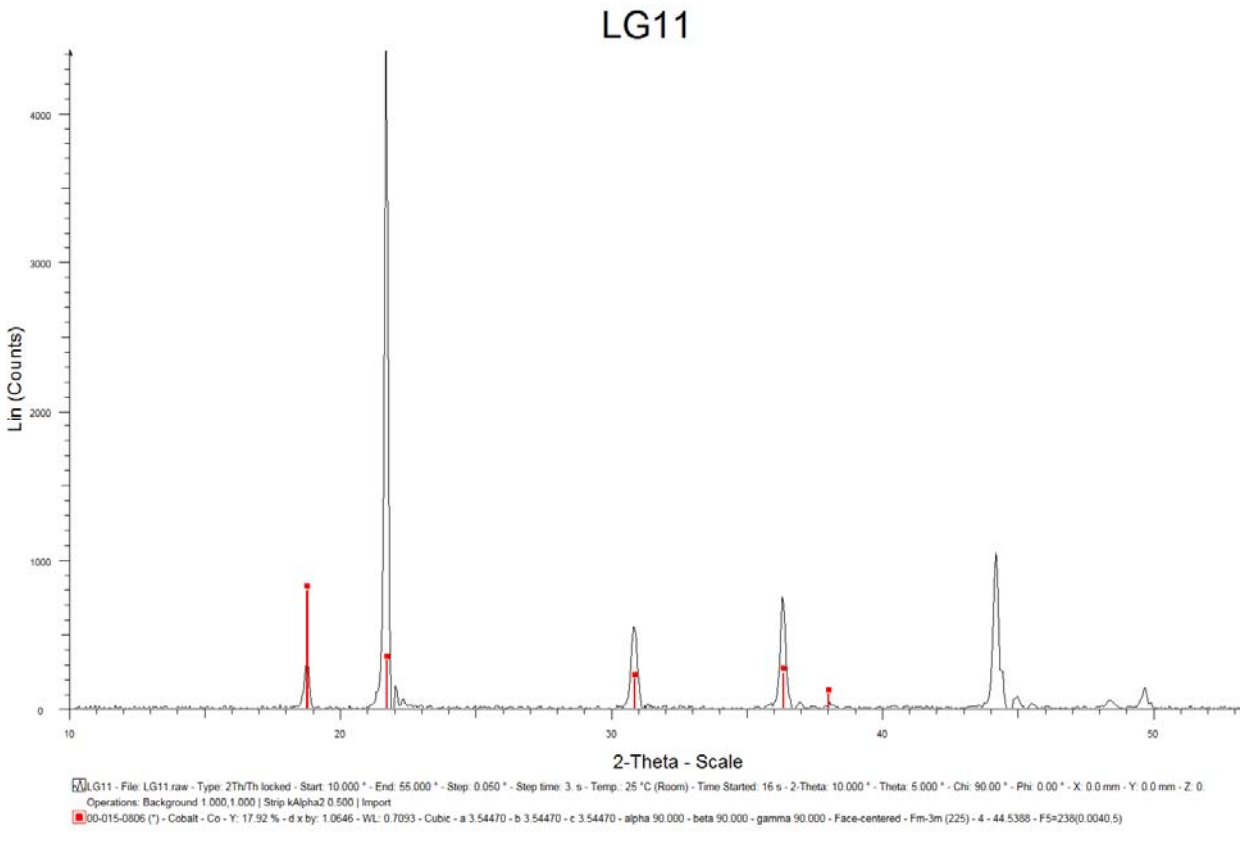


a)

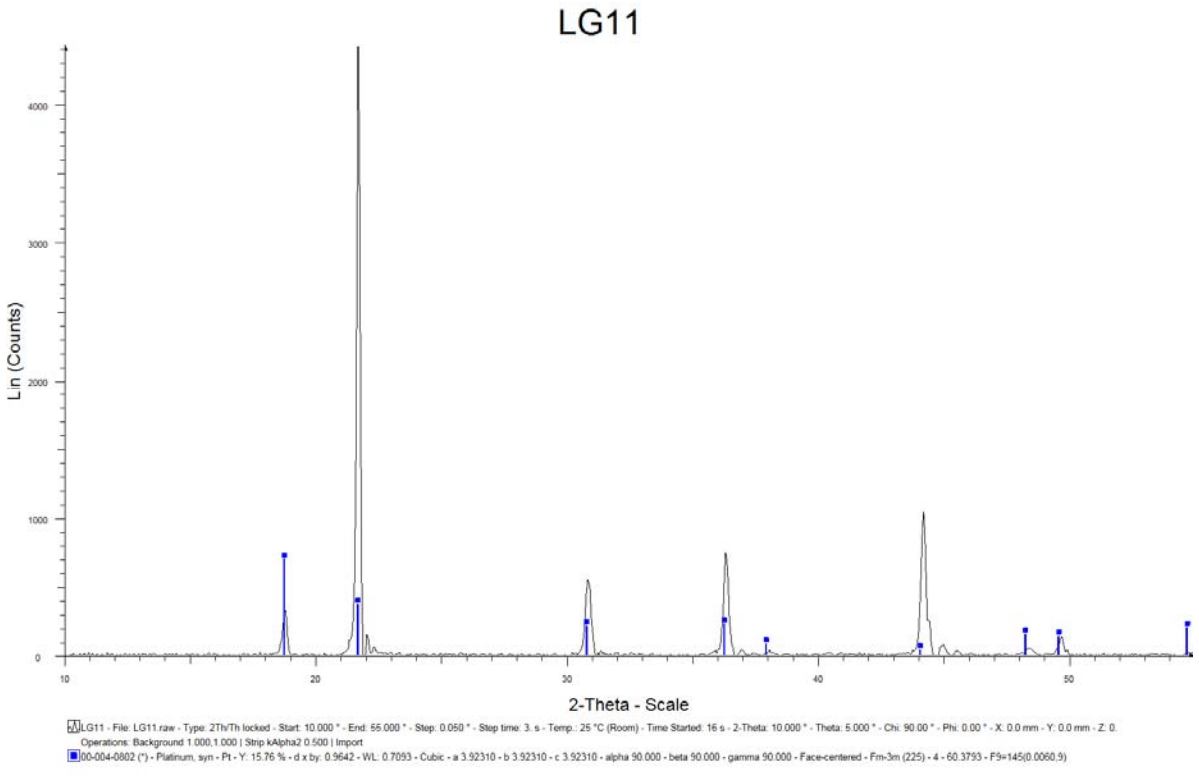


b)

Figure 4.62. XRD spectrum of LG 11 (Nominal Co_{40}:Pt_{50}:Ru_{10}) in the as-cast condition showing a comparison with both a) fcc Co and b) Pt peaks.



a)



b)

Figure 4.63. XRD spectrum of LG 11 (Nominal Co_{40}:Pt_{50}:Ru_{10}) in the as-cast condition showing the a) fcc Co and b) Pt peaks after shifting.

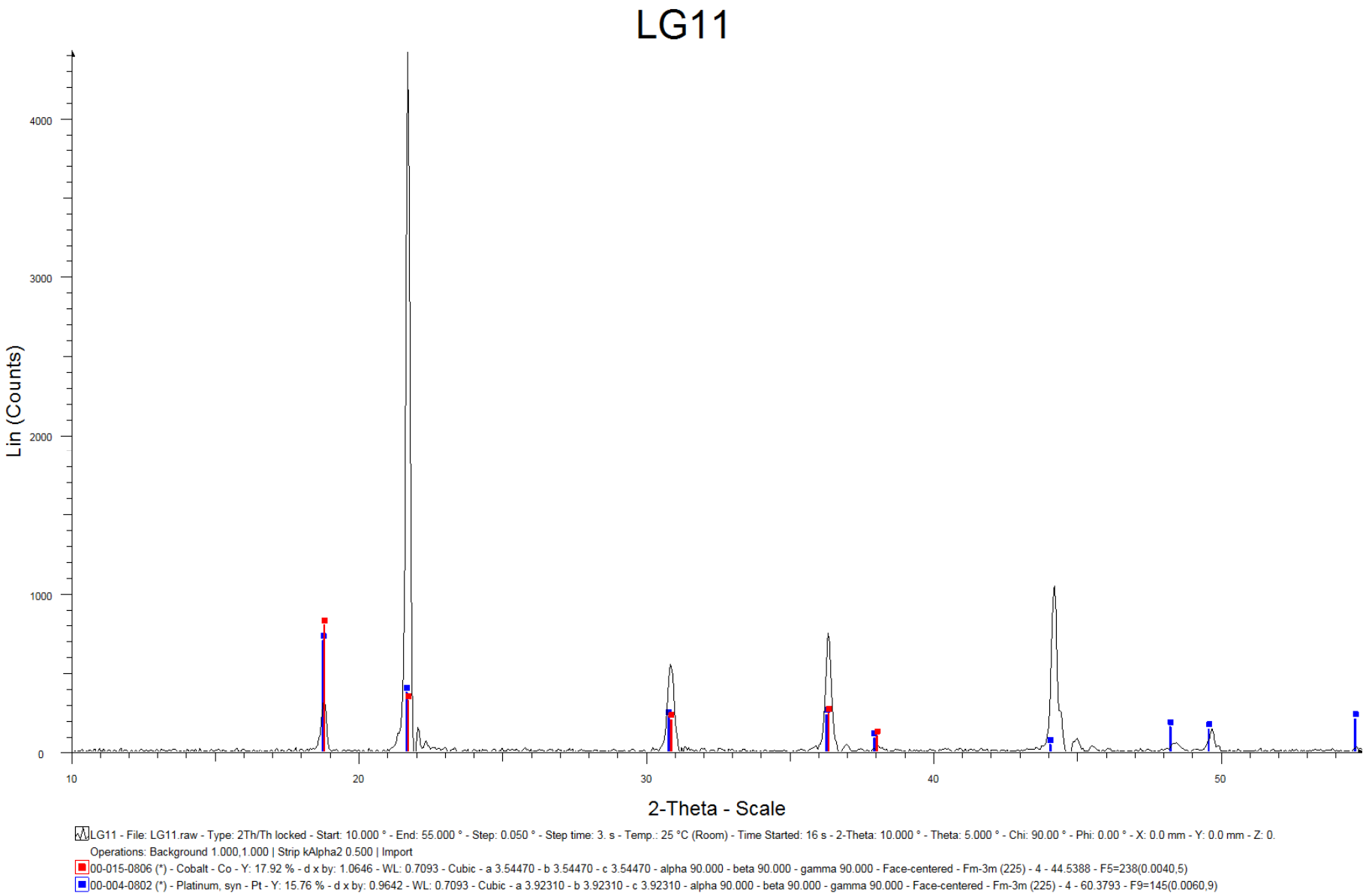


Figure 4.64. XRD spectrum of LG 11 (Nominal Co_{40}:Pt_{50}:Ru_{10}) in the as-cast condition, with both shifted fcc Co and Pt peaks overlaid.

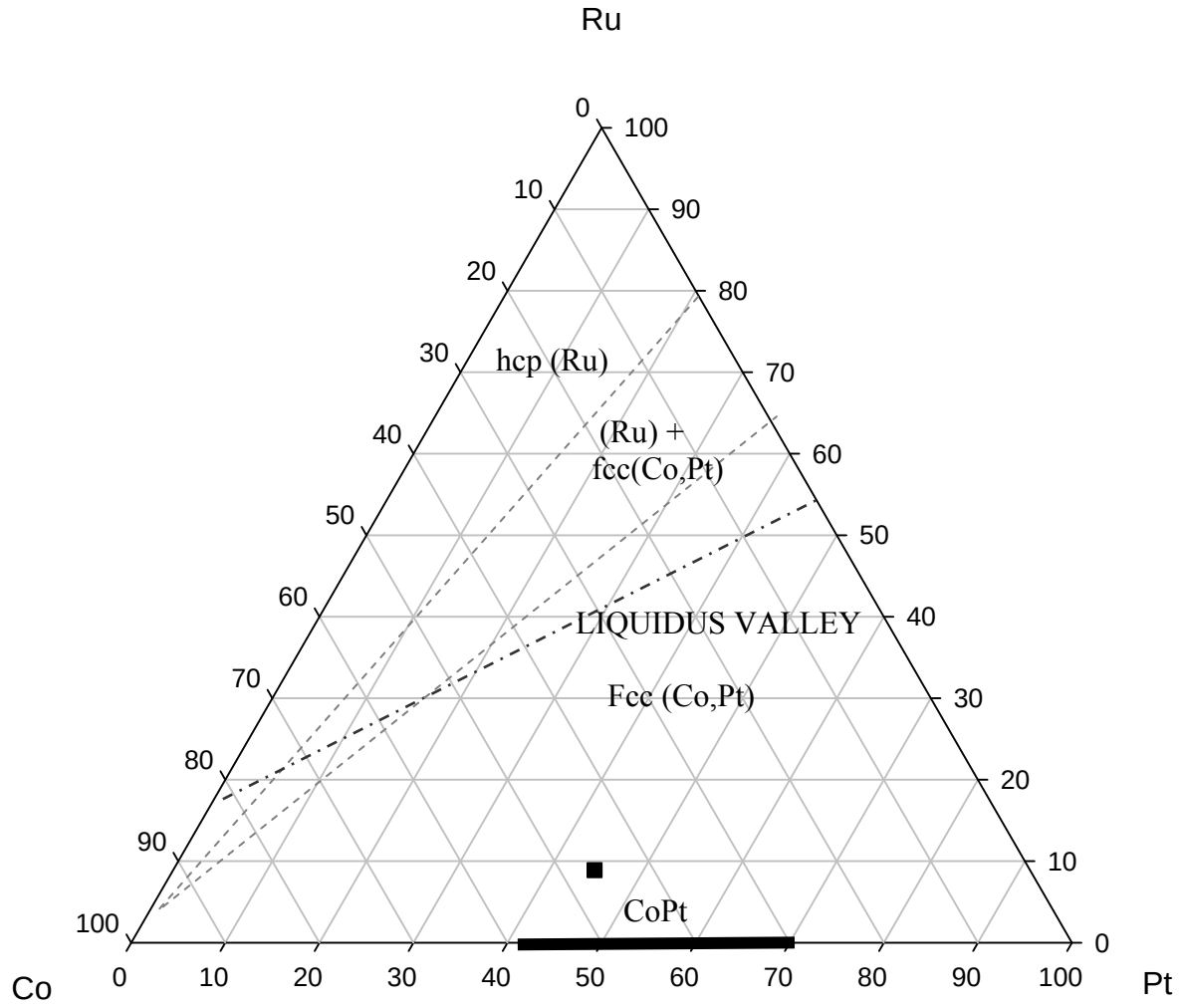


Figure 4.65. EDS analyses of LG 11 (Nominal Co_{40}:Pt_{50}:Ru_{10}) in the as-cast condition (at.%).

Table 4.22. Unidentified peaks in the as-cast condition.

2θ (°)	**Intensity**
22	150
31.2	25
37	50
45	100

LG 12 (Nominal Co_{15}:Pt_{75}:Ru_{10})

The composition of LG 12 (Nominal Co_{15}:Pt_{75}:Ru_{10}) was chosen to lie near the $CoPt_3$ ordering phenomenon in the Co-Pt system. As with alloy LG 11, this was done to check the extent of ordering into the ternary system. The microstructure is shown in Figure 4.66 and consists of a grey matrix with no evidence of coring. Table 4.23 gives the EDS phase analyses for the nominal Co_{15}:Pt_{75}:Ru_{10} alloy in the as-cast condition, showing that there is almost no Co present in the alloy and most of the Co had been lost due to an error while weighing out the different elements. The actual composition is plotted in Figure 4.68. The XRD spectrum shows that only Pt was detected (Figure 4.67), with no need to shift the peaks. There was a high signal to background ratio with neat, narrow peaks, although some small, unidentified peaks (shown in Table 4.24) were visible. The peaks were compared to the oxides of the elements of the alloy but no match was found.

The solidification sequence for the alloy is as follows: $L \rightarrow$ fcc(Co,Pt).

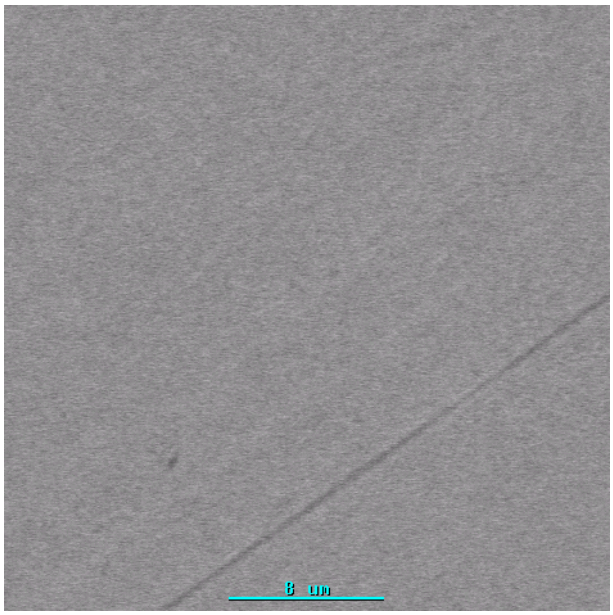


Figure 4.66. BEI of LG 12 (Nominal Co_{15}:Pt_{75}:Ru_{10}) in the as-cast condition, showing the grey (Co,Pt) matrix.

Table 4.23. EDS analyses of LG 12 (Nominal Co_{15}:Pt_{75}:Ru_{10}) in the as-cast condition (at.%).

Phase description	Pt (at.%)	Ru (at.%)	Co (at.%)	Phase	Phase Proportion (%)
Overall	94.1 ± 0.7	5.4 ± 0.2	0.5 ± 0.5	fcc(Co,Pt)	~100 fcc(Co,Pt)

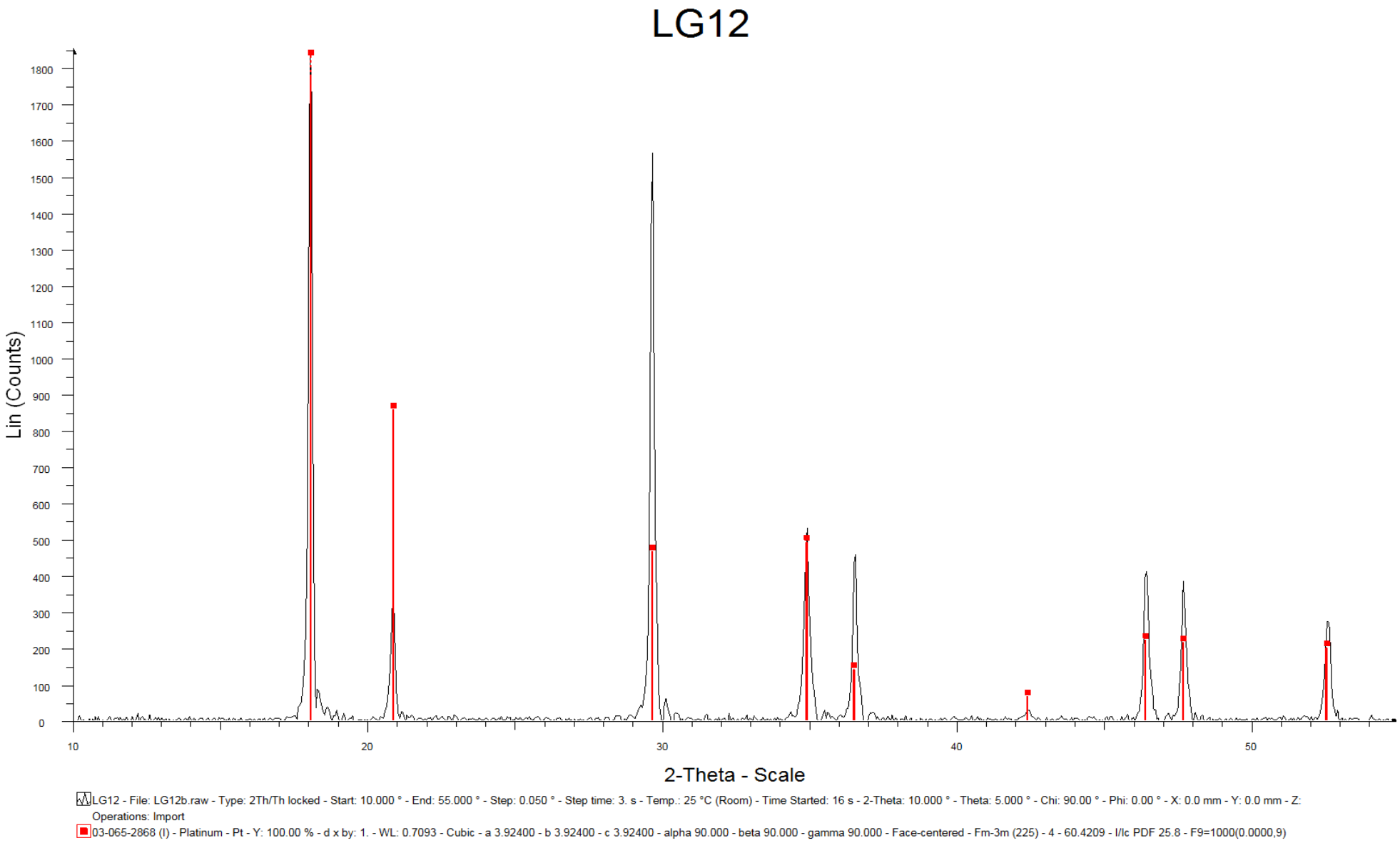


Figure 4.67. XRD spectrum of LG 12 (Nominal $Co_{15}:Pt_{75}:Ru_{10}$) in the as-cast condition, with the Pt peaks overlaid.

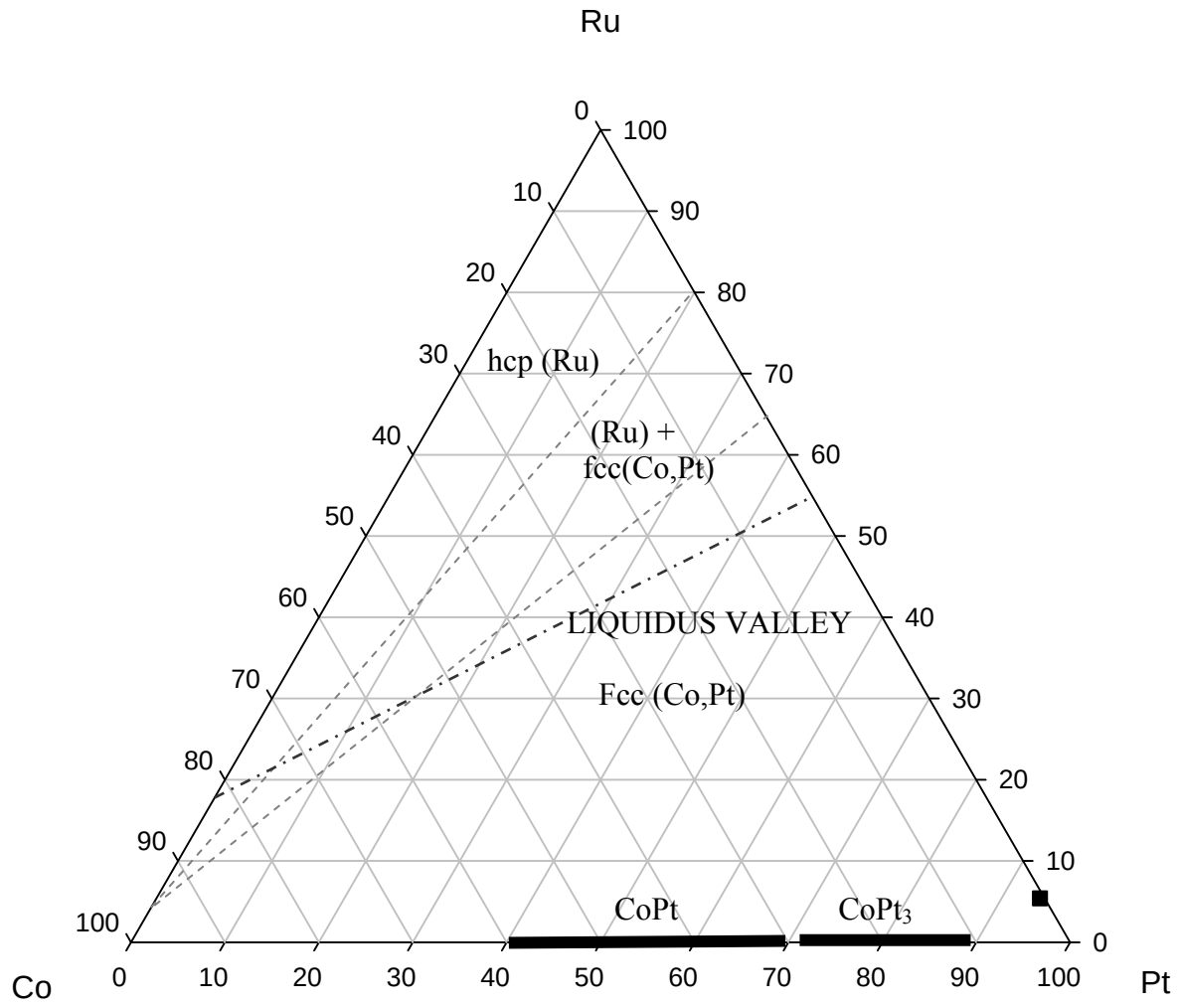


Figure 4.68. EDS analyses of LG 12 (Nominal Co_{15}:Pt_{75}:Ru_{10}) in the as-cast condition (at.%).

Table 4.24. Unidentified peaks in the as-cast condition.

2θ (°)	**Intensity**
18.5	175
30.2	50
34.3	20
35.5	25

LG 13 (Nominal Co_{90}:Pt_5:Ru_5)

LG 13 (nominal Co_{90}:Pt_5:Ru_5) appears to be a single-phase alloy (Figure 4.69), and Table 4.25 gives the EDS phase analyses in the as-cast condition. The actual composition is plotted in Figure 4.73. A very good XRD spectrum was obtained for this alloy, with a high signal to background ratio with peaks that were fairly broad, indicating a range of compositions. Some small unidentified peaks can be seen and are shown in Table 4.26. In Figure 4.70 hcp εCo and fcc Co peaks were identified, thus two phases were identified, even though a second phase was not clearly seen in the microstructure. After shifting of the lines, the spectra in Figure 4.71 show a good fit for the fcc Co and εCo. Both the cubic and hexagonal Co lines are shown on the spectrum in Figure 4.72.

The solidification sequence for the alloy is: L + hcp εCo → fcc (Co,Pt)

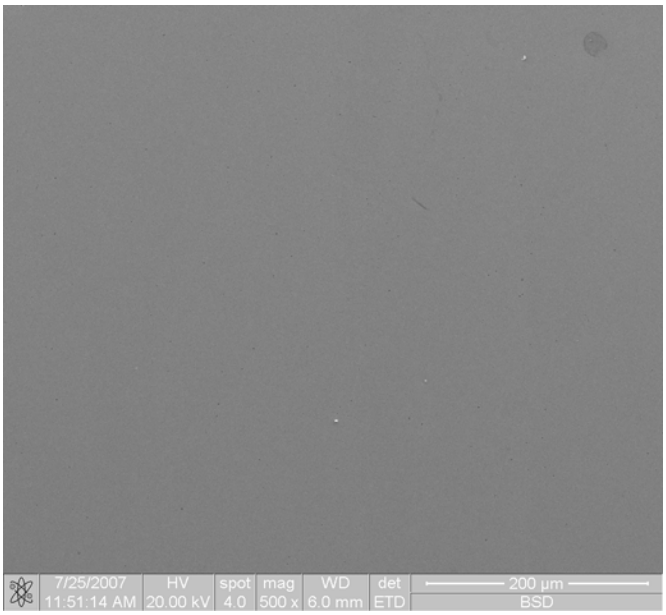
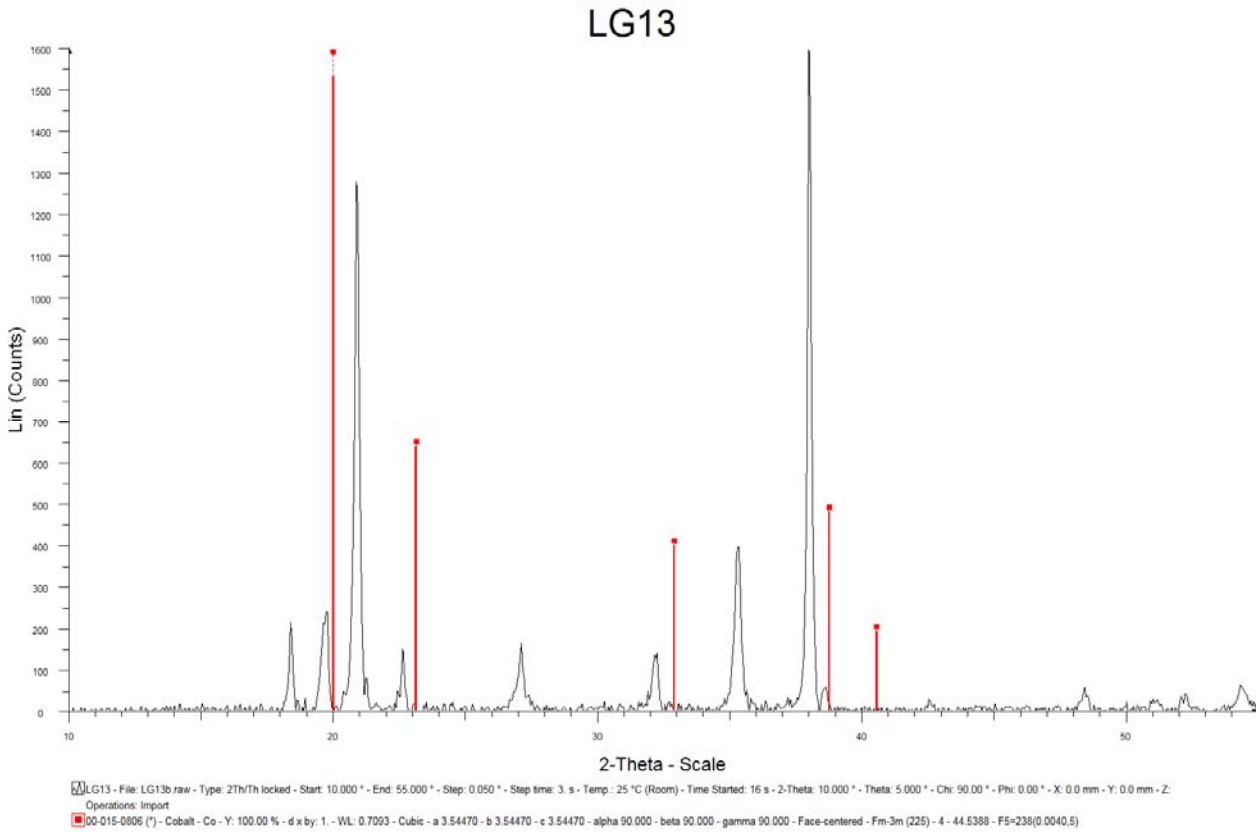


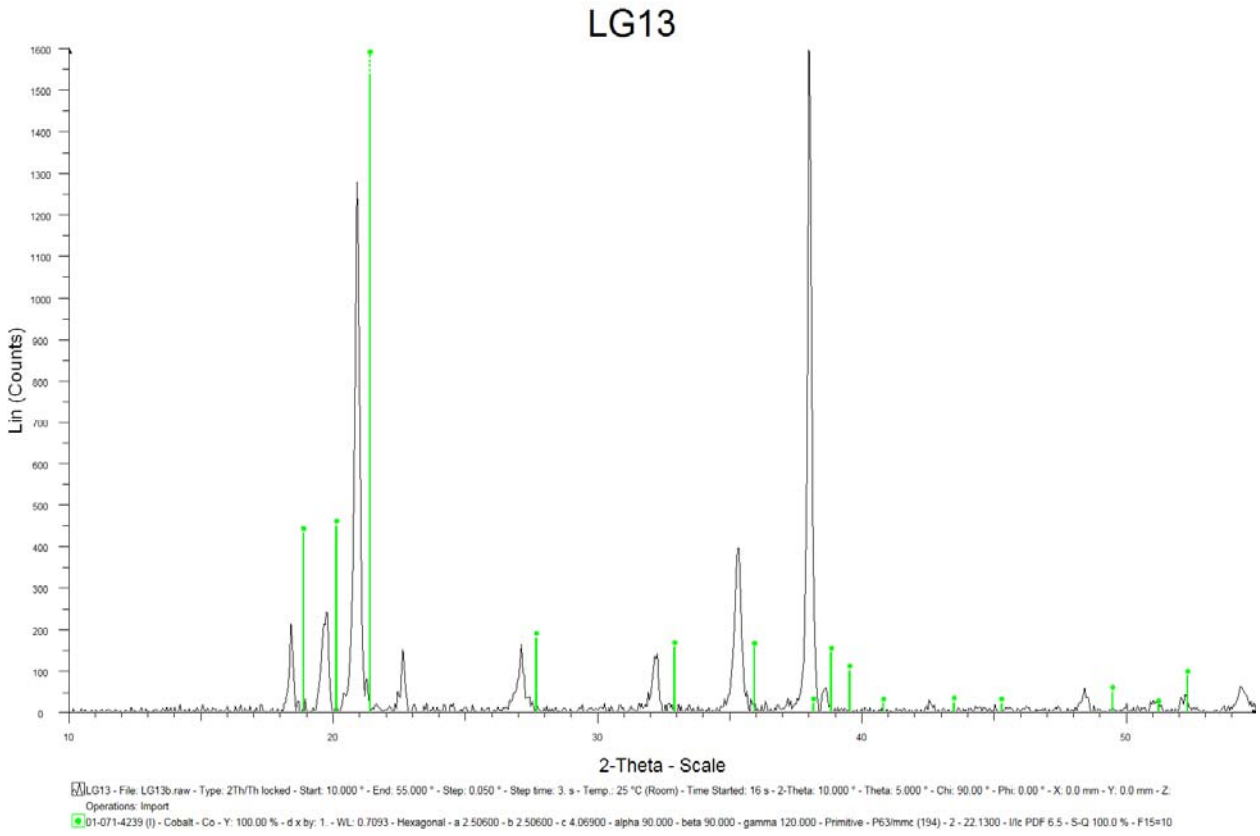
Figure 4.69. BEI of LG 13 (nominal Co_{90}:Pt_5:Ru_5) in the as-cast condition showing a grey (Co,Pt) matrix.

Table 4.25. EDS analyses of LG13 (nominal Co_{90}:Pt_5:Ru_5) in the as-cast condition (at.%).

Phase description	Pt (at.%)	Ru (at.%)	Co (at.%)	Phase	Phase Proportion (%)
Overall	5.0 ± 0.6	5.1 ± 0.5	89.9 ± 0.8	fcc (Co,Pt)	~100 fcc (Co,Pt)

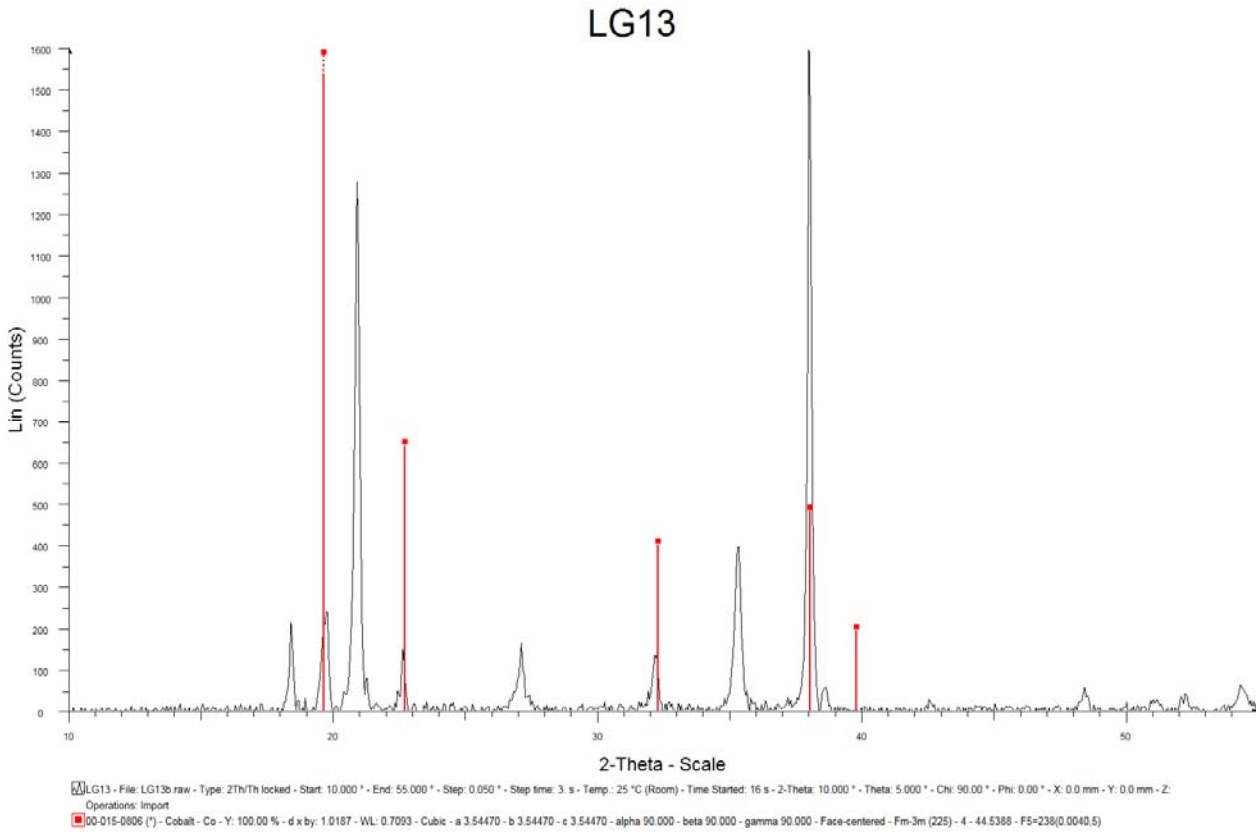


a)

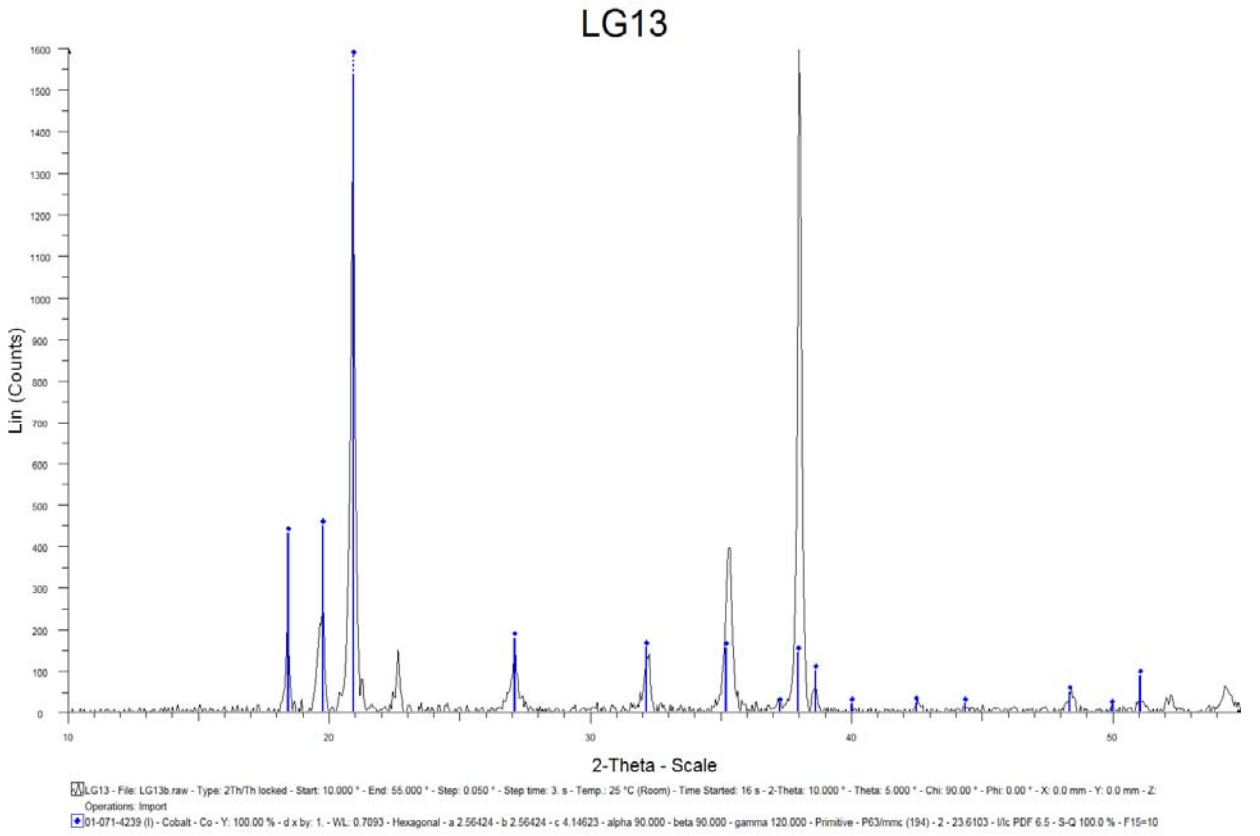


b)

Figure 4.70. XRD spectrum of LG 13 (nominal Co_{90}:Pt_5:Ru_5) in the as-cast condition showing a comparison with both a) fcc Co and b) hcp εCo peaks.



a)



b)

Figure 4.71. XRD spectrum of LG 13 (nominal Co_{90}:Pt_5:Ru_5) in the as-cast condition showing the a) fcc Co and b) hcp εCo peaks after shifting.

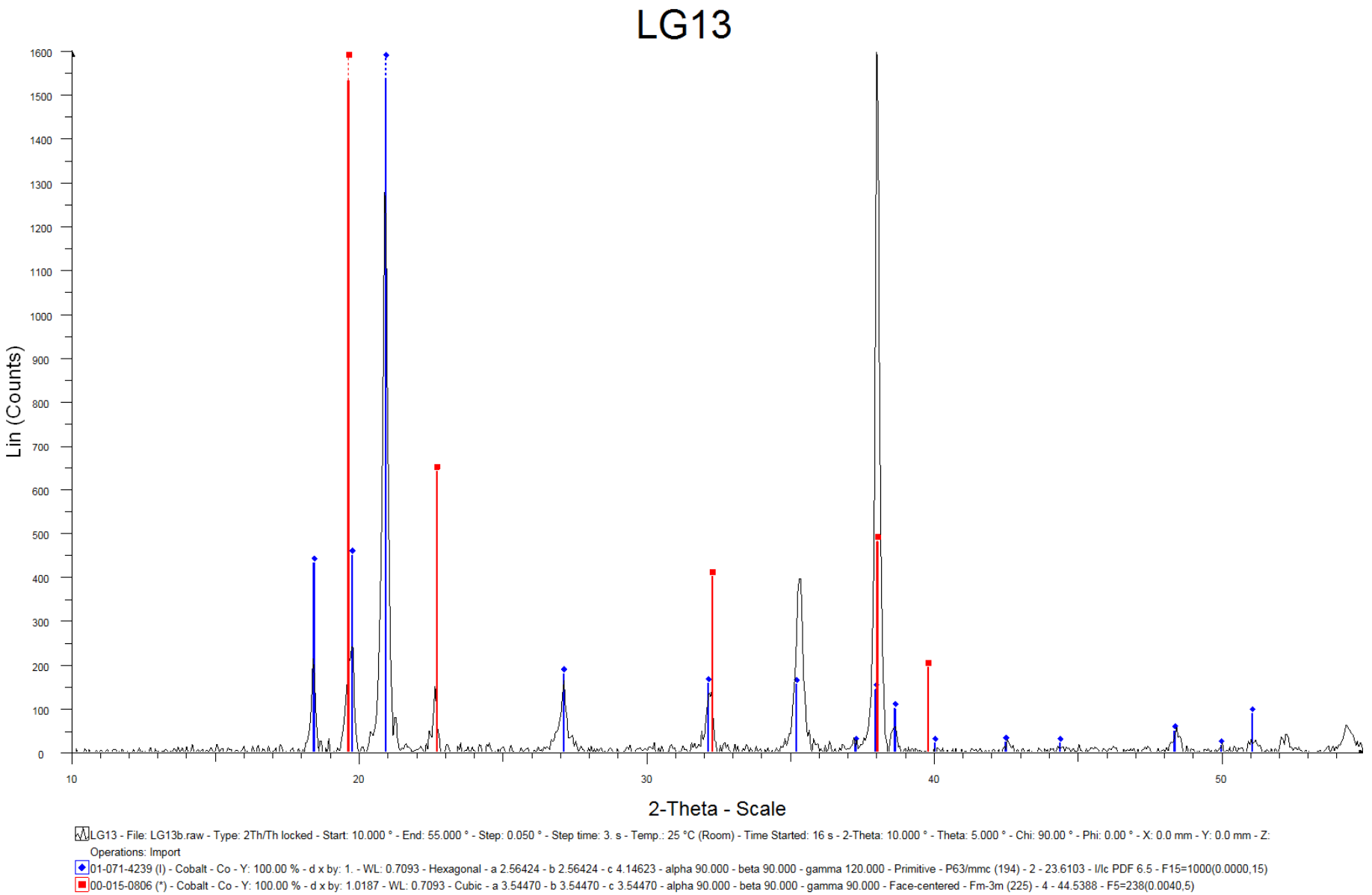


Figure 4.72. XRD spectrum of LG 13 (nominal Co_{90}:Pt_5:Ru_5) in the as-cast condition, with the shifted fcc Co and hcp εCo peaks overlaid.

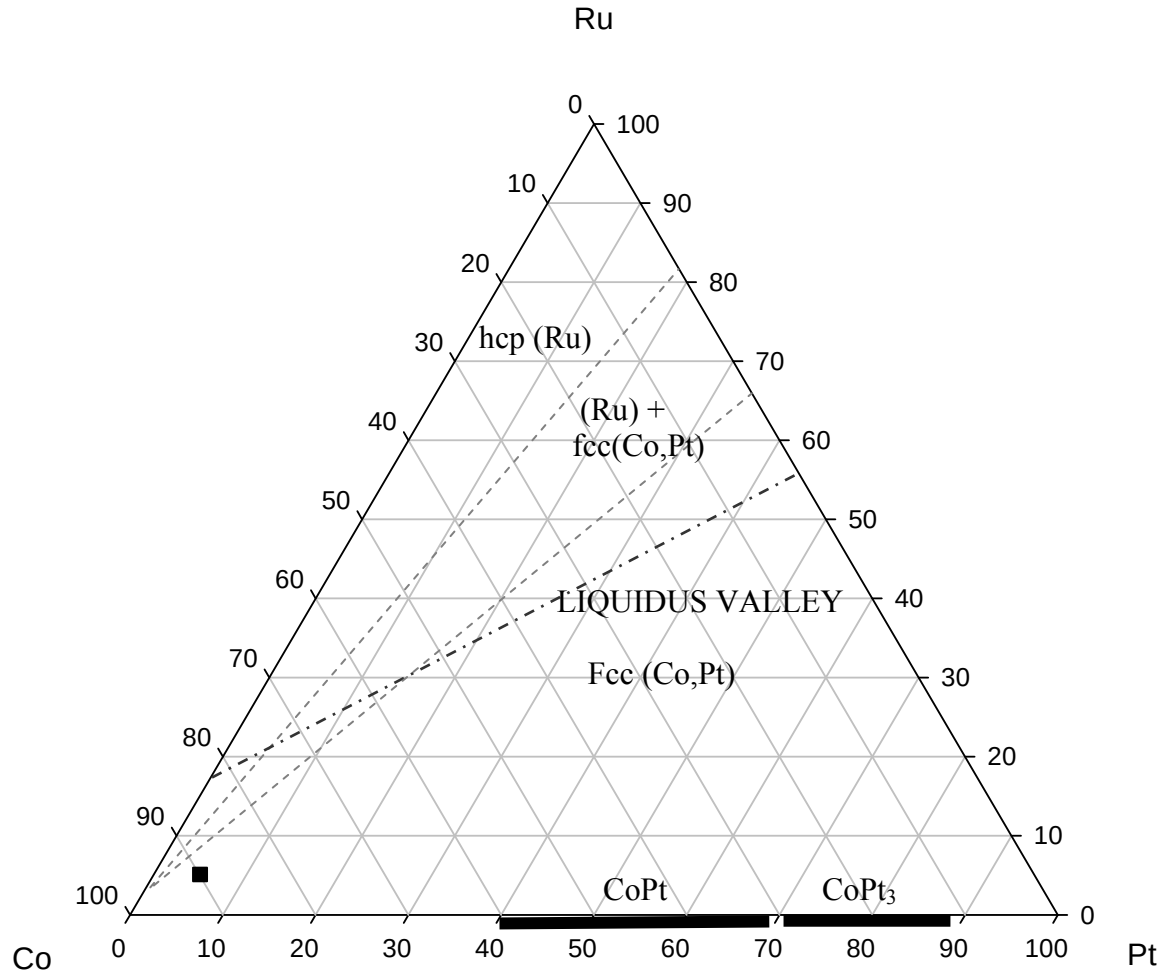


Figure 4.73. EDS analyses of LG 13 (nominal Co_{90}:Pt_5:Ru_5) in the as-cast condition (at.%).

Table 4.26. Unidentified peaks in the as-cast condition.

2θ	**Intensity**
20.5	50
21.5	75

LG 14 (Nominal Co_{80}:Pt_{10}:Ru_{10})

LG 14 (Nominal Co_{80}:Pt_{10}:Ru_{10}) is a two-phase alloy with dark dendrites in a light matrix (Figure 4.74). Very fine porosity was visible through out the alloy. Table 4.27 gives the EDS phase analyses for the LG 14 (Nominal Co_{80}:Pt_{10}:Ru_{10}) alloy in the as-cast condition and the composition is plotted in Figure 4.77. The XRD results confirmed the presence of mainly single phase, hcp εCo (Figure 4.75), and barely discernable fcc (Co,Pt) peaks (e.g. at ~ 19.5°, 23° and 32°) some small, unidentified peaks were visible and are shown in Table 4.28. A comparison was made with the oxide peaks for the elements present but no match was found. Figure 4.76 shows the spectrum with the identifying lines overlaid on the hcp εCo peaks. The XRD spectrum showed a fairly high signal to background ratio with fairly neat narrow peaks.

The solidification sequence for the alloy is: L + hcp εCo → fcc (Co,Pt)

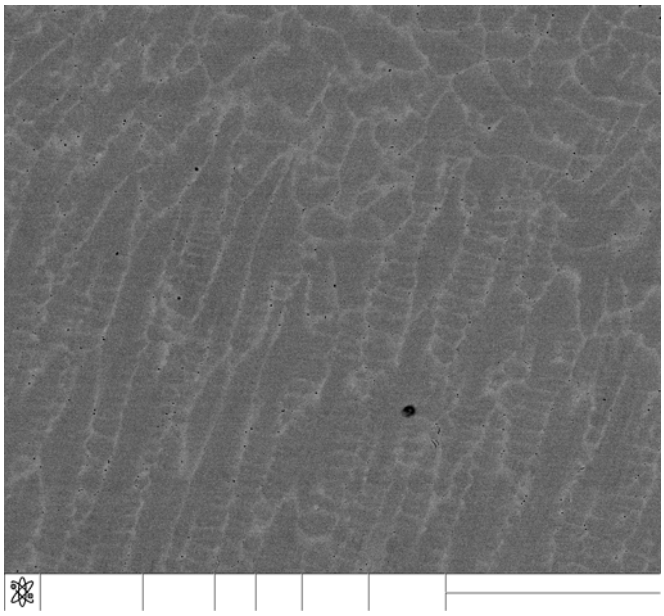


Figure 4.74. BEI of LG 14 (nominal Co_{80}:Pt_{10}:Ru_{10}) in the as-cast condition showing cored ε(Co) dendrites in a light fcc(Co,Pt) matrix.

Table 4.27. EDS analyses of LG 14 (nominal Co_{80}:Pt_{10}:Ru_{10}) in the as-cast condition (at.%).

Phase description	Pt (at.%)	Ru (at.%)	Co (at.%)	Phase	Phase Proportion (%)
Overall	8.3 ± 0.3	8.5 ± 0.4	83.2 ± 0.3	-	-
Dark	7.8 ± 0.9	11.2 ± 0.3	81.0 ± 0.7	hcp ε(Co)	~75
Light	10.4 ± 0.5	7.2 ± 0.8	82.4 ± 0.7	fcc(Co,Pt)	~25

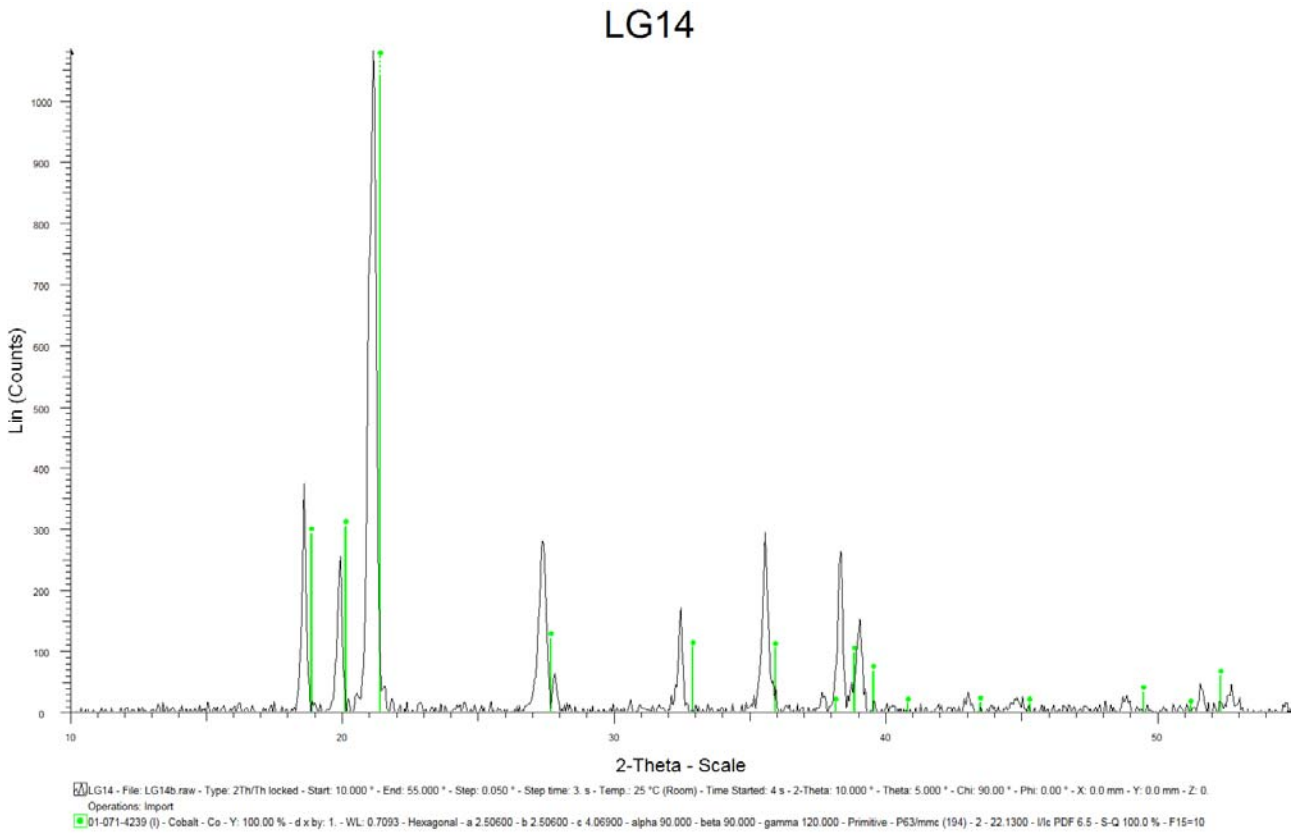


Figure 4.75. XRD spectrum of LG 14 (nominal Co_{80}:Pt_{10}:Ru_{10}) in the as-cast condition showing a comparison with hexagonal hcp εCo.

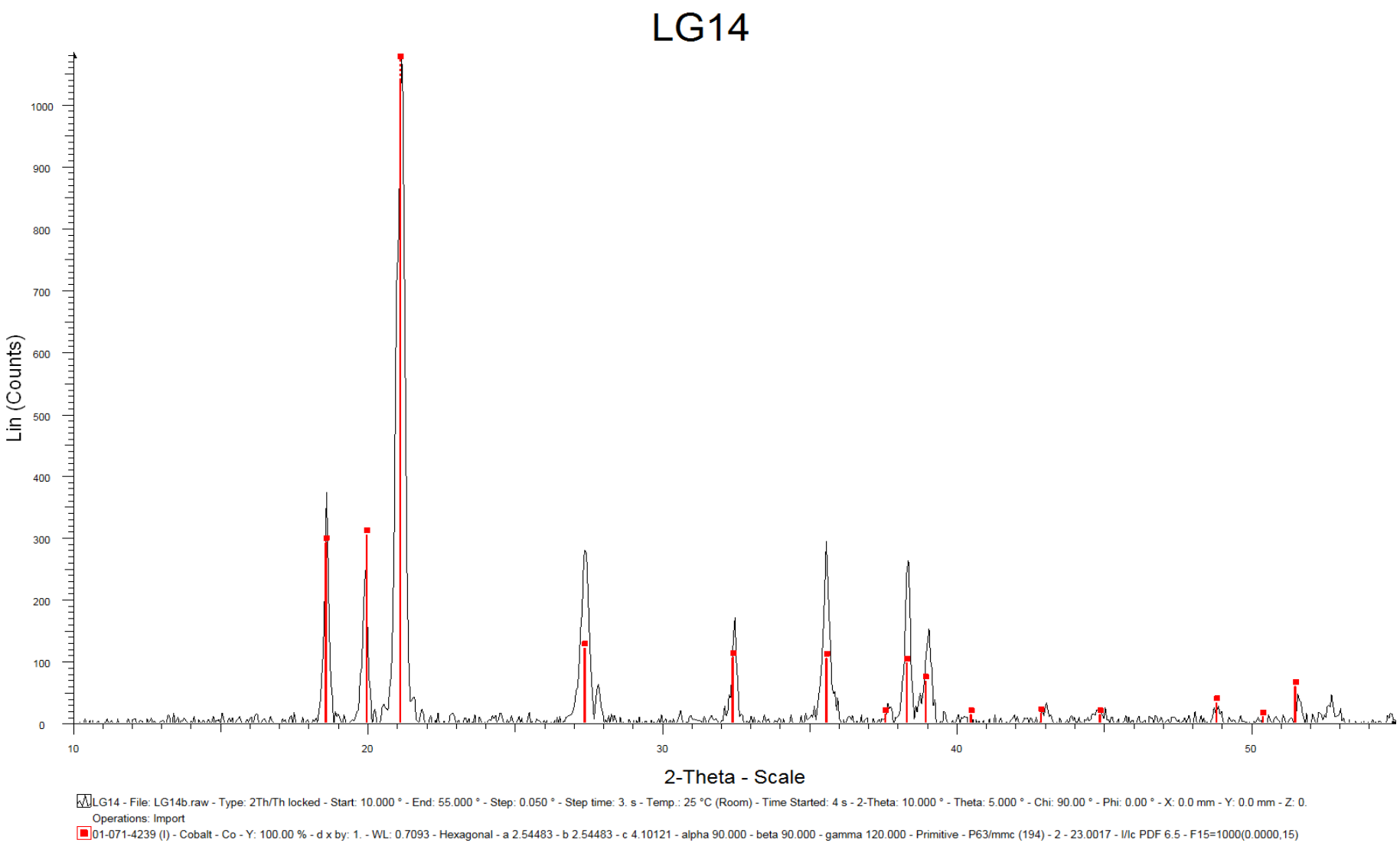


Figure 4.76. XRD spectrum of LG 14 nominal (Co_{80}:Pt_{10}:Ru_{10}) in the as-cast condition, showing the shifted peak matches for hcp ε Co.

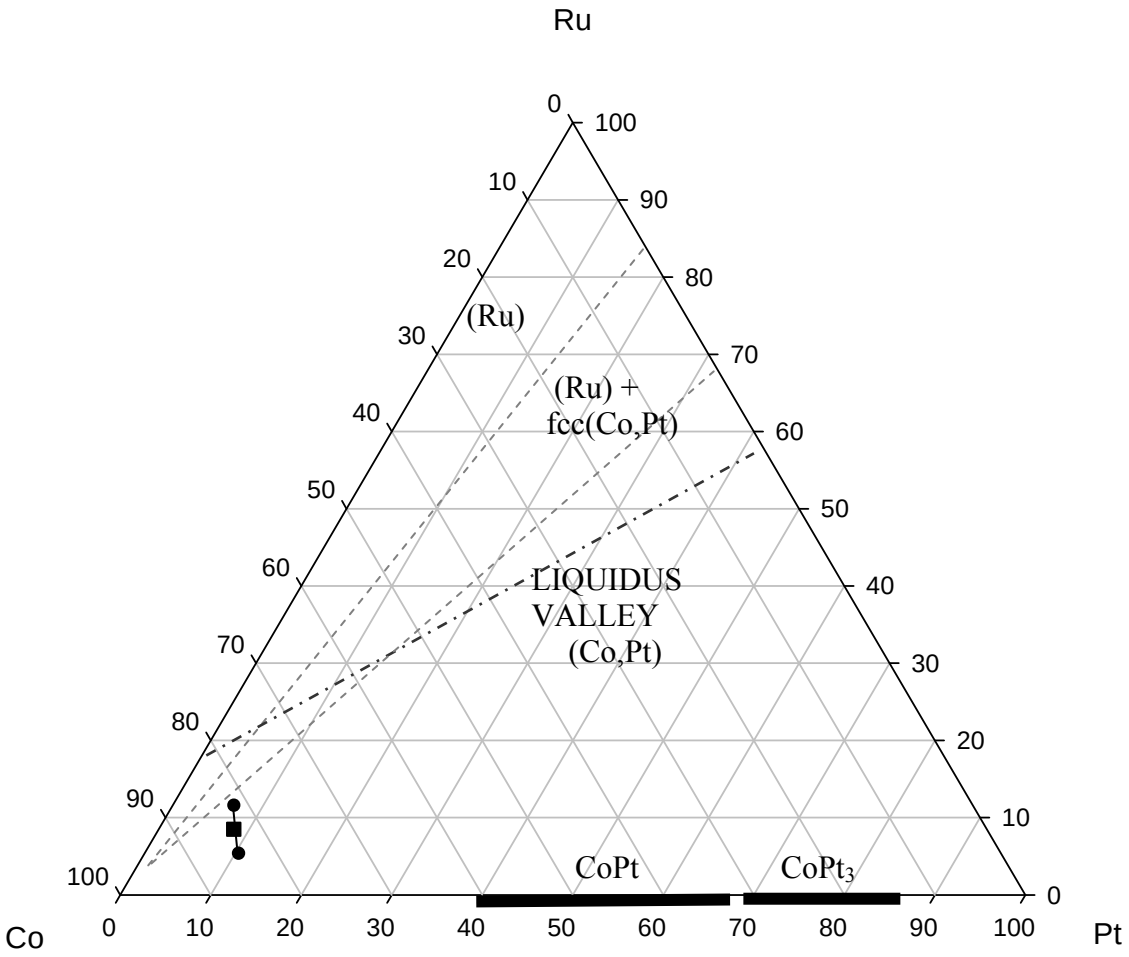


Figure 4.77. EDS analyses of LG 14 nominal (Co_{80}:Pt_{10}:Ru_{10}) in the as-cast condition (at.%).

Table 4.28. Unidentified peaks in the as-cast condition.

2θ	**Intensity**
19	10
20.5	25
21.5	35
28.5	50
32	25

LG 15 (Nominal Co_{30}:Pt_{20}:Ru_{50})

The microstructure of as-cast LG 15 (nominal Co_{30}:Pt_{20}:Ru_{50}) shows a two-phase structure (Figure 4.78), consisting of dark dendrites in lighter matrix. The (Ru) dendrites formed first, and then the fcc (Co,Pt). Very fine porosity is visible. The XRD spectrum that was obtained for the alloy is very clear, showing a high signal to background ratio with a good match for Ru and Pt (Figure 4.79). The peaks were not as narrow as for the previous alloys, which suggest some coring in the phases. Figure 4.80 show the spectra with the Pt peaks that were shifted to the right and the Ru peaks that were shifted to the left. Some of the smaller peaks shown in Table 4.30 were not identified. All known peaks for different combinations of the elements and their oxides were made but no match was found. Judging from the height of the peaks, there are almost equal amounts of the (Ru) and fcc(Co,Pt) phases present in the alloy. Comparing this to the microstructure, it can be seen that there was more fcc(Co,Pt). The EDS phase analyses for the alloy is shown in Table 4.29 and the actual composition is plotted in Figure 4.82. The overall did not lie on the tie-line between the two phases, but is nearly within experimental error.

The solidification sequence for the alloy is: $L + (Ru) \rightarrow$ fcc (Co,Pt)

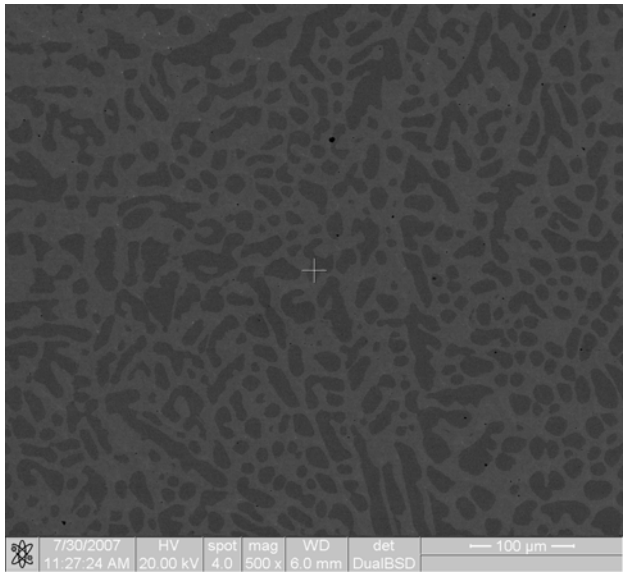
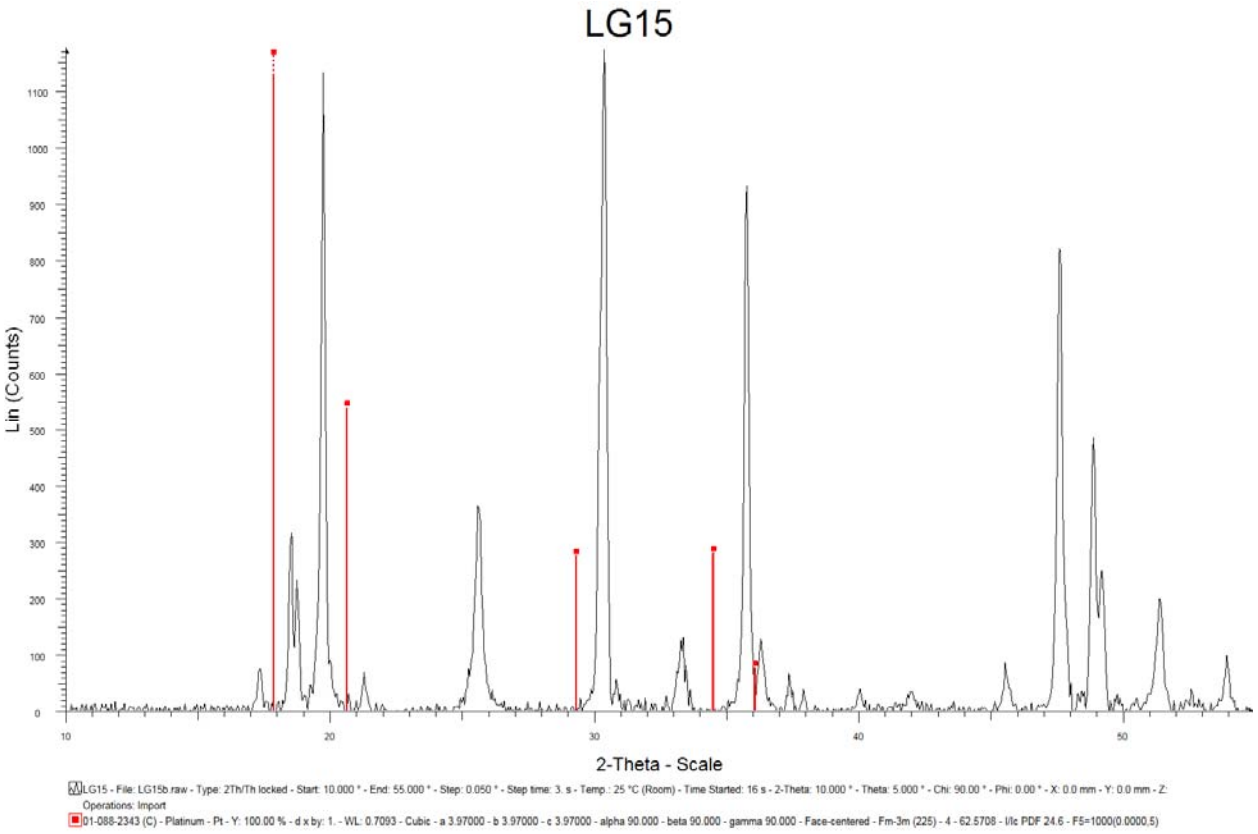


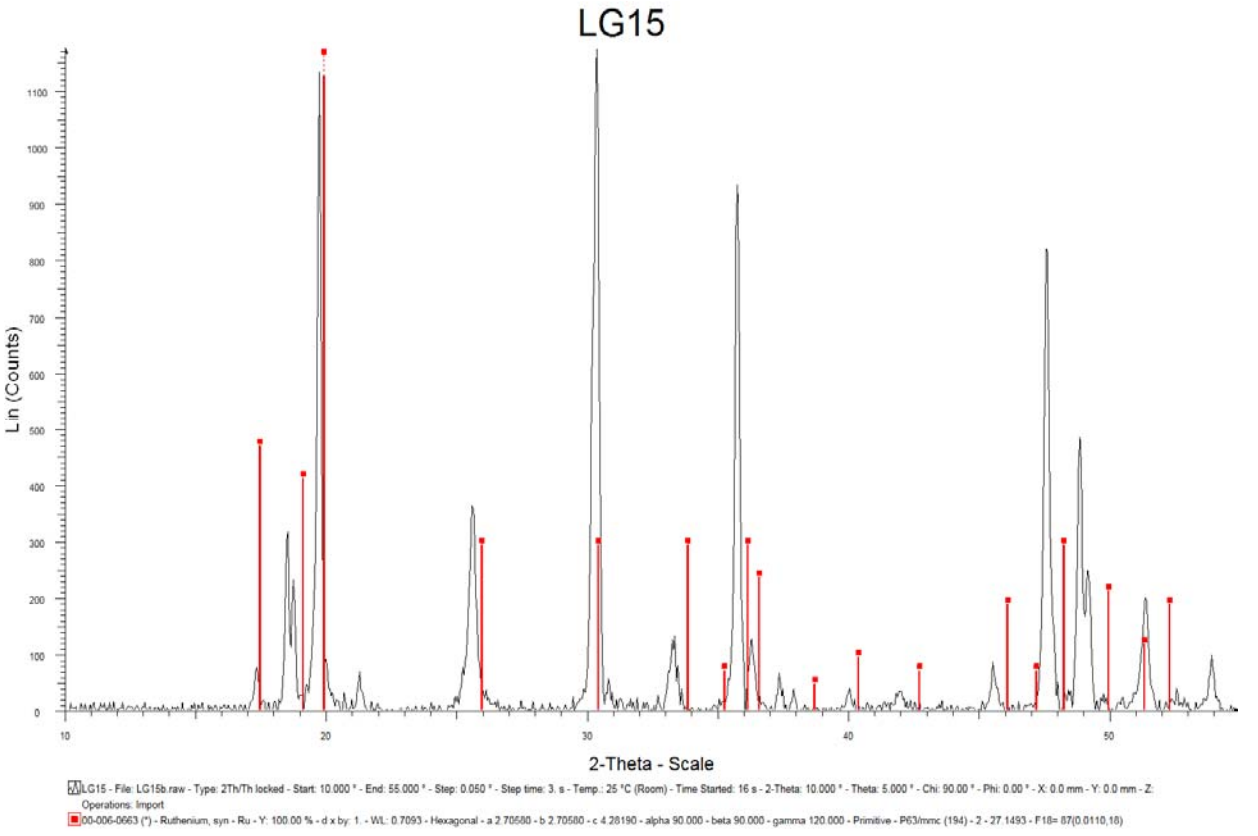
Figure 4.78. BEI of LG 15 (nominal Co_{30}:Pt_{20}:Ru_{50}) in the as-cast condition showing dark, (Ru) dendrites in a lighter, fcc(Co,Pt) matrix.

Table 4.29 EDS analyses of LG 15 (nominal Co_{30}:Pt_{20}:Ru_{50}) in the as-cast condition (at.%).

Phase description	Pt (at.%)	Ru (at.%)	Co (at.%)	Phase	Phase Proportion (%)
Overall	20.4 ± 0.3	55.7 ± 0.5	23.9 ± 0.5	-	-
Dark	18.5 ± 0.5	63.6 ± 0.4	17.9 ± 0.6	(Ru)	~40
Light	26.6 ± 0.8	43.4 ± 0.7	30.0 ± 0.3	fcc(Co,Pt)	~60

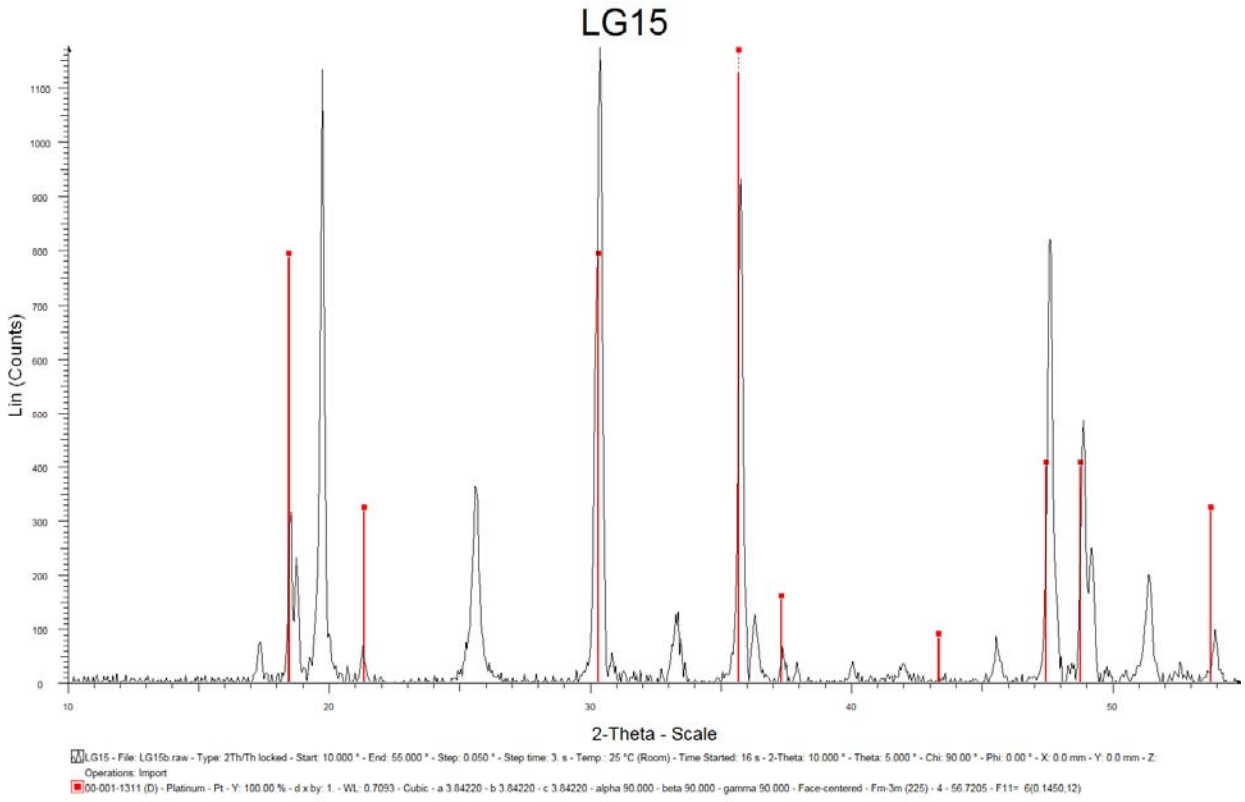


a)

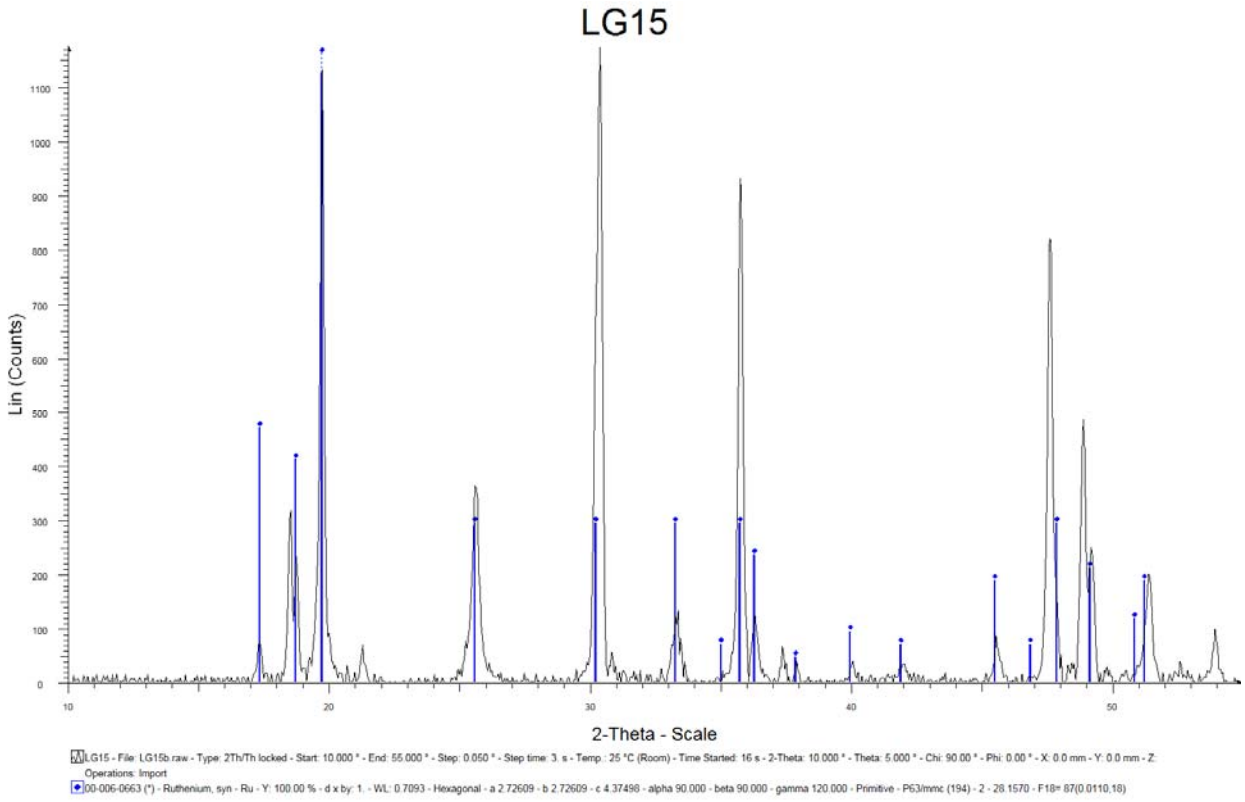


b)

Figure 4.79. XRD spectrum of LG 15 (nominal Co_{30}:Pt_{20}:Ru_{50}) in the as-cast condition showing a comparison with a) Pt and b) Ru.



a)



b)

Figure 4.80. XRD spectrum of LG 15 (nominal Co_{30}:Pt_{20}:Ru_{50}) in the as-cast condition showing the a) Pt and b) Ru peaks after shifting.

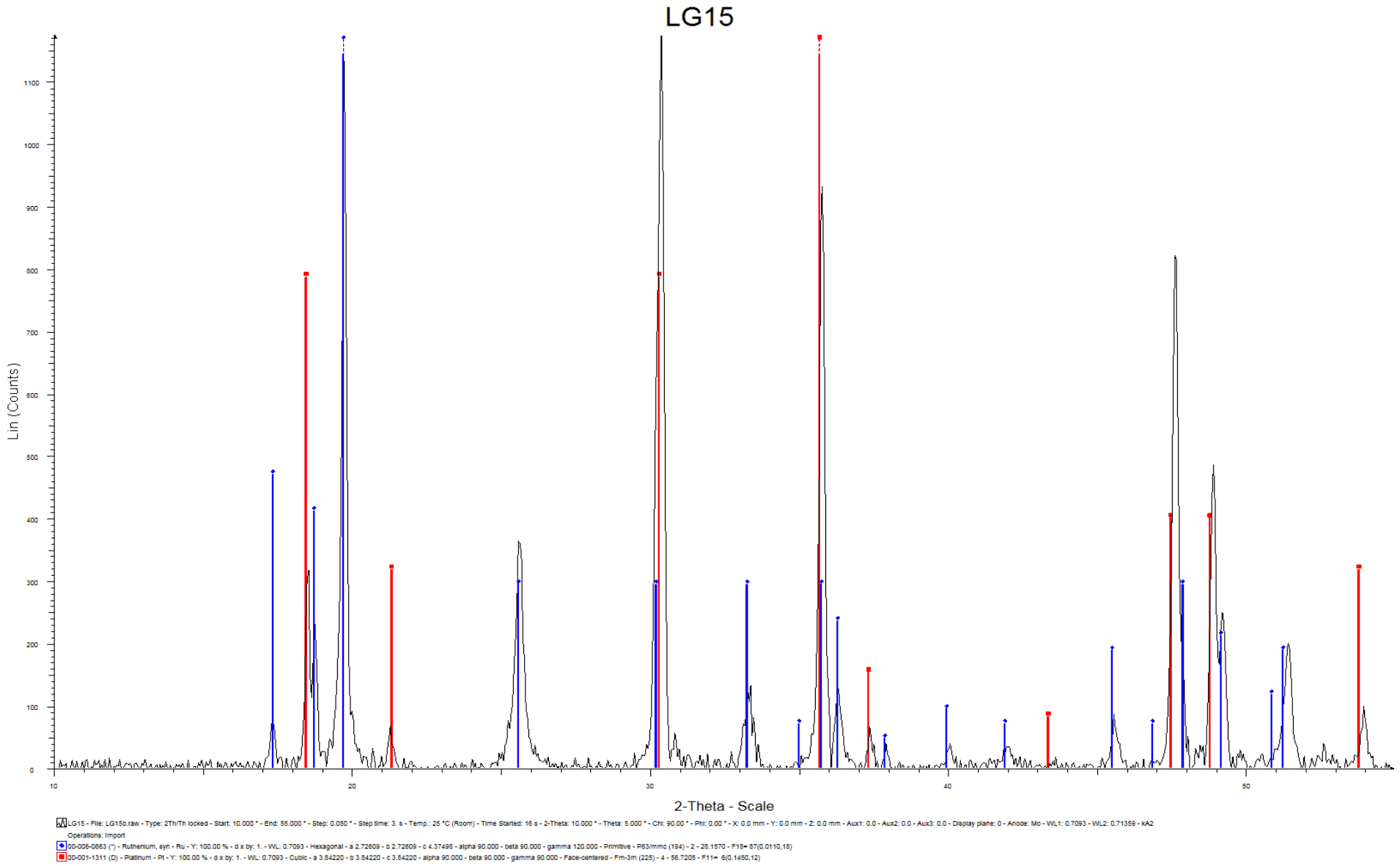


Figure 4.81. XRD spectrum of LG 15 (nominal Co_{30}:Pt_{20}:Ru_{50}) in the as-cast condition, with both Pt and Ru peaks overlaid.

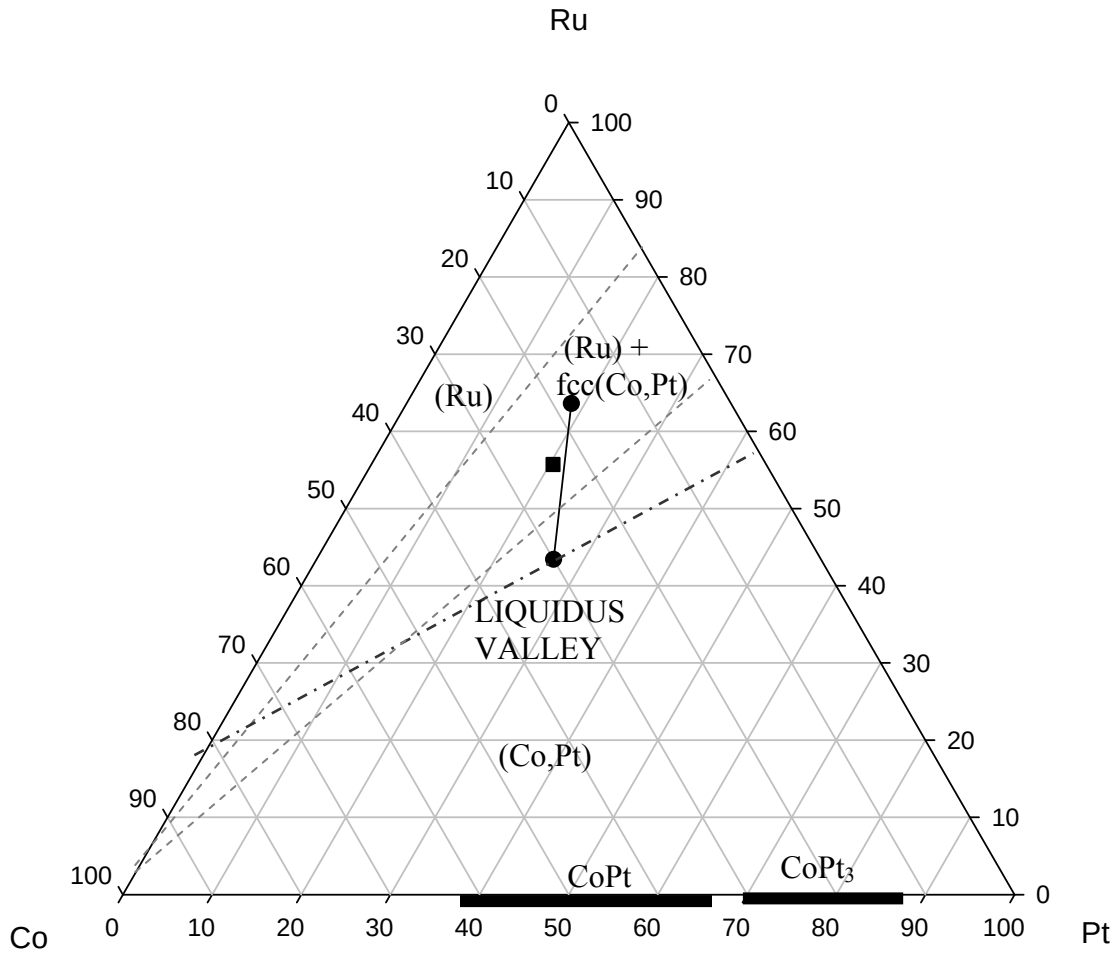


Figure 4.82. EDS analyses of LG 15 (nominal Co_{30}:Pt_{20}:Ru_{50}) in the as-cast condition (at.%).

Table 4.30. Unidentified peaks in the as-cast condition.

2θ	**Intensity**
19	50
20	100
25	25
31	50
32	25

LG 16 (Nominal Co_{60}:Pt_{20}:Ru_{20})

The microstructure of alloy LG 16 (Nominal Co_{60}:Pt_{20}:Ru_{20}) (Figure 4.83) shows a single-phase matrix with a few very fine pores are visible. The XRD spectrum (Figures 4.84 – 4.85) is very good and shows a high signal to background ratio with very narrow peaks. The peaks on the spectrum correspond well with εCo with a small amount of (Co,Pt) present (Figure 4.84). The spectrum is shown again in Figure 4.85 with the εCo lines shifted to the left and the Pt lines shifted to the right. In Figure 4.86, both εCo and Pt lines are combined on the same spectrum. Judging by the height of the ε(Co) and Pt peaks, there is ≤10% (Co,Pt) present. The small unidentified peaks are shown in Table 4.32 The EDS phase analyses for this alloy is shown in Table 4.31 and the actual composition is plotted in Figure 4.87.

The solidification sequence for the alloy is: $L + \varepsilon Co \rightarrow (Co,Pt)$

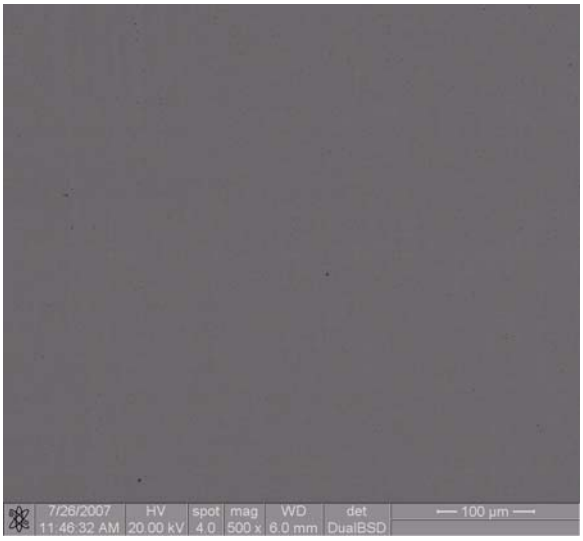
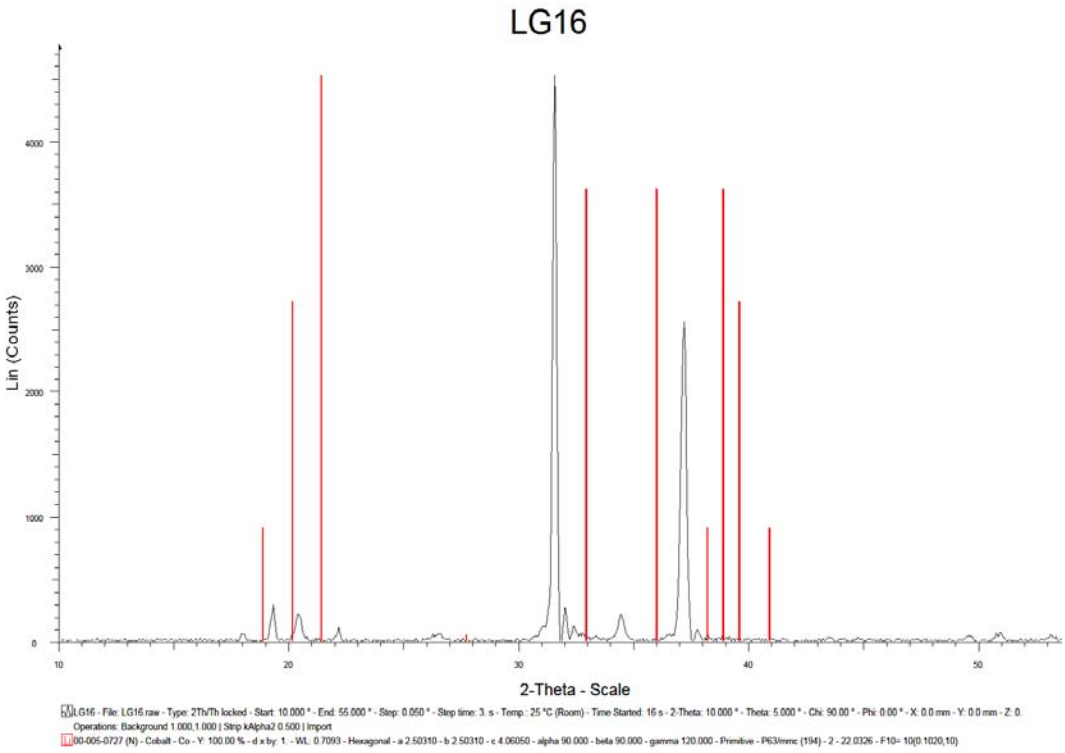


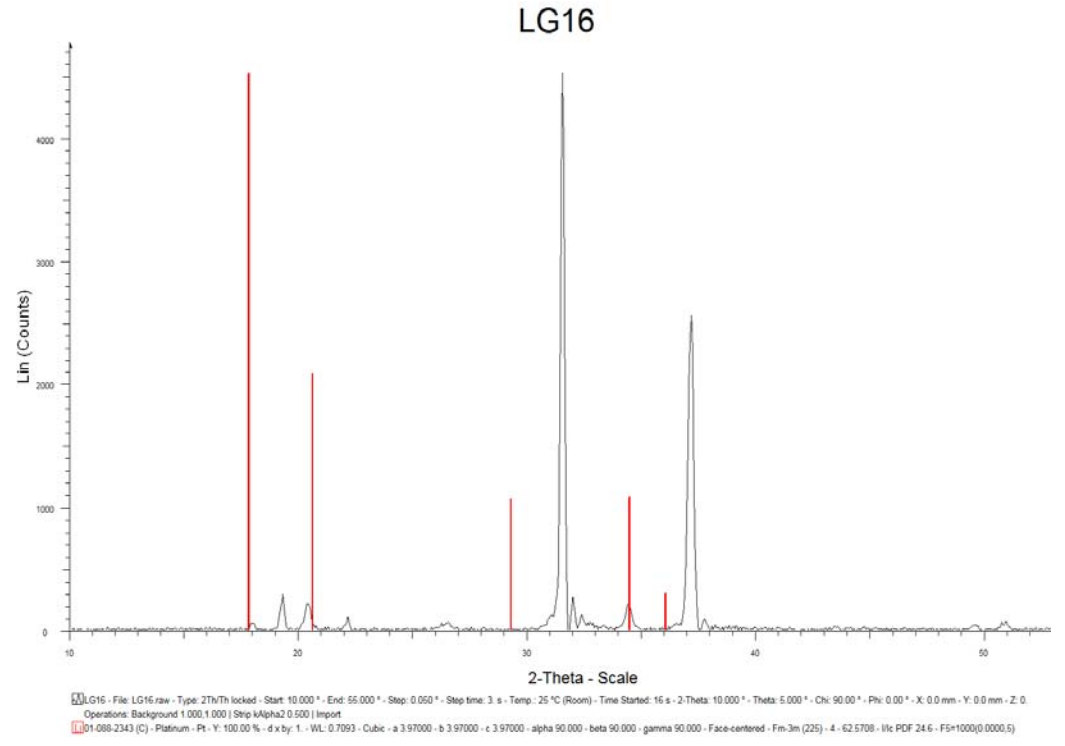
Figure 4.83. LG 16 (Nominal Co_{60}:Pt_{20}:Ru_{20}) in the as-cast condition showing a single (Co,Pt) phase structure.

Table 4.31. Analyses LG 16 (Nominal Co_{60}:Pt_{20}:Ru_{20}) in the as-cast condition (at.%).

Phase description	Pt (at.%)	Ru (at.%)	Co (at.%)	Phase	Phase Proportion (%)
Overall	20.3±0.2	19.8±0.9	59.9±0.8	εCo + small amount (Co,Pt)	≤90 εCo (XRD)

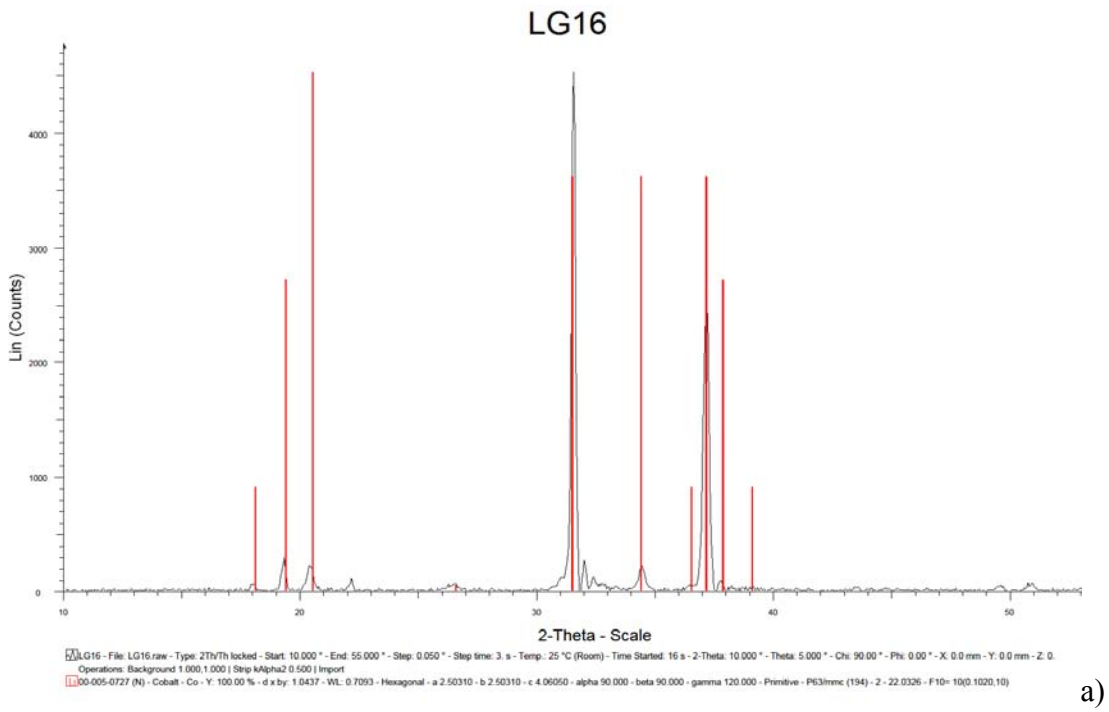


a)

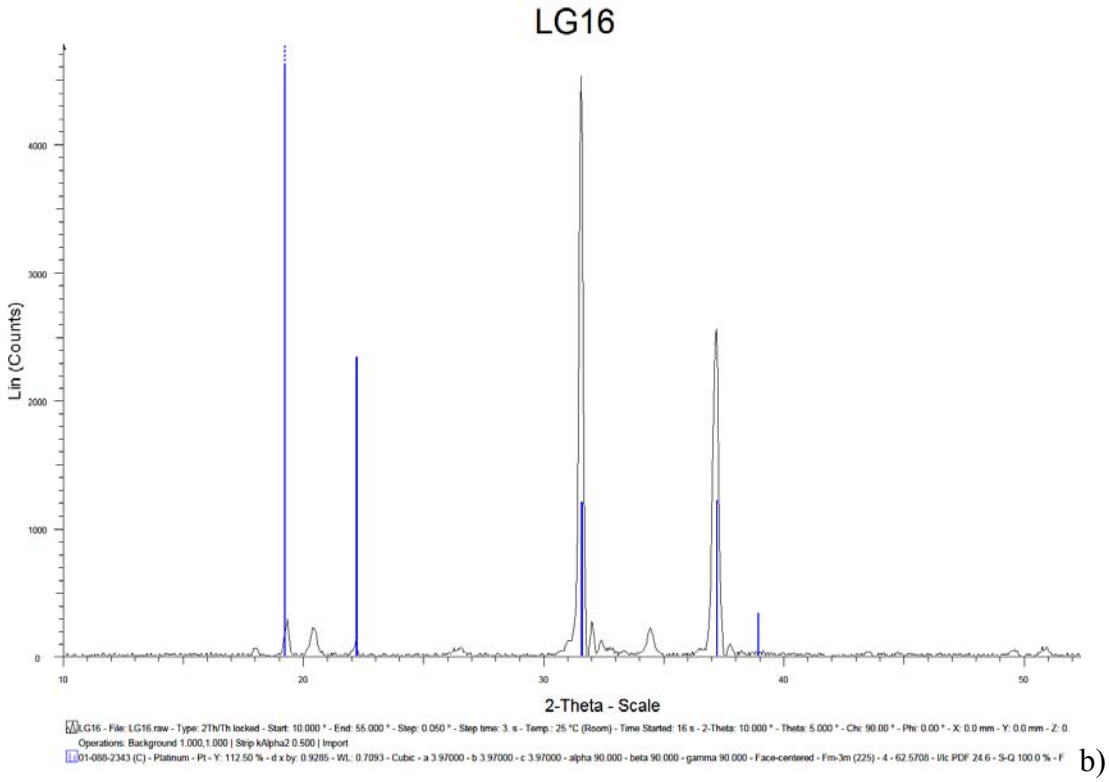


b)

Figure 4.84. XRD spectrum of LG 16 (Nominal Co_{60}:Pt_{20}:Ru_{20}) in the as-cast condition showing a comparison with a) εCo and b) Pt.



a)



b)

Figure 4.85. XRD spectrum of LG 16 (Nominal Co_{60}:Pt_{20}:Ru_{20})in the as-cast condition showing a comparison with a) εCo and b) Pt after shifting.

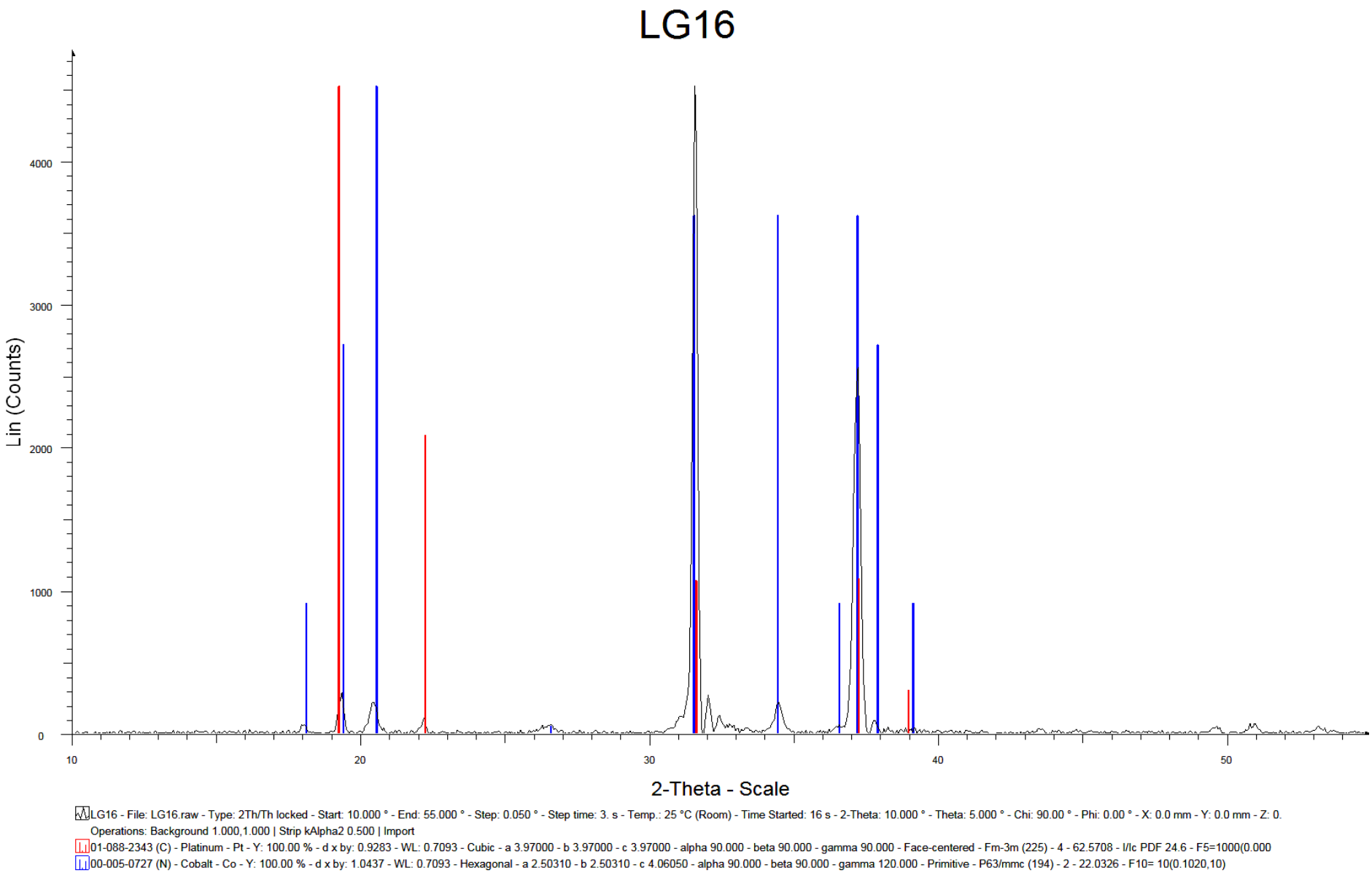


Figure 4.86. *XRD spectrum of LG 16 (Nominal Co_{60}:Pt_{20}:Ru_{20}) in the as-cast condition with both ε Co and Pt overlaid.*

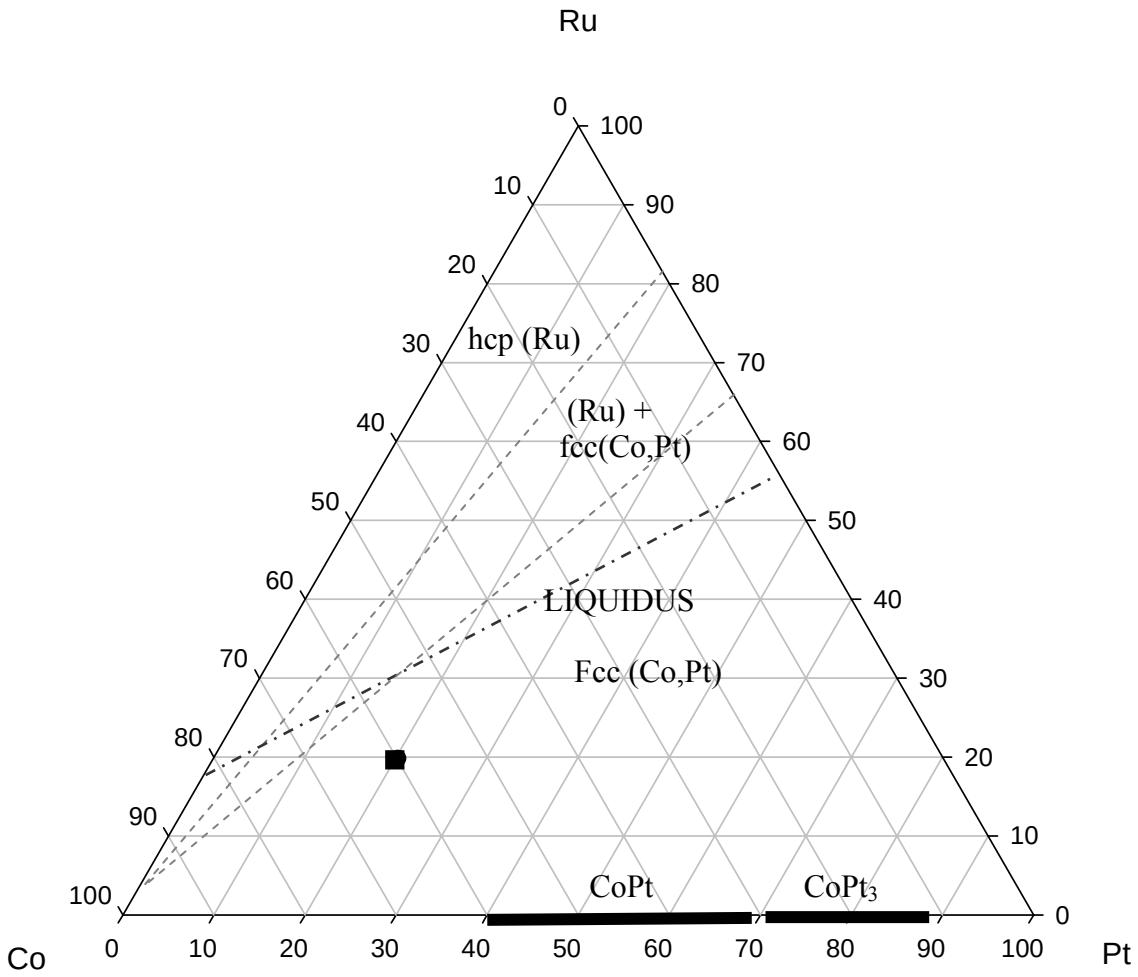


Figure 4.87. EDS analysis of LG 16 (Nominal Co_{60}:Pt_{20}:Ru_{20}) in the as-cast condition (at.%).

Table 4.32. Unidentified peaks in the as-cast condition.

2θ	**Intensity**
21.5	50
31	100
32.2	300

LG 17 (Nominal $Co_{10}:Pt_{30}:Ru_{60}$)

The micrograph in Figure 4.88 shows the microstructure of LG 17 (Nominal $Co_{10}:Pt_{30}:Ru_{60}$). Two phases are visible: a light phase that was identified as fcc(Co,Pt), and a dark phase that was identified as ε(Ru). The XRD spectrum shows a quite poor signal to background ratio. The peaks are narrow and show a good fit to Ru and Pt (Figure 4.89). Figure 4.90 shows the spectrum with the lines shifted. Figure 4.91 shows the XRD spectrum with the Ru and Pt peaks overlaid. Judging from the height of the peaks it appears that there is slightly more (Ru) than fcc(Co,Pt) present, although the microstructure shows that there is over 80% (Ru). Two unidentified peaks are shown in Table 4.34. The EDS phase analyses for this alloy is shown in Table 4.33 and the actual composition is plotted in Figure 4.92. The overall was on the tie-line between the two phases.

The solidification sequence for the alloy is: $L + (Ru) \rightarrow fcc(Co,Pt)$

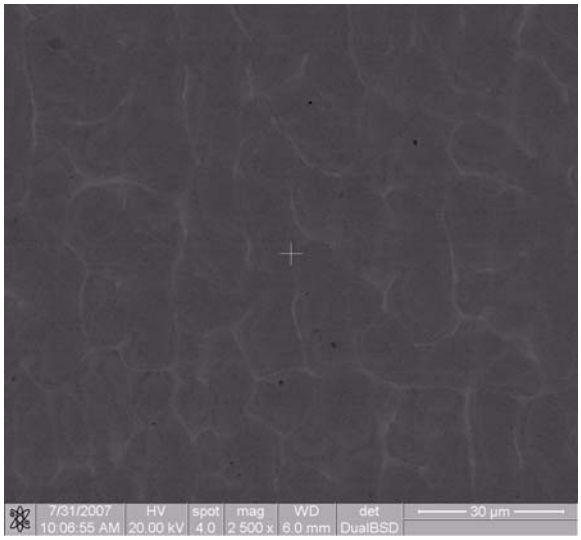
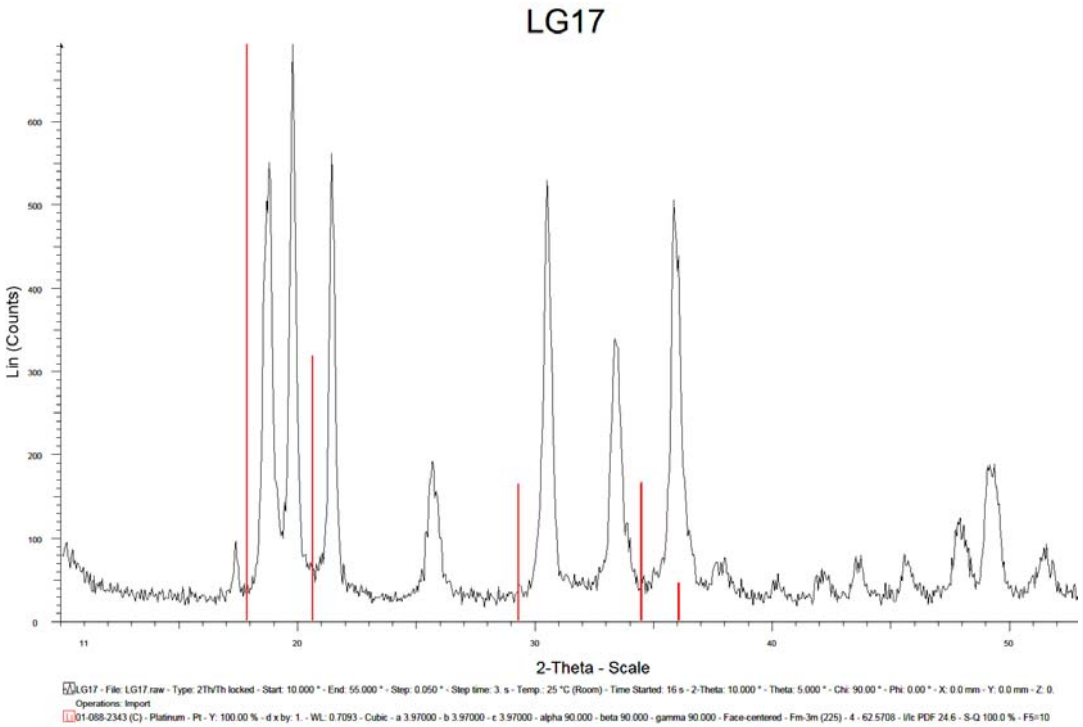


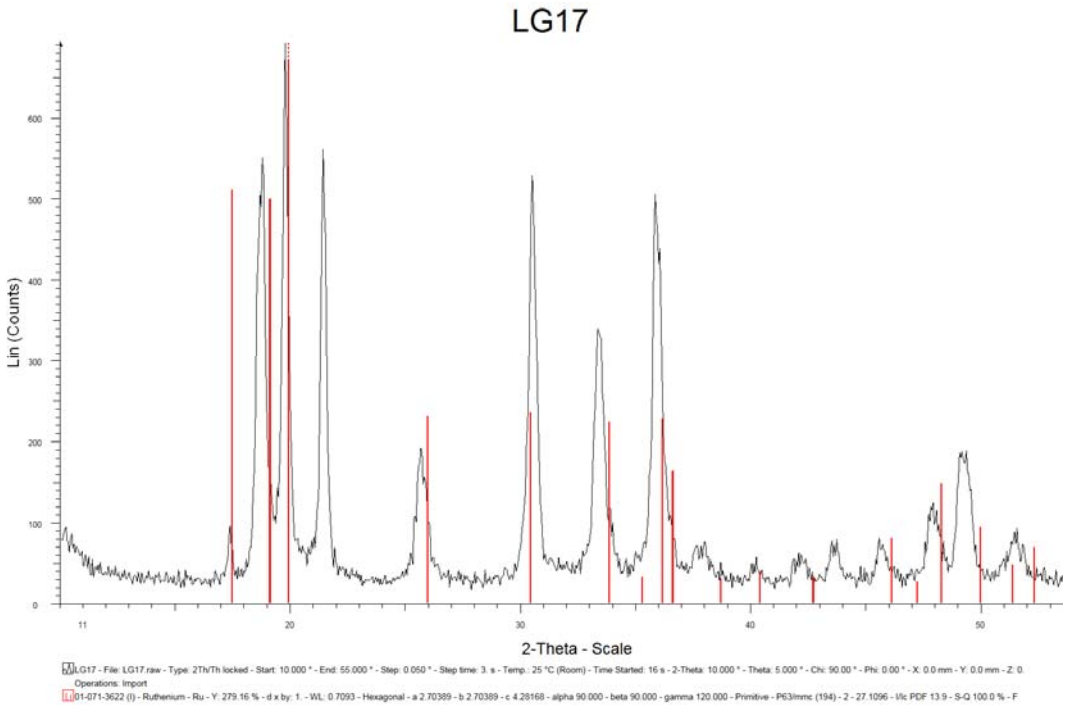
Figure 4.88. BEI of LG 17 (Nominal $Co_{10}:Pt_{30}:Ru_{60}$) in the as-cast condition showing dark (Ru) and fcc (Co,Pt) light phase.

Table 4.33. EDS analyses LG 17 (Nominal $Co_{10}:Pt_{30}:Ru_{60}$) in the as-cast condition (at.%).

Phase description	Pt (at.%)	Ru (at.%)	Co (at.%)	Phase	Phase Proportion (%)
Overall	30.3 ± 1.2	63.8 ± 1.1	5.9 ± 1.0	-	-
Dark	32.3 ± 1.5	60.6 ± 1.0	7.1 ± 0.9	(Ru)	~80
Light	50.9 ± 1.3	19.7 ± 1.1	29.4 ± 0.9	fcc(Co,Pt)	~20

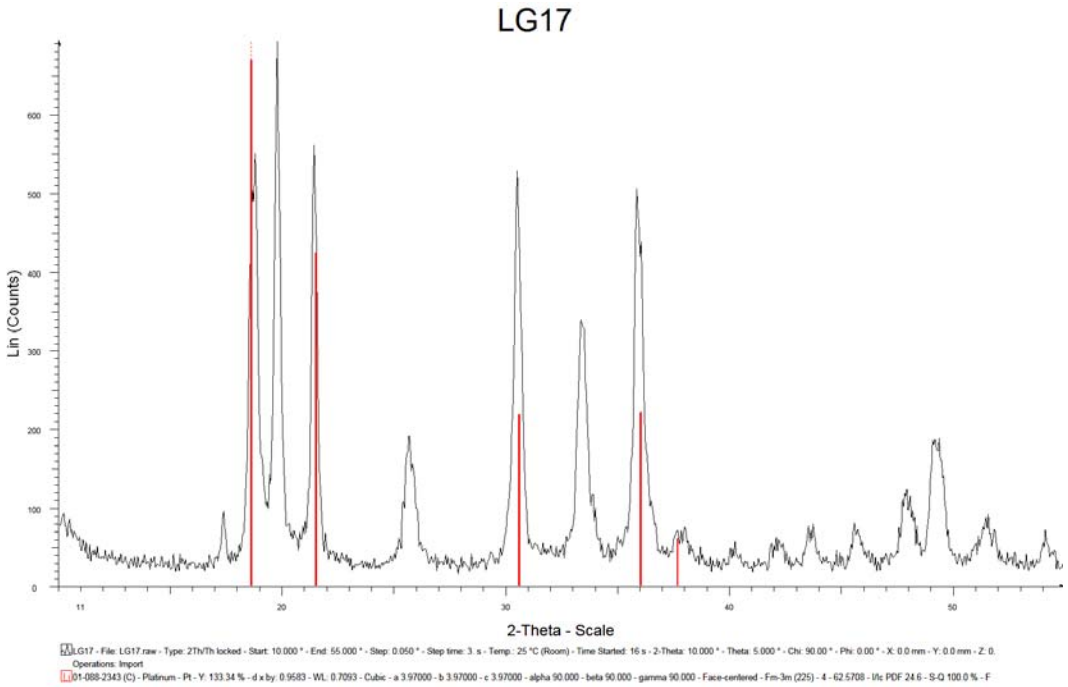


a)

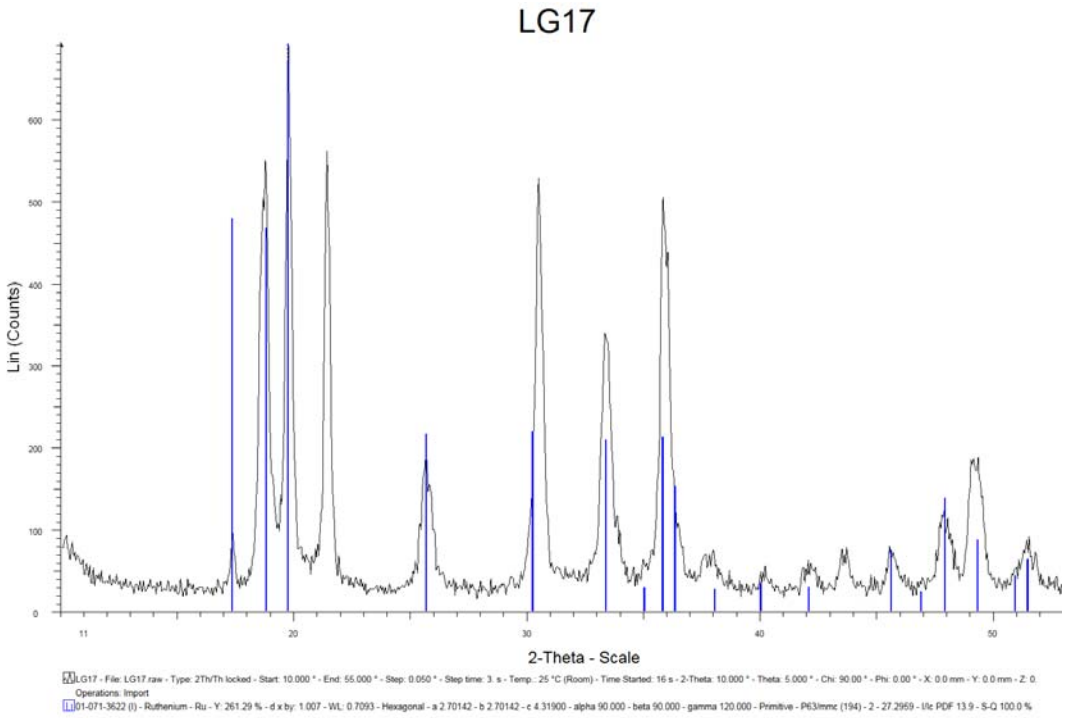


b)

Figure 4.89. XRD spectrum of LG 17 (Nominal Co_{10}:Pt_{30}:Ru_{60}) in the as-cast condition showing a comparison with a) Pt and b) Ru.



a)



b)

Figure 4.90. XRD spectrum of LG 17 (Nominal Co_{10}:Pt_{30}:Ru_{60}) in the as-cast condition showing a comparison with a) Pt and b) Ru after shifting.

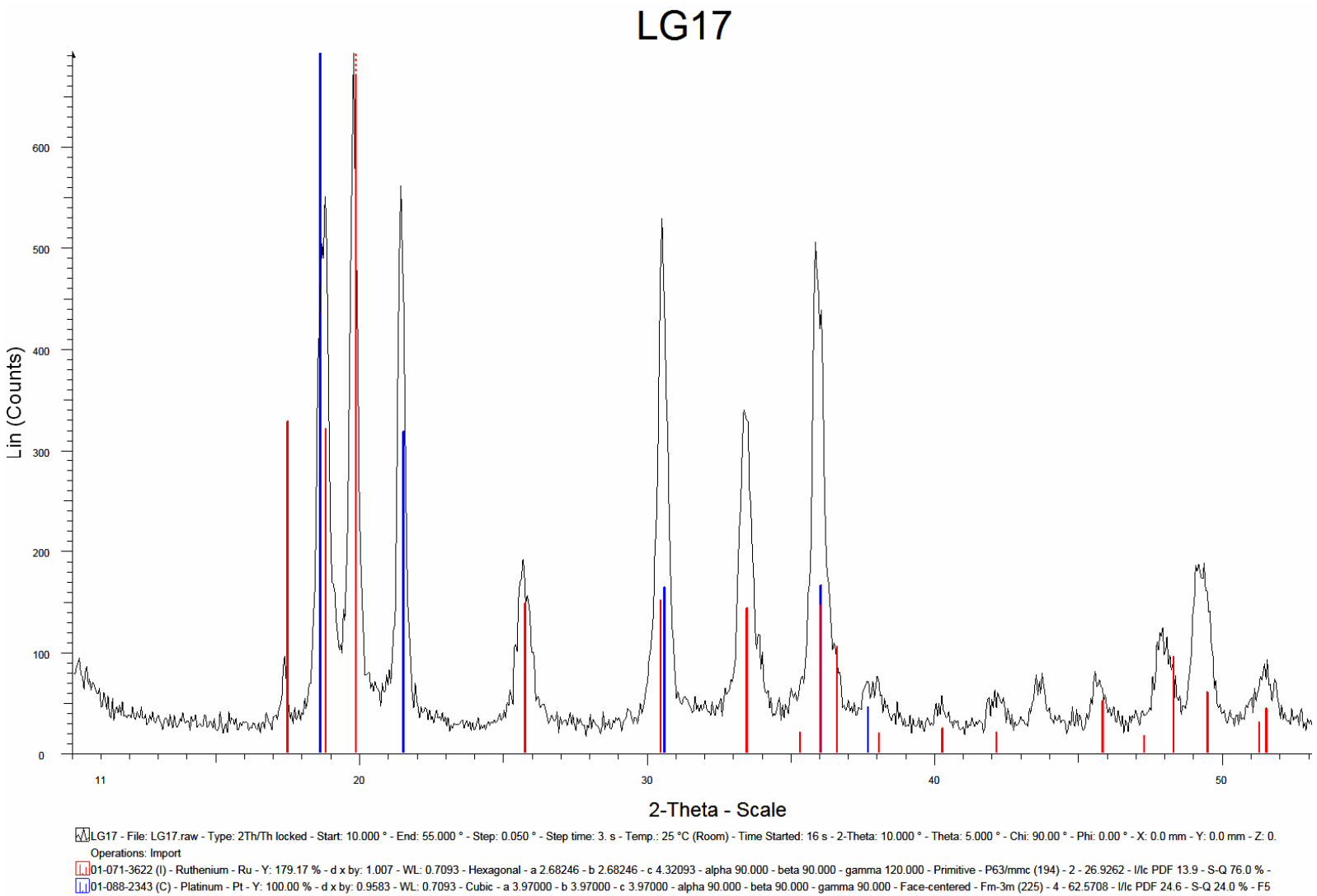


Figure 4.91. XRD spectrum of LG 17 (Nominal $Co_{10}:Pt_{30}:Ru_{60}$) in the as-cast condition with both Ru and Pt overlaid.

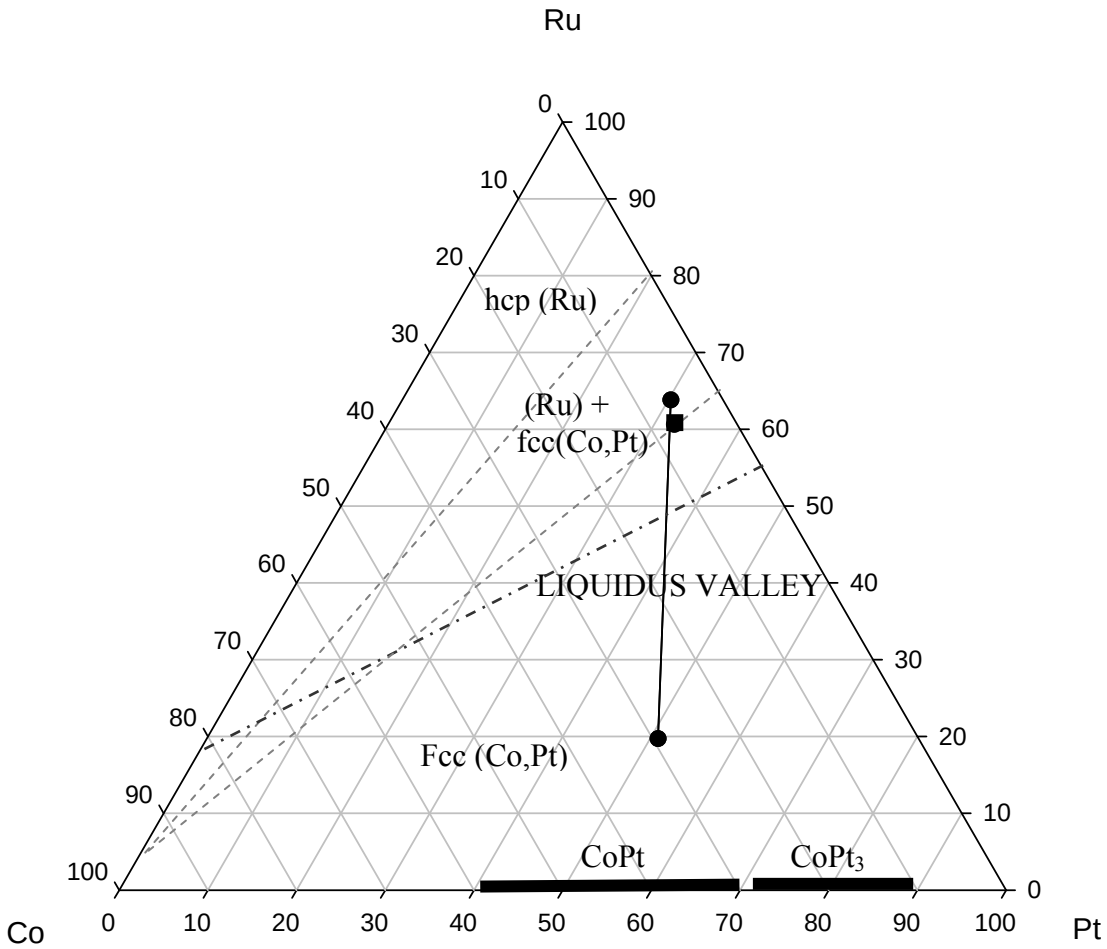


Figure 4.92. EDS analyses of LG 17 (Nominal $Co_{10}:Pt_{30}:Ru_{60}$) in the as-cast condition (at.%).

Table 4.34. Unidentified peaks in the as-cast condition.

2θ	**Intensity**
19	175
43.5	75

LG 18 (Nominal Co_{20}:Pt_{30}:Ru_{50})

The micrograph in Figure 4.93 shows the as-cast microstructure of LG 18 (Nominal Co_{20}:Pt_{30}:Ru_{50}). Two phases are visible: a light phase that is identified as fcc(Co,Pt) and a dark phase that is identified as (Ru). The XRD spectrum (Figures 4.94 and 4.95) shows a fair signal to background ratio. There are two unidentified peaks that are shown in Table 4.36. The peaks are quite wide and show a good fit to Ru and Pt. Judging from the height of the peaks it appears that there is 75% fcc(Co,Pt) and 25% (Ru) present, although the microstructure shows a more even distribution. The EDS phase analyses for this alloy is shown in Table 4.35 and the actual composition is plotted in Figure 4.97. The overall composition was on the tie-line.

The solidification sequence for the alloy is: $L + (Ru) \rightarrow fcc(Co,Pt)$

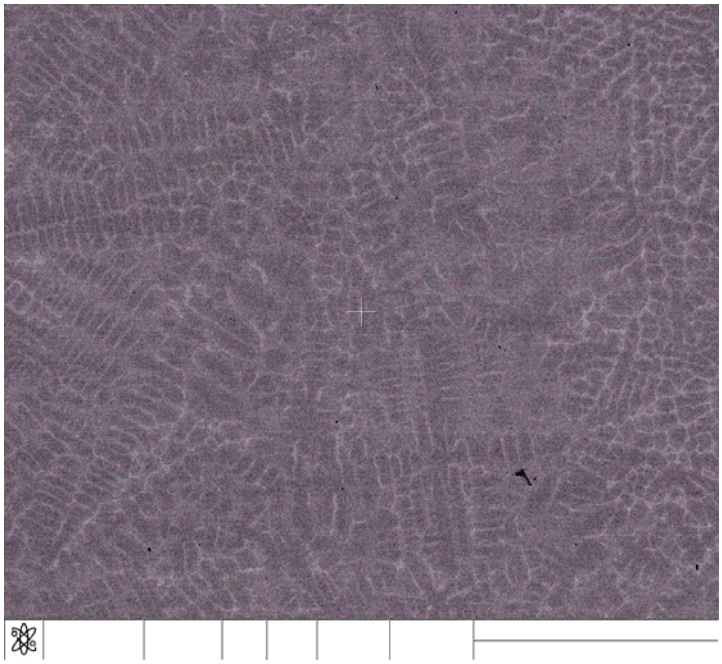
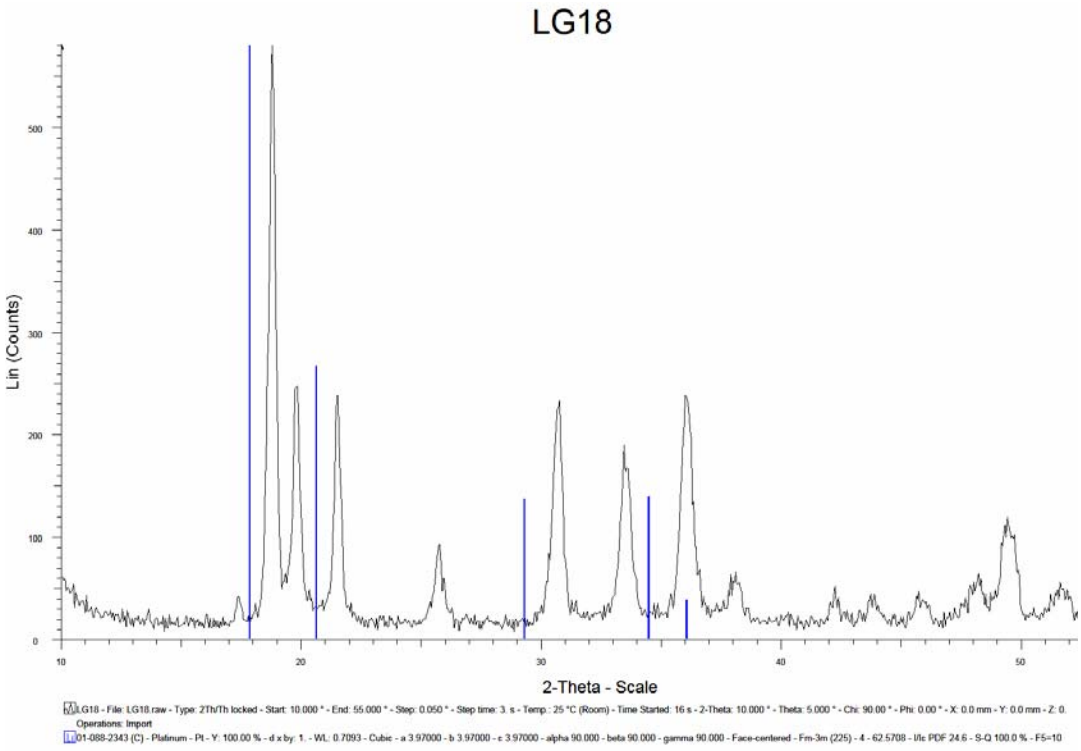


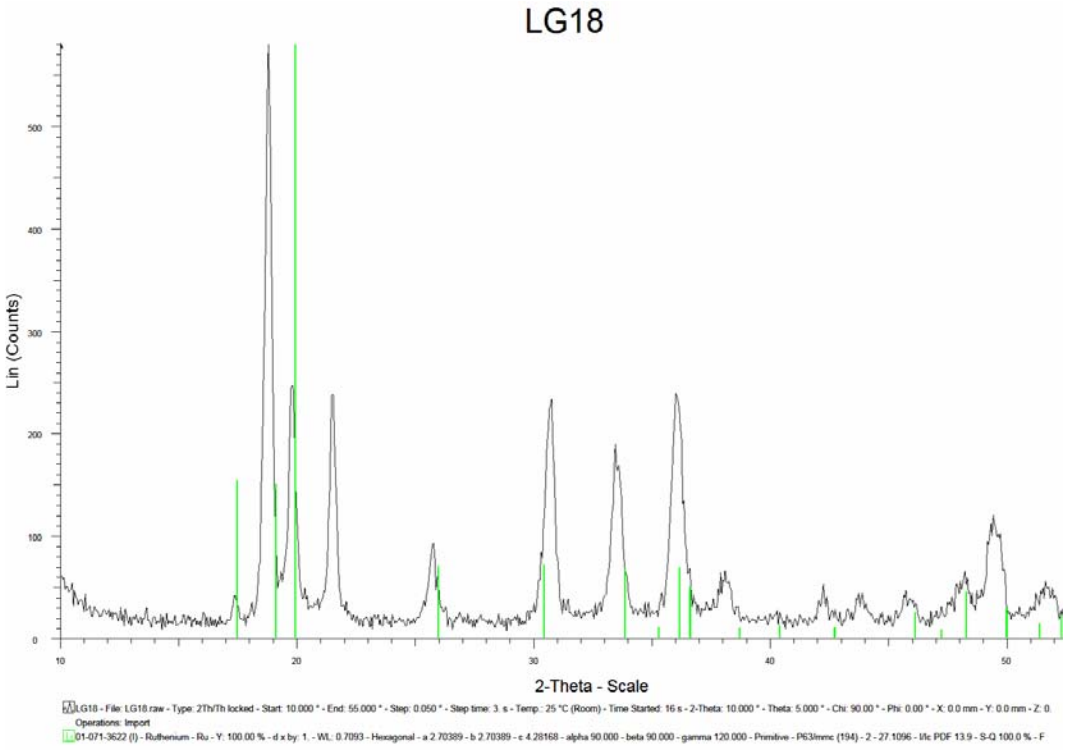
Figure 4.93. LG 18 (Nominal Co_{20}:Pt_{30}:Ru_{50}) in the as-cast condition showing dark (Ru) and light fcc fcc(Co,Pt) phase.

Table 4.35. Analyses LG 18 (Nominal Co_{20}:Pt_{30}:Ru_{50}) in the as-cast condition (at.%).

Phase description	Pt (at.%)	Ru (at.%)	Co (at.%)	Phase	Phase Proportion (%)
Overall	29.2 ± 1.2	58.6 ± 1.2	12.2 ± 0.5	-	-
Dark	26.4 ± 3.6	64.6 ± 2.5	9 ± 2.3	(Ru)	~25
Light	41.1 ± 2.2	31.2 ± 7.2	27.7 ± 5.0	fcc(Co,Pt)	~75

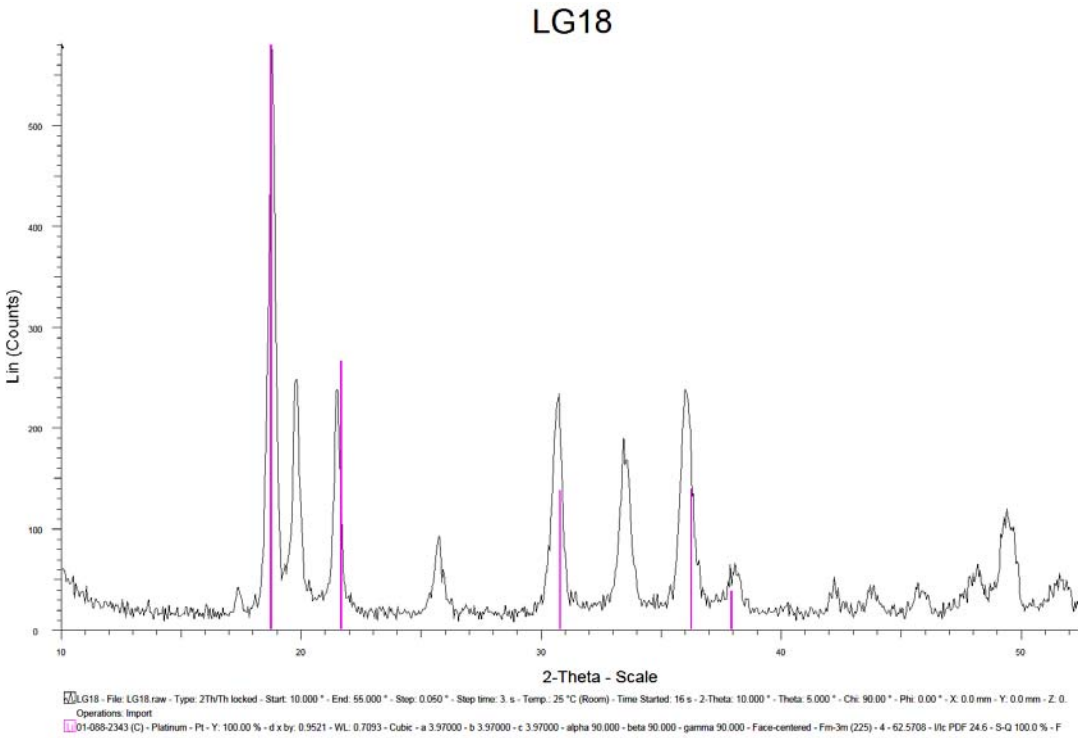


a)

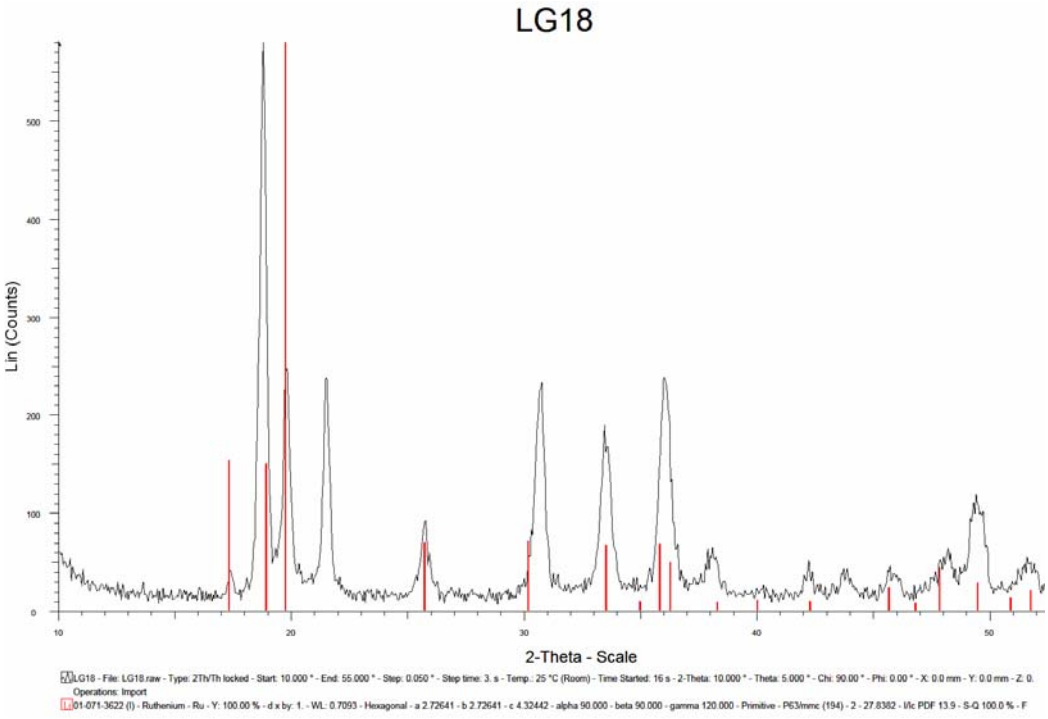


b)

Figure 4.94. XRD spectrum of LG 18 (Nominal Co_{20}:Pt_{30}:Ru_{50}) in the as-cast condition showing a comparison with a) Pt and b) Ru.



a)



b)

Figure 4.95. XRD spectrum of LG 18 (Nominal Co_{20}:Pt_{30}:Ru_{50}) in the as-cast condition showing a comparison with a) Pt and b) Ru after shifting.

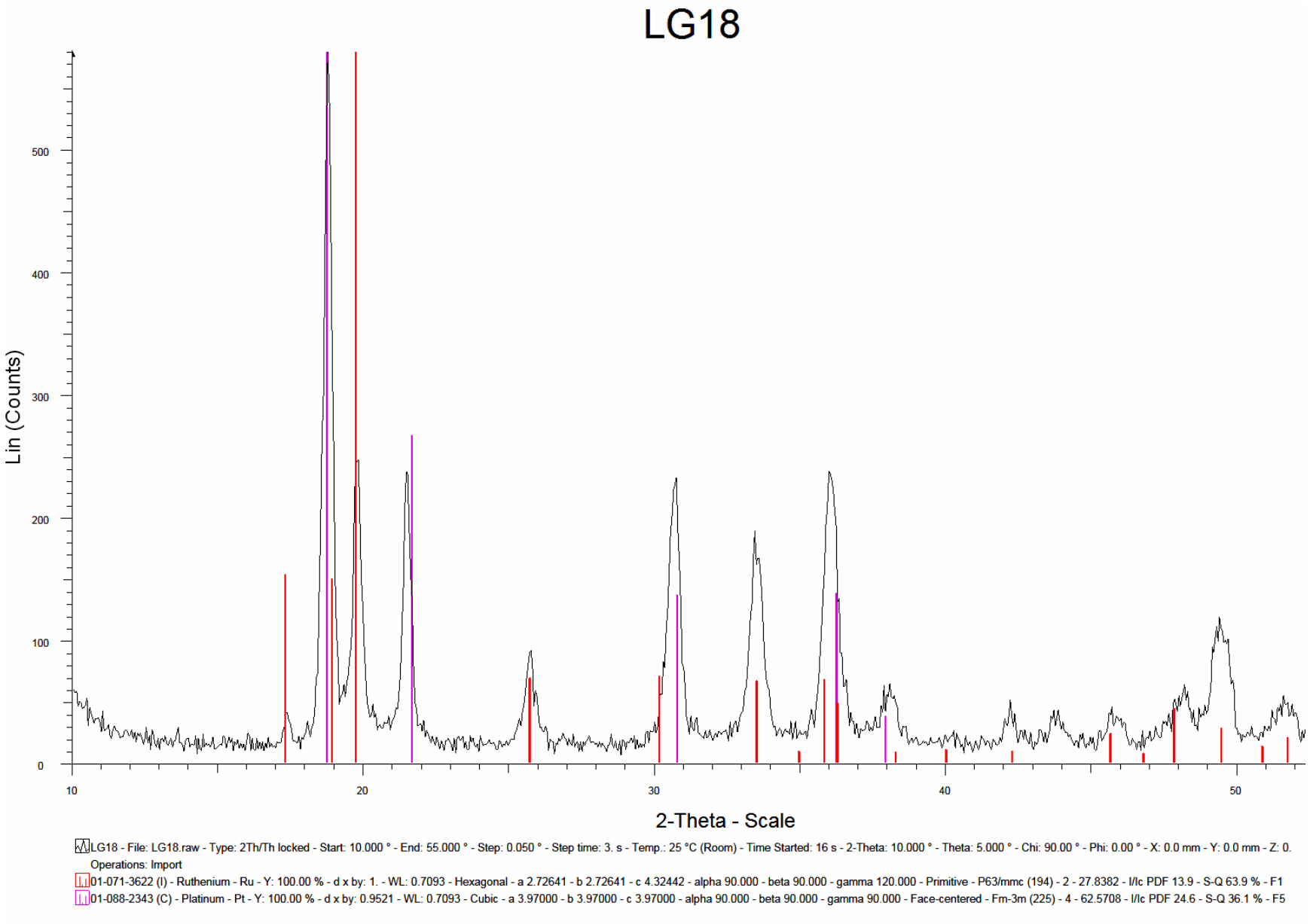


Figure 4.96. XRD spectrum of LG 18 (Nominal Co_{20}:Pt_{30}:Ru_{50}) in the as-cast condition with both Ru and Pt overlaid.

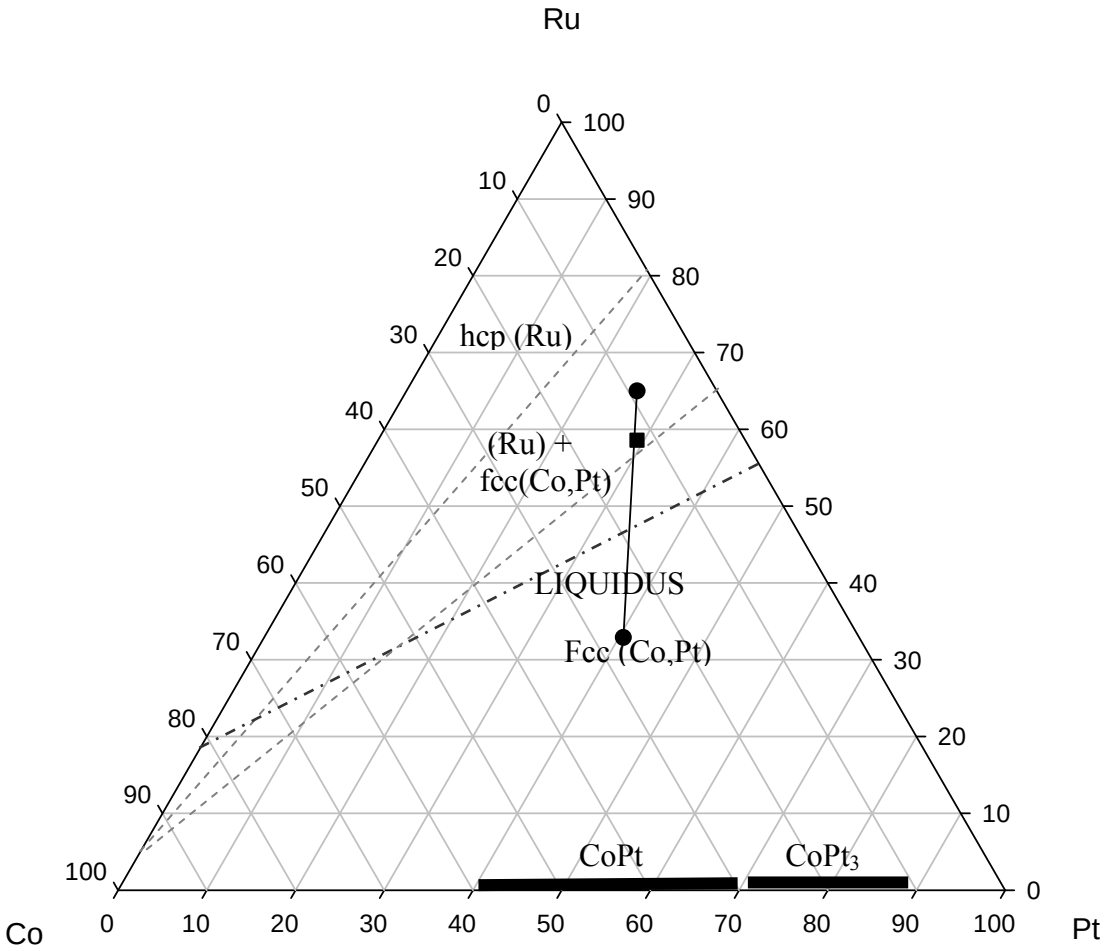


Figure 4.97. EDS analyses of LG 18 (Nominal Co_{20}:Pt_{30}:Ru_{50}) in the as-cast condition (at.%).

Table 4.36. Unidentified peaks in the as-cast condition.

2θ	**Intensity**
19	175
20.2	50
44	75

LG 19 (Nominal Co_{50}:Pt_{20}:Ru_{30})

The micrograph in Figure 4.98 shows the as-cast microstructure of LG 19 (Nominal Co_{50}:Pt_{20}:Ru_{30}). There are two phases visible that were identified as (Ru) and fcc (Co,Pt). The XRD spectrum (Figures 4.99 and 4.100) shows a fair signal to background ratio and the peaks are quite wide and show a good fit to Ru and Pt. Judging from the height of the peaks on the XRD spectrum, it appears that there are roughly equal amounts of fcc(Co,Pt) and ε(Ru) present, although the micrograph shows that there is more fcc (Co,Pt). The EDS phase analyses for this alloy is shown in Table 4.37 and the actual composition is plotted in Figure 4.102. The alloy overall was not on the tie-line joining the two phases.

The solidification sequence for the alloy is: $L + (Ru) \rightarrow fcc(Co,Pt)$

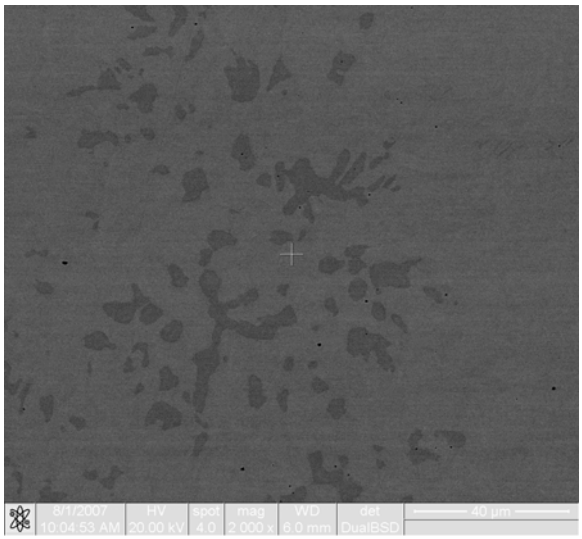
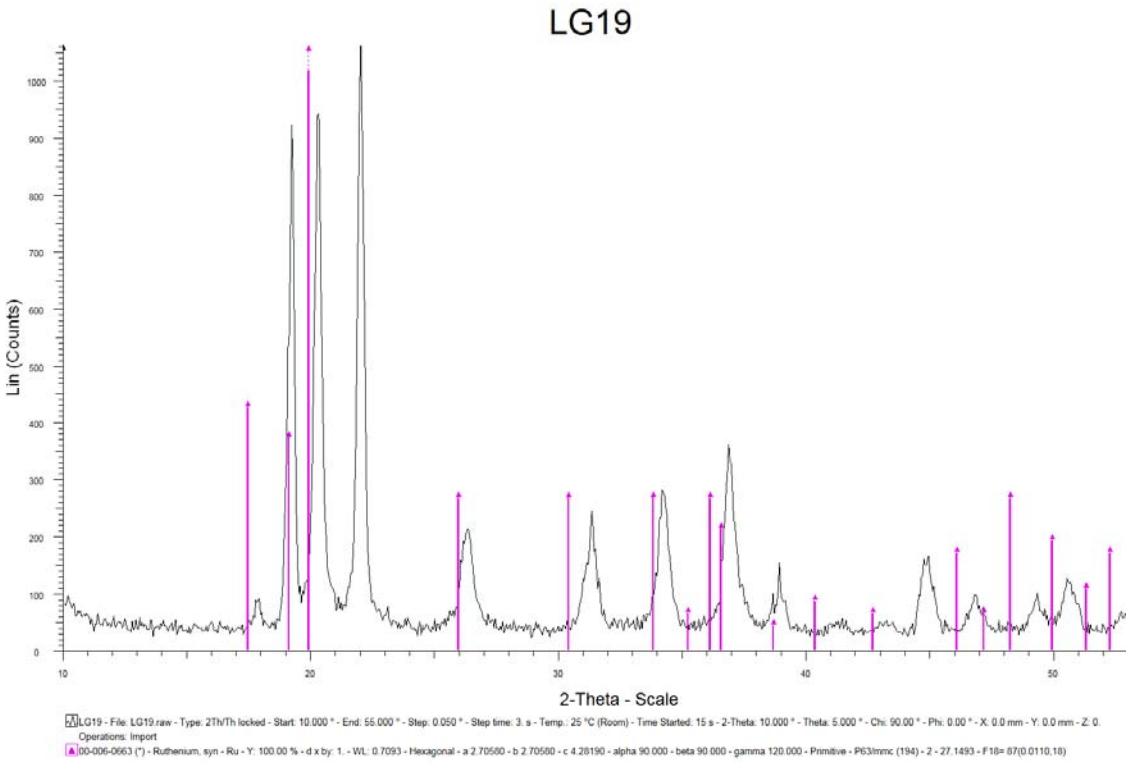


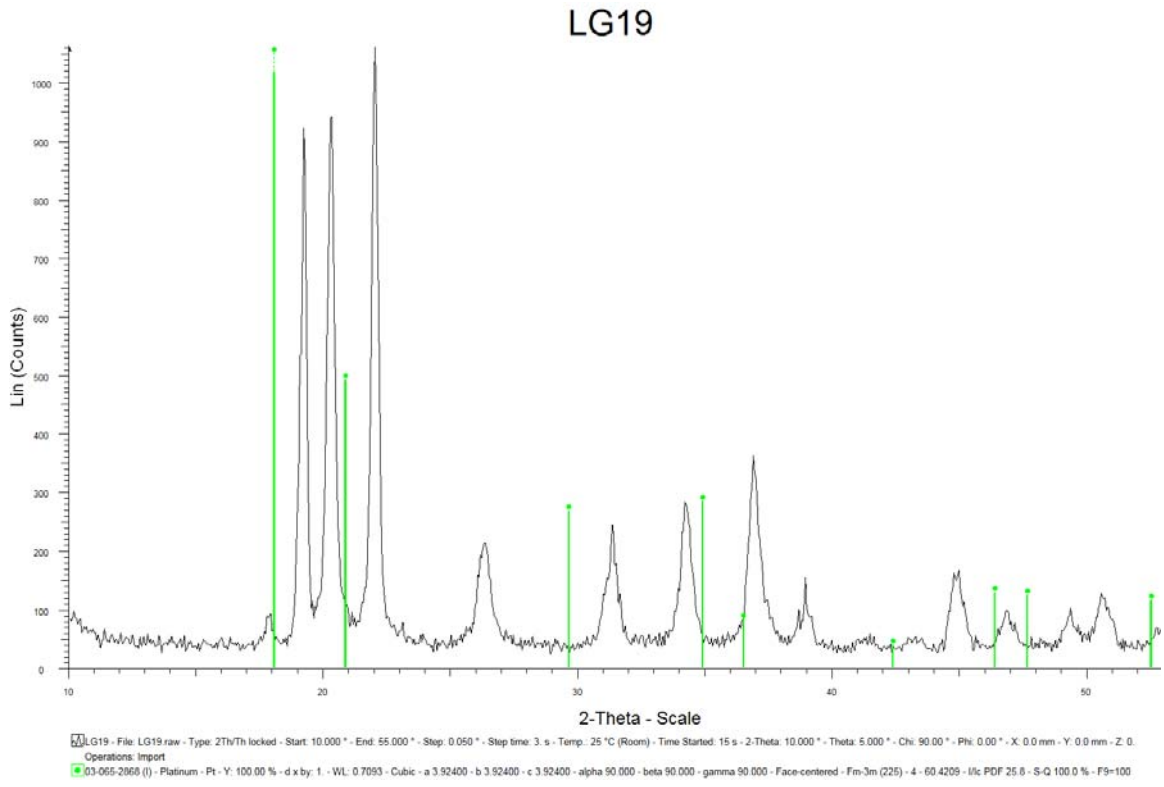
Figure 4.98. BEI of LG 19 (Nominal Co_{50}:Pt_{20}:Ru_{30}) in the as-cast condition showing dark (Ru) and light fcc(Co,Pt).

Table 4.37. EDS analyses LG 19 (Nominal Co_{50}:Pt_{20}:Ru_{30}) in the as-cast condition (at.%).

Phase description	Pt (at.%)	Ru (at.%)	Co (at.%)	Phase	Phase Proportion (%)
Overall	25.1	27.6	47.3	-	-
Dark	16.8	49.3	33.9	(Ru)	~40
Light	25.0	23.5	51.5	fcc(Co,Pt)	~60

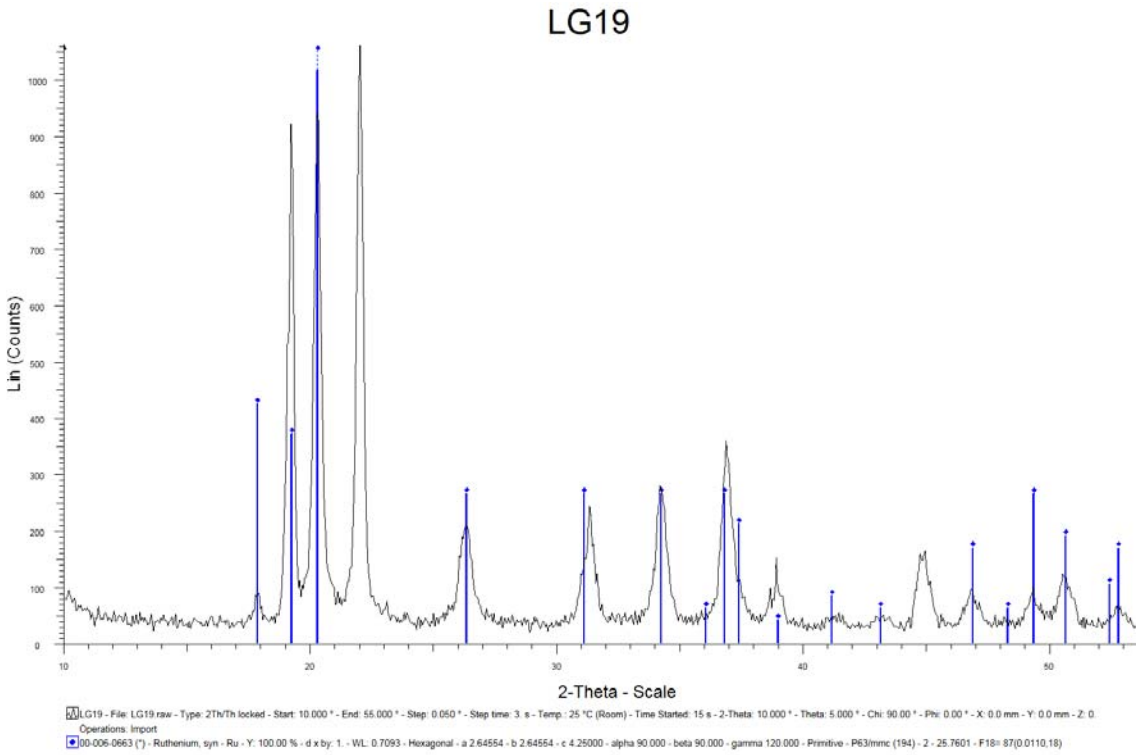


a)

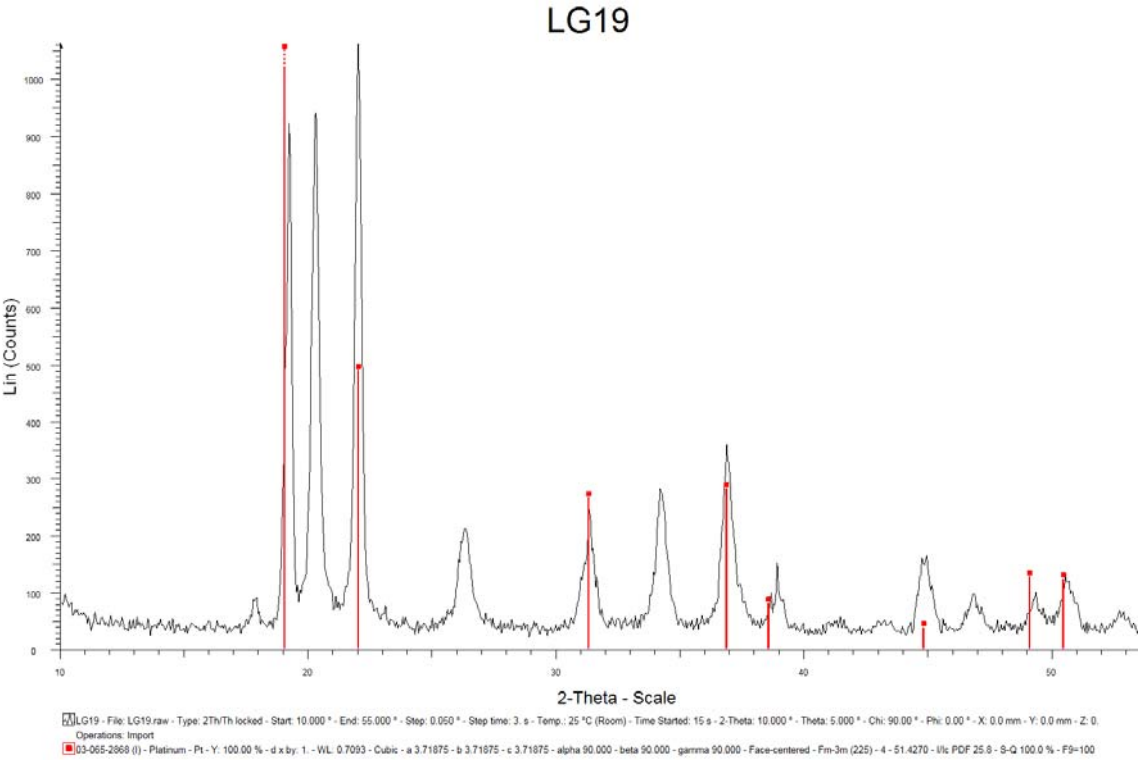


b)

Figure 4.99. XRD spectrum of LG 19 (Nominal Co_{50}:Pt_{20}:Ru_{30}) in the as-cast condition showing a comparison with a) Ru and b) Pt.



a)



b)

Figure 4.100. XRD spectrum of LG 19 (Nominal Co_{50}:Pt_{20}:Ru_{30}) in the as-cast condition showing a comparison with a) Ru and b) Pt after shifting.

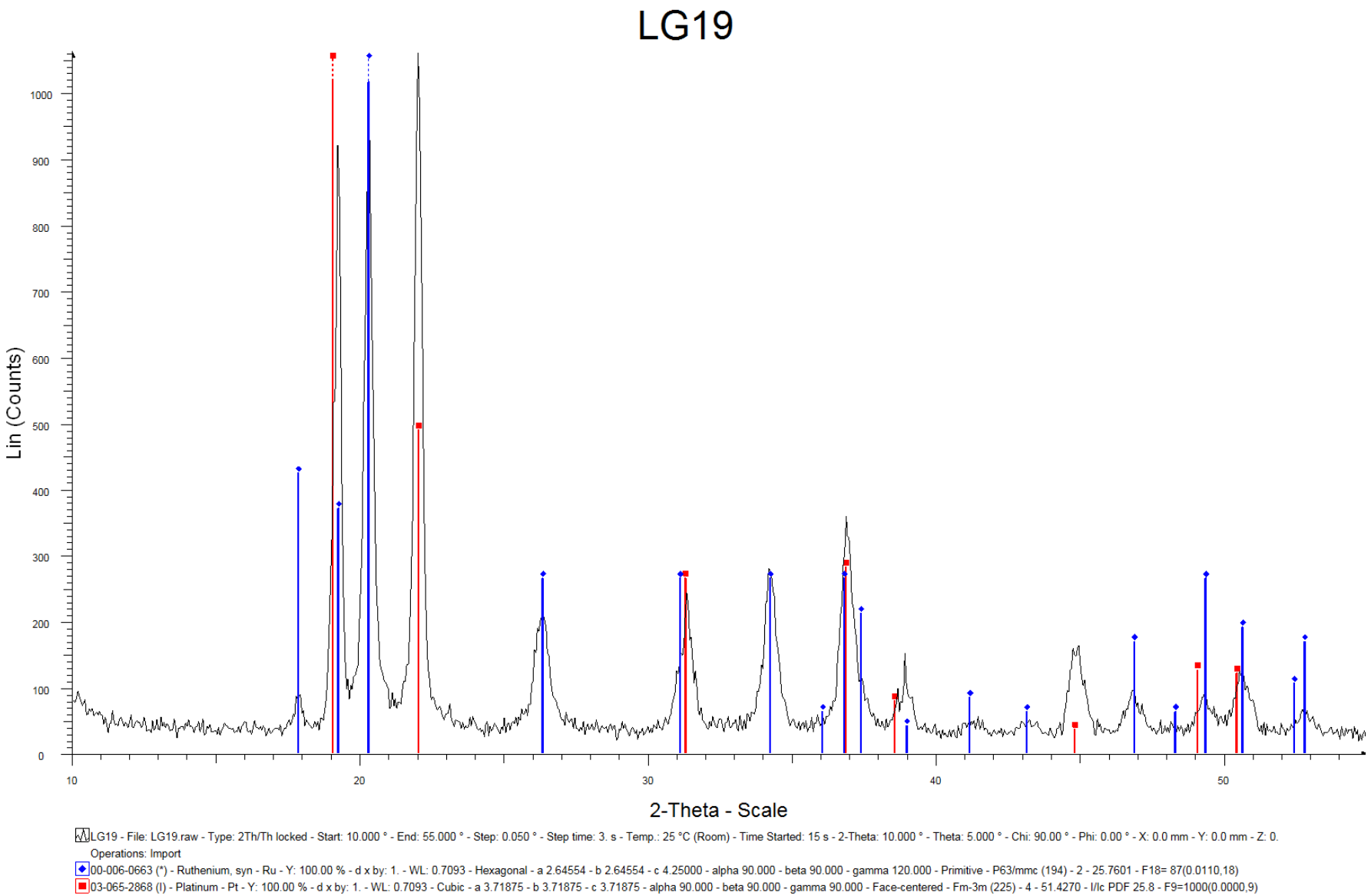


Figure 4.101. XRD spectrum of LG 19 (Nominal Co_{50}:Pt_{20}:Ru_{30}) in the as-cast condition with both Ru and Pt overlaid.

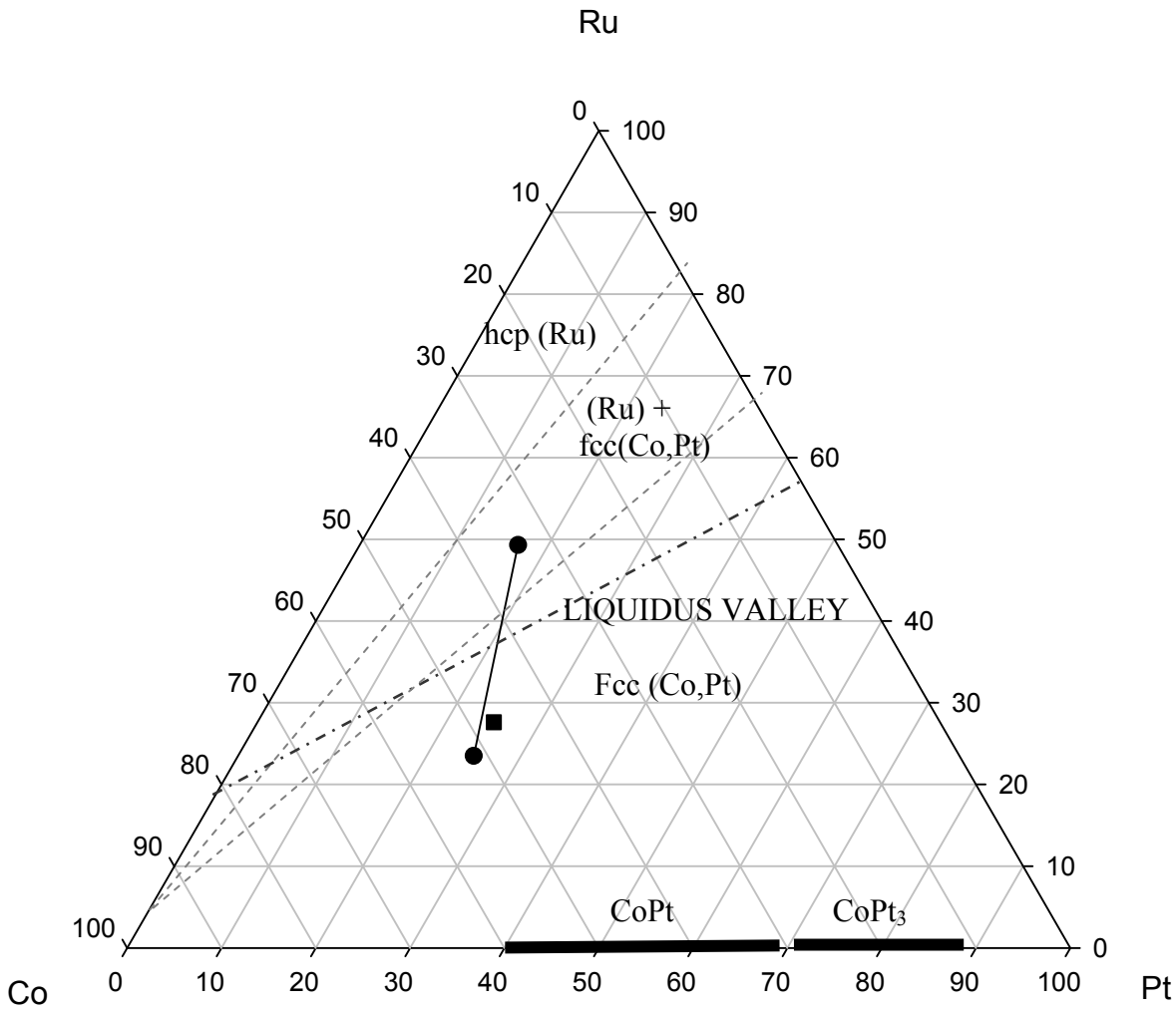


Figure 4.102. EDS analyses of LG 19 (Nominal Co_{50}:Pt_{20}:Ru_{30}) in the as-cast condition (at.%).

4.2.2 Alloys after Heat Treatment at 1000°C for 1000 hours and Water Quenching

LG13 (Nominal Co_{90}:Pt_5:Ru_5)

The heat treated LG13 (Nominal Co_{90}:Pt_5:Ru_5) appeared to consist of a single phase or a very fine two-phase microstructure as shown in Figure 4.103. The EDS analyses are shown in Table 4.38 and plotted in Figure 4.107. However, the XRD spectrum shows that there are two phases present (Figure 4.104). The peaks on the XRD spectrum are identified as ε(Co) and a small amount of fcc(Co,Pt). In Figure 4.105, the identifying lines were shifted and show a good fit for ε(Co) and Pt. Unidentified peaks were visible and are shown in Table 4.39. Figure 4.106 shows the XRD spectrum with both the shifted ε(Co) and Pt peaks overlaid. The signal to background ratio for the spectrum is high and the peaks are neat and narrow.

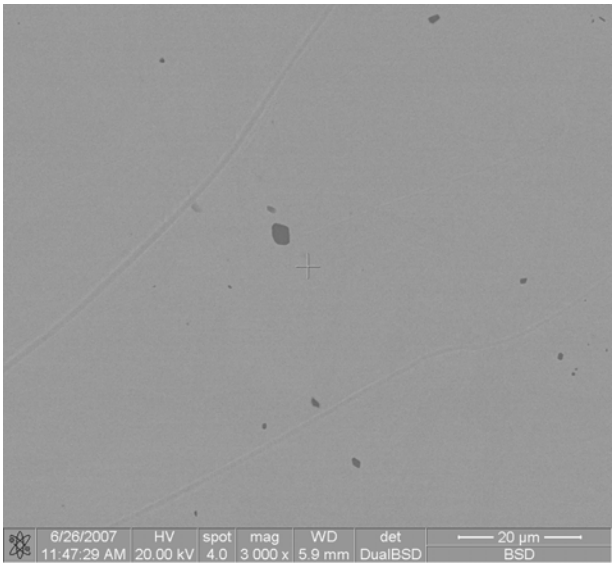
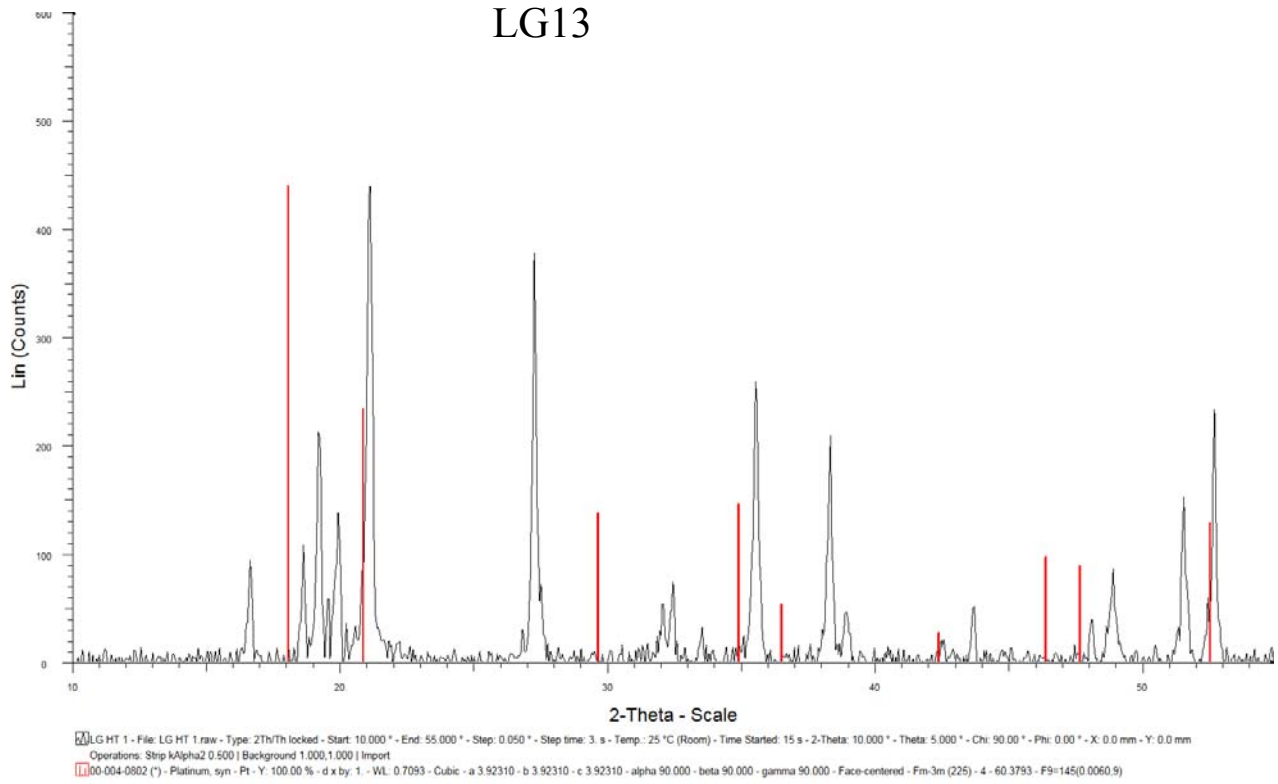


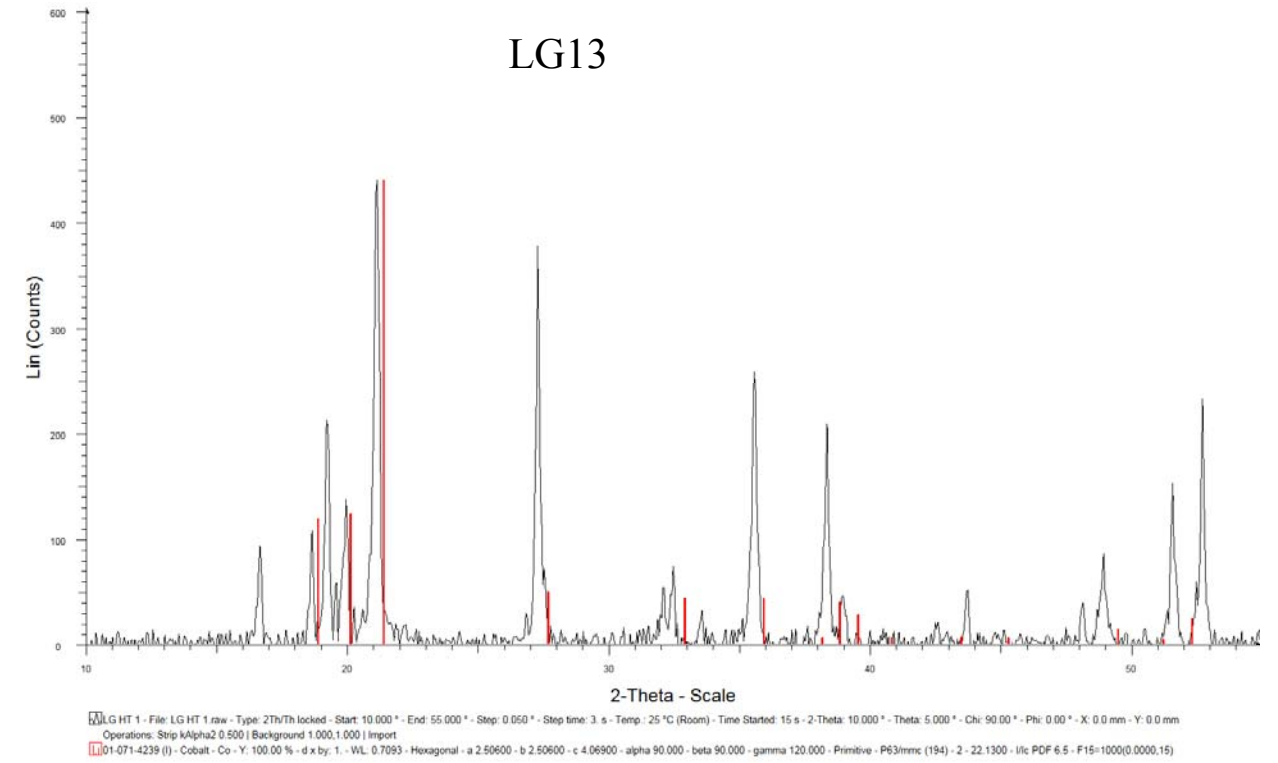
Figure 4.103. BEI of LG13 (Nominal Co_{90}:Pt_5:Ru_5) in the heat treated and water quenched condition showing an apparent (Co,Pt) single phase matrix, or fine two-phase microstructure.

Table 4.38. Analyses of LG13 (Nominal Co_{90}:Pt_5:Ru_5) in the heat treated condition (at.%).

Phase description	Pt (at.%)	Ru (at.%)	Co (at.%)	Phase	Phase Proportion (%)
Overall	7.6 ± 1.5	5.0 ± 1.3	87.4 ± 2.0	hcp εCo + fcc(Co,Pt)	-

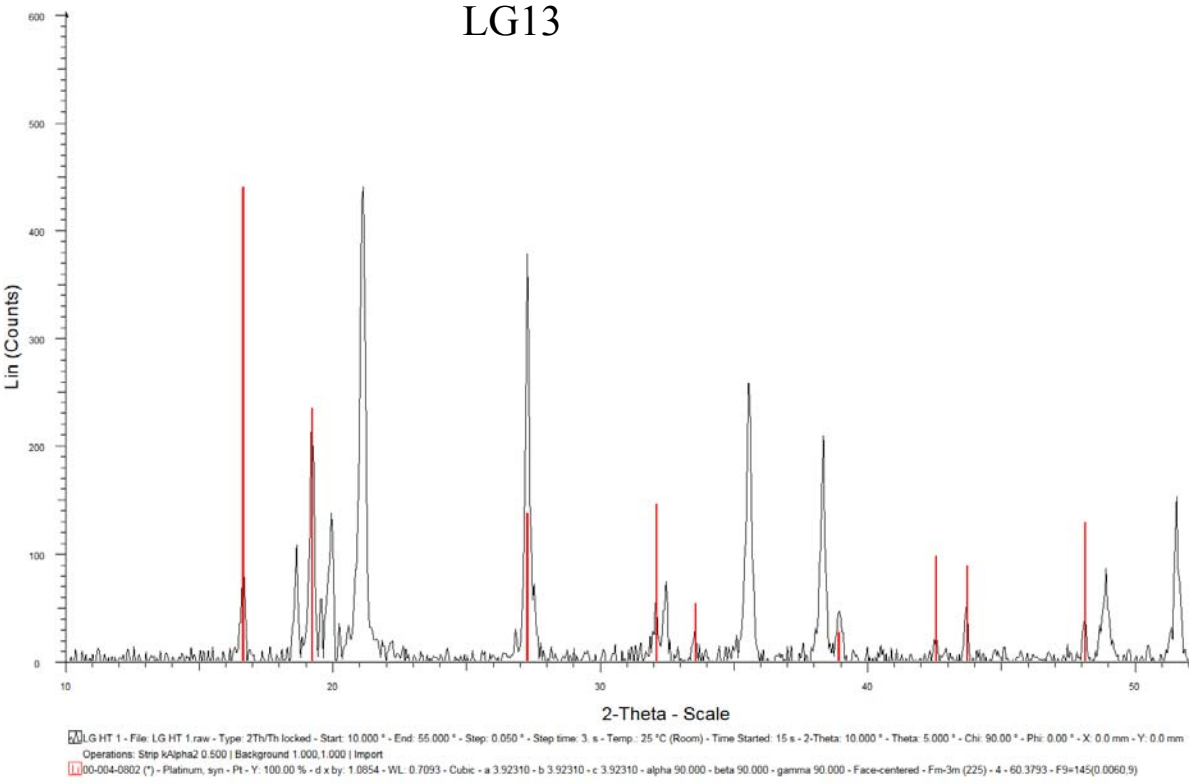


a)

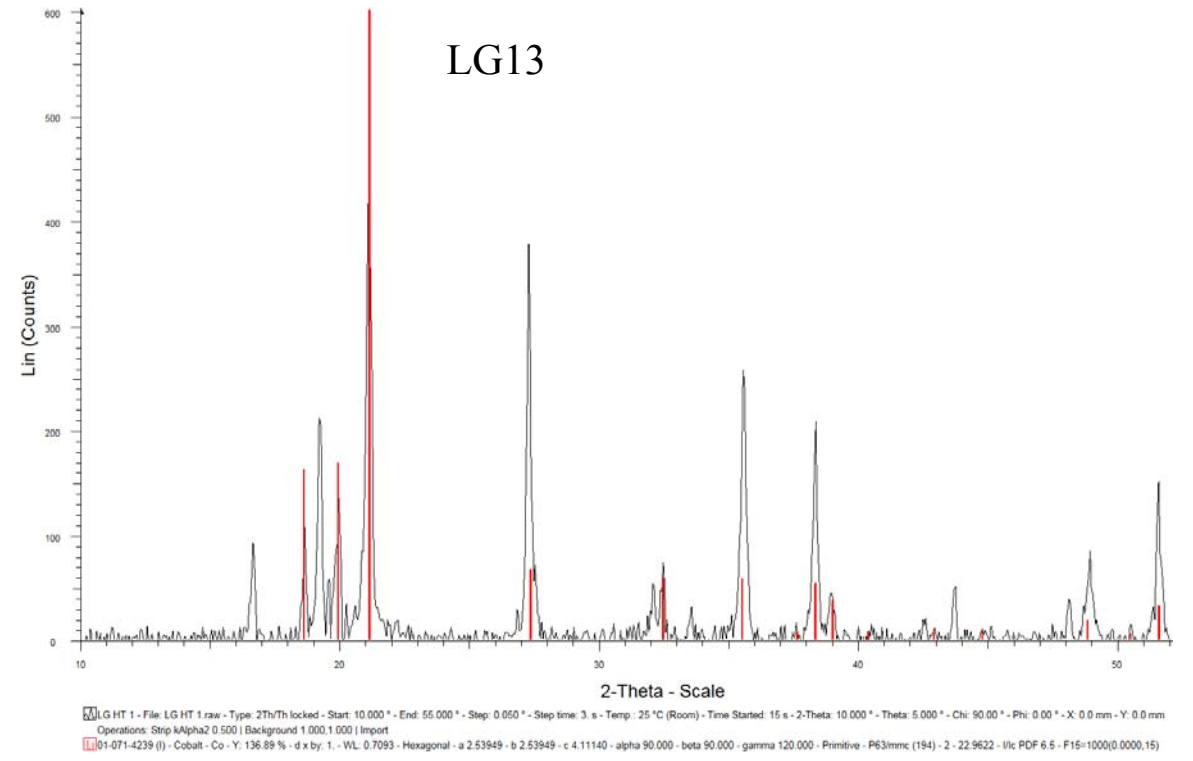


b)

Figure 4.104. XRD spectrum of LG13 (Nominal Co_{90}:Pt_5:Ru_5) in the heat treated condition showing a comparison with a) Pt and b) εCo.



a)



b)

Figure 4.105. XRD spectrum of LG13 (Nominal Co_{90}:Pt_5:Ru_5) in the heat treated condition showing a comparison with a) Pt and b) εCo after shifting.

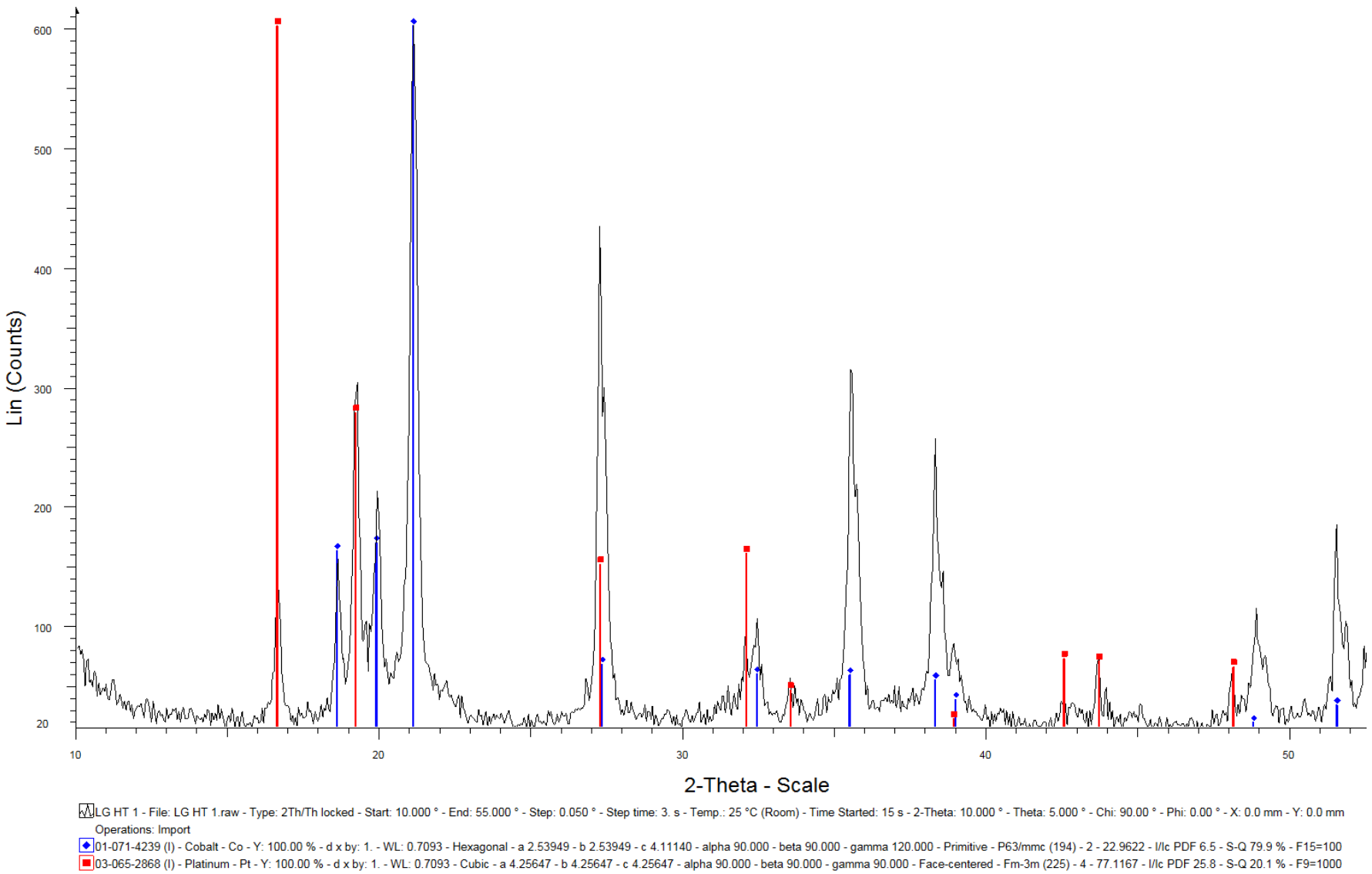


Figure 4.106. XRD spectrum of LG13 (Nominal Co_{90}:Pt_5:Ru_5) in the heat treated condition with both εCo and Pt overlaid.

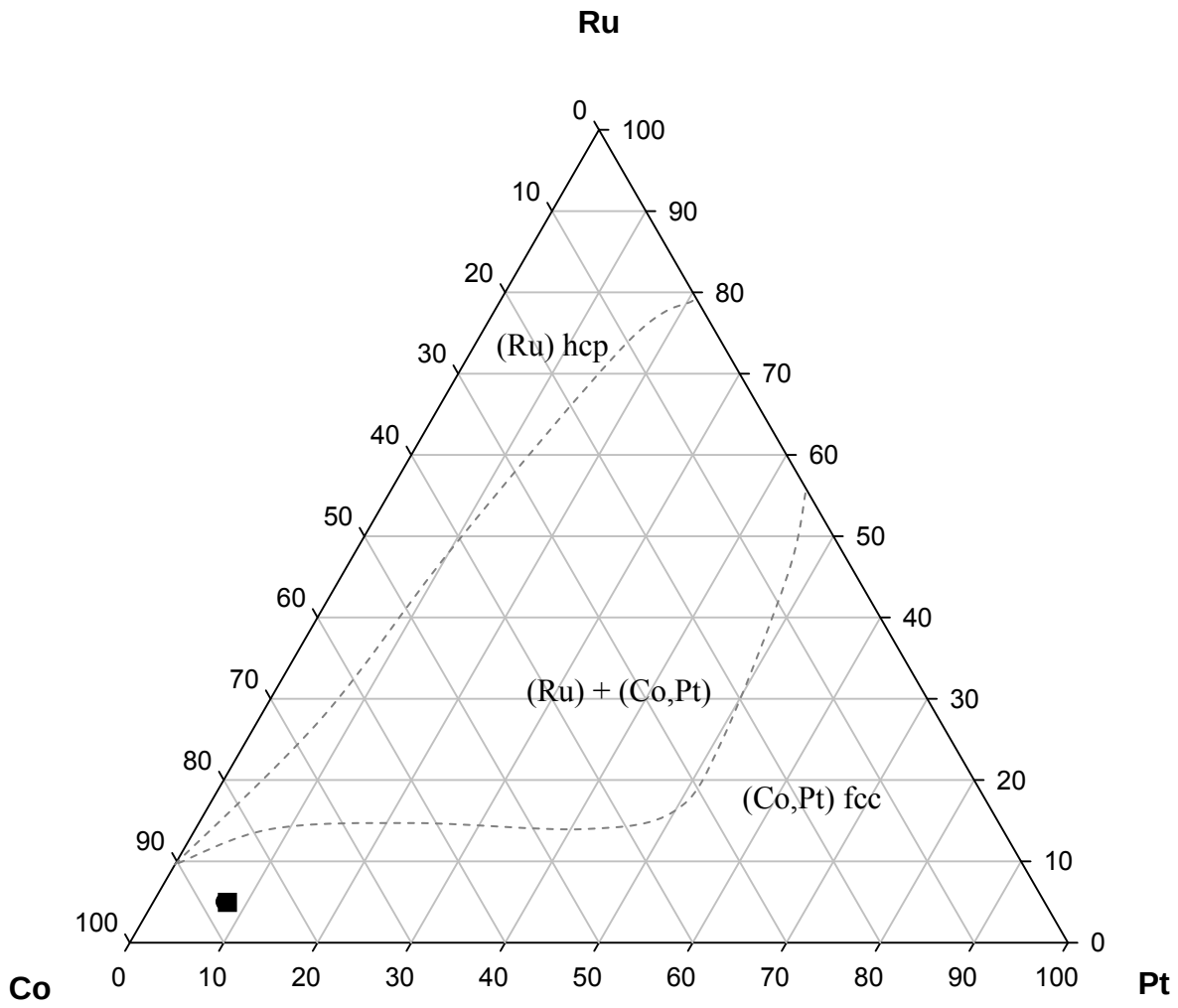


Figure 4.107. EDS analyses of LG13 (Nominal Co_{90}:Pt_5:Ru_5) in the heat treated condition (at.%).

Table 4.39. Unidentified peaks formed after heat treatment.

2θ	**Intensity**
19.5	100
21	50
26.8	50

LG 14 (Nominal Co_{80}:Pt_{10}:Ru_{10})

LG 14 (Nominal Co_{80}:Pt_{10}:Ru_{10}) appears as a single phase alloy, with just discernable fine precipitates (Figure 4.108) but was identified as containing both ε(Co) and fcc (Co,Pt) by XRD analyses (Figure 4.109). The two-phase microstructure could be very fine. Figure 4.110 show a good fit for εCo and Pt after shifting the identifying lines. Some unidentified peaks were found and are shown in Table 4.41. Figure 4.111 shows the XRD spectrum with the shifted peaks overlaid, where Pt peaks were used for the fcc solid solution. The signal to background ratio is fairly high and the peaks are quite wide. The EDS analyses is shown in Table 4.40 and plotted in Figure 4.112.

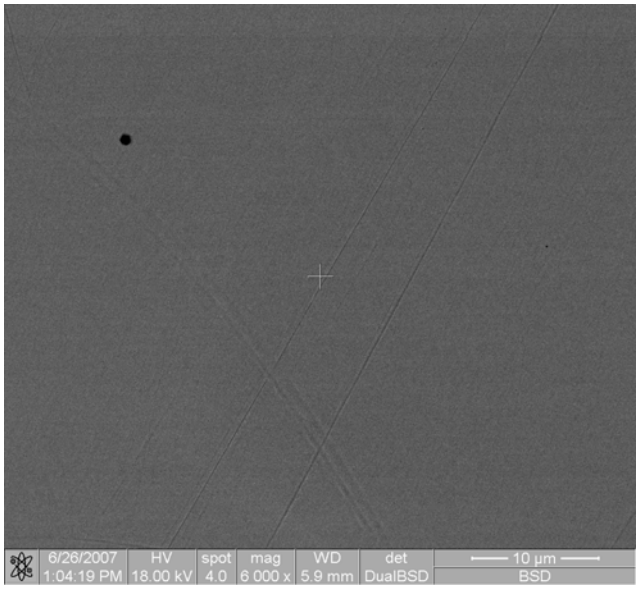
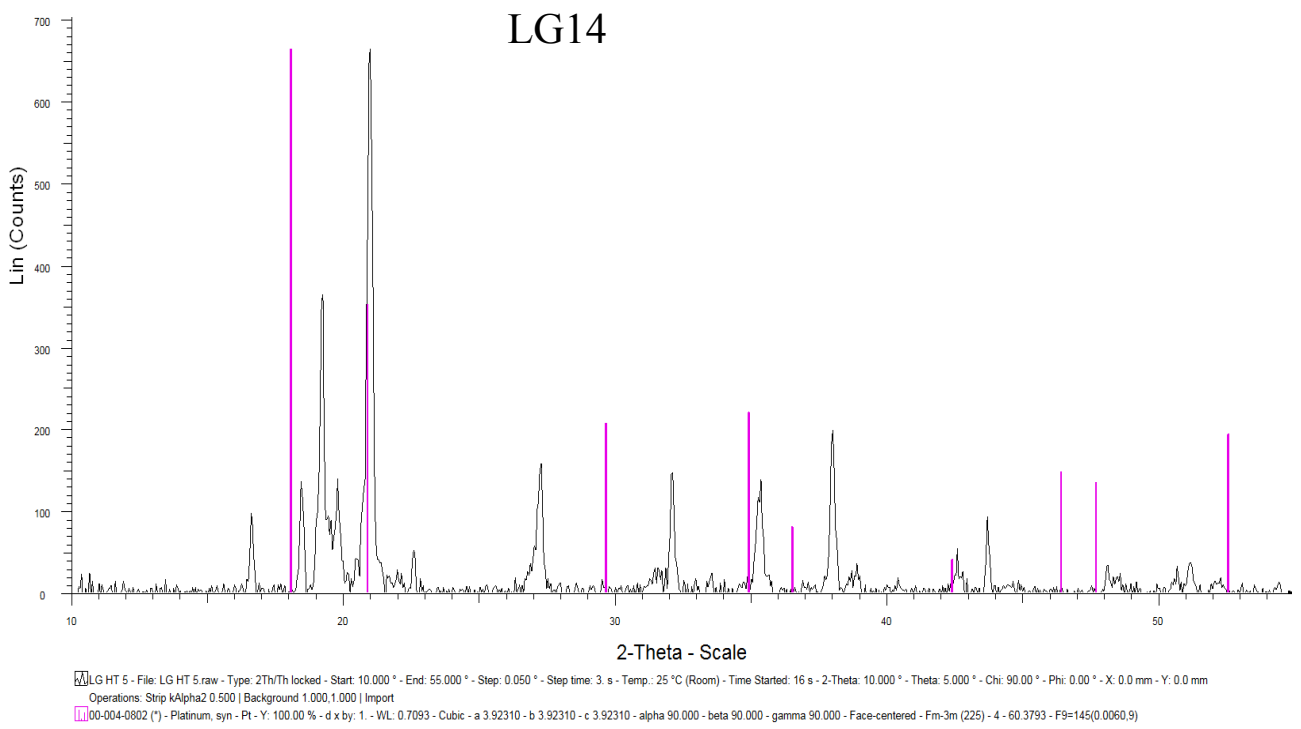


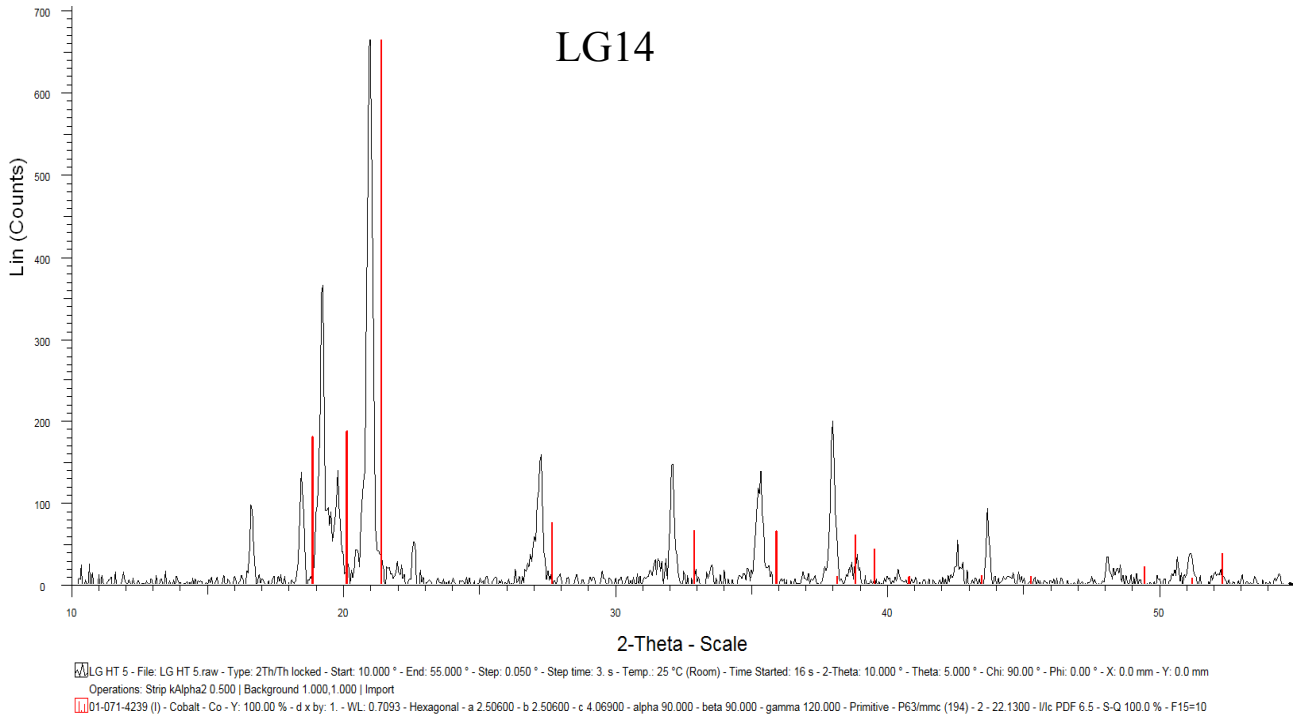
Figure 4.108. BEI of LG 14 (Nominal Co_{80}:Pt_{10}:Ru_{10}) in the heat treated and water quenched condition showing a grey matrix containing ε(Co)and fcc(Co,Pt).

Table 4.40. Analyses of LG14 (Nominal Co_{80}:Pt_{10}:Ru_{10}) in the heat treated condition (at.%).

Phase description	Pt (at.%)	Ru (at.%)	Co (at.%)	Phase	Phase Proportion (%)
Overall	10.9 ± 1.2	7.5 ± 1.3	81.6 ± 1.5	ε(Co) + fcc(Co,Pt)	-

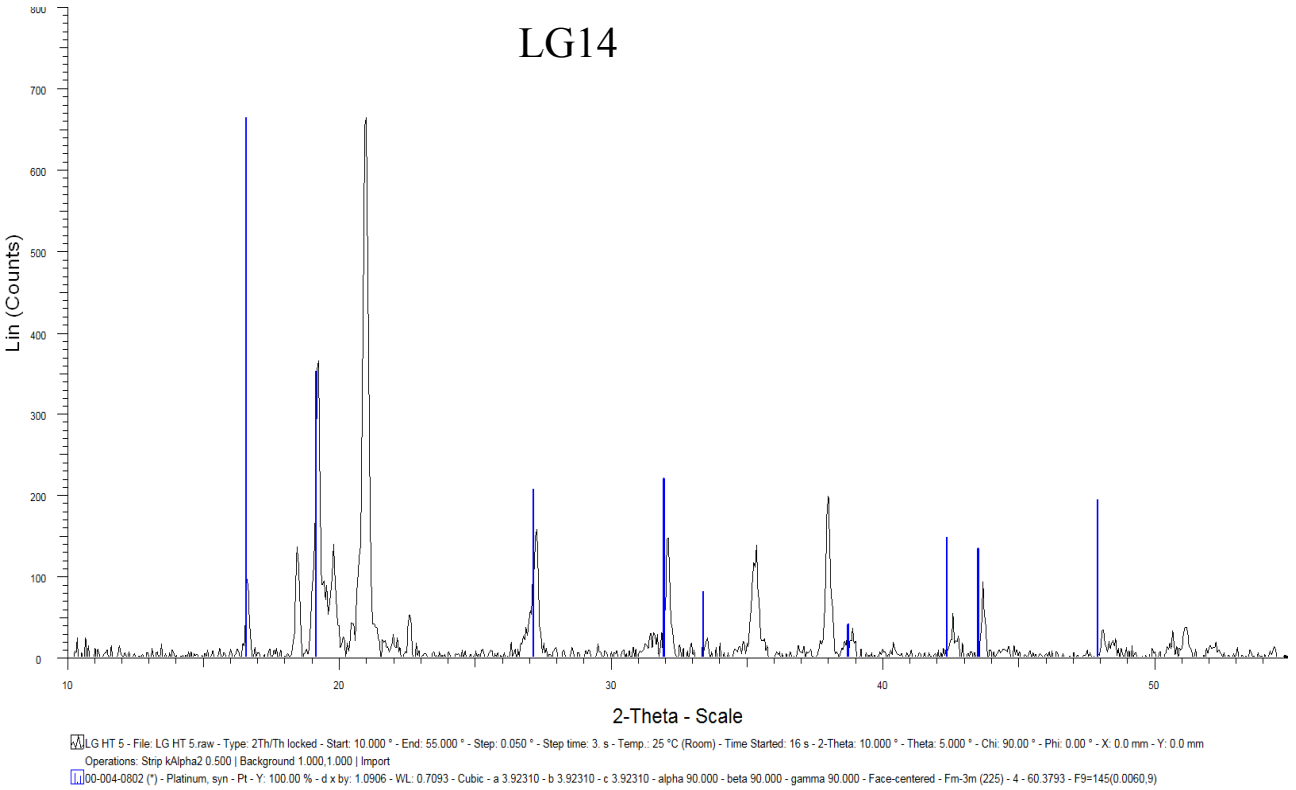


a)

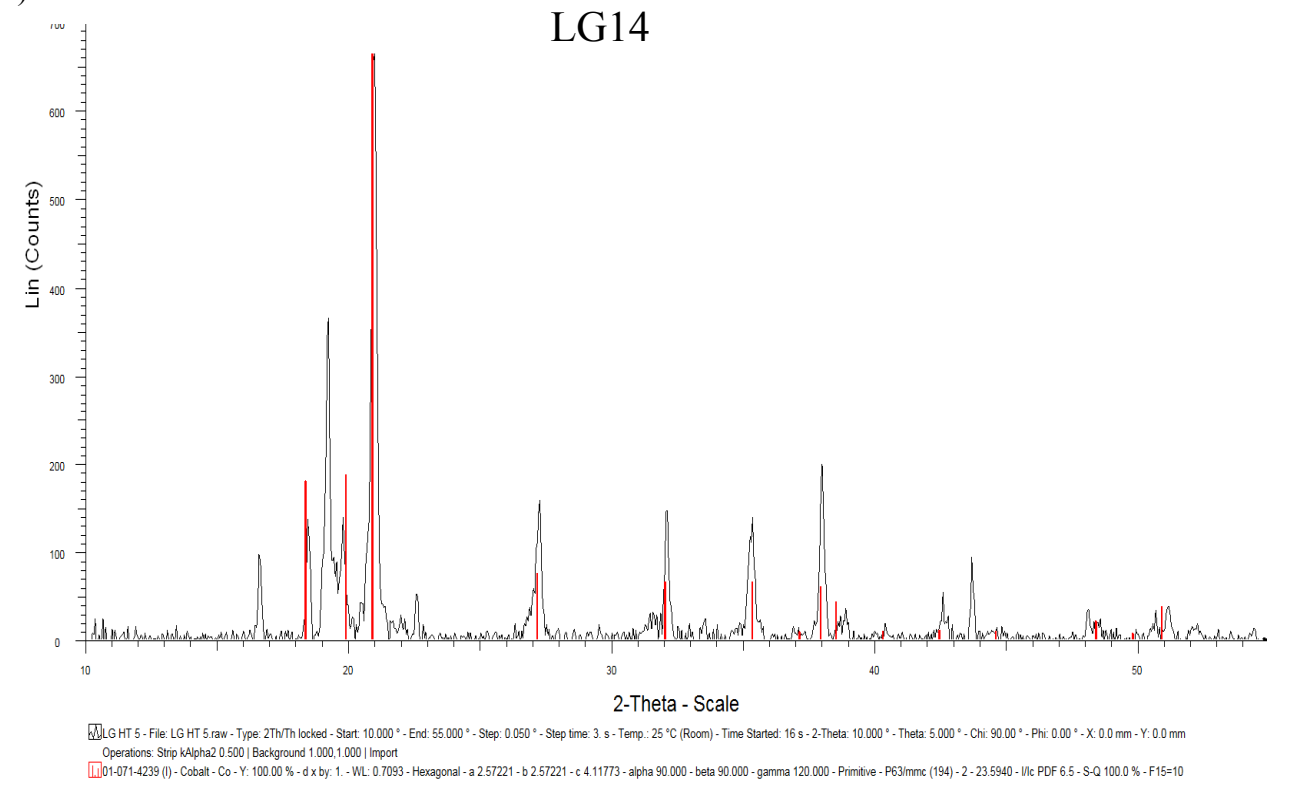


b)

Figure 4.109. XRD spectrum of LG14 (Nominal Co_{80}:Pt_{10}:Ru_{10}*) in the heat treated condition showing a comparison with a) Pt and b)* εCo.



a)



b)

Figure 4.110. XRD spectrum of LG14 (Nominal Co_{80}:Pt_{10}:Ru_{10}*) in the heat treated condition showing a comparison with a) Pt and b) εCo after shifting.*

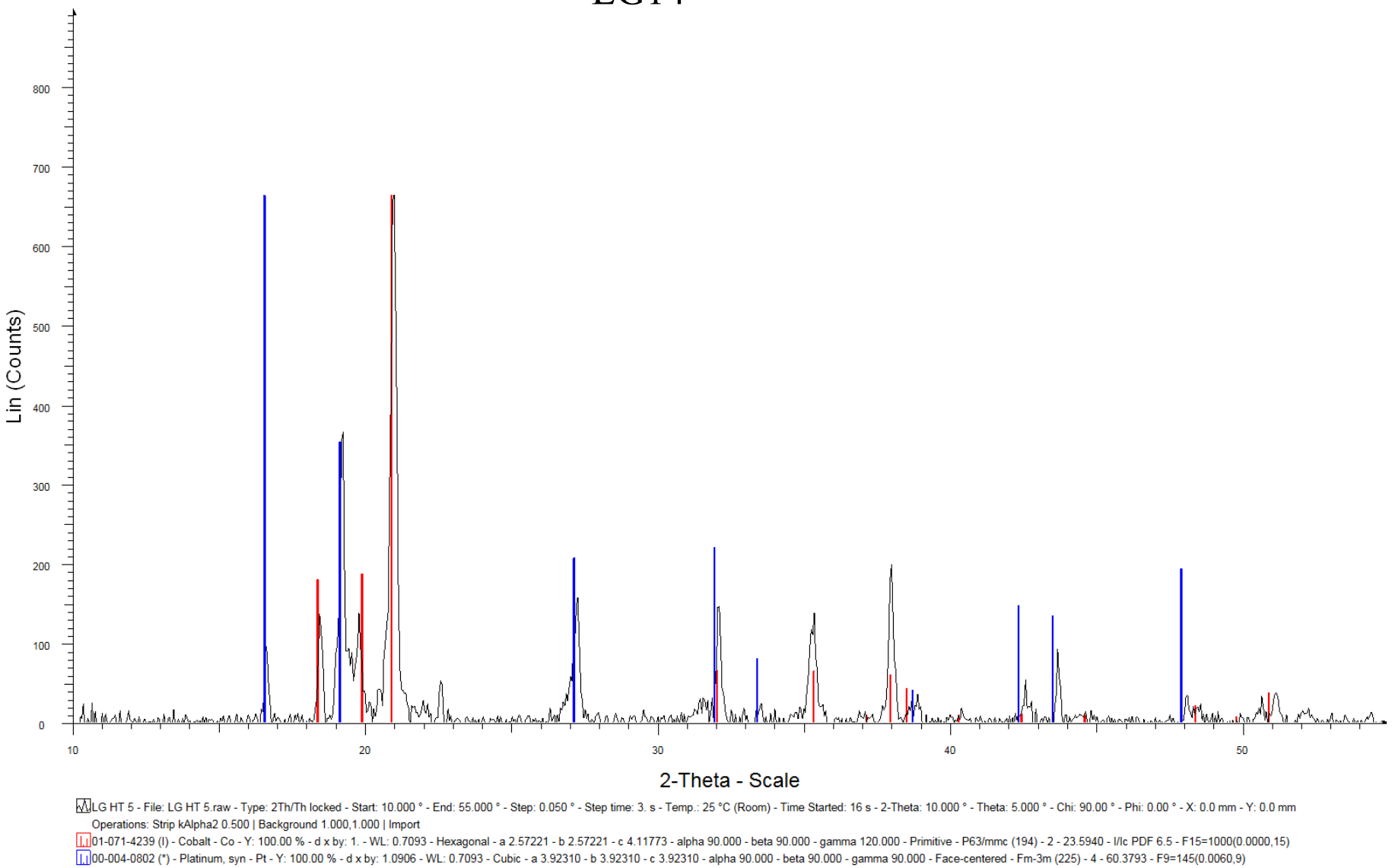


Figure 4.111. XRD spectrum of LG 14 (Nominal Co_{80}:Pt_{10}:Ru_{10}) in the heat treated condition with both εCo and Pt overlaid.

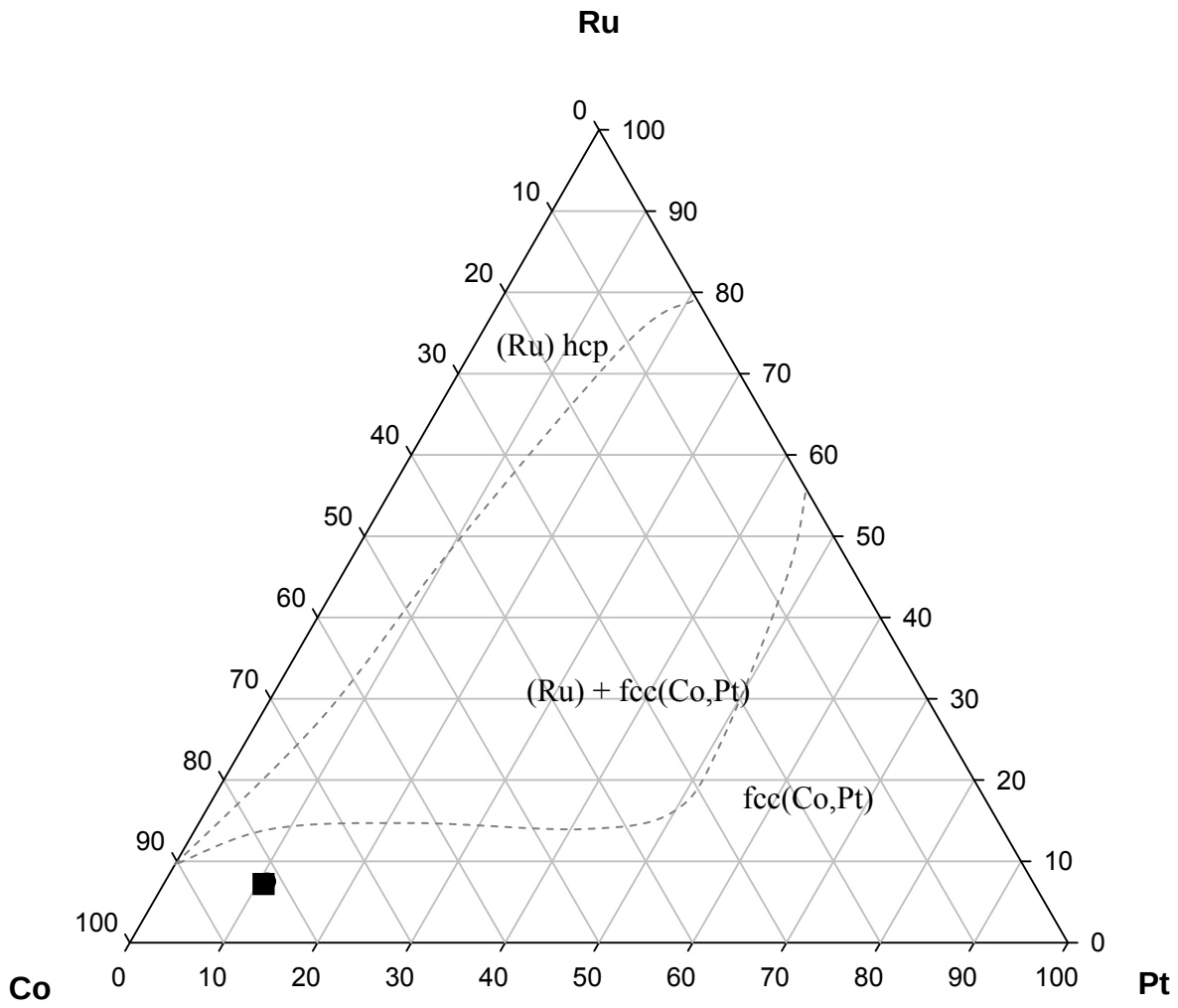


Figure 4.112. EDS analyses of LG 14 (Nominal Co_{80}:Pt_{10}:Ru_{10}) in the heat treated condition (at.%).

Table 4.41. Unidentified peaks formed after heat treatment.

2θ	**Intensity**
22	100
22.5	25
26.2	25
31.5	50

LG 15 (Nominal Co_{30}:Pt_{20}:Ru_{50})

LG 15 (Nominal Co_{30}:Pt_{20}:Ru_{50}) consisted of two phases as shown in the micrograph in Figure 4.113. The black shapes visible in the micrograph are porosity. The dark phase was identified as the (Ru) phase, and appeared mostly as a needle-like structure. The light matrix consisted of fcc(Co,Pt). The needles varied considerably in size as shown in Figure 4.113. The phases were identified through XRD analyses as (Ru) and fcc(Co,Pt) as shown in the Figure 4.114. Figure 4.115 shows the XRD spectrum with the shifted lines. Figure 4.116 shows the XRD spectrum with the (Ru) and fcc(Co,Pt) peaks overlaid. Unidentified peaks are visible and shown in Table 4.43. The peak at $2\theta \approx 13°$ is associated the plasticene in which the sample was mounted for XRD analysis. The EDS analyses are shown in Table 4.42 and the actual compositions are plotted in Figure 4.117. The medium phase in Table 4.42 consists of a fine mixture of the light matrix and the dark needles. The overall composition did not lie on a tie-line, which shows, together with the unidentified XRD lines, that there might be a third phase (perhaps the fine needles).

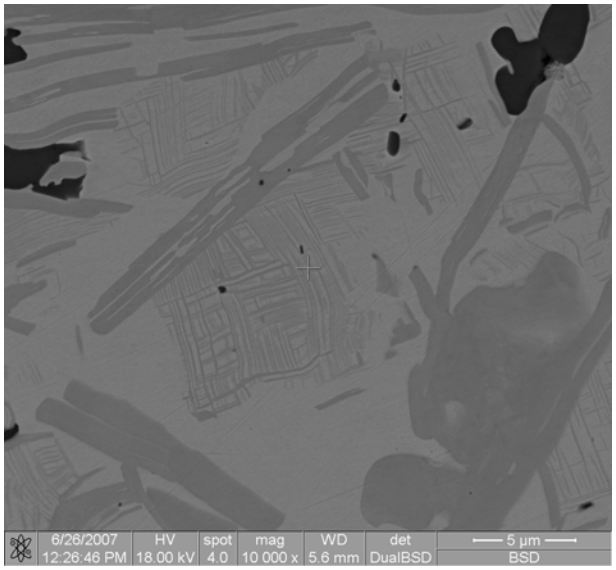
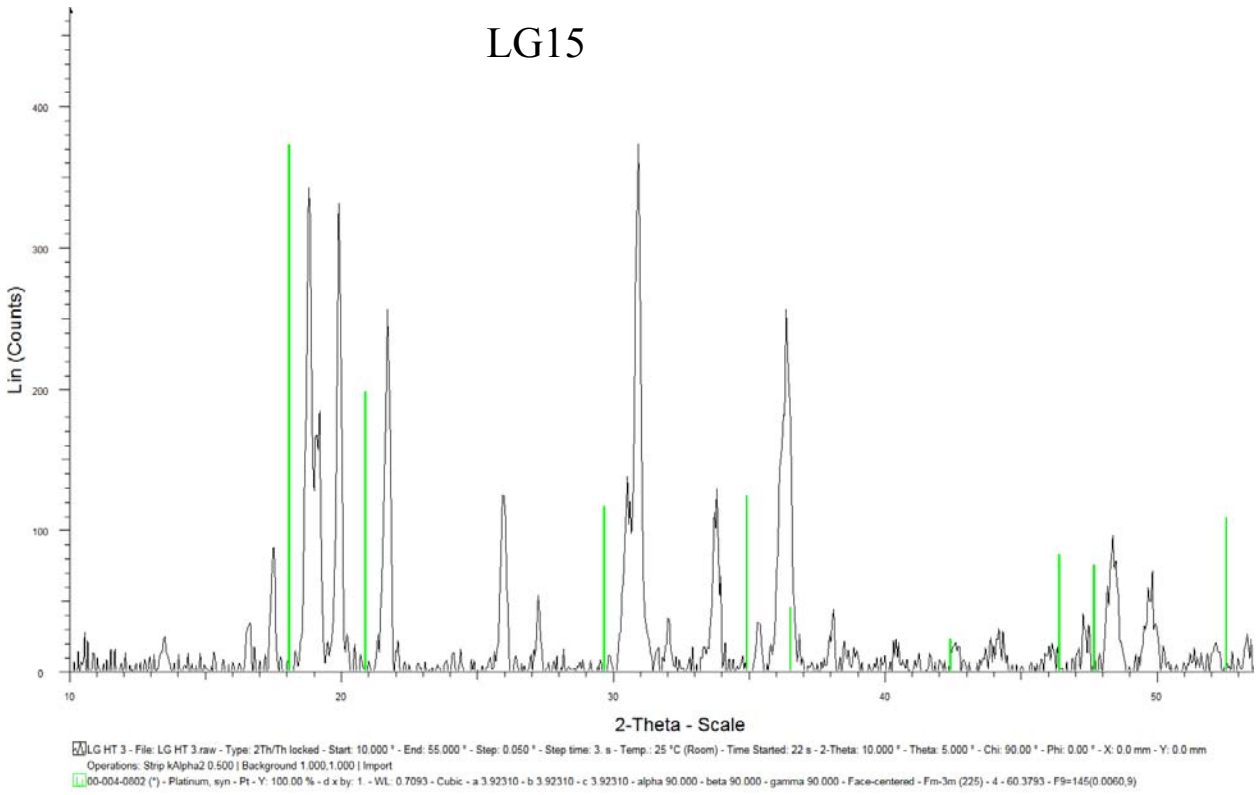


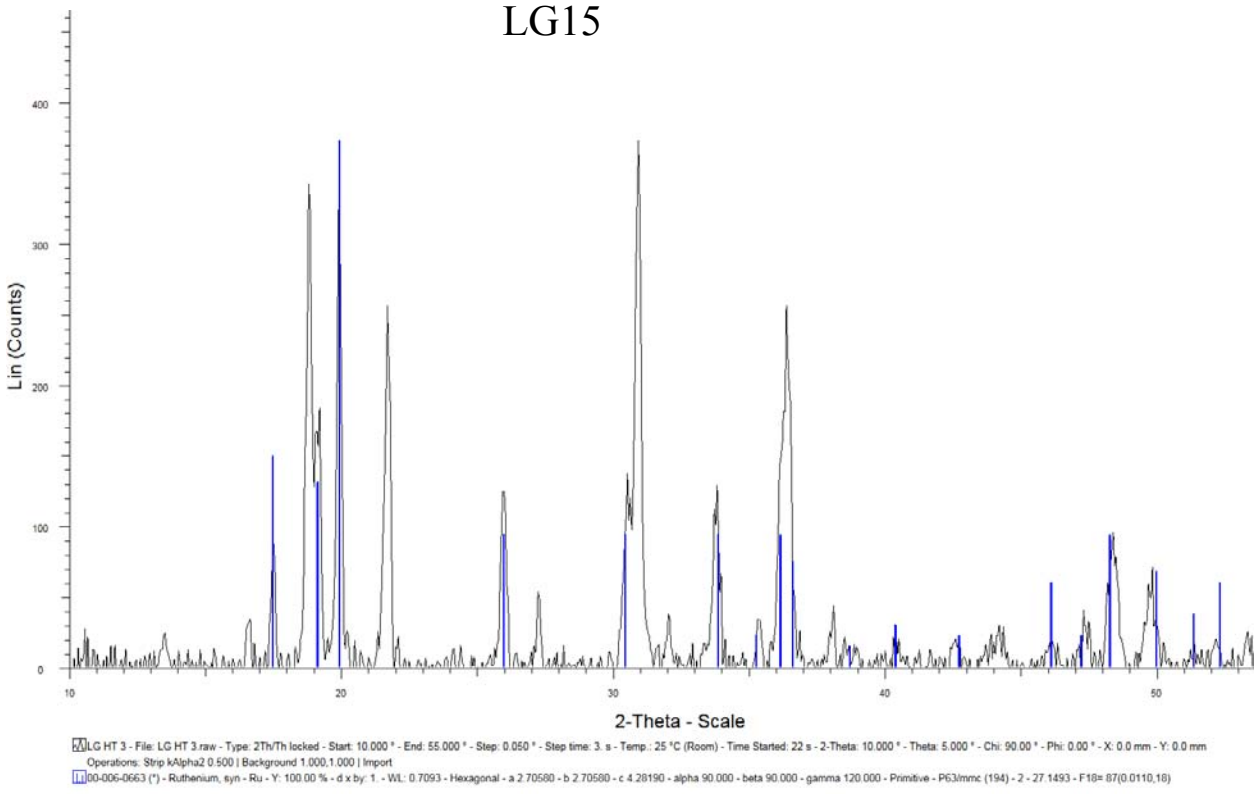
Figure 4.113. BEI of LG 15 (Nominal Co_{30}:Pt_{20}:Ru_{50}) in the heat treated condition showing light matrix fcc(Co,Pt) with dark second phase (Ru).

Table 4.42. EDS analyses of LG15 (Nominal Co_{30}:Pt_{20}:Ru_{50}) in the heat treated condition (at.%).

Phase description	Pt (at.%)	Ru (at.%)	Co (at.%)	Phase	Phase Proportion (%)
Overall	20.4 ± 0.6	55.7 ± 0.5	23.9 ± 0.7	-	-
Light	44.1 ±1.2	11.6 ± 1.3	44.3 ± 1.6	fcc(Co,Pt)	~30
Medium	33.6 ± 0.1	31.3 ± 0.4	35.1 ± 0.3	(Ru) + fcc(Co,Pt)	~30
Dark	15.4 ± 1.9	70.3 ± 2.1	14.3 ± 2.3	(Ru)	~40

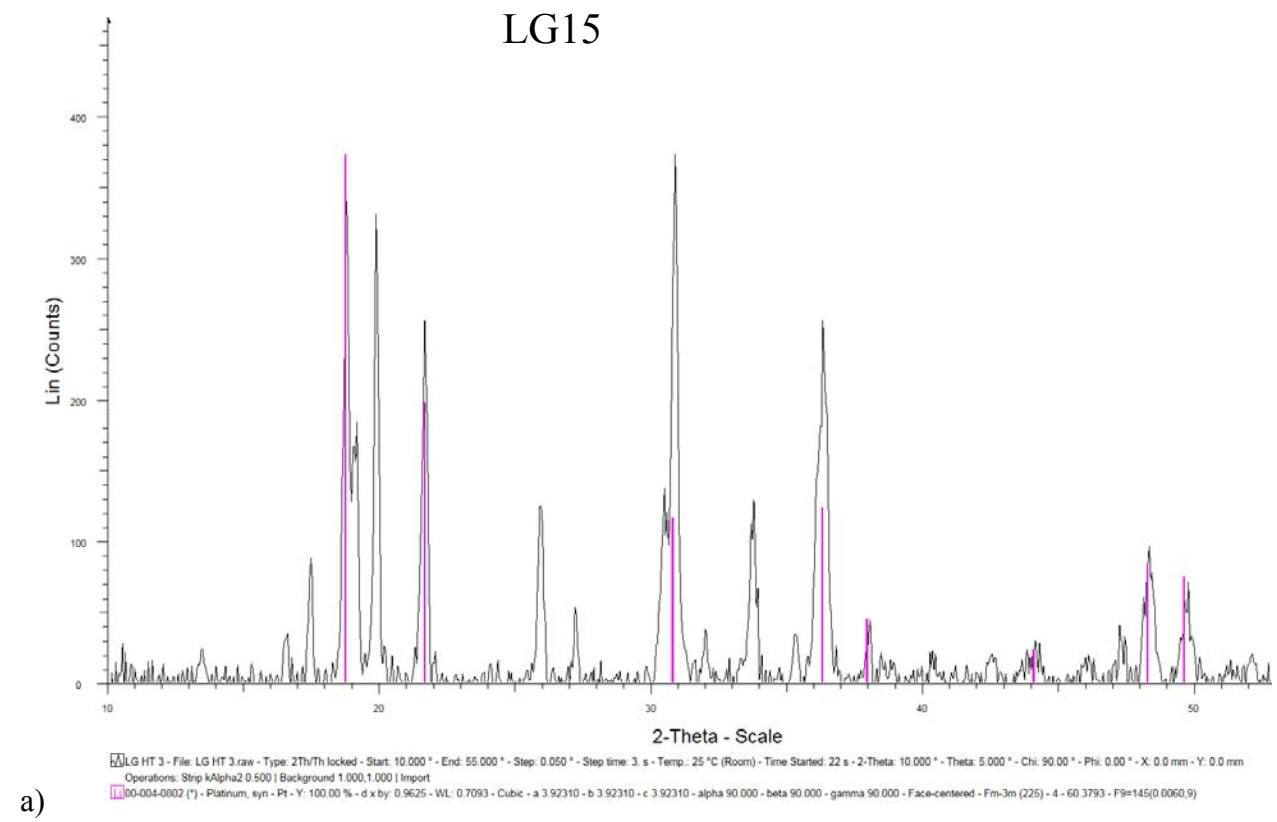


a)

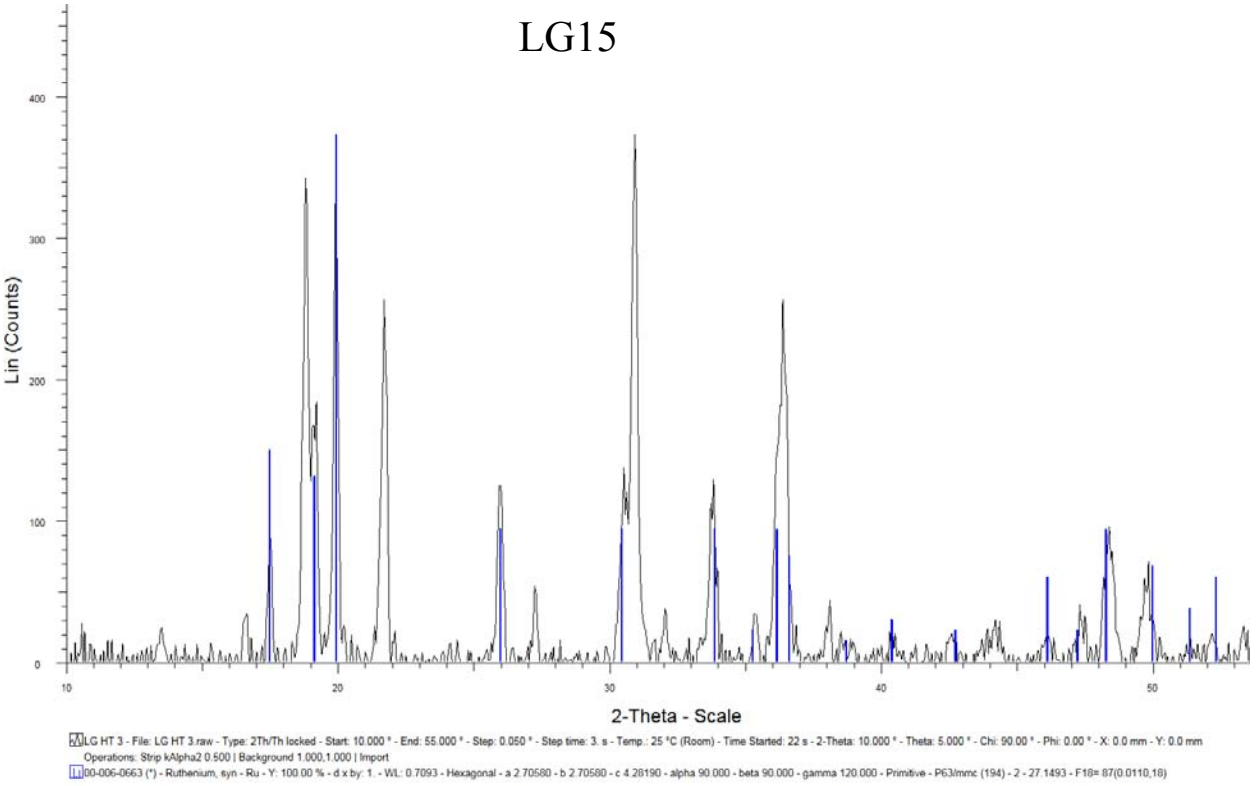


b)

Figure 4.114. XRD spectrum of LG 15 (Nominal Co_{30}:Pt_{20}:Ru_{50}) in the heat treated condition showing a comparison with a) Pt and b) Ru.



a)



b)

Figure 4.115. XRD spectrum of LG 15 (Nominal Co_{30}:Pt_{20}:Ru_{50}) in the heat treated condition showing a comparison with a) Pt and b) Ru after shifting.

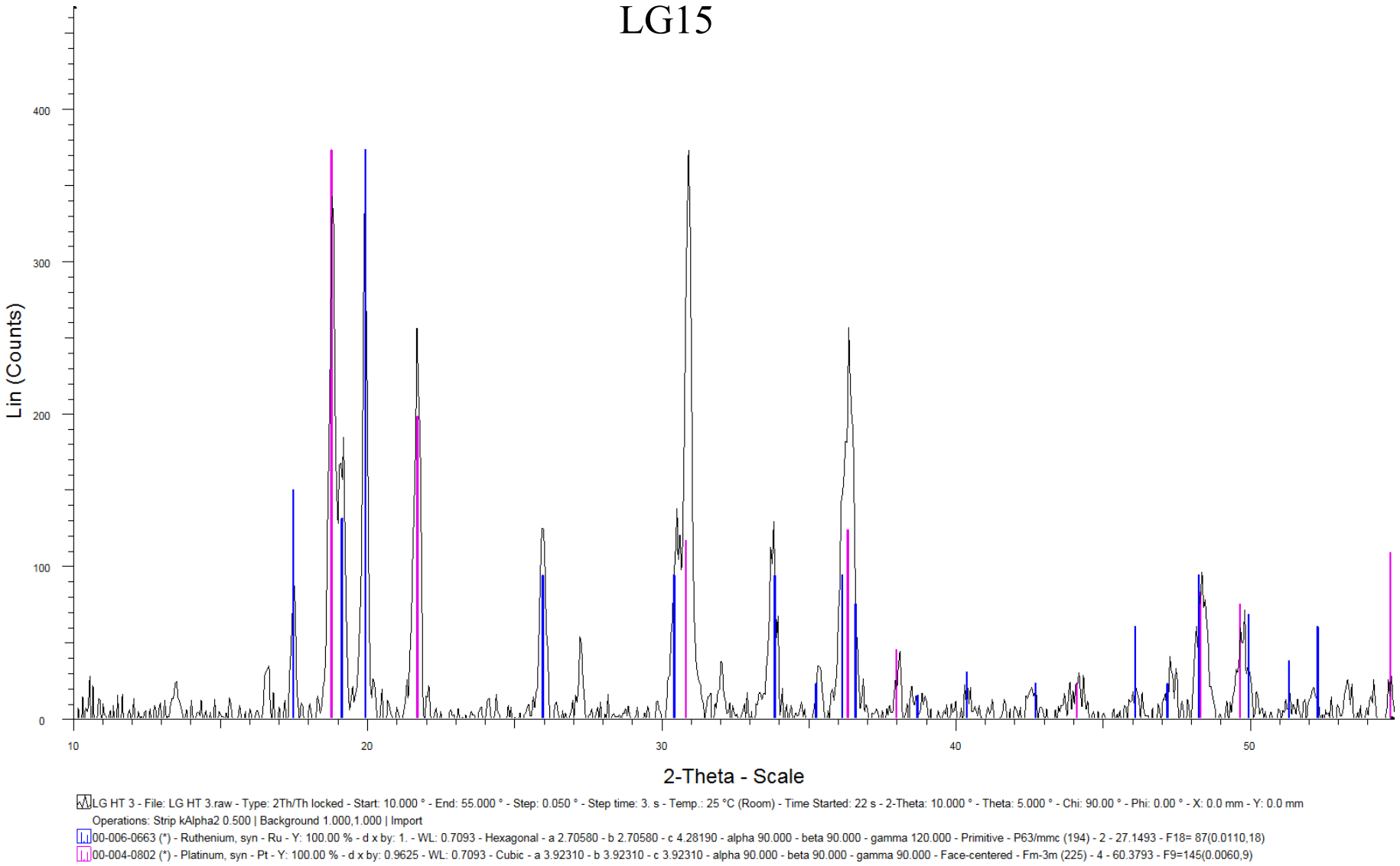


Figure 4.116. XRD spectrum of LG 15 (Nominal Co_{30}:Pt_{20}:Ru_{50}) in the heat treated condition with both Ru and Pt overlaid.

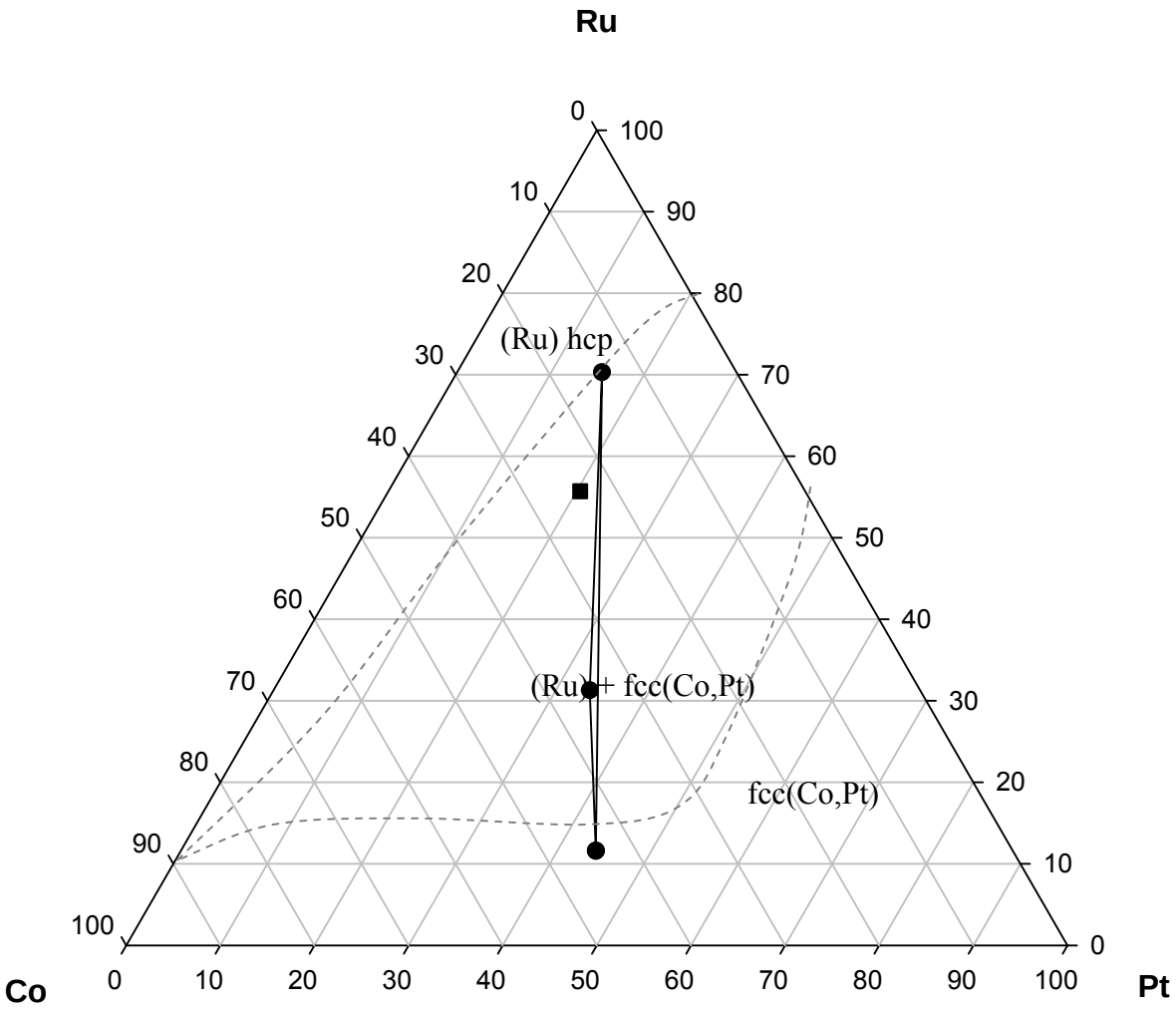


Figure 4.117. EDS analyses of LG 15 (nominal Co_{30}:Pt_{20}:Ru_{50}) in the heat treated condition (at.%).

Table 4.43 Unidentified peaks formed after heat treatment.

2θ	**Intensity**
16.5	30
27	50
32	30

LG 16 (Nominal Co_{60}:Pt_{20}:Ru_{20})

LG 16 (NominalCo_{60}:Pt_{20}:Ru_{20}) consisted of two phases as shown in the micrograph in Figure 4.118: dark needle-like (Ru) in a light fcc(Co,Pt) matrix. This was confirmed by XRD, and the spectrum is shown in Figure 4.119. Figure 4.120 shows the spectrum with the shifted Ru and Co lines, and Figure 4.121 shows the XRD spectrum with the Ru and Co peaks overlaid. Unidentified peaks are visible and can be seen in Table 4.45. The peak visible at $2\theta \approx 13.5$ was identified as plasticene. The EDS analyses are shown in Table 4.44 and the actual compositions are plotted in Figure 4.122. However, the dark phase was too small to analyse (< 3μm across) and these results can only be used as an indication. The higher errors in the analyses for the overall and light phase are likely to be due to fine precipitation in the matrix, which can be discerned from Figure 4.118.

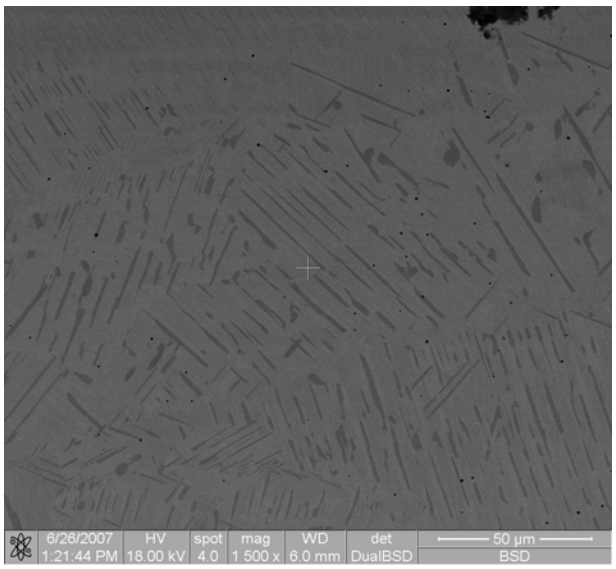
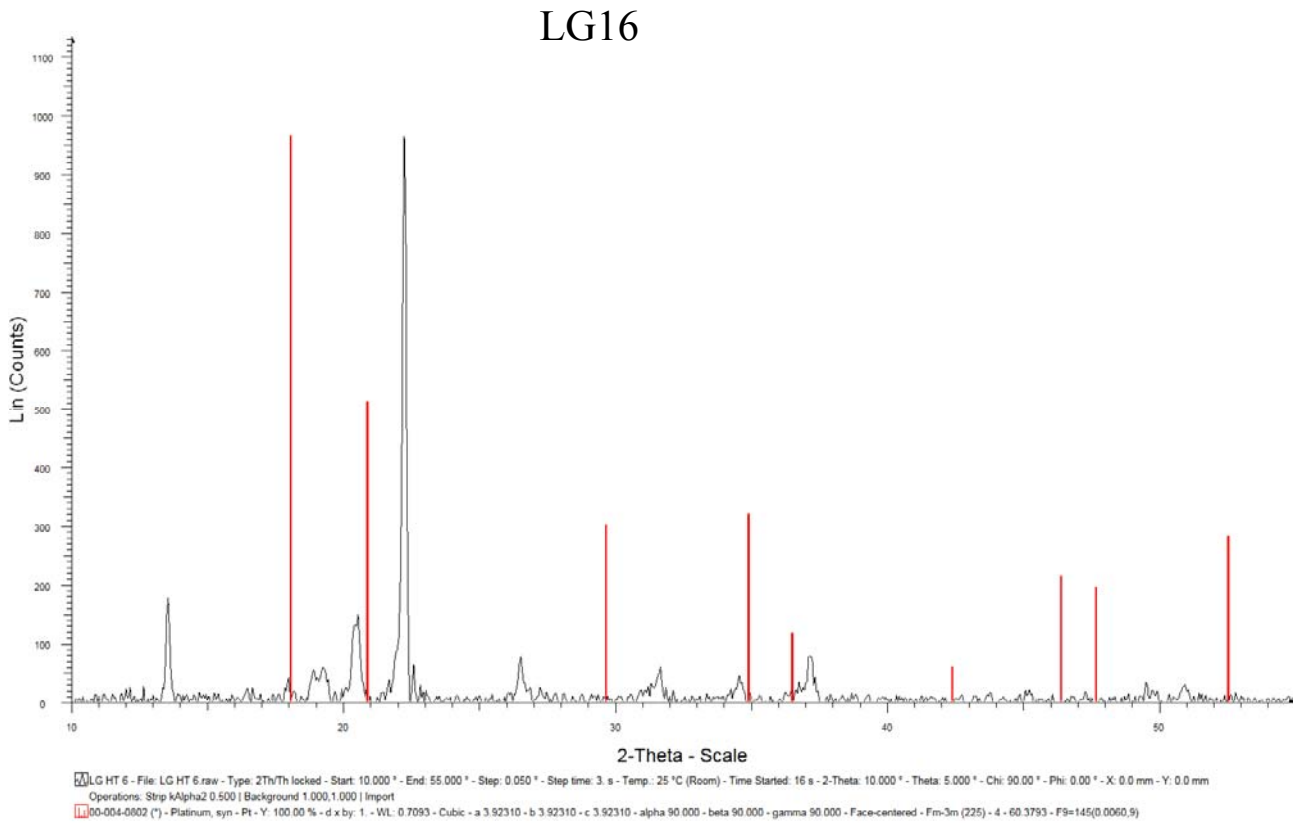


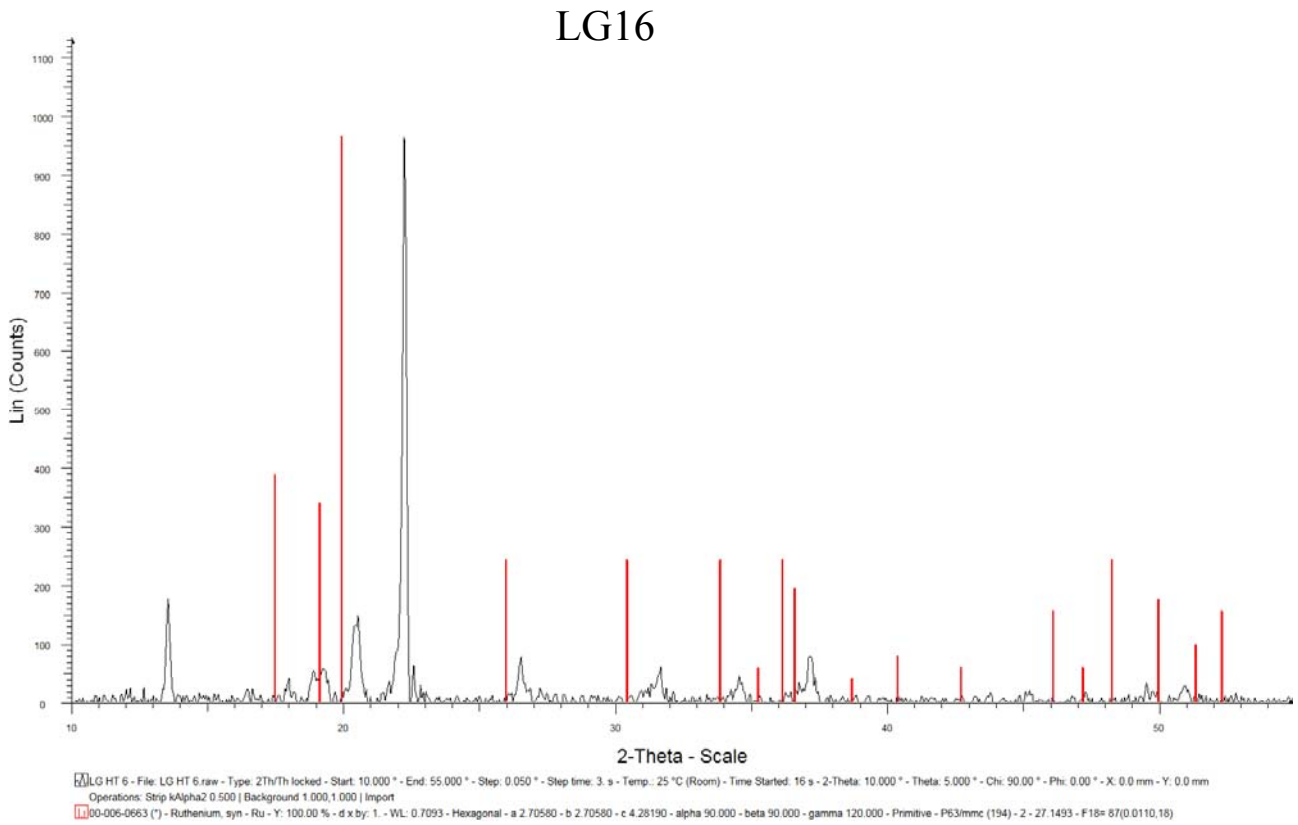
Figure 4.118. BEI of LG 16 (Nominal Co_{60}:Pt_{20}:Ru_{20}) heat treated condition showing a dark second phase (Ru) in a light matrix fcc(Co,Pt).

Table 4.44. EDS analyses of LG16 (Nominal Co_{60}:Pt_{20}:Ru_{20}) in the heat treated condition (at.%).

Phase description	Pt (at.%)	Ru (at.%)	Co (at.%)	Phase	Phase Proportion (%)
Overall	24.6 ± 2.2	14.8 ± 1.4	60.6 ± 1.0	-	-
Light	25.1 ± 1.3	16.2 ± 1.3	58.7 ± 0.6	fcc(Co,Pt)	~70
Dark	11.6 ± 0.6	46.6 ± 1.3	41.8 ± 0.3	(Ru)	~30

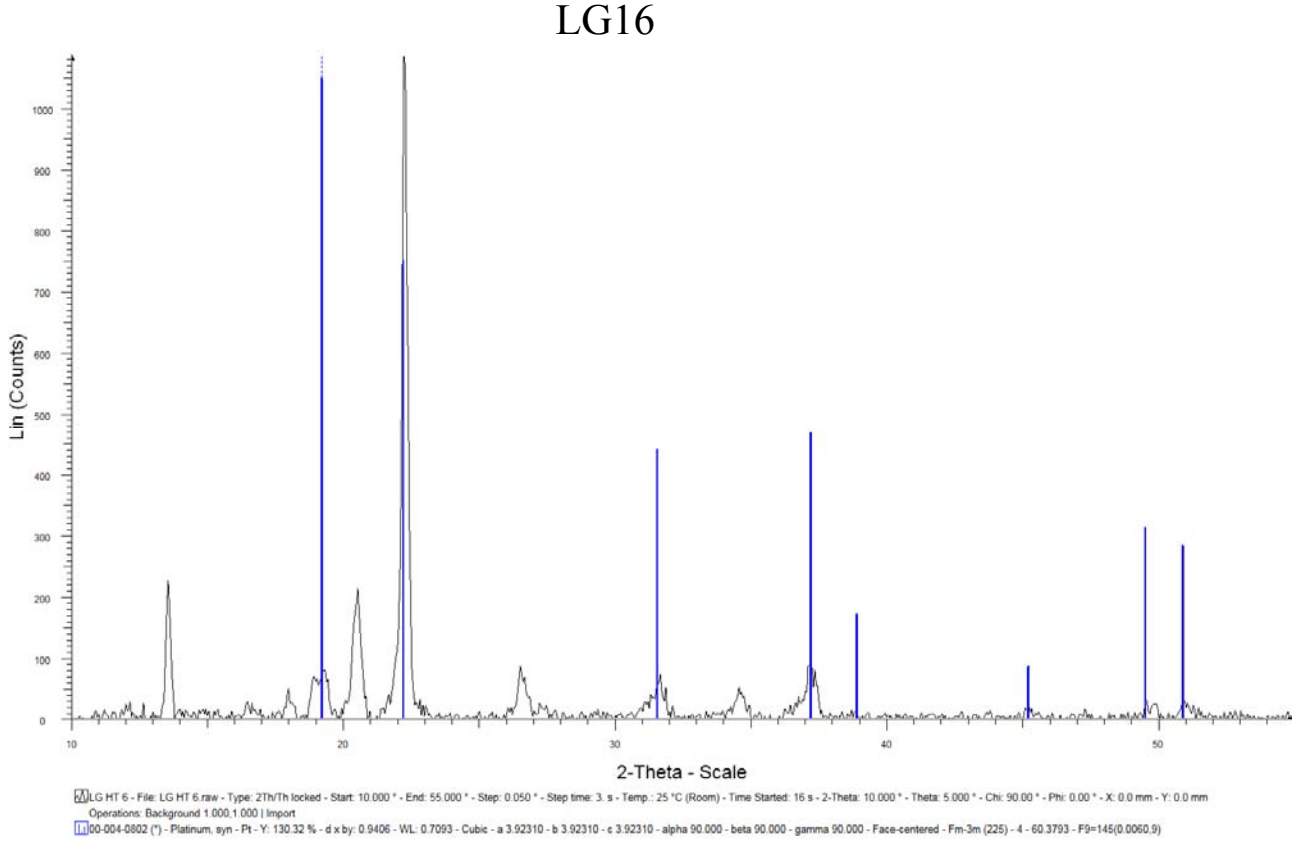


a)

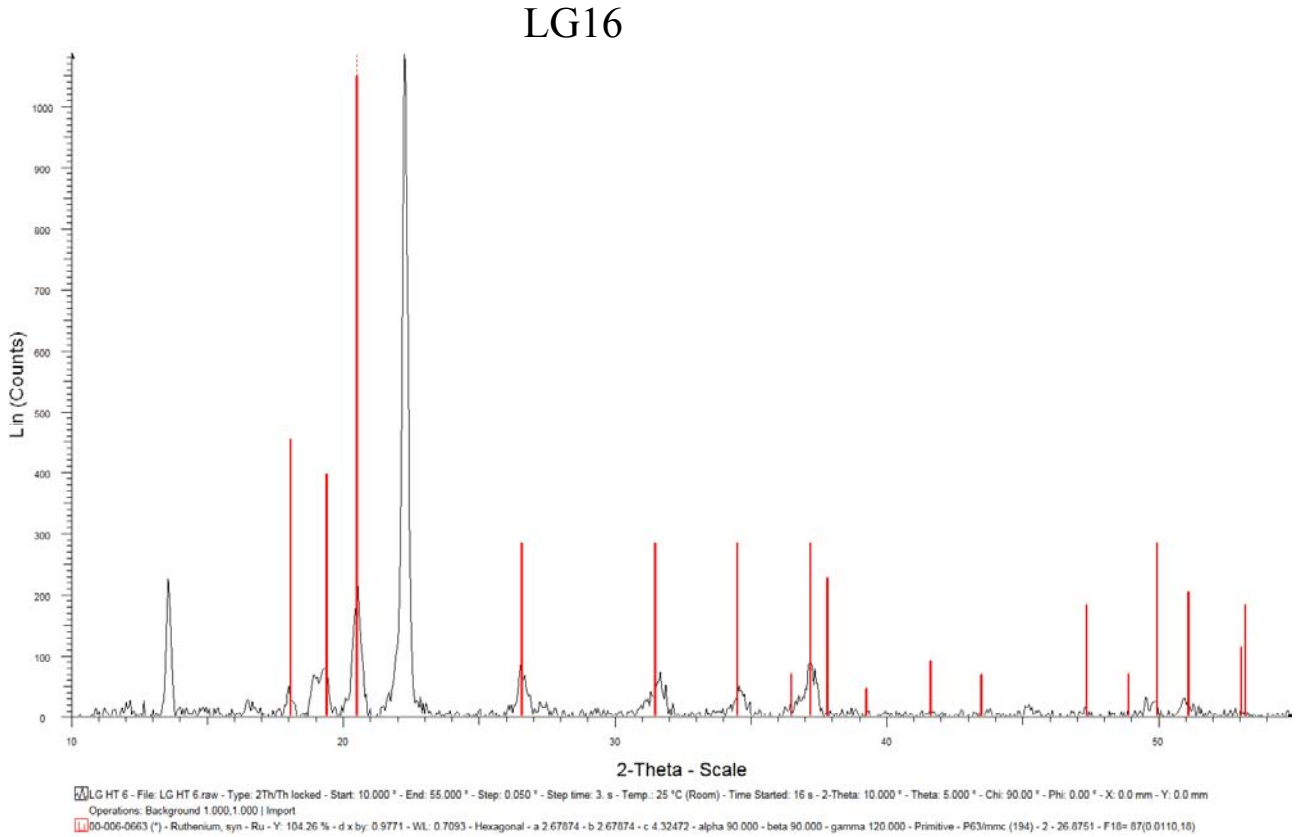


b)

Figure 4.119. XRD spectrum of LG16 (Nominal Co_{60}:Pt_{20}:Ru_{20}) in the heat treated condition showing a comparison with a) Pt and b) Ru.



a)



b)

Figure 4.120. XRD spectrum of LG 16 (Nominal Co_{60}:Pt_{20}:Ru_{20}) in the heat treated condition showing a comparison with a) Pt and b) Ru after shifting.

LG16

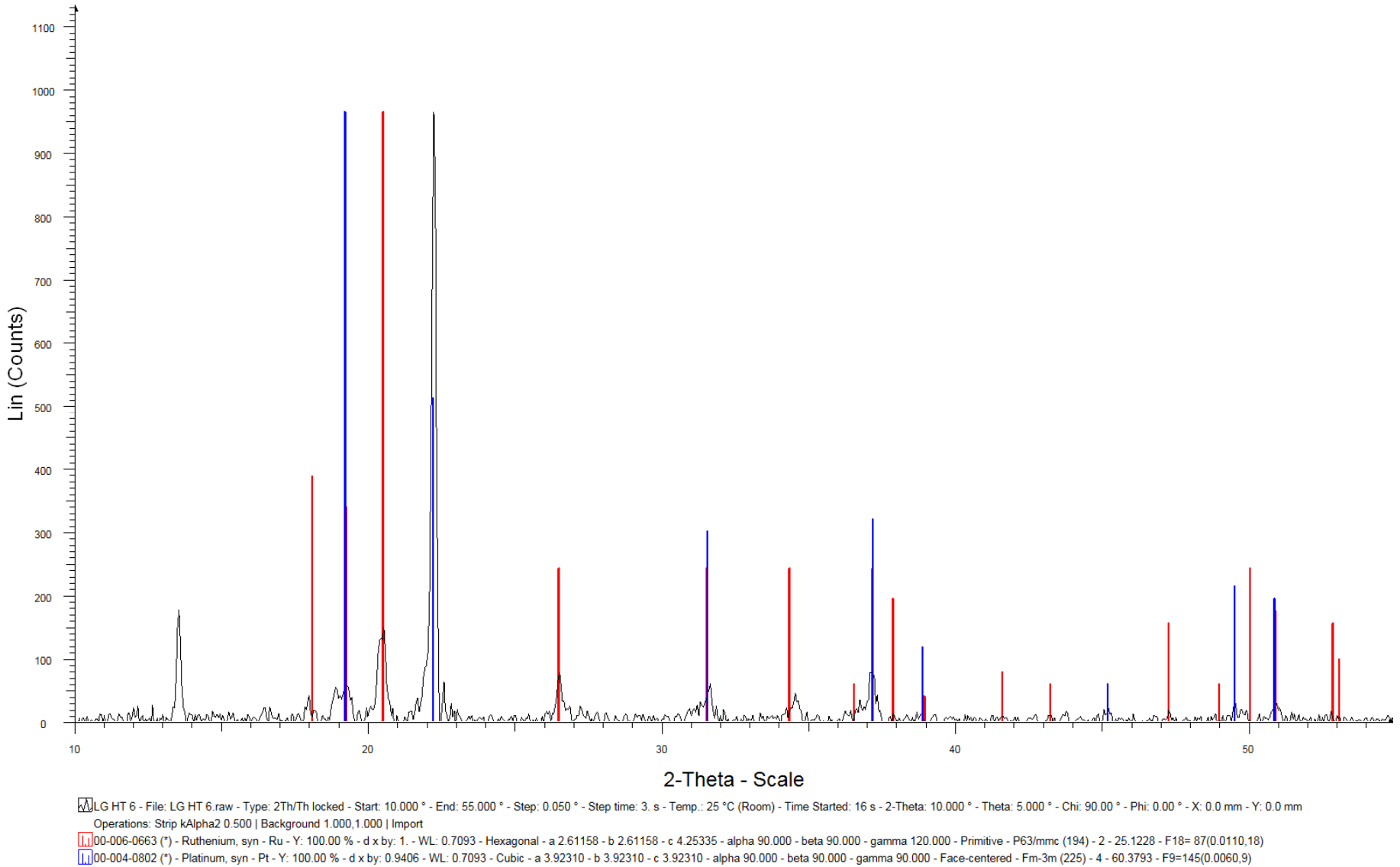


Figure 4.121. XRD spectrum of LG 16 (Nominal Co_{60}:Pt_{20}:Ru_{20}) in the heat treat condition with both Pt and Ru overlaid.

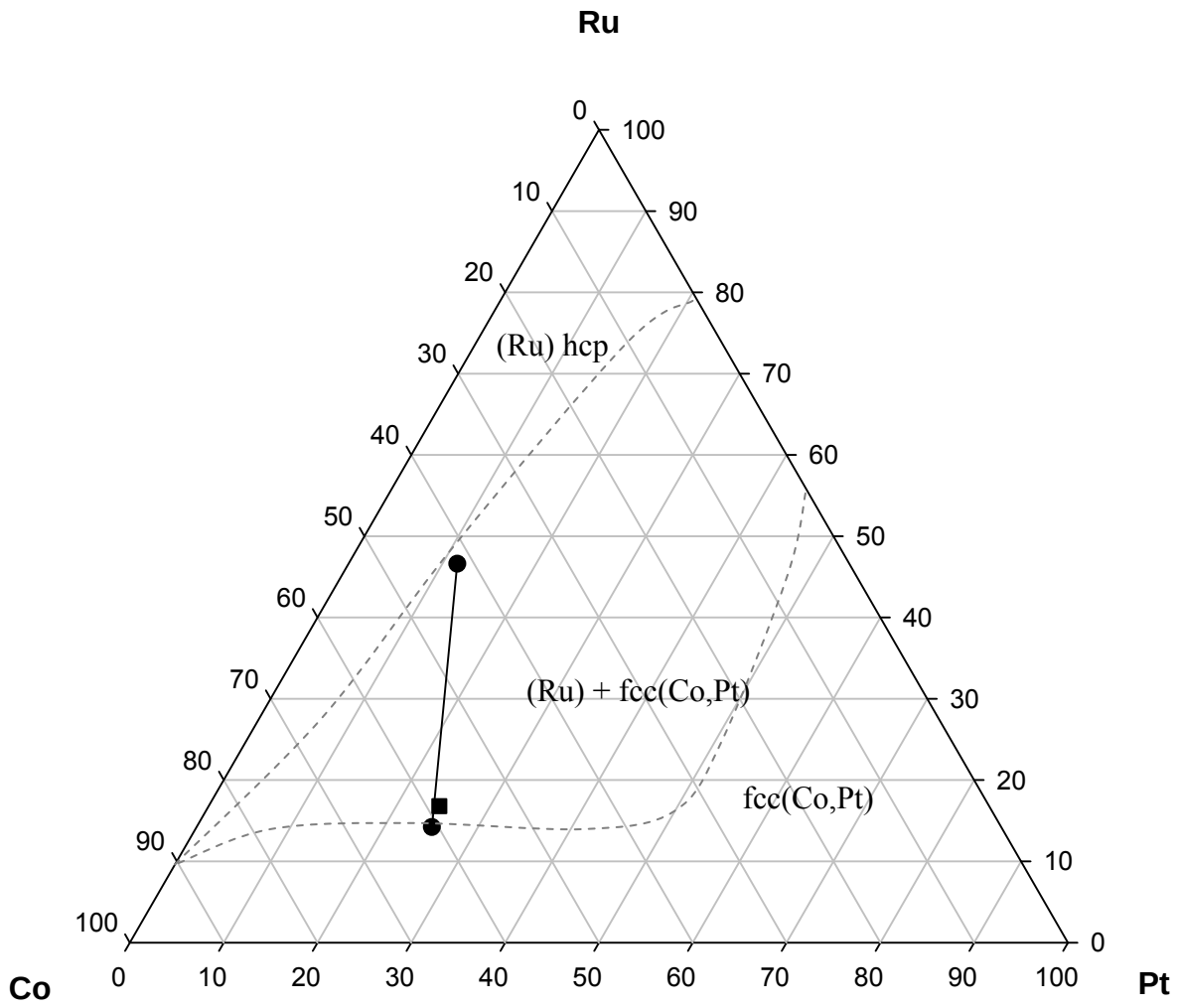


Figure 4.122. EDS analyses of LG 16 (Nominal Co_{60}:Pt_{20}:Ru_{20}) in the heat treated condition (at.%).

Table 4.45. Unidentified peaks formed after heat treatment.

2θ	**Intensity**
18.8	50
21.5	25
22.5	20
32	25

LG 17 (Nominal Co_{10}:Pt_{30}:Ru_{60})

The microstructure of LG 17 (Nominal Co_{10}:Pt_{30}:Ru_{60}) appeared to consist of three phases as shown in Figure 4.123. XRD analyses confirmed only two phases ((Ru) and fcc(Co,Pt)) and the spectrum is shown in Figure 4.124. The light phase is Pt-rich fcc(Co,Pt) and the darkest phase is (Ru), which mainly formed in the light phase. The medium dendrites consist of a mixture of the light matrix and fine (Ru) needles. Although most of the structure of the dendrites was very fine, there were some needles that could be analysed. They had the same composition as the larger dark needles (Figure 4.123). The XRD spectrum in Figure 4.125 shows the peaks after the lines were shifted. Figure 4.126 shows the XRD spectrum with the (Ru) and fcc(Co,Pt) peaks overlaid. The signal to background ratio is high and the peaks neat and narrow. A plasticene peak is visible at $2\theta \approx 13.5$. Some unidentified peaks are shown in Table 4.46. The EDS analyses are shown in Table 4.45 and the actual compositions are plotted in Figure 4.127. There were fairly high errors on some of the analyses

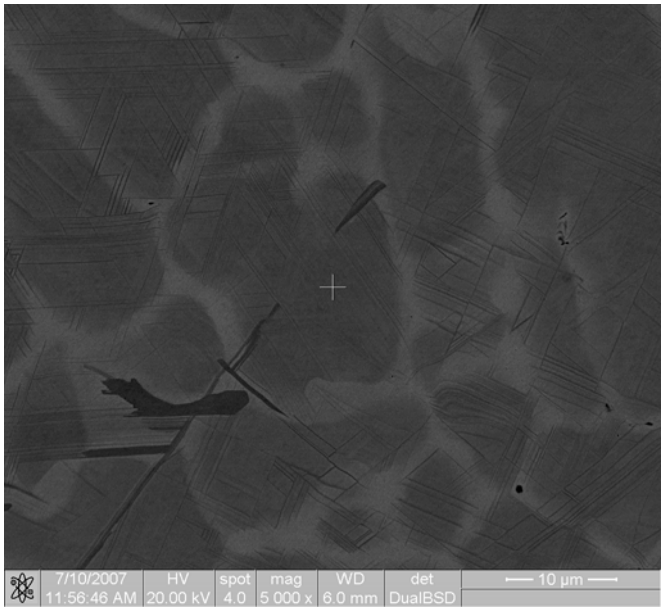
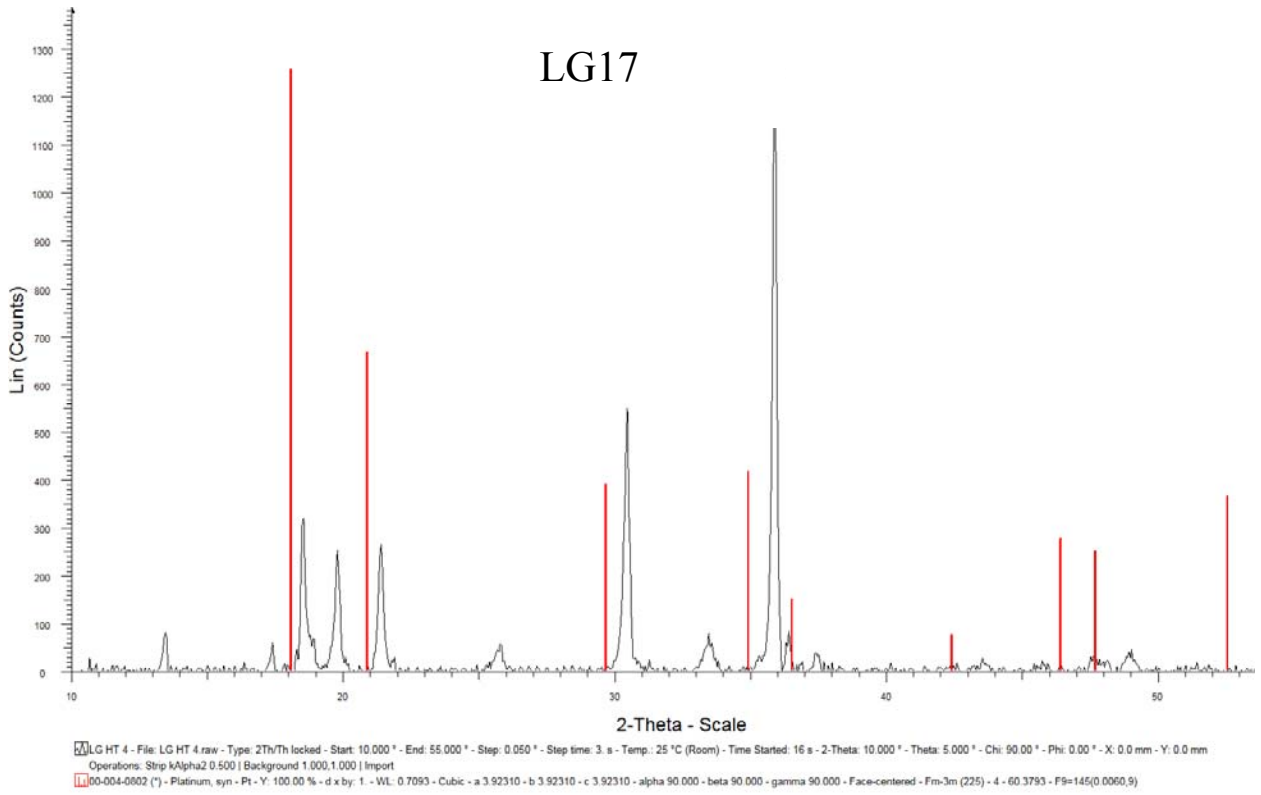


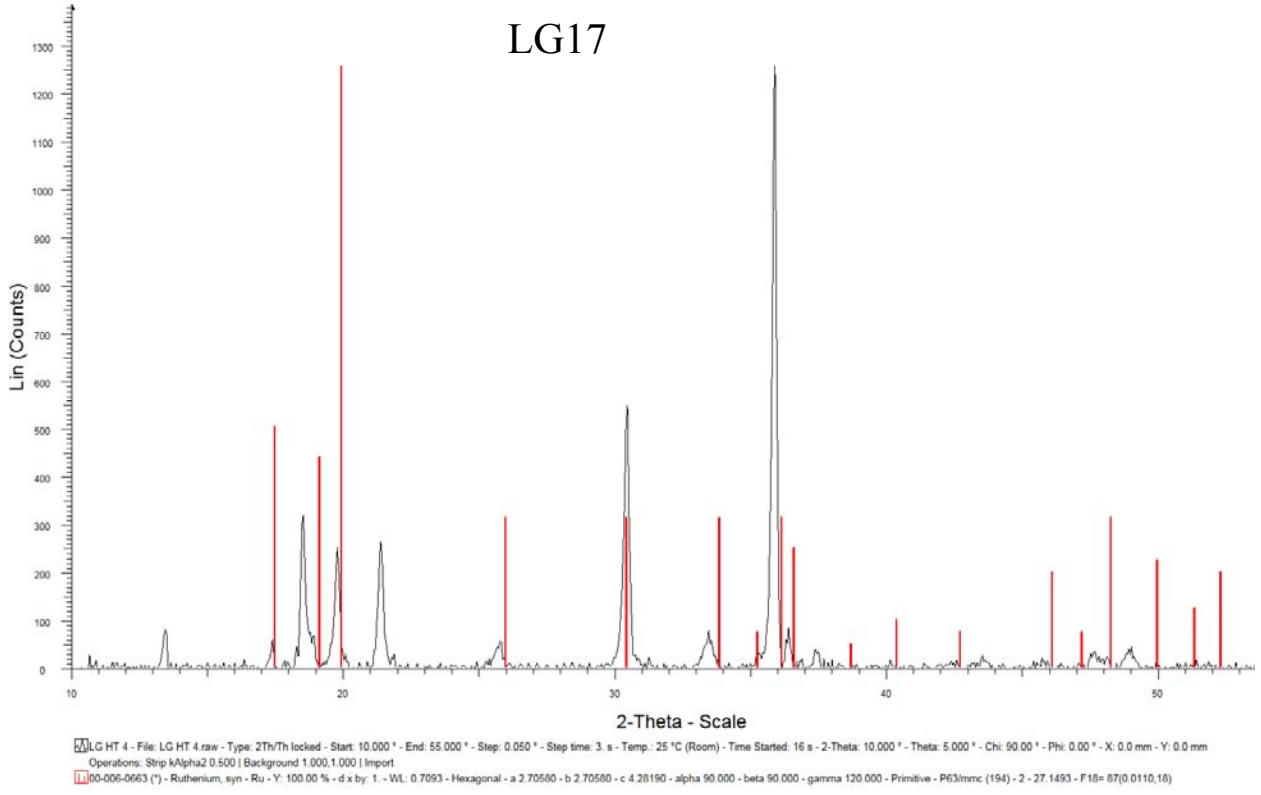
Figure 4.123. BEI of LG 17 (Nominal Co_{10}:Pt_{30}:Ru_{60}) heat treated condition showing a dark second phase (Ru) in a light matrix fcc(Co,Pt) and dark Ru needles.

Table 4.45. EDS analyses of LG 17 (Co_{60}:Pt_{20}:Ru_{20}) in the heat treated condition (at.%).

Phase description	Pt (at.%)	Ru (at.%)	Co (at.%)	Phase	Phase Proportion (%)
Overall	35.2 ± 1.2	55.0 ± 0.6	9.8 ± 0.2	-	-
Light	46.3 ± 1.3	42.2 ± 0.3	11.5 ± 0.3	fcc(Co,Pt)	~40
Medium	31.4 ± 0.6	62.6 ± 1.6	6.0 ± 1.0	(Ru) + fcc(Co,Pt)	~50
Dark needles	21.5 ± 0.2	73.6 ± 1.3	4.9 ± 2.3	(Ru)	~10

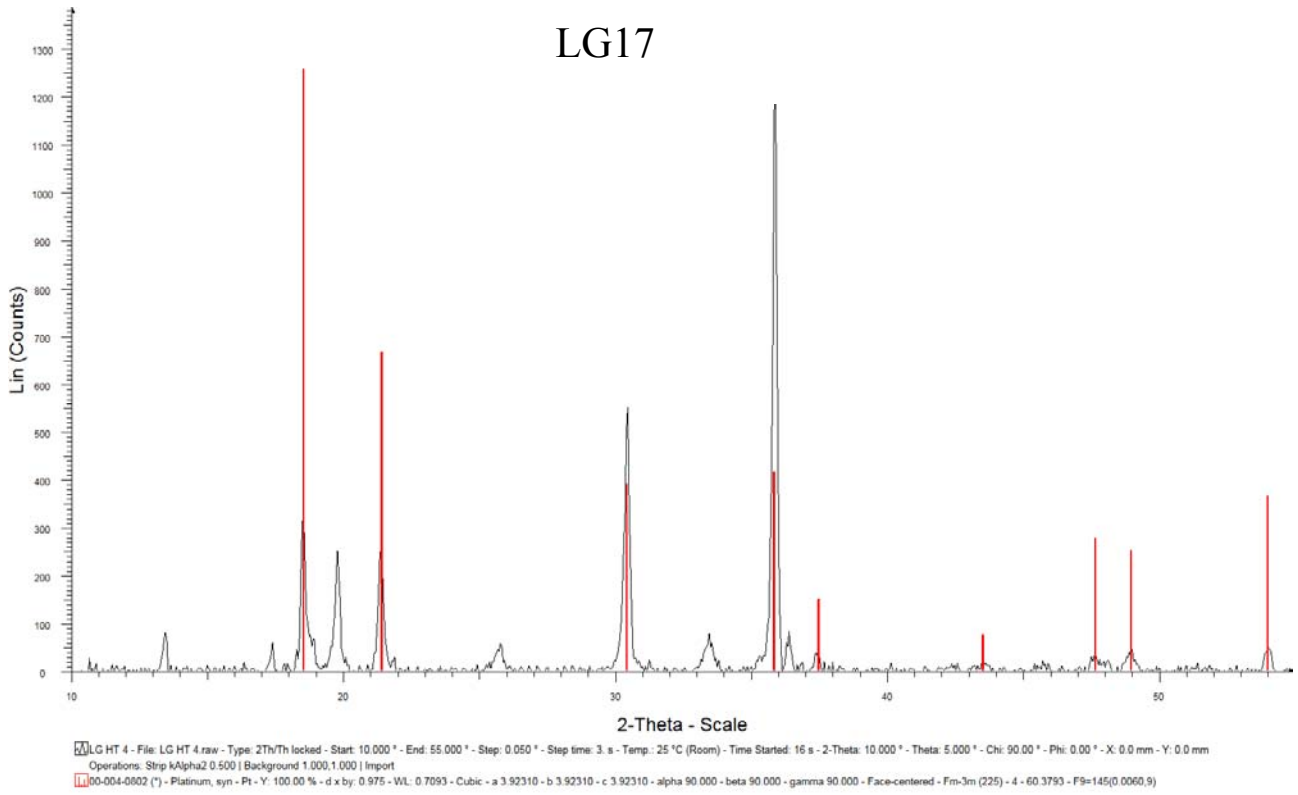


a)

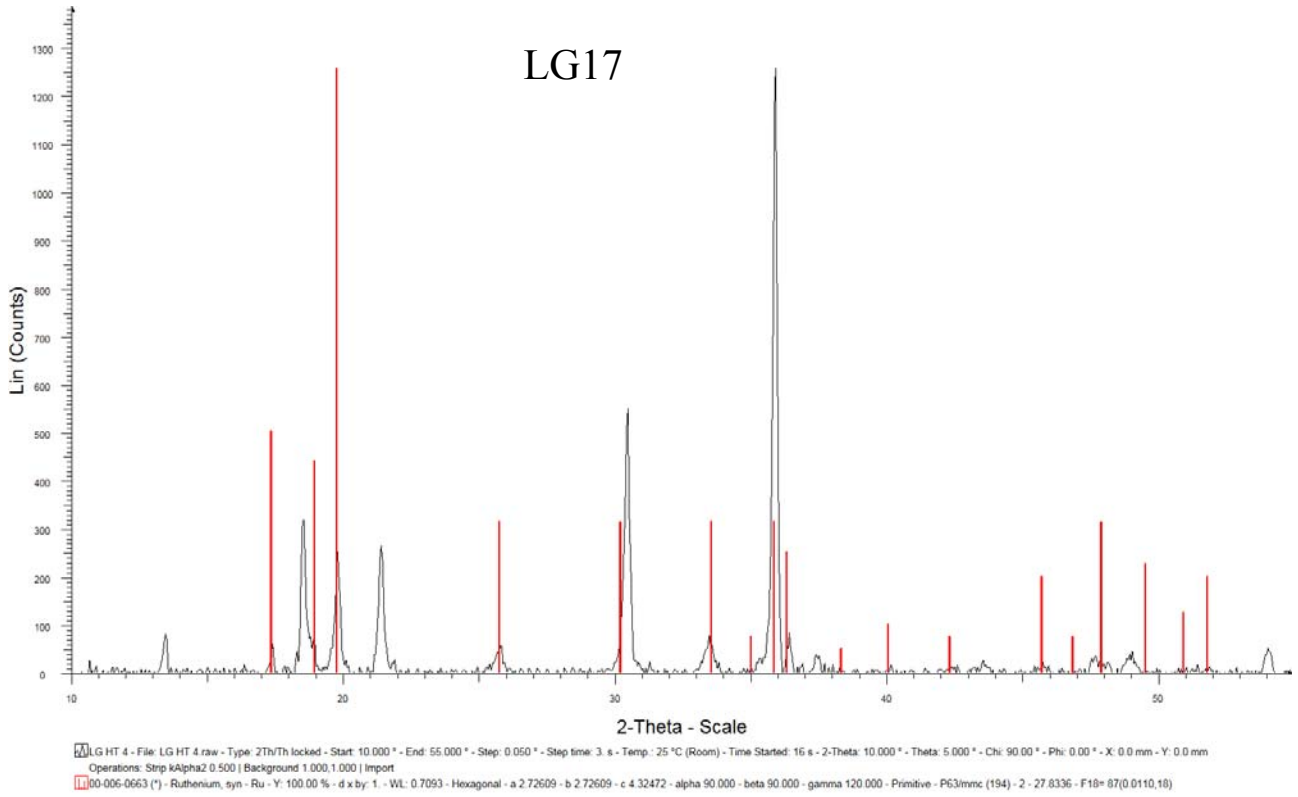


b)

Figure 4.124. XRD spectrum of LG 17 (Co_{60}:Pt_{20}:Ru_{20}) in the heat treated condition showing a comparison with a) Pt and b) Ru.



a)



b)

Figure 4.125. XRD spectrum of LG 17 (Co_{60}:Pt_{20}:Ru_{20}) in the heat treated condition showing a comparison with a) Pt and b) Ru after shifting.

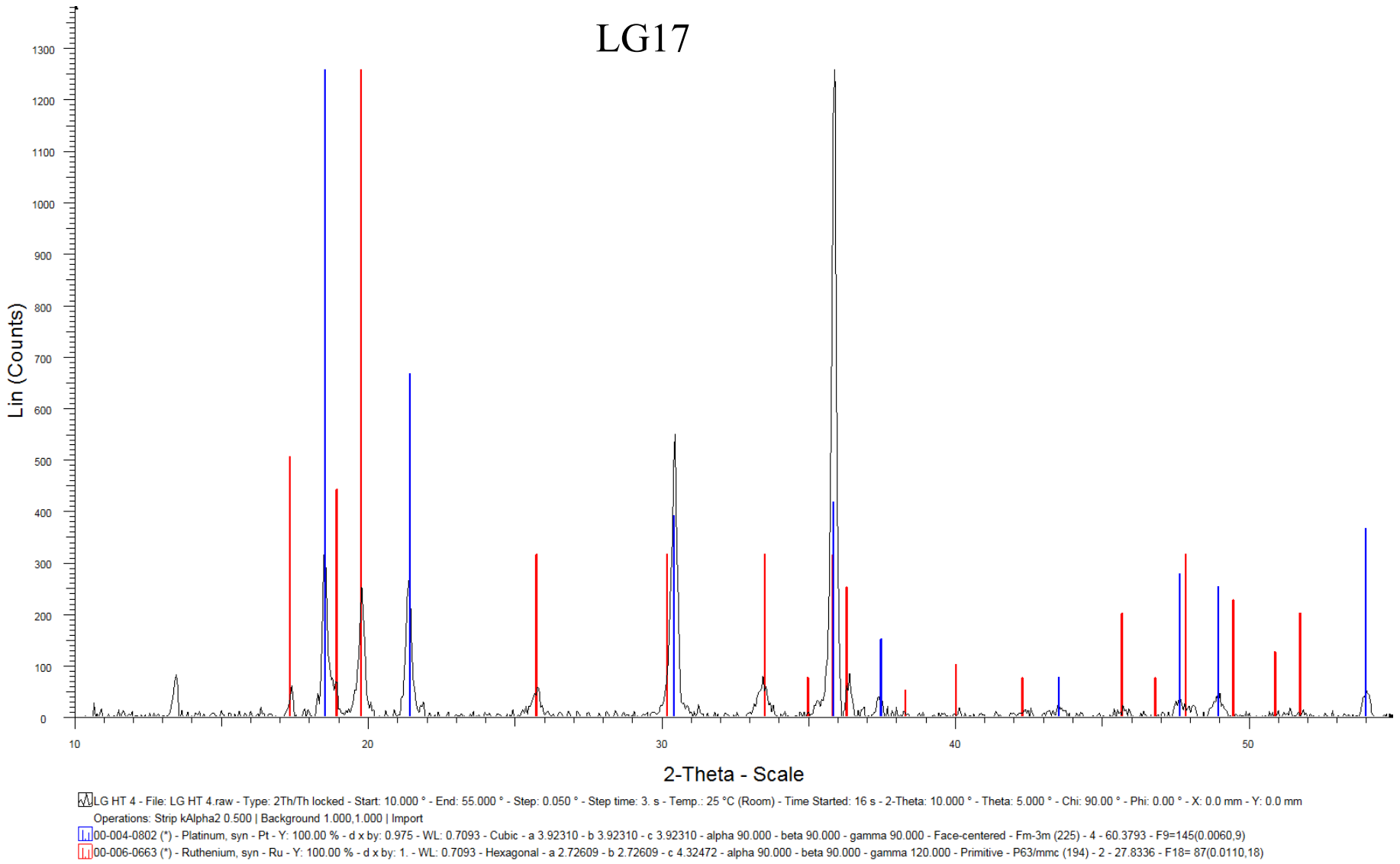


Figure 4.126. XRD spectrum of LG 17 (Co_{60}:Pt_{20}:Ru_{20}) in the heat treat condition with both Pt and Ru overlaid.

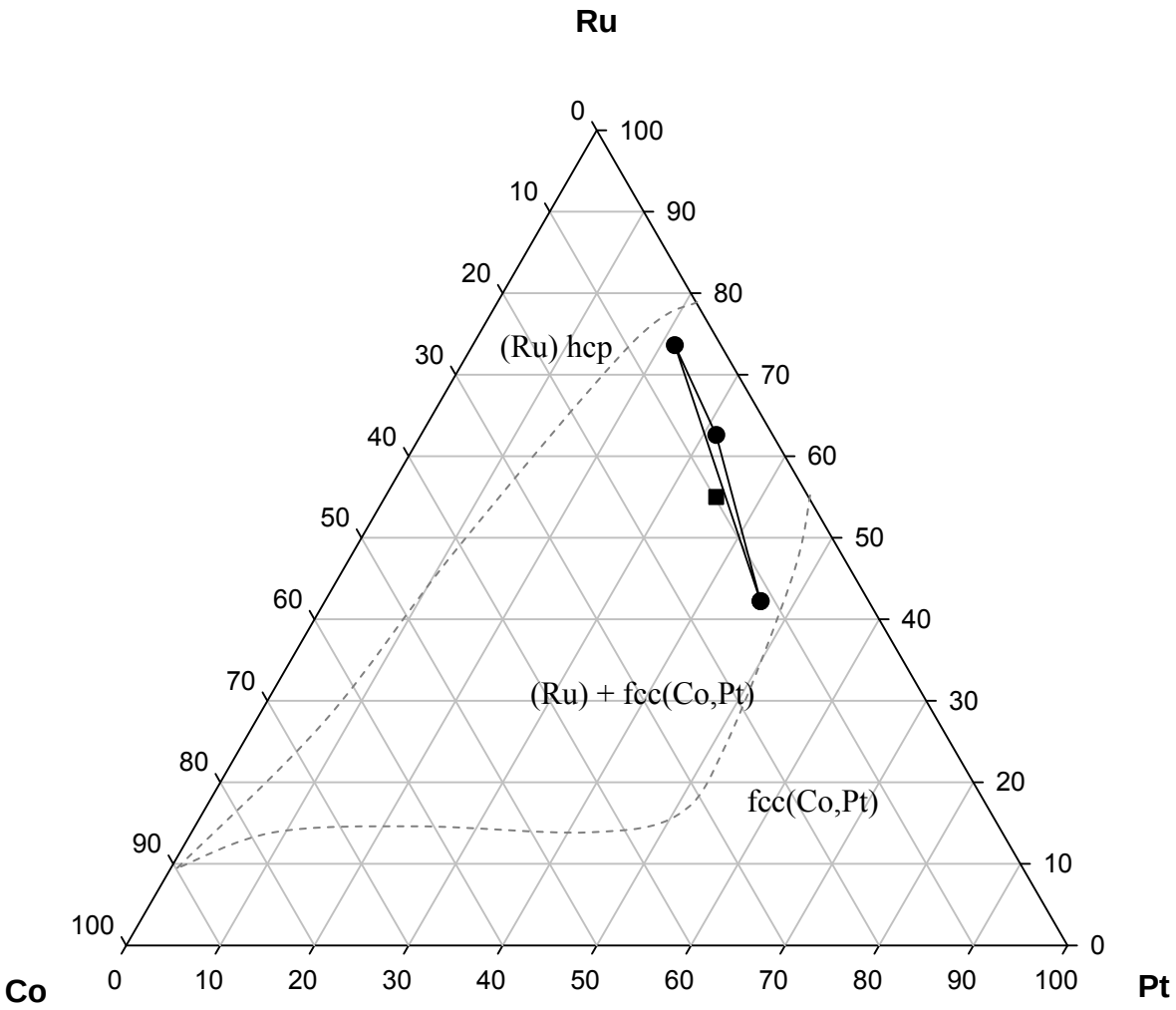


Figure 4.127. EDS analyses of LG 17 (Co_{60}:Pt_{20}:Ru_{20}) in the heat treated condition (at.%).

Table 4.46. Unidentified peaks formed after heat treatment.

2θ	**Intensity**
18	10
21.9	20
31	20
41.5	25

LG 18 (Nominal Co_{20}:Pt_{30}:Ru_{50})

The microstructure of LG 18 (Nominal Co_{20}:Pt_{30}:Ru_{50}) is shown in Figure 4.128. There appeared to be three phases and they were identified through XRD analyses (Figure 4.129). The XRD spectrum in Figure 4.130 shows the peaks with the shifted lines and Figure 4.131 shows the XRD spectrum with the peaks overlaid. The large peak visible at 2θ ≈13.5 is the plasticene in which the sample was mounted for XRD analysis. The unidentified peaks in the spectrum are shown in Table 4.48. The dark needle-like structures consists of (Ru), the medium dendrites consist of very fine (Ru) needles the light fcc(Co,Pt) matrix and the light, interdendritic phase is Pt-rich fcc(Co,Pt). The EDS analyses are shown in Table 4.47 and the actual compositions are plotted in Figure 4.132.

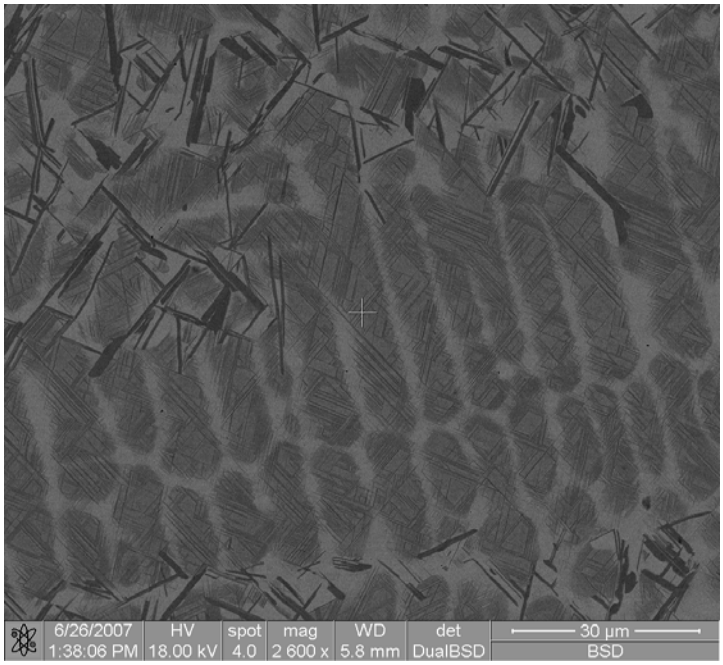
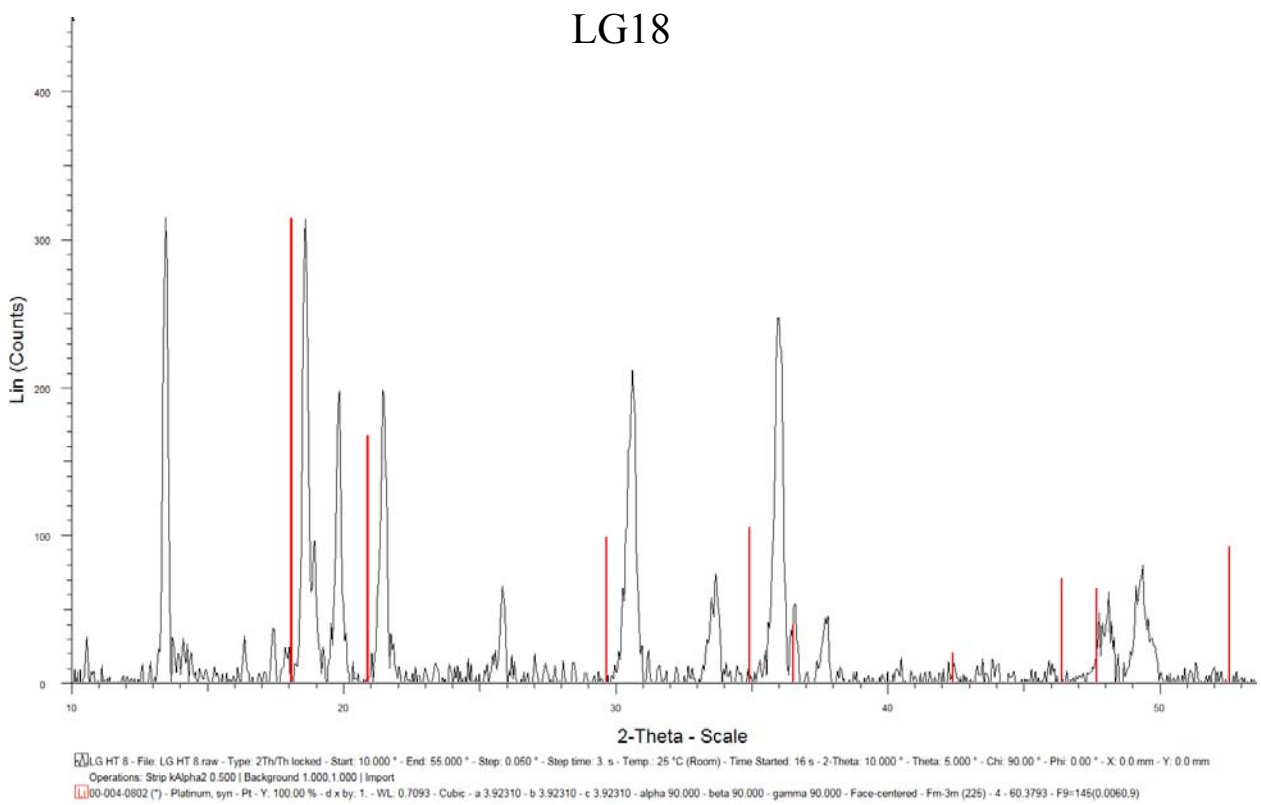


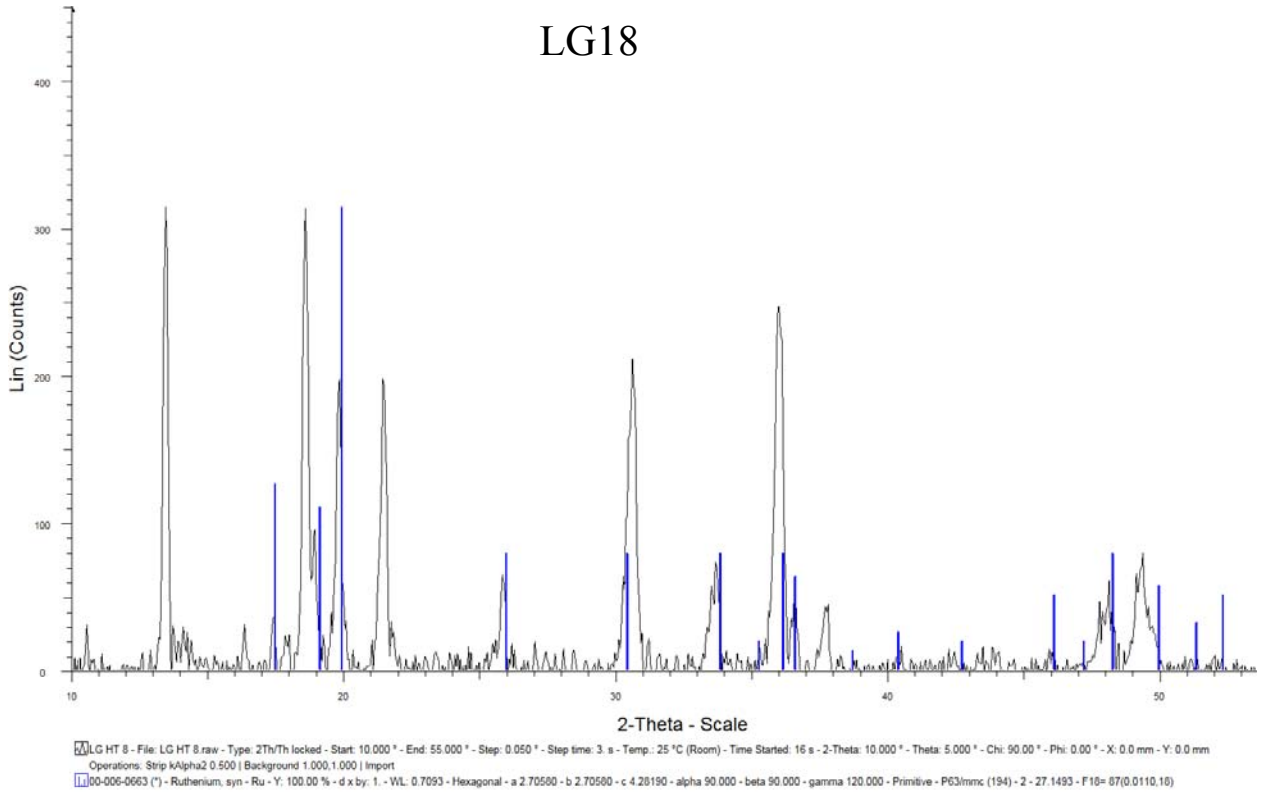
Figure 4.128. BEI of LG 18 (Nominal Co_{20}:Pt_{30}:Ru_{50}) heat treated condition showing the mixed dendrites containing a mixture of (Ru) and fcc(Co,Pt) in a light matrix fcc(Co,Pt) with dark (Ru) needles.

Table 4.47. EDS analyses of LG18 (Nominal Co_{20}:Pt_{30}:Ru_{50}) in the heat treated condition (at.%).

Phase description	Pt (at.%)	Ru (at.%)	Co (at.%)	Phase	Phase Proportion (%)
Overall	48.7 ± 0.2	20.5 ± 2.0	30.8 ± 0.9	-	-
Light	50.2 ± 0.3	17.4 ± 1.3	32.4 ± 2.3	fcc(Co,Pt)	~20
Medium	30.6 ± 0.9	56.6 ± 1.2	12.8 ± 1.5	fcc(Co,Pt) + (Ru)	~60
Dark	18.0 ± 1.6	73.9 ± 0.9	8.1 ± 0.2	(Ru)	~20

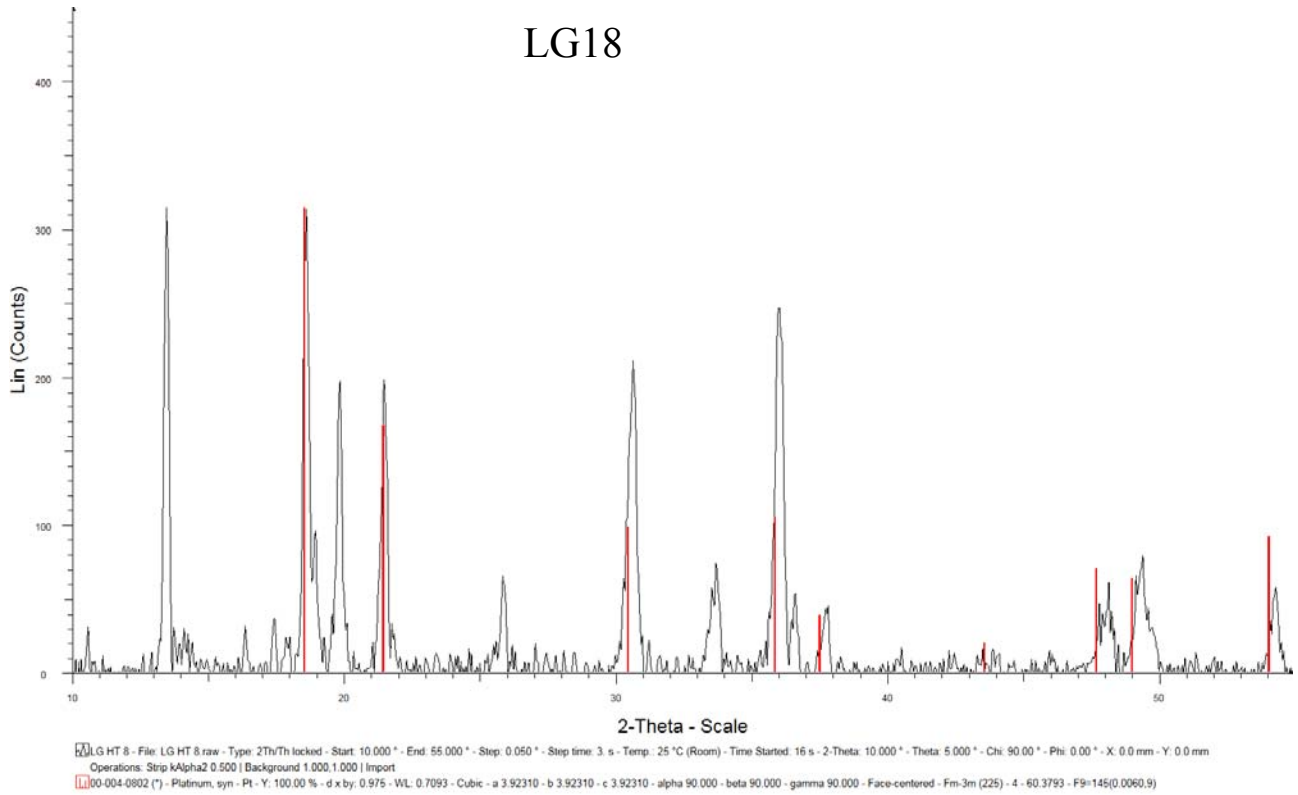


a)

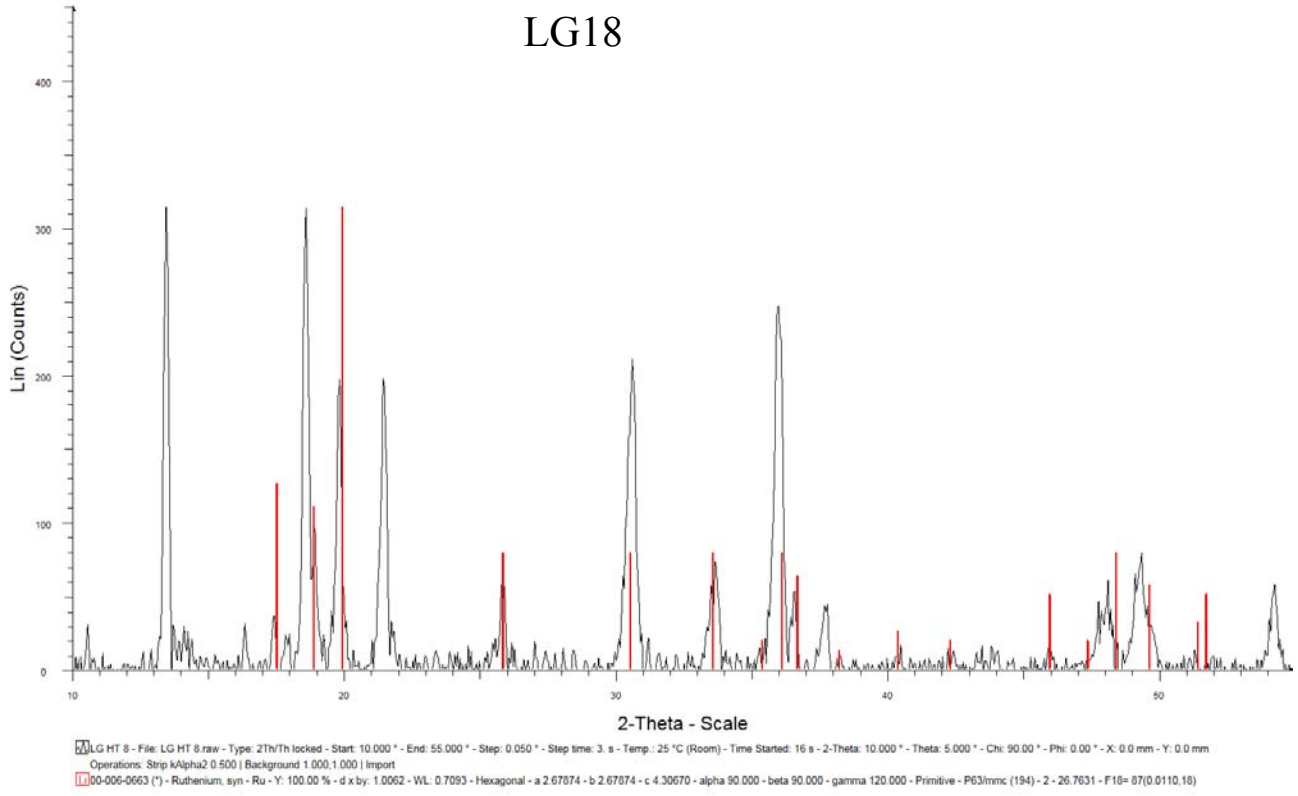


b)

Figure 4.129. XRD spectrum of LG 18 (Nominal Co_{20}:Pt_{30}:Ru_{50}) in the heat treated condition showing a comparison with a) Pt and b) Ru.



a)



b)

Figure 4.130. XRD spectrum of LG 18 (Nominal Co_{20}:Pt_{30}:Ru_{50}) in the heat treated condition showing a comparison with a) Pt and b) Ru.

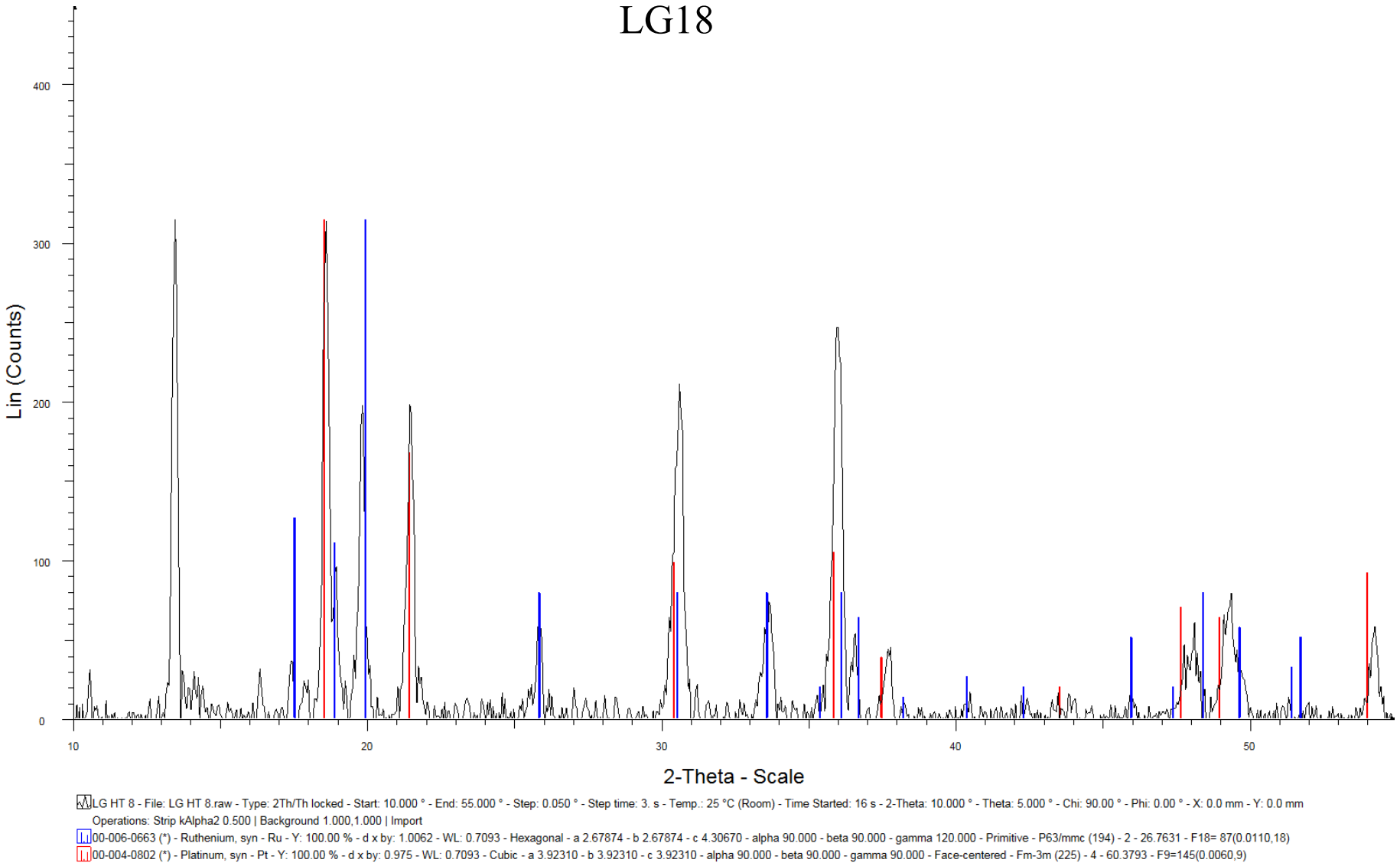


Figure 4.131. XRD spectrum of LG 18 (Nominal Co_{20}:Pt_{30}:Ru_{50}) in the heat treat condition with both Pt and Ru overlaid.

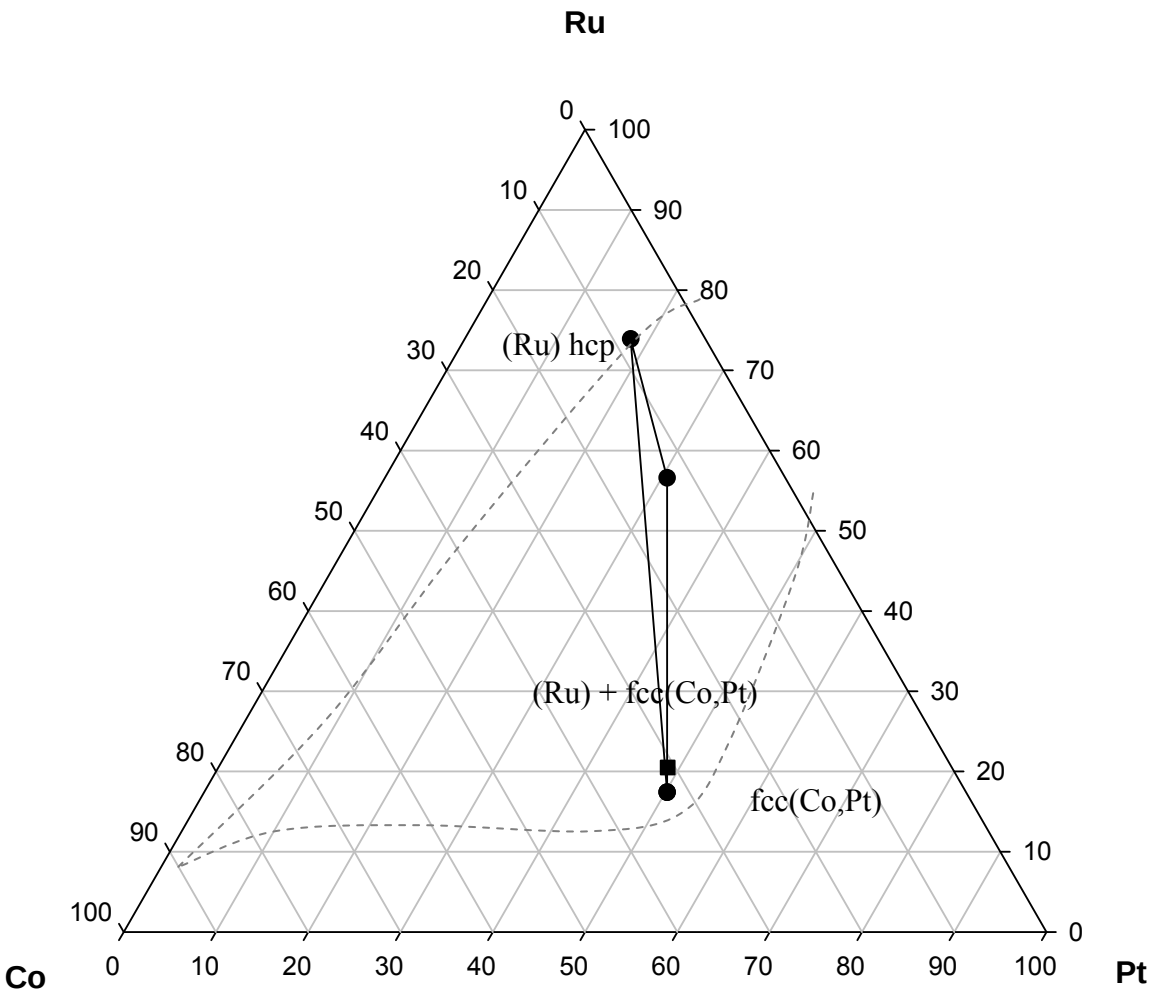


Figure 4.132. EDS analyses of LG 18 (Nominal Co_{20}:Pt_{30}:Ru_{50}) in the heat treated condition (at.%).

Table 4.48. Unidentified peaks formed after heat treatment.

2θ	**Intensity**
10.5	30
14	30
14.5	30
16.5	30
18	25
19	50
19.5	40
21	20
21.8	30
31	20
33.5	40
36.5	40

LG 19 (Nominal Co_{50}:Pt_{20}:Ru_{30})

LG 19 (Nominal Co_{50}:Pt_{20}:Ru_{30}) also appears to consist of three phases, (Figure 4.133), but only two phases, (Ru) and fcc(Co,Pt), were identified by XRD (Figure 4.134) and was quite different from the previous samples. The light fcc(Co,Pt) phase lies between the medium phase, which was actually a mixture of fine dark (Ru) needles and the light fcc(Co,Pt) phase, as a thin film surrounding the dark (Ru) phase. The needles lie very clearly in the light phase. The XRD spectrum is shown in Figure 4.134. In Figure 4.135 the Ru and Pt lines are shifted to fit the peaks and in Figure 4.136 both the Ru and Pt peaks are overlaid which then shows a good fit for (Ru) and fcc(Co,Pt). The spectrum shows a high signal to background ratio and has neat narrow peaks. The peak visible at $2\theta \approx 13.5$ is plasticene. Unidentified peaks are visible and shown in Table 4.50. The EDS analyses are shown in Table 4.49 and the actual compositions are plotted in Figure 4.137.

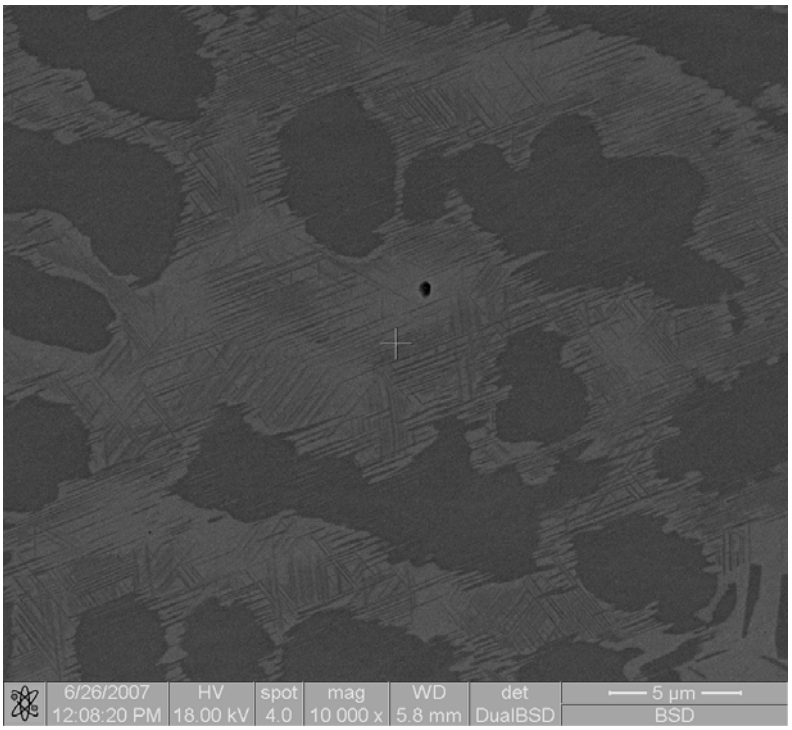
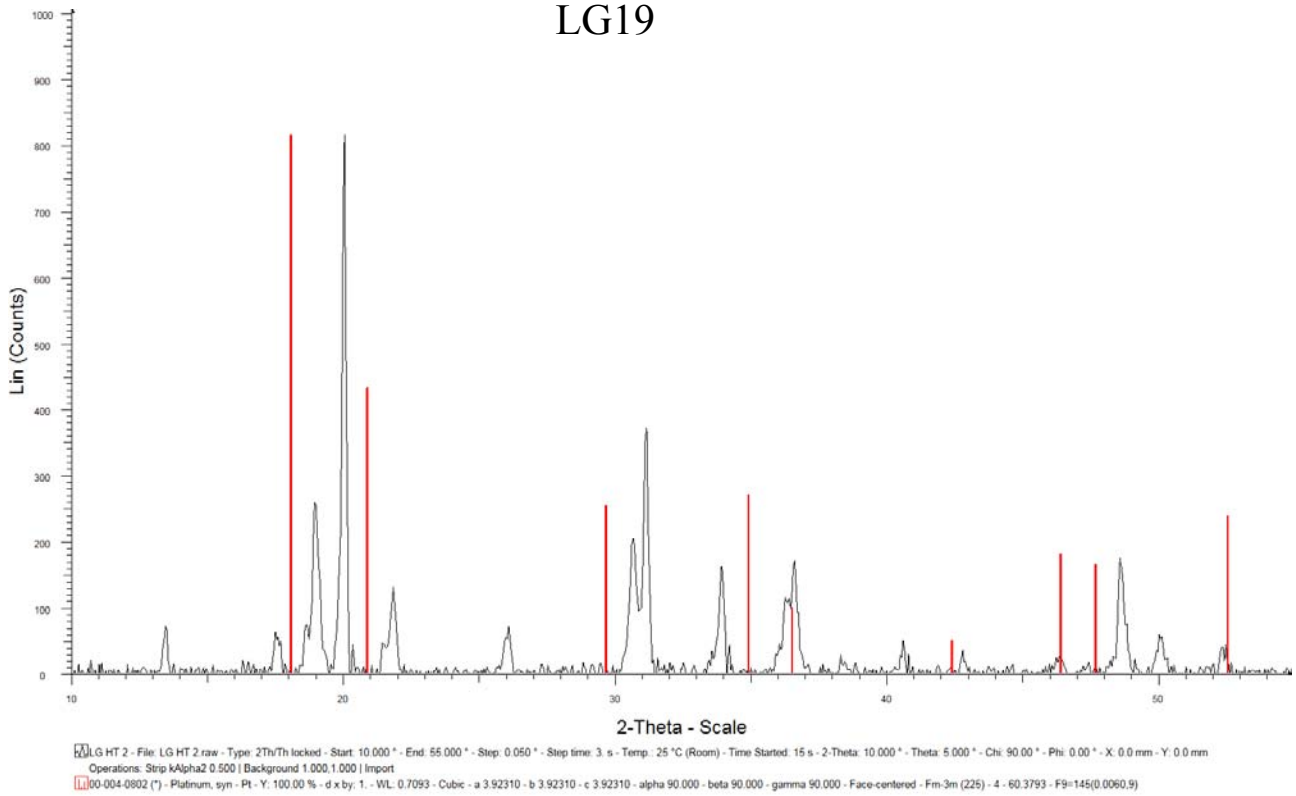


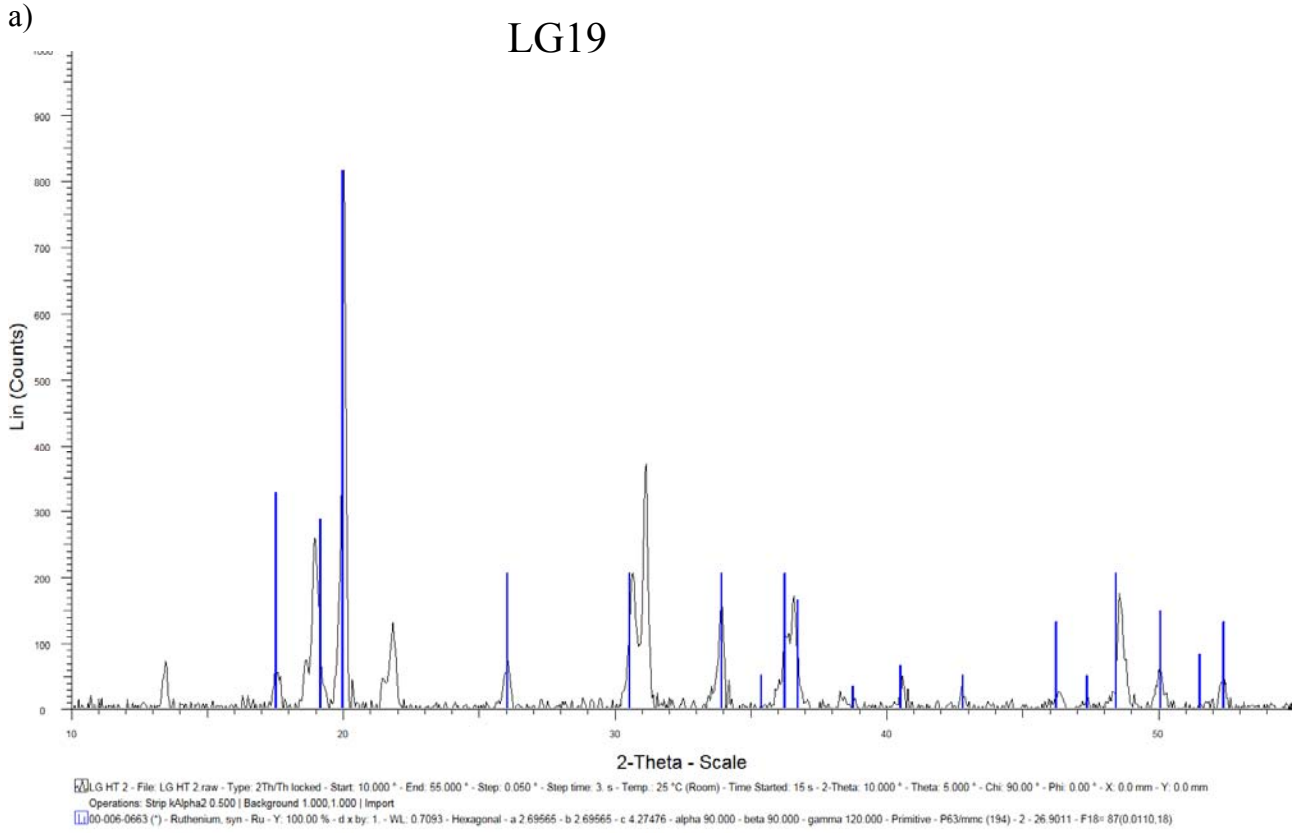
Figure 4.133. BEI of LG 19 (Nominal Co_{50}:Pt_{20}:Ru_{30}) heat treated condition showing a dark second phase (Ru) in a light matrix fcc(Co,Pt) and dark (Ru) needles.

Table 4.49. EDS analyses of LG19 (Co_{50}:Pt_{20}:Ru_{30}) in the heat treated condition (at.%).

Phase description	Pt (at.%)	Ru (at.%)	Co (at.%)	Phase	Phase Proportion (%)
Overall	25.4 ± 1.6	44.3 ± 0.6	30.3 ± 1.9	-	-
Light	40.4 ± 1.3	12.7 ± 0.2	46.9 ± 2.6	fcc(Co,Pt)	~20
Medium	27.4 ± 1.0	39.4 ± 0.8	33.2 ± 2.3	fcc(Co,Pt) + (Ru)	~50
Dark	16.7 ± 1.9	65.7 ± 1.6	17.6 ± 1.0	(Ru)	~30

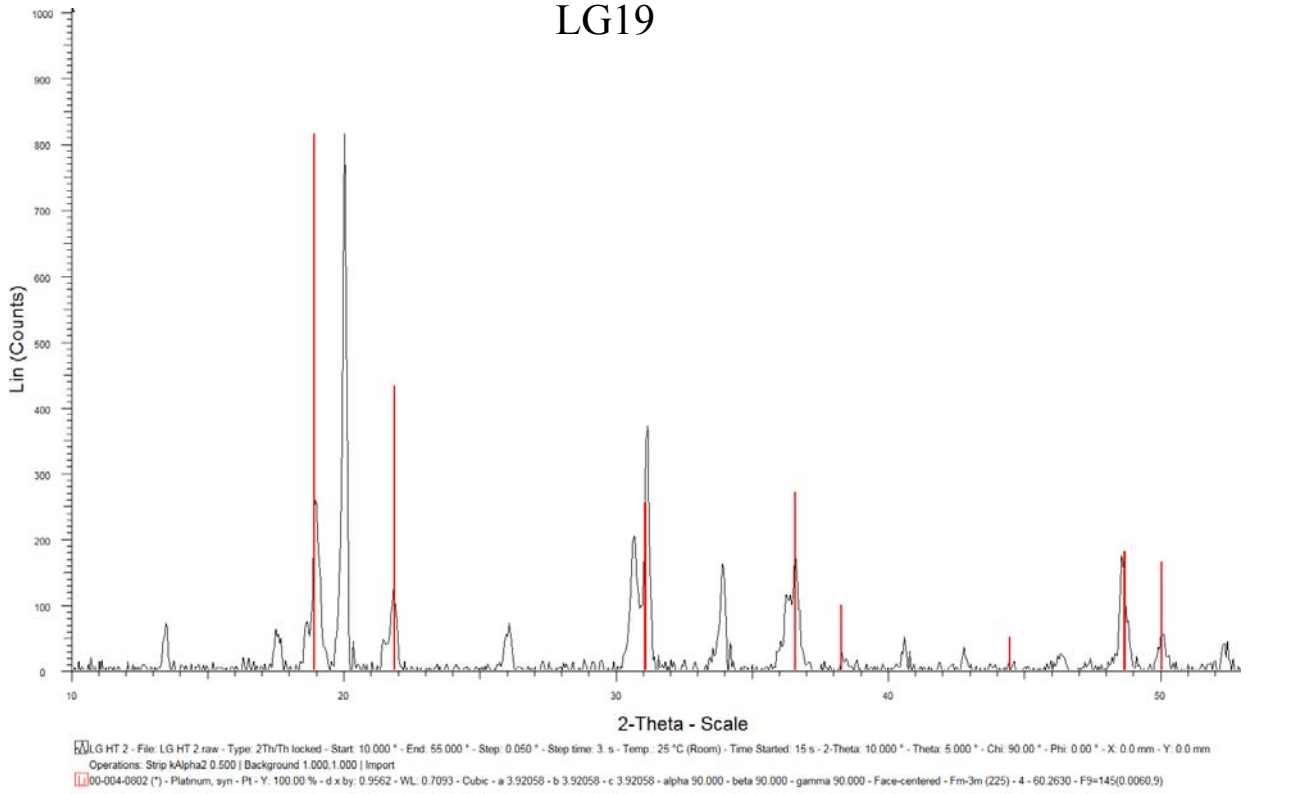


a)

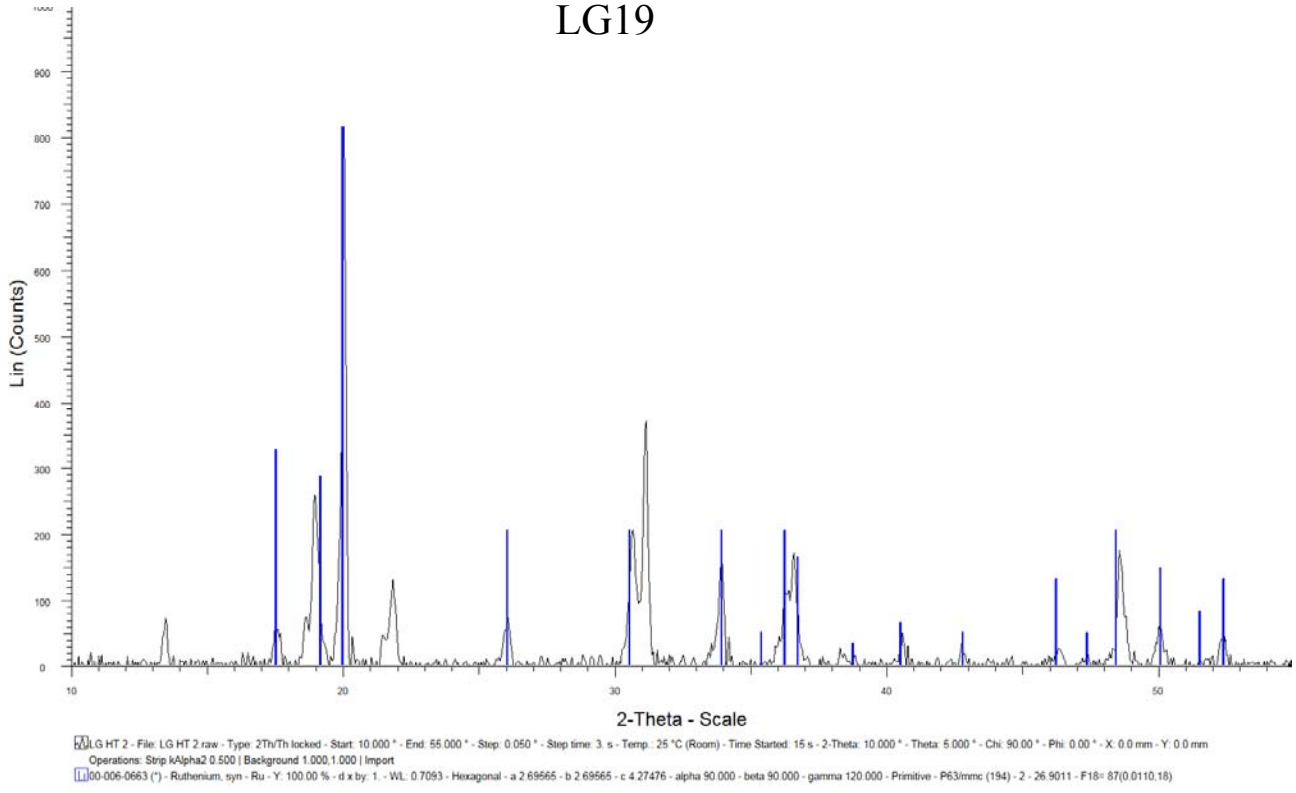


b)

Figure 4.134. XRD spectrum of LG 19 (Co_{50}:Pt_{20}:Ru_{30}) in the heat treated condition showing a comparison with a) Pt and b) Ru.



a)



b)

Figure 4.135. XRD spectrum of LG 19 (Co_{50}:Pt_{20}:Ru_{30}) in the heat treated condition showing a comparison with a) Pt and b) Ru after shifting.

LG19

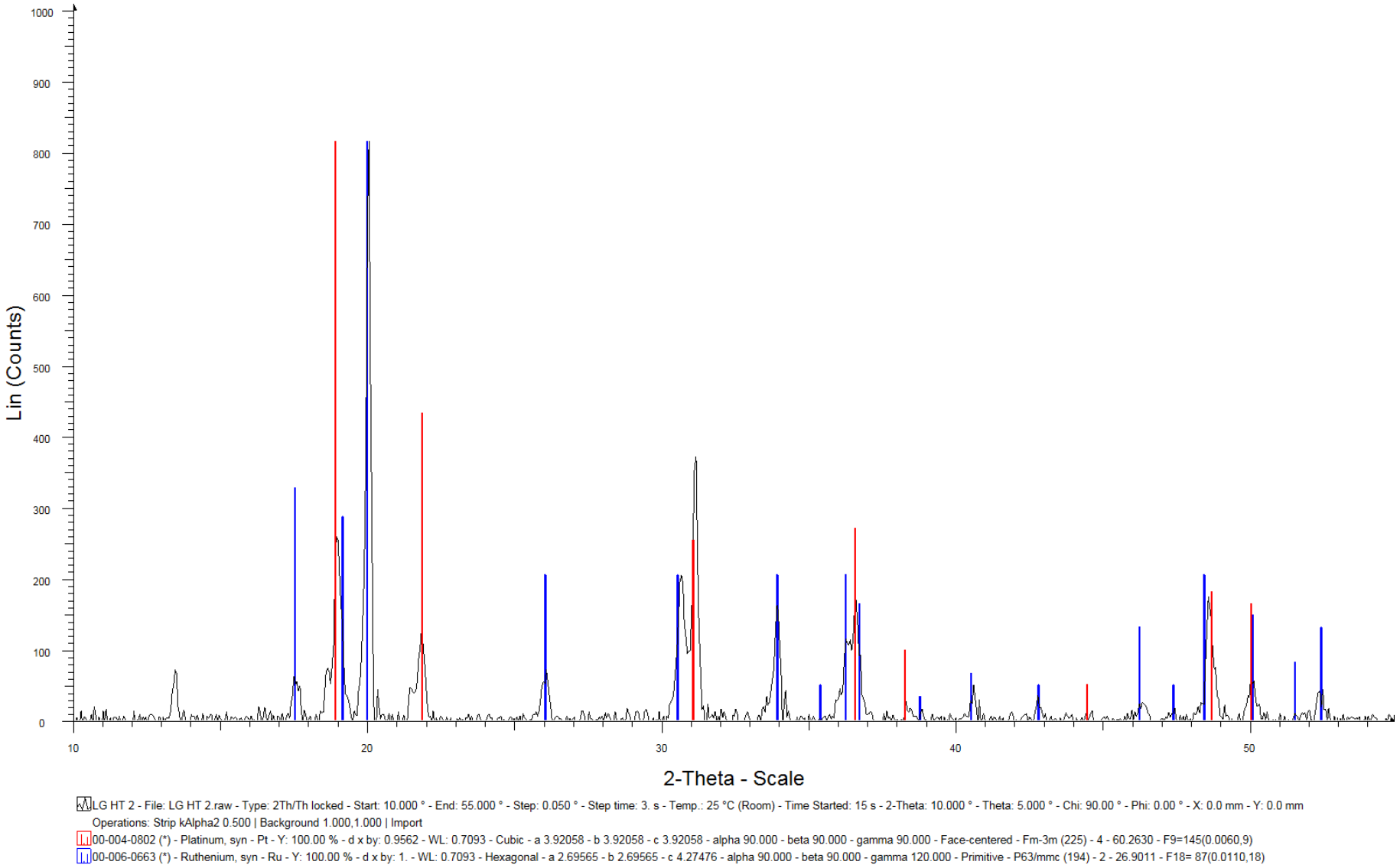


Figure 4.136. XRD spectrum of LG 19 (Nominal Co_{50}:Pt_{20}:Ru_{30}) in the heat treat condition with both Pt and Ru overlaid.

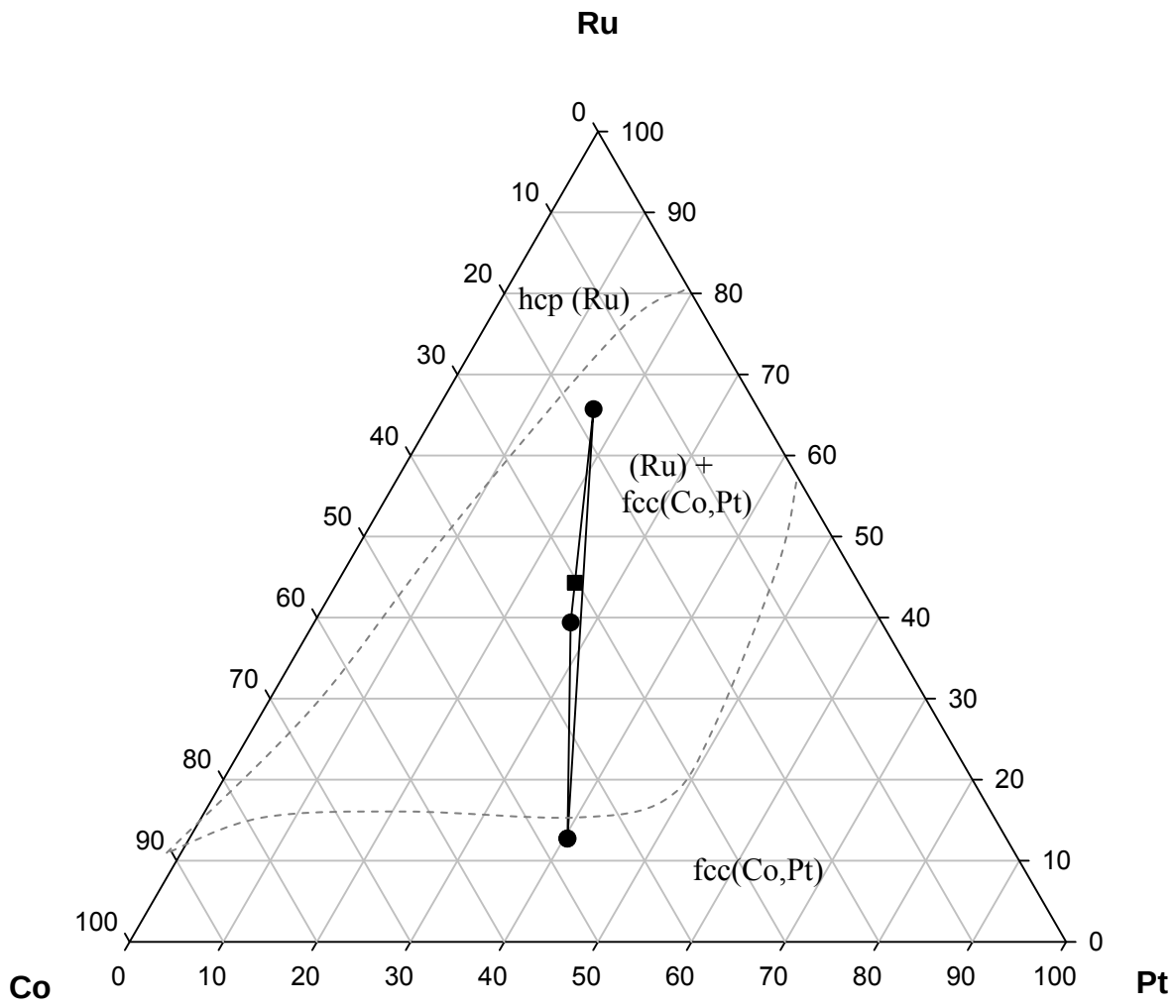


Figure 4.137. EDS analyses of LG 19 (Nominal Co_{50}:Pt_{20}:Ru_{30}) in the heat treated condition (at.%).

Table 4.50. Unidentified peaks formed after heat treatment.

2θ	**Intensity**
18.5	75
21.5	50
31.5	50
36.5	50

4.2.4 Ordering Heat Treatment at 500°C

LG 11 (Nominal Co_{40}:Pt_{50}:Ru_{10})

LG 11 (Nominal Co_{40}:Pt_{50}:Ru_{10}) experienced some changes after the heat treatment at 500°C to promote ordering. The microstructure in Figure 4.138 shows a single phase alloy, and the microstructure had not changed after heat treatment. Compared to the as-cast spectrum in Figure 4.64 the XRD spectrum in Figure 4.139 show a good match with the ordered phase CoPt. There are more peaks visible (some superlattice peaks are appearing during heat treatment) and they are wider, which could be expected as a change in texture took place during heat treatment. The peak at $2\theta \approx 13.5$ is the plasticene in which the sample was mounted. The EDS analysis are shown in Table 4.51 and the composition is plotted in Figure 4.140.

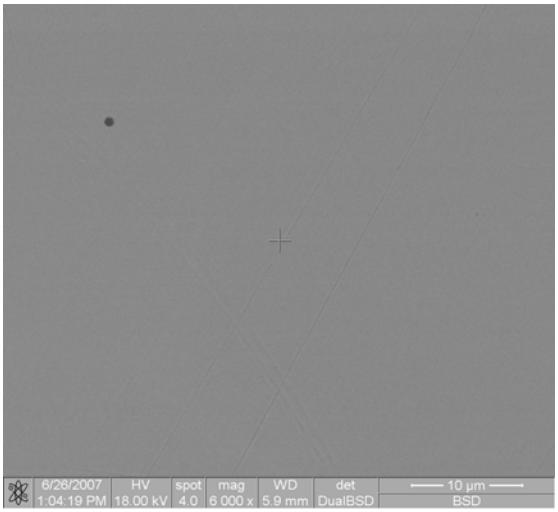


Figure 4.138. BEI of LG 11 (Nominal Co_{40}:Pt_{50}:Ru_{10}) after ordering heat treatment and water quench consisting of the CoPt phase.

Table 4.51. EDS analyses of LG 11 (Nominal Co_{40}:Pt_{50}:Ru_{10}) after ordering heat treatment.

Phase description	Pt (at.%)	Ru (at.%)	Co (at.%)	Phase	Phase Proportion (%)
Overall	47.5 ± 0.8	9.2 ± 0.1	43.3 ± 0.6	CoPt	-

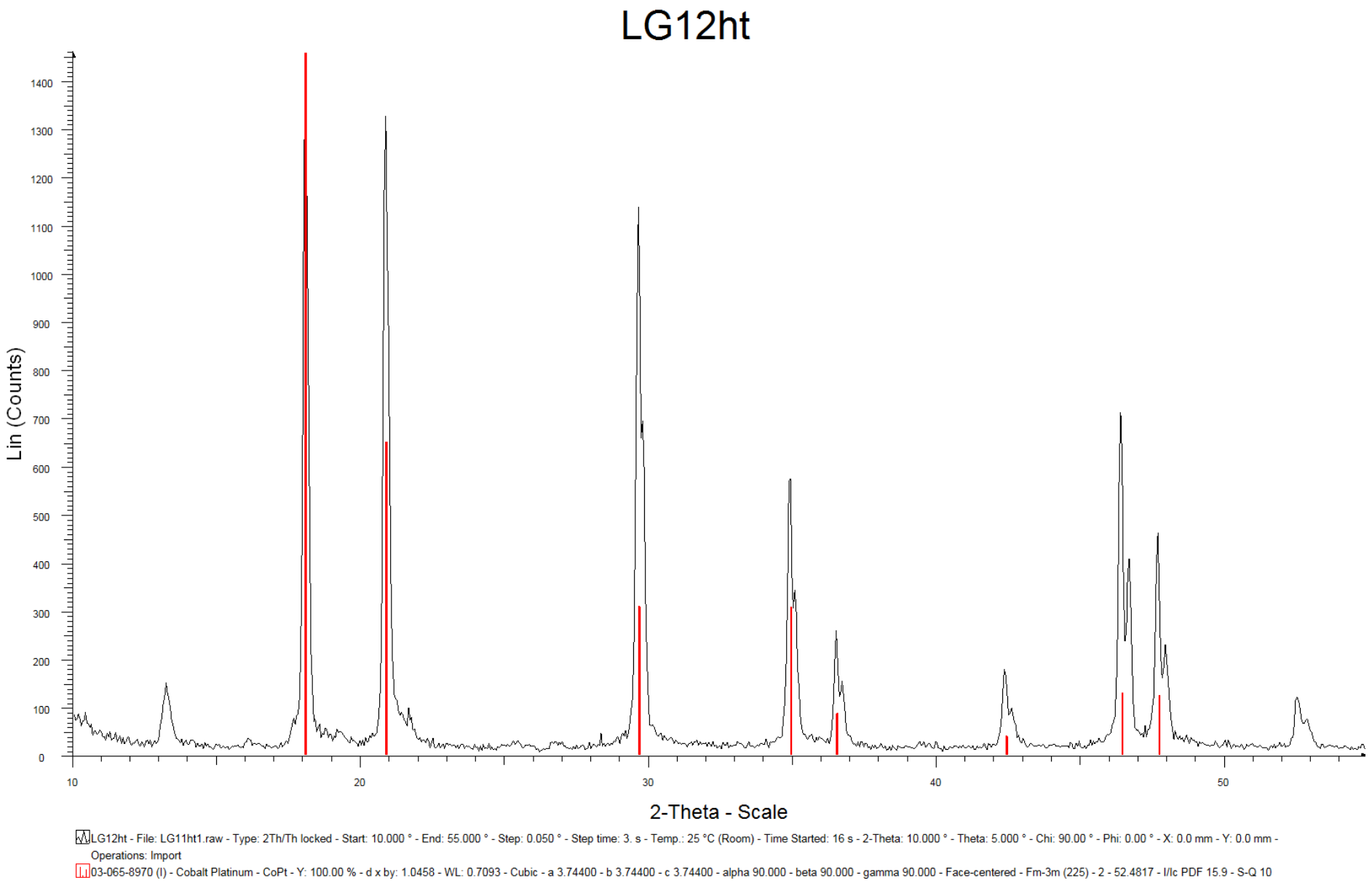


Figure 4.139. XRD spectrum of LG 11 (Nominal Co_{40}:Pt_{50}:Ru_{10}) in the heat treated condition showing a comparison with CoPt

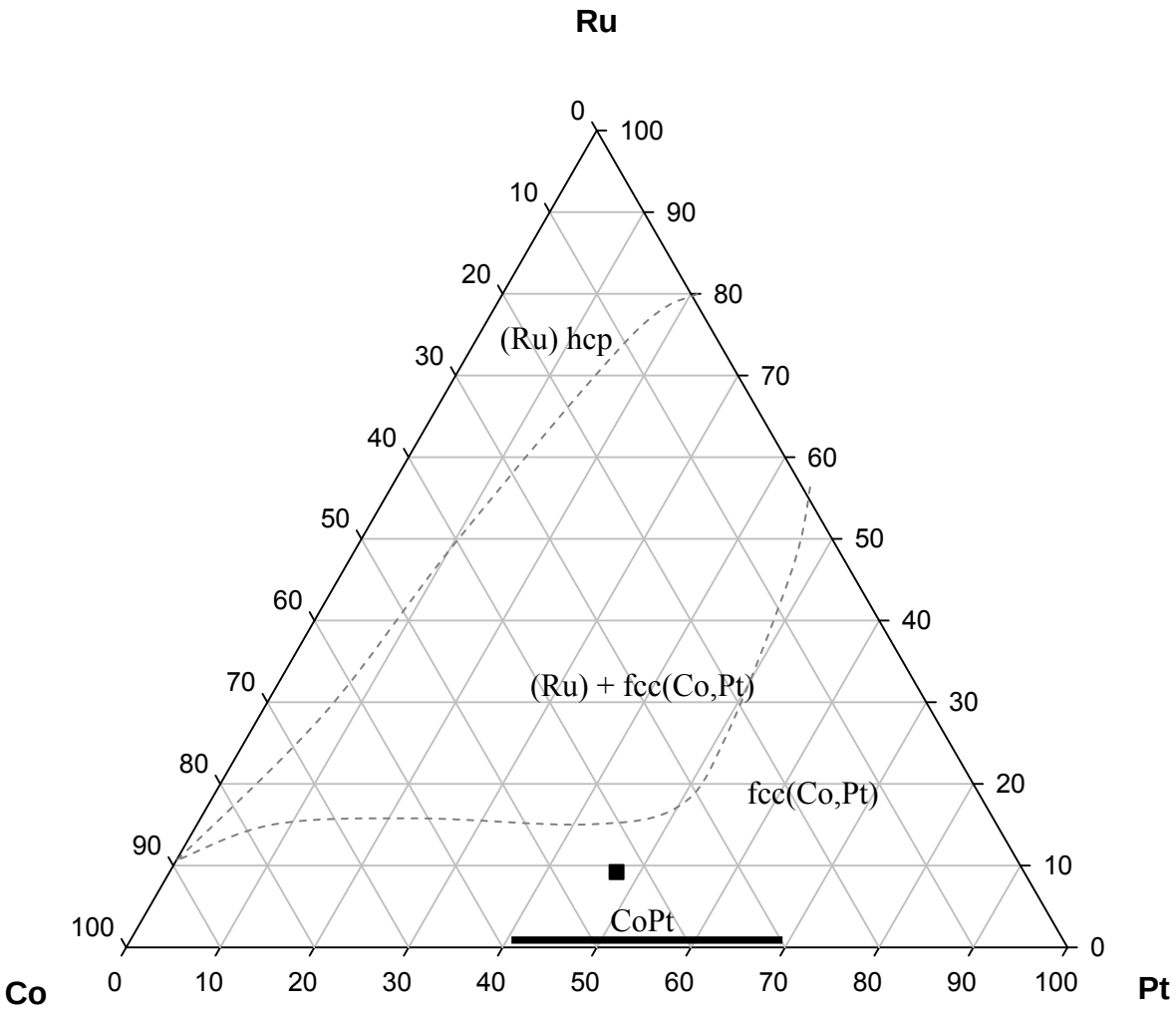


Figure 4.140. EDS analyses of LG 11 (Nominal Co_{40}:Pt_{50}:Ru_{10}) in the heat treated condition (at.%).

Table 4.52. Unidentified peaks formed after heat treatment.

2θ	**Intensity**
21.8	100
35.2	300
37	150
42.5	75
46.8	400
48	200
52	100

LG 12 (Nominal Co_{15}:Pt_{75}:Ru_{10})

The microstructure of LG 12 (Nominal Co_{15}:Pt_{75}:Ru_{10}) (Figure 4.141) showed no change after the ordering heat treatment. However, the XRD spectrum in Figure 4.142 showed that some change took place. A large unidentified peak is visible at $2\theta \approx 21.8°$. Several smaller peaks are also visible and are shown in Table 4.54. The large unidentified peak could be related to the Pt-Ru system since there is no data available from below 1000°C on the Pt-Ru phase diagram (Figure 2.2). The rest of the peaks were identified as Pt. The EDS analyses are shown in Table 4.53 and the composition is plotted in Figure 4.143.

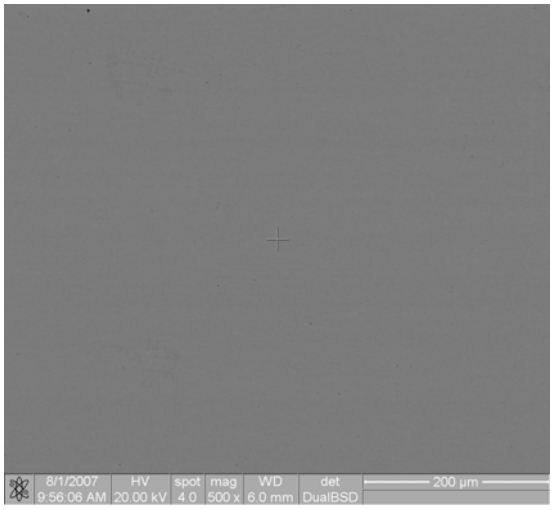


Figure 4.141. BEI of LG 12 (Nominal Co_{15}:Pt_{75}:Ru_{10}) after ordering heat treatment and water quench consisting of single phase (Pt) .

Table 4.53. EDS analyses of LG 12 (Nominal Co_{15}:Pt_{75}:Ru_{10}) after ordering heat treatment (at.%).

Phase description	Pt (at.%)	Ru (at.%)	Co (at.%)	Phase	Phase Proportion (%)
Overall	93.6 ± 0.4	6.2 ± 0.3	0.2 ± 0.0	fcc(Pt)	-

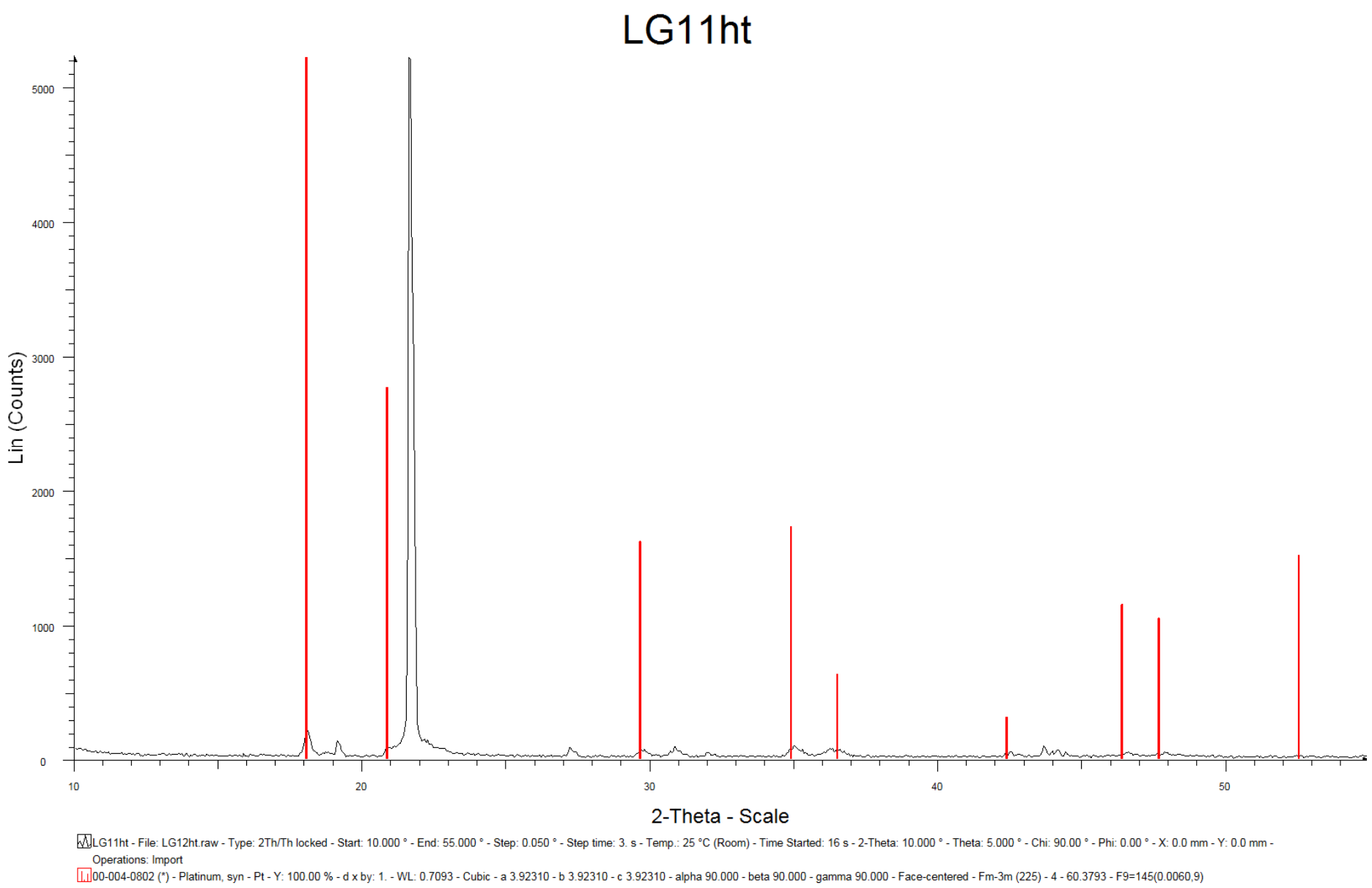


Figure 4.142. XRD spectrum of LG 12 (Nominal Co_{15}:Pt_{75}:Ru_{10}) in the heat treated condition with the Pt peaks overlaid.

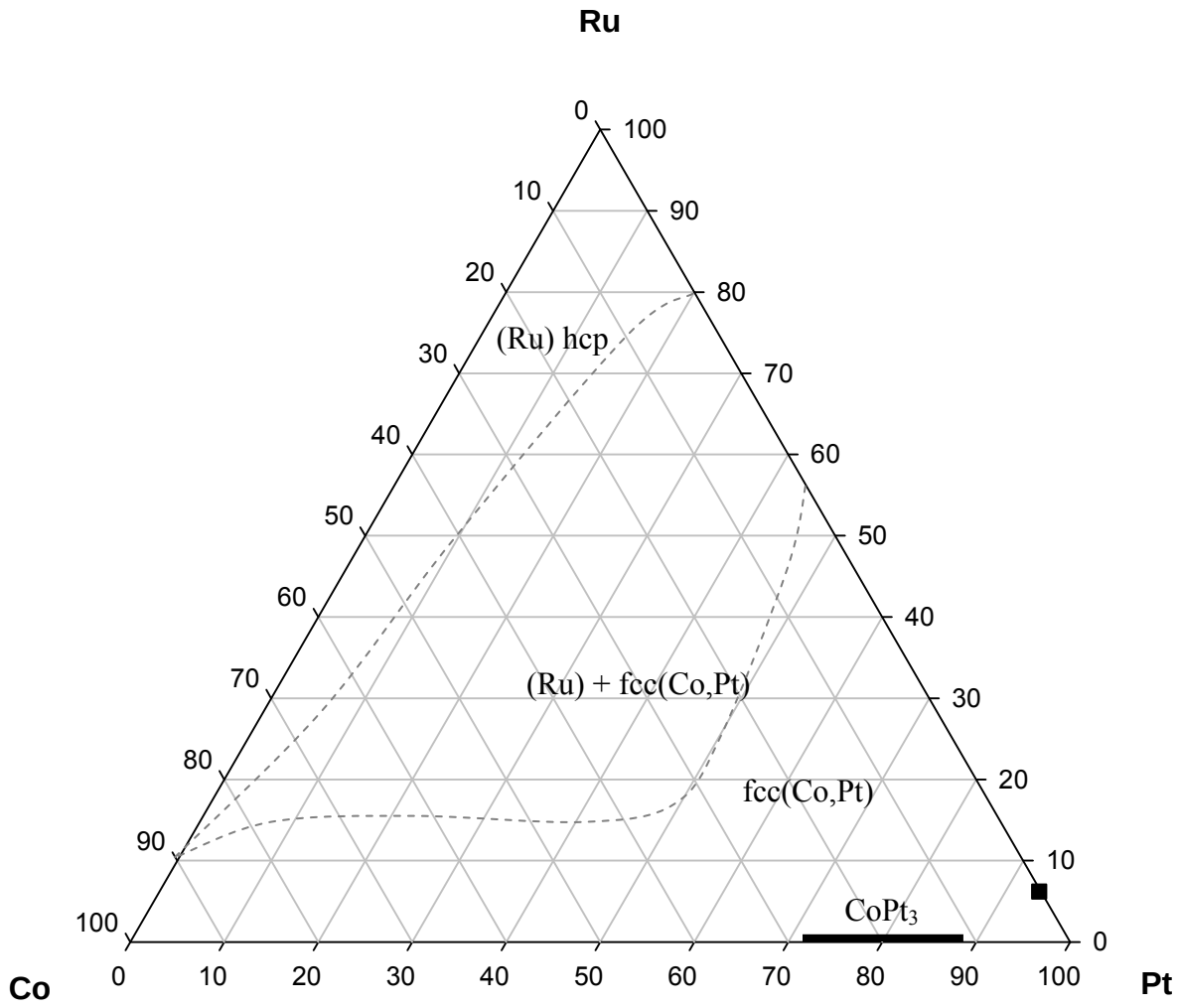


Figure 4.143. EDS analyses of LG 12 (Nominal Co_{15}:Pt_{75}:Ru_{10}) in the heat treated condition (at.%).

Table 4.54. Unidentified peaks formed after heat treatment.

2θ	**Intensity**
19.2	100
21.8	5000
27.2	100
31	100
32	100
44.8	100
45	100

4.3 Mechanical Properties

4.3.1 Ni-Pt-Ru Hardness and Toughness

The results of the hardness measurements on the as-cast alloys are shown in Table 4.55 and the values are superposed on the solidification projection in Figure 4.144.

The hardest alloys are LG5, LG4, LG3, LG2 and LG 6. These alloys are two-phase and consist of various amounts of (Ru) and (Ni,Pt), with very low Pt content. A second group of alloys (LG 2 and LG 7) is single-phase and lie in the Ru-rich area of the (Ni,Pt) phase field and also have high hardnesses. The softest alloys (LG 8, LG 9, LG 10 and LG 1) consisted of single-phase (Ni,Pt), except LG 9 that was two-phase. It can be noted that these four alloys had the highest Pt content. LG 1 is the softest and contains 47.7 at. % Pt and 4.5 at. % Ru.

Table 4.55. Hardness values of the as-cast Ni-Pt-Ru alloys.

Alloy	**As-Cast Hardness (HV_{10})**	**Phases**	**Phase proportions (%)**
LG 1	281 ± 26	(Ni,Pt)	100 (Ni,Pt)
LG 2	483 ± 21	(Ni,Pt)	100 (Ni,Pt)
LG 3	551 ± 11	(Ni,Pt)	100 (Ni,Pt)
LG 4	564 ± 38	(Ni,Pt), (Ru)	~60 (Ni,Pt): ~40 (Ru)
LG 5	567 ± 45	(Ni,Pt), (Ru)	~60 (Ni,Pt): ~40 (Ru)
LG 6	446 ± 67	(Ni,Pt), (Ru)	~76 (Ni,Pt): ~24 (Ru)
LG 7	426 ± 13	(Ni,Pt)	100 (Ni,Pt)
LG 8	390 ± 25	(Ni,Pt)	100 (Ni,Pt)
LG 9	362 ± 30	(Ni,Pt), (Ru)	~32 (Ni,Pt): ~68 (Ru)
LG 10	319 ± 28	(Ni,Pt)	100 (Ni,Pt)

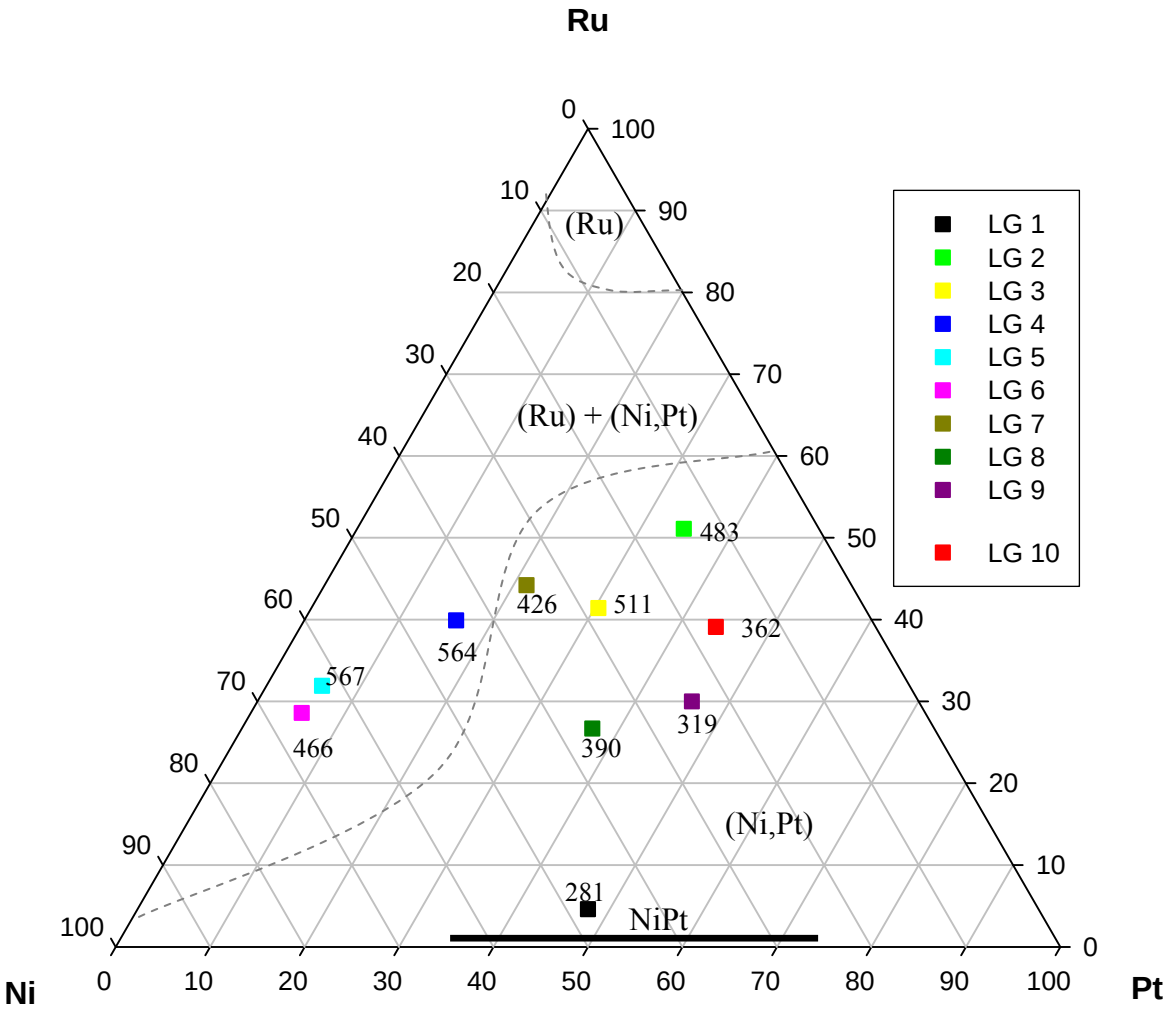


Figure 4.144. Hardness (HV_{10}) values of the as-cast Ni-Pt-Ru alloys superposed on the solidification projection (at.%).

The results of the hardness measurements on the heat treated alloys are shown in Table 4.56 and the values are superposed on the solidification projection in Figure 4.145.

The hardest alloys after heat treatment are LG 3, LG 4, LG 8 and LG 2. These alloys are located in the two-phased area and can be considered Ru-rich, although the hardest alloy had a very fine mixture of needles in the matrix ("mix" in Table 4.56). Alloys LG 7 and LG 9 were two-phase and showed mid-range hardness. Alloy LG 10 is located in the single-phase (Ni,Pt) area that has a high Pt content. Alloys LG 5 and LG 6 show the lowest hardness, and are nearest the Ni-Ru binary. The alloys are located in the two-phase (Ru) and (Ni,Pt) area. They lie in the Ni-rich side of the two-phase area.

Table 4.56. Hardness values of the heat treated Ni-Pt-Ru alloys.

Alloy	Annealed Hardness (HV_{10})	Phases	Phase Proportions (%)
LG 1	479 ± 23 (HT at 500°C)	Ordered fcc	100 NiPt
LG 2	401 ± 40	(Ni,Pt), (Ru)	~40 (Ni,Pt): ~60 (Ru)
LG 3	526 ± 22	(Ni,Pt), (Ru)	~20 (Ni,Pt): ~16 (Mix): ~64 (Ru)
LG 4	464 ± 47	(Ni,Pt), (Ru)	~56 (Ni,Pt): ~44 (Ru)
LG 5	298 ± 12	(Ni,Pt), (Ru)	~60 (Ni,Pt): ~40 (Ru)
LG 6	275 ± 23	(Ni,Pt), (Ru)	~72 (Ni,Pt): ~28 (Ru)
LG 7	390 ± 46	(Ni,Pt), (Ru)	~40 (Ni,Pt): ~60 (Ru)
LG 8	428 ± 11	(Ni,Pt), (Ru)	~54 (Ni,Pt): ~44 (Ru)
LG 9	348 ± 17	(Ni,Pt), (Ru)	~45 (Ni,Pt), ~55 (Ru)
LG 10	319 ± 18	(Ni,Pt)	100 (Ni,Pt)

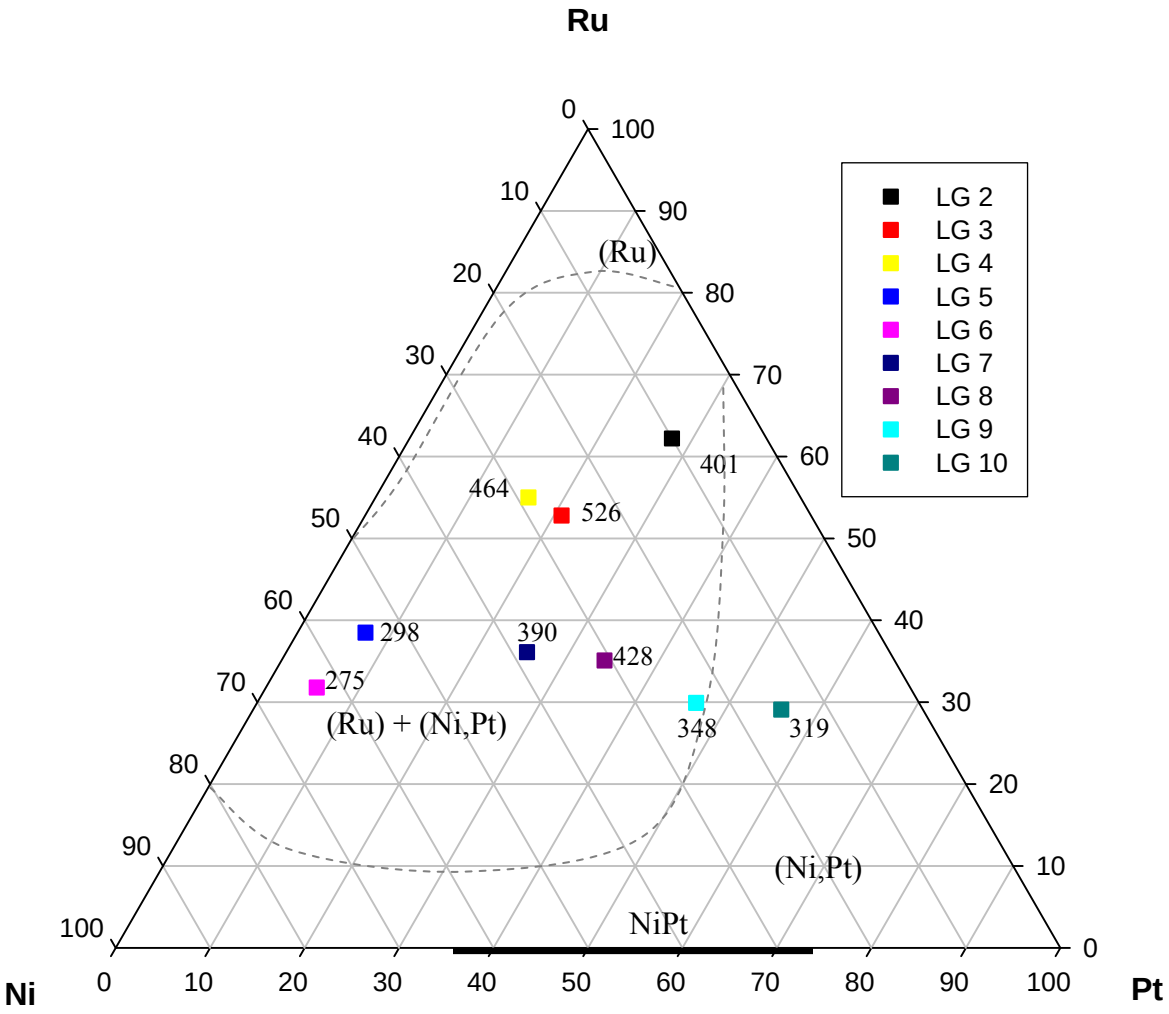


Figure 4.145. Hardness (HV_{10}) values of the heat treated Ni-Pt-Ru alloys superposed on the 1000°C isothermal section (at.%).

The various slip modes of the as-cast Ni-Pt-Ru alloys are shown in Figure 4.146 and are superposed on the solidification projection in Figure 4.147. No specific trend could be observed between the slip mode and the phase present in each sample. There was slight pin-cushioning on Alloys 2, 3, 5 and 6, which are in the two-phase region (although other alloys are in this region, and do not show pin-cushioning). Some of the indentations had irregular edges (LG 7, LG 8 and LG 10), and two of these (LG 7 and LG 8) had pile-up at the indentation edges.

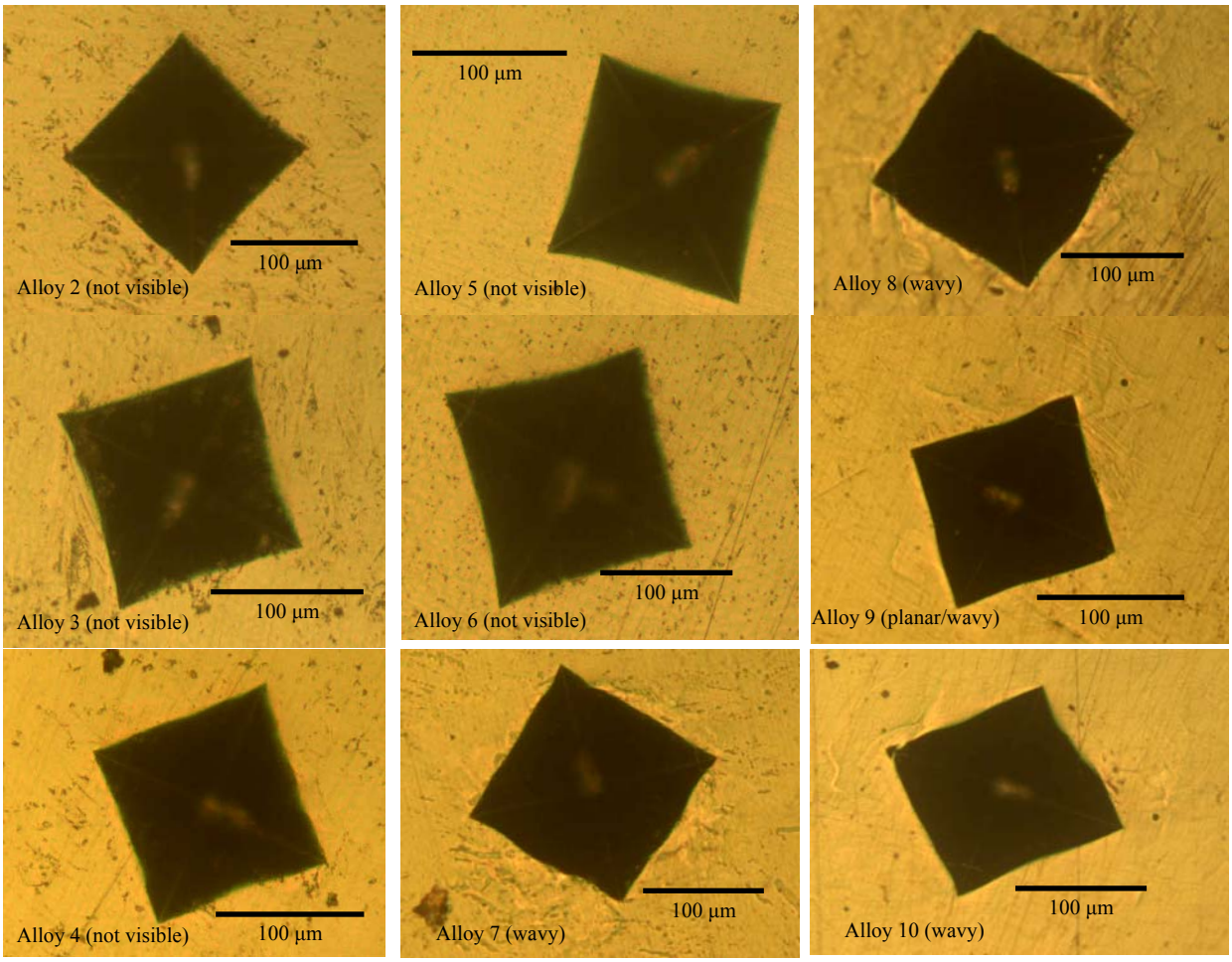


Figure 4.146. Micrographs of the hardness indentations in the Ni-Pt-Ru alloys (as-cast), showing the mode of slip.

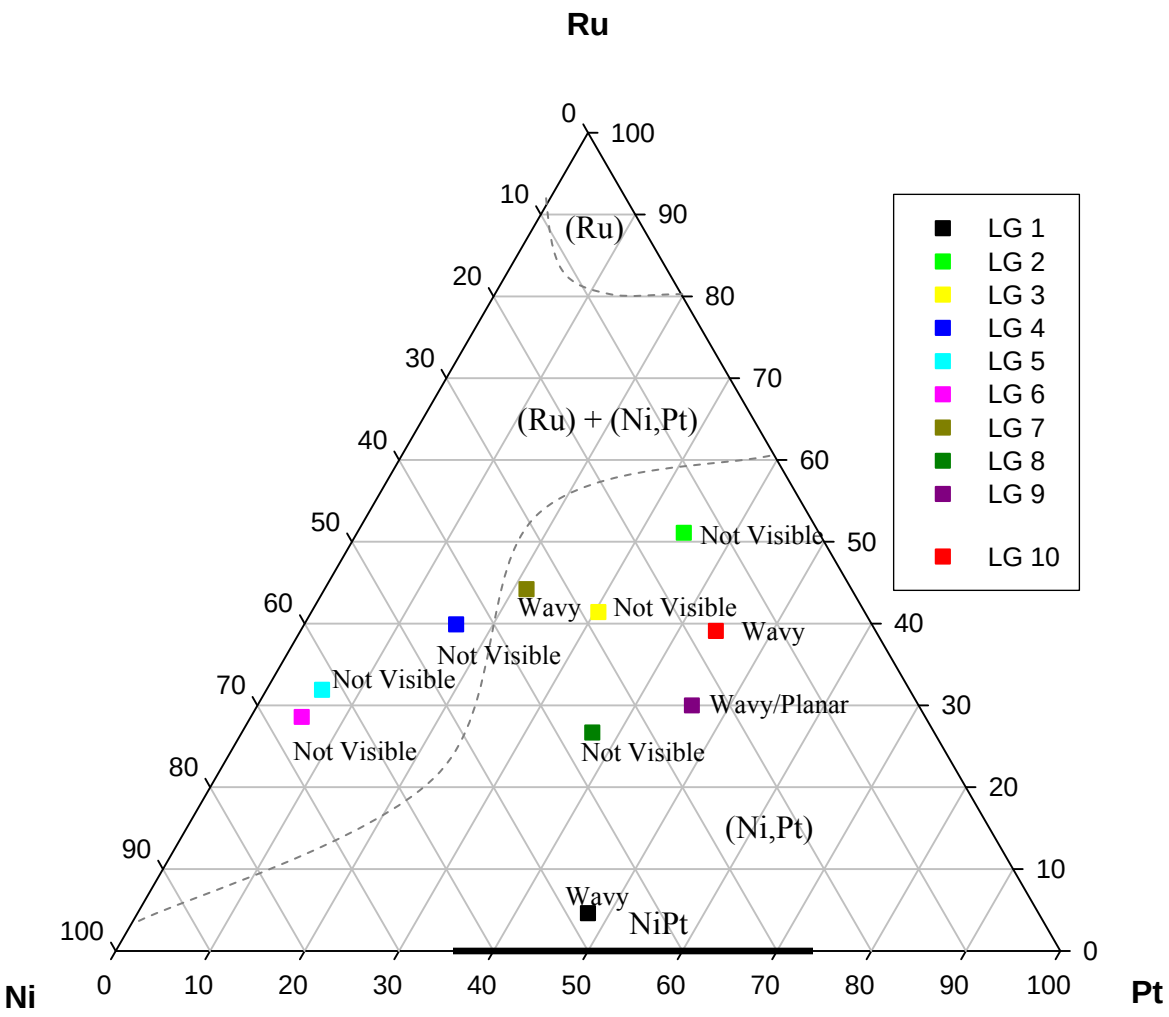


Figure 4.147. Mode of slip of the as-cast Ni-Pt-Ru alloys superposed on the solidification projection (at.%).

The various slip modes of the heat treated Ni-Pt-Ru alloys are shown in Figure 4.148 and is superposed on the solidification projection in Figure 4.149. The indentations were much more regular than those from the as-cast samples, and only LG 9 and LG 10 had slightly irregular indentations, and had a high proportion of fcc. Material pile-up at the indentation edge was seen in LG 7 and LG 8.

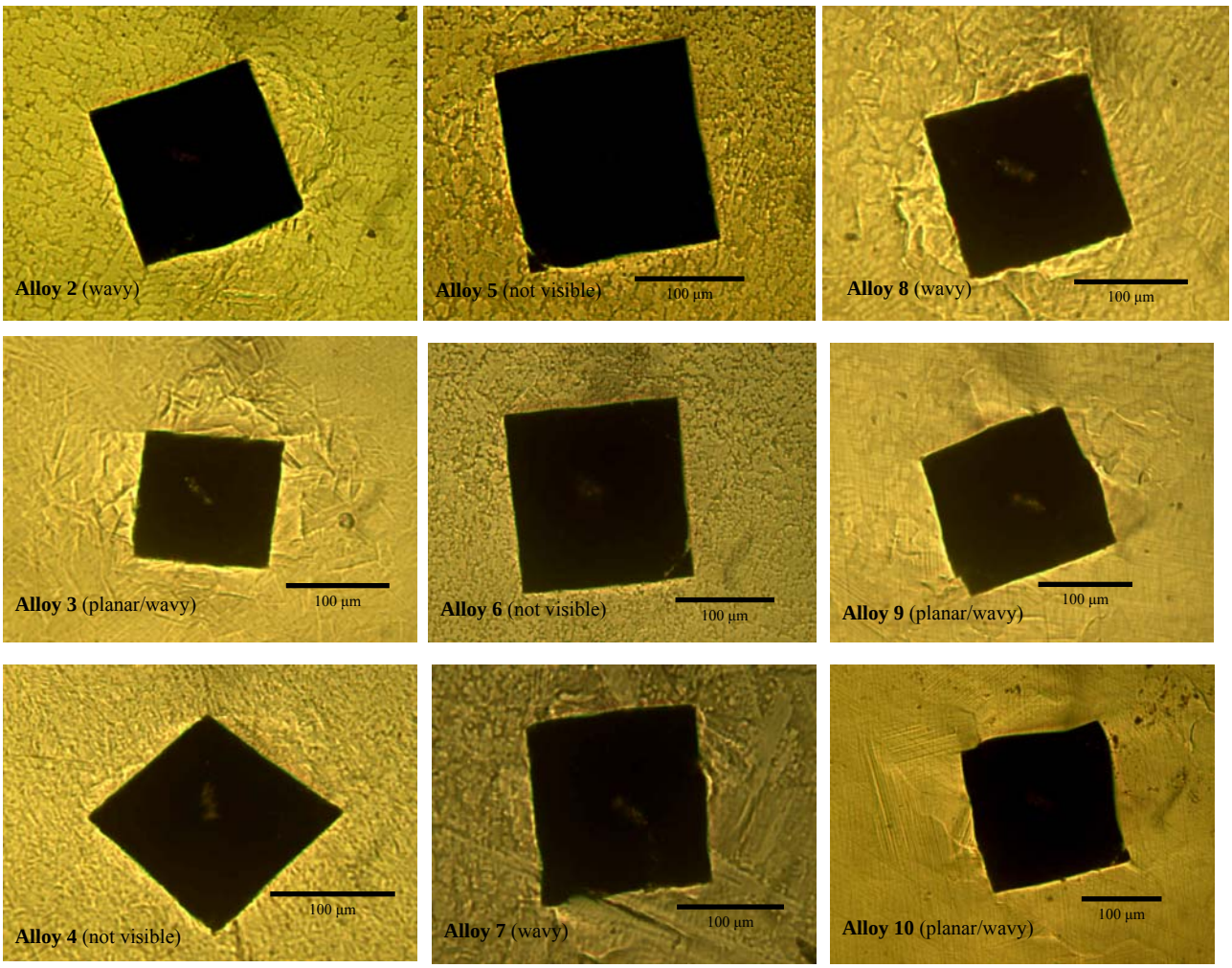


Figure 4.148. Micrographs of the hardness indentations in the heat treated Ni-Pt-Ru alloys, showing the mode of slip.

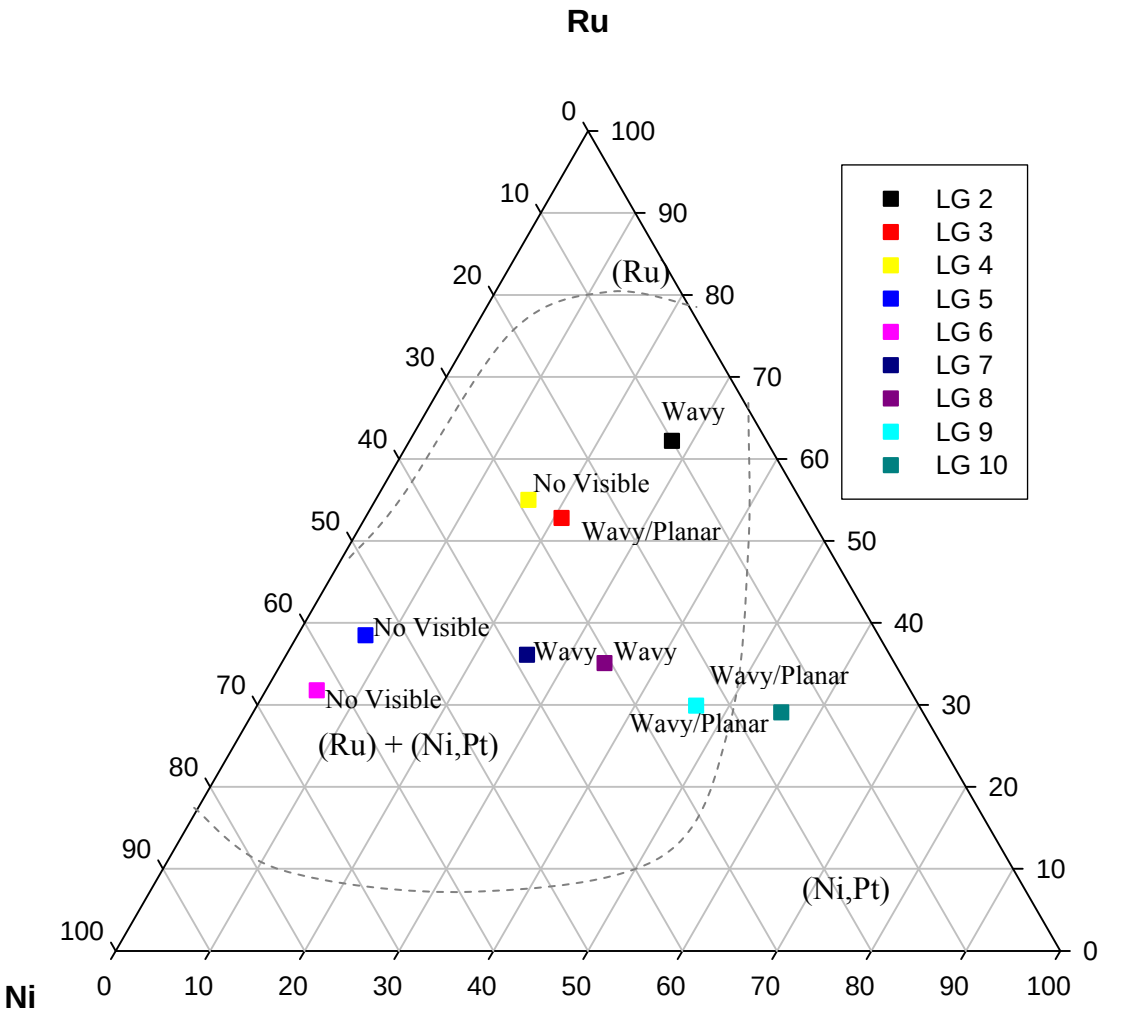


Figure 4.149. Mode of slip of the heat treated Ni-Pt-Ru alloys superposed on the 1000°C isothermal section (at.%).

The hardness for the as-cast and annealed alloys is compared in Table 4.57.

Table 4.57. Comparison of as-cast and heat treated hardness values.

Alloy	As-Cast Hardness (HV_{10})	Phase	Slip Mode	Annealed Hardness (HV_{10})	Phase	Slip Mode
Alloy 1	281 ± 26	(Ni,Pt)	Wavy	479 ± 23	NiPt	Wavy
Alloy 2	483 ± 21	(Ni,Pt)	Not visible	401 ± 40	(Ni,Pt), (Ru)	Wavy
Alloy 3	551 ± 11	(Ni,Pt)	Not visible	526 ± 22	(Ni,Pt), (Ru)	Planar/ wavy
Alloy 4	564 ± 38	(Ni,Pt), (Ru)	Not visible	464 ± 47	(Ni,Pt), (Ru)	Not visible
Alloy 5	567 ± 45	(Ni,Pt), (Ru)	Not visible	298 ± 12	(Ni,Pt), (Ru)	Not visible
Alloy 6	446 ± 67	(Ni,Pt), (Ru)	Not visible	275 ± 23	(Ni,Pt), (Ru)	Not visible
Alloy 7	426 ± 13	(Ni,Pt)	Wavy	390 ± 46	(Ni,Pt), (Ru)	Wavy
Alloy 8	390 ± 25	(Ni,Pt)	Not visible	428 ± 11	(Ni,Pt), (Ru)	Wavy
Alloy 9	362 ± 30	(Ni,Pt), (Ru)	Planar/ wavy	348 ± 17	(Ni,Pt), (Ru)	Planar/ wavy
Alloy10	319 ± 28	(Ni,Pt)	Wavy	319 ± 18	(Ni,Pt)	Planar/ wavy

The following changes took place after heat treating the as-cast alloys at 1000°C for 1000 hours:

LG 1 was made to check the extent of ordering in the (Ni,Pt) phase and was annealed at 500°C. It was relatively soft in the as-cast state (281 HV_{10}). Ordering was observed in the XRD spectrum in Figure 4.59.

The hardness of LG 2 decreased from 483 HV_{10} to 401 HV_{10}. The as-cast microstructure was single-phase (Ni,Pt) but changed to two-phased (Ru) and (Ni,Pt) after annealing. The phase proportions for the two phases are 40% (Ni,Pt) and 60% (Ru).

LG 3 consisted of single-phase (Ni,Pt) and changed to two-phased (Ru) and (Ni,Pt) after annealing. The hardness also decreased slightly from 551 HV_{10} to 526 HV_{10}. The slip mode became visible as planer and wavy slip. The proportions of the phase were 20% (Ni,Pt), 64% (Ru) and 16% mixture of fine (Ru) needles in a (Ni,Pt) matrix.

LG 4 was a two-phased alloy in both the as-cast and annealed states, but after annealing had lost considerable Ni. The hardness decreased from to 564 HV_{10} to 464 HV_{10}. The (Ru) and (Ni,Pt) structures coarsened during annealing and the slip mode was not visible in either condition. A new phase, NiO, was deduced to exist, which would account for the loss of Ni and the XRD pattern.

The hardness of LG 5 decreased from 567 HV_{10} to 298 HV_{10} during annealing. The two-phased (Ru) and (Ni,Pt) structure coarsened and the slip mode was not visible in either condition. The phase proportions are 60% (Ni,Pt) and 40% (Ru) before and after annealing.

The hardness of LG 6 decreased from 446 HV_{10} to 275 HV_{10} due to the coarsening of the two-phased [(Ru), (Ni,Pt)] structure The slip mode was not visible in either the as-cast or annealed conditions. The phase proportions changed significantly after annealing and would have contributed to the large drop in hardness (60% (Ni,Pt) and 40% (Ru) in the as-cast state, to 72% (Ni,Pt) and 28% (Ru) after annealing).

The hardness values of LG 7 decreased slightly from 426 HV_{10} to 390 HV_{10}. The as-cast (Ni,Pt) structure changed to a two-phase (Ru) and (Ni,Pt) structure. The slip mode remained wavy. The phase proportions are 60% (Ni,Pt) and 40% (Ru).

The hardness values of LG 8 increased slightly from 390 HV_{10} to 428 HV_{10}. The single-phase (Ni,Pt) became a two-phase (Ru) and (Ni,Pt) structure. The wavy slip mode remained unchanged. The phase proportions were 56% (Ni,Pt) and 44% (Ru).

LG 9 had no significant change in hardness (362 HV_{10} to 348 HV_{10}) and changed to (Ru) and (Ni,Pt) during annealing. The slip mode showed both planar and wavy behaviour in the as-cast condition, which remained unchanged after annealing. The phase proportions did not change significantly during heat treatment (32% (Ni,Pt) and 68% (Ru) for as-cast, to 45% (Ni,Pt) and 55% (Ru) after annealing).

LG 10 showed no change in hardness (319 HV_{10}) since it remained a single-phase (Ni,Pt) alloy. As in the as-cast condition, the slip mode showed planar and wavy behaviour after annealing.

No specific trend could be observed between the slip mode and the phase present in each sample. The alloys in the Ni-Pt-Ru system are tough and stay tough after heat treatment. This is confirmed

by the presence of the planar and wavy slip bands visible in most of the as-cast and heat treated alloys and the absence of cracking.

4.3.2 Co-Pt-Ru Hardness and Toughness

The results of the hardness measurements on the as-cast alloys are shown in Table 4.58 and the values are superposed on the solidification projection in Figure 4.150.

The alloys with the highest hardness are LG 15, LG 17, LG 18 and LG 19. These alloys all consisted of (Co,Pt) and (Ru). The softest alloys are LG 11 and LG 12. They are lying in the low Ru and high Pt/Co area of the (Co,Pt) phase. LG 13, LG 14 and LG16 are of mid-range hardness and lie in the high Co, low Ru area of the (Co,Pt) phase. LG 13 and LG 14 consisted of (Co,Pt) and ε(Co) phases.

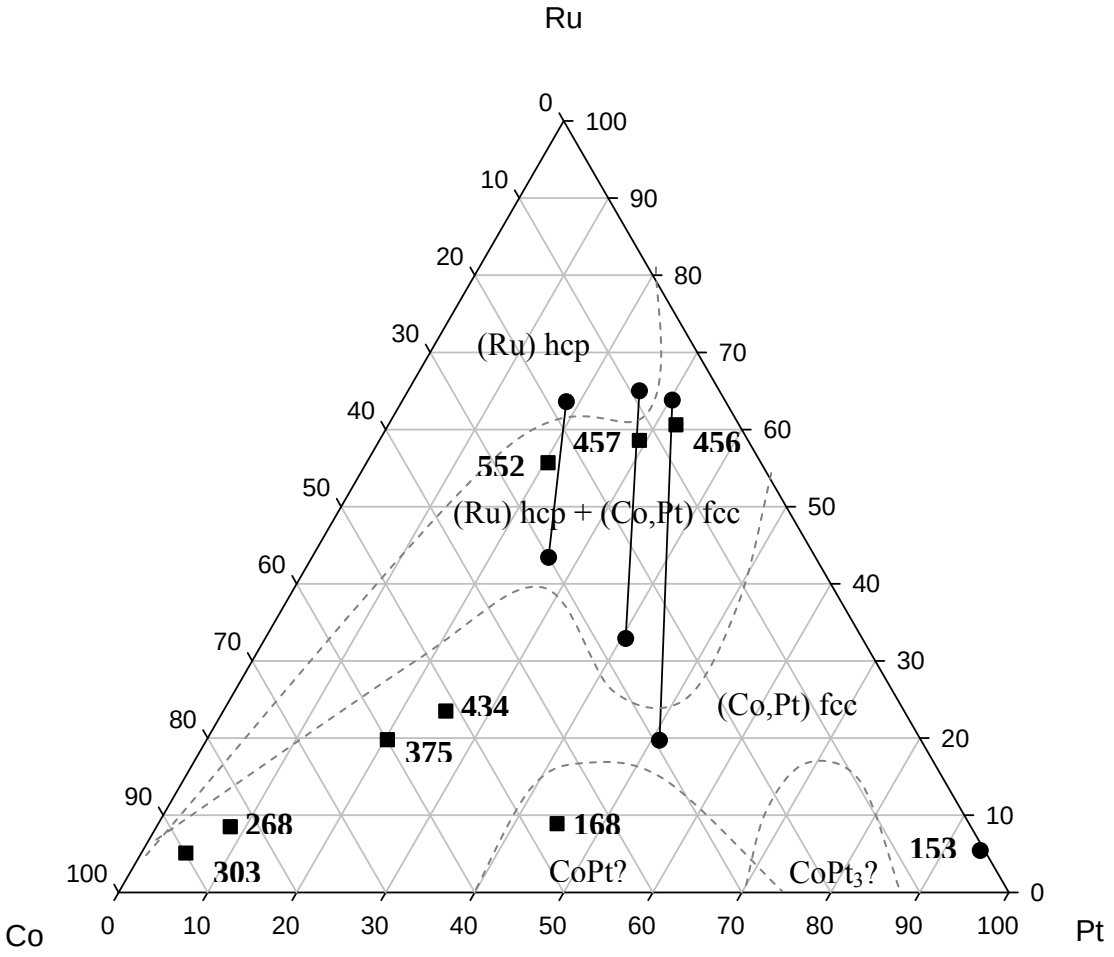


Figure 4.150. Hardness values (HV_{10}) of the as-cast Co-Pt-Ru alloys superposed on the solidification projection (at.%).

Table 4.58. Hardness values and phase proportions of the as-cast Co-Pt-Ru alloys.

Alloy	Hardness (HV_{10})	Phase	Phase Proportions (%)
LG 11	153 ± 12	(Co,Pt)	100 (Co,Pt)
LG 12	168 ± 5	(Co,Pt)	100 (Co,Pt)
LG 13	303 ± 43	(Co,Pt), ε(Co)	Higher proportion of ε(Co)
LG 14	264 ± 48	ε(Co)	100 ε(Co)
LG 15	552 ± 16	(Co,Pt), (Ru)	~60 (Co,Pt): `40 (Ru)
LG 16	375 ± 29	(Co,Pt)	100 (Co,Pt)
LG 17	456 ± 65	(Co,Pt), (Ru)	~20 (Co,Pt): ~80 (Ru)
LG 18	457 ± 25	(Co,Pt), (Ru)	~25 (Co,Pt): ~75 (Ru)
LG 19	434 ± 12	(Co,Pt), (Ru)	~60 (Co,Pt): ~40 (Ru)

The results of the hardness measurements on the heat treated alloys are shown in Table 4.59 (where "Mix" refers to a fine mixture of the two phases) and the values are superposed on the solidification projection in Figure 4.151.

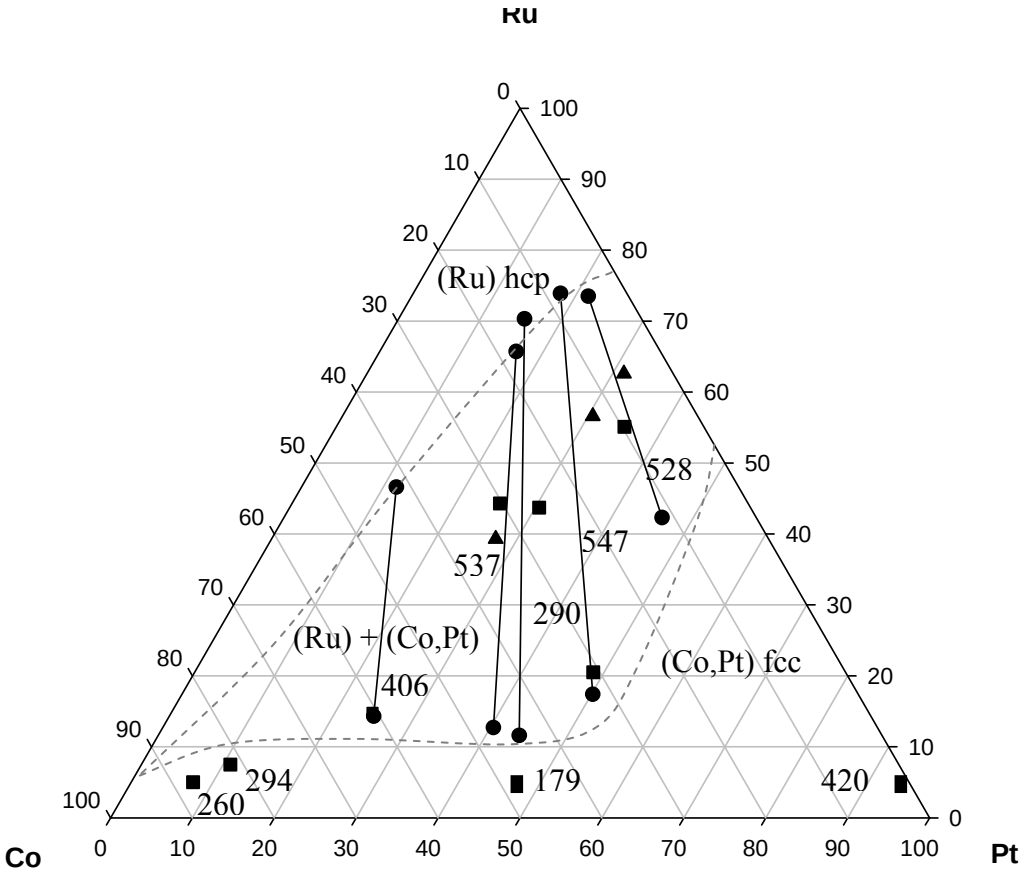


Figure 4.151. Vickers Hardness (HV_{10}) values for the heat treated Co-Pt-Ru alloys superposed on the 1000°C isothermal section.

Table 4.59. Hardness values of the heat treated Co-Pt-Ru alloys.

Alloy	Hardness (HV_{10})	Phase	Phase Proportions (%)
LG 11	420 ± 43	CoPt	100 CoPt
LG 12	179 ± 23	(Co,Pt)	100 (Co,Pt)
LG 13	260 ± 40	(Co,Pt), ε(Co)	Higher proportion of ε(Co)
LG 14	294 ± 14	(Co,Pt), ε(Co)	~50 (Co,Pt): ~50 ε(Co)
LG 15	290 ± 36	(Co,Pt), (Ru)	~30 (Co,Pt): ~30 (Mix): ~40 (Ru)
LG 16	406 ± 9	(Co,Pt), (Ru)	~70 (Co,Pt): ~30 (Ru)
LG 17	528 ± 15	(Co,Pt), (Ru)	~40 (Co,Pt): ~50 (Mix): ~10 (Ru)
LG 18	547 ± 11	(Co,Pt), (Ru)	~20 (Co,Pt): ~60 (Mix): ~20 (Ru)
LG 19	537 ± 41	(Co,Pt), (Ru)	~20 (Co,Pt): ~50 (Mix): ~30 (Ru)

The hardness indentations and slip modes for the as-cast alloys are shown in Figure 4.152 and the values are superposed on the solidification projection in Figure 4.153. The indentation for LG 14 shows a prior scratch. There were slightly irregular indentations for LG 11, LG 12, LG 16 and LG 19. Slight pin-cushioning was observed in LG 13, LG 14, LG 18 and LG 19.

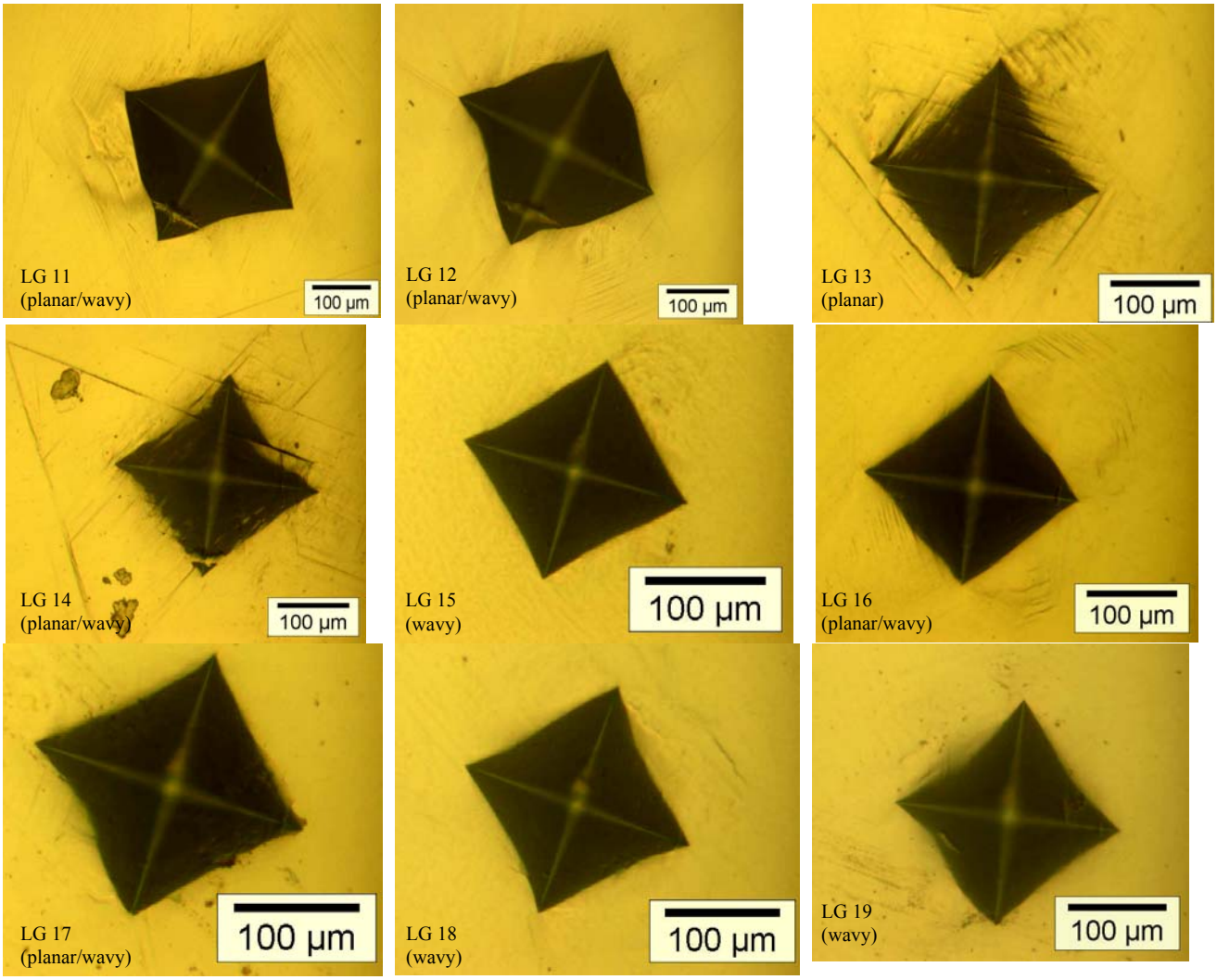


Figure 4.152. Micrographs of the hardness indentations in the as-cast Co-Pt-Ru alloys showing the mode of slip.

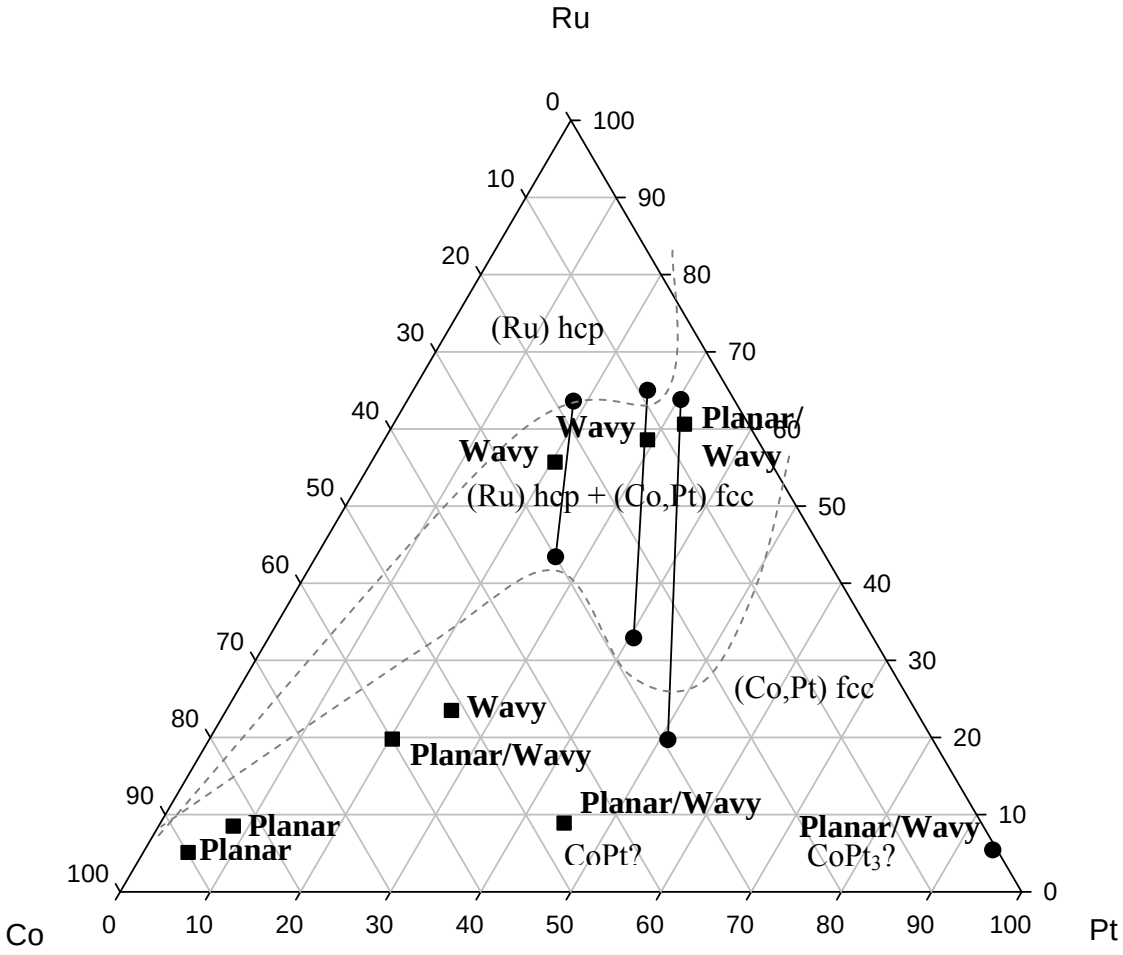


Figure 4.153. Mode of slip of the as-cast Co-Pt-Ru alloys superposed on the solidification projection (at.%).

The hardness indentations and slip modes for the heat treated alloys are shown in Figure 4.154 and the values are superposed on the isothermal section in Figure 4.155.

The indentations for LG 13 and LG 14 show both planar slip and pin-cushioning. Alloys LG 15, LG 16, LG 17 and LG 18 and LG 19 show slight pin-cushioning. The crack on the diamond indentor can be clearly seen in LG 13 and LG 14.

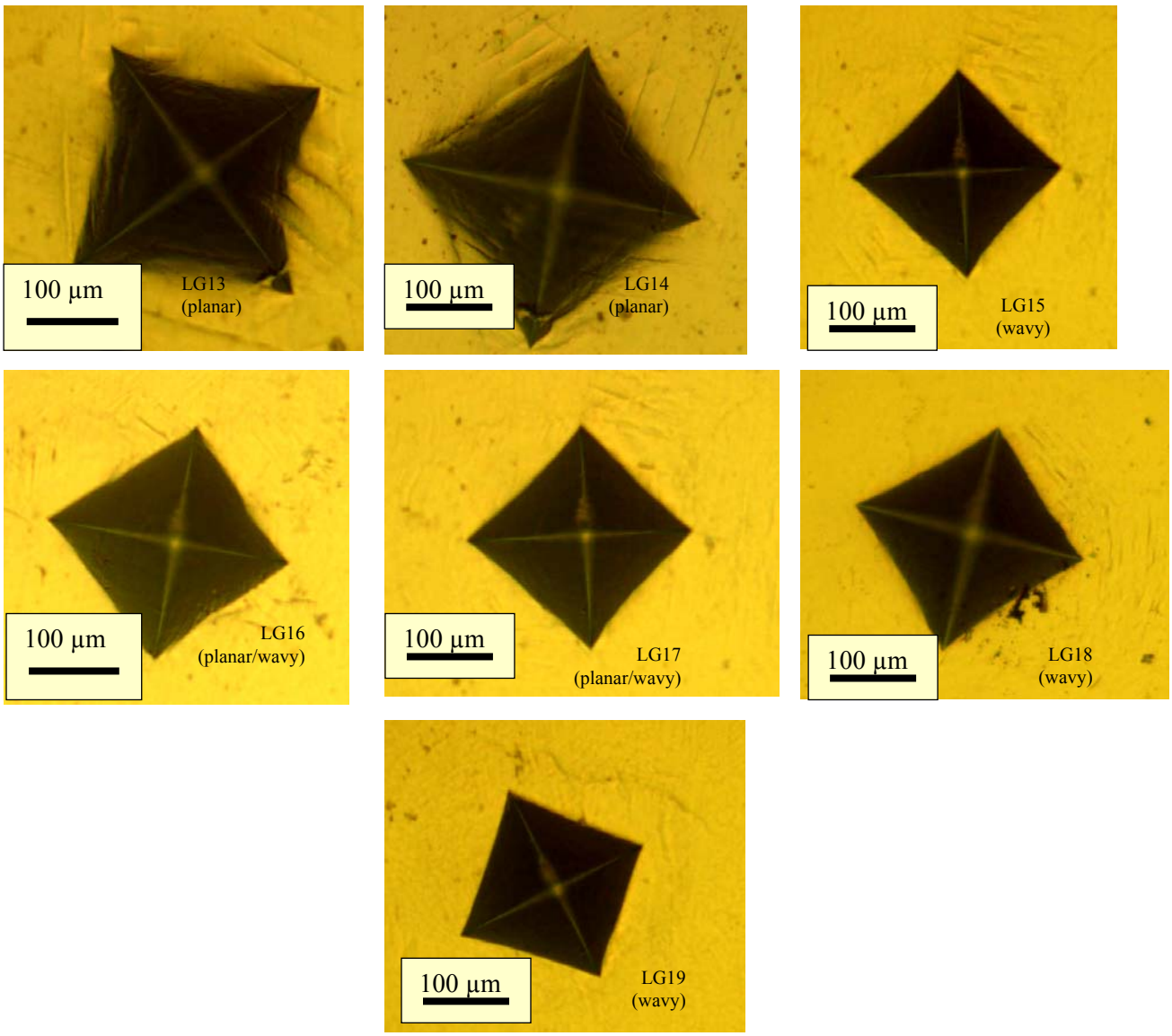


Figure 4.154. Micrographs of the hardness indentations in the heat treated Co-Pt-Ru alloys showing the mode of slip.

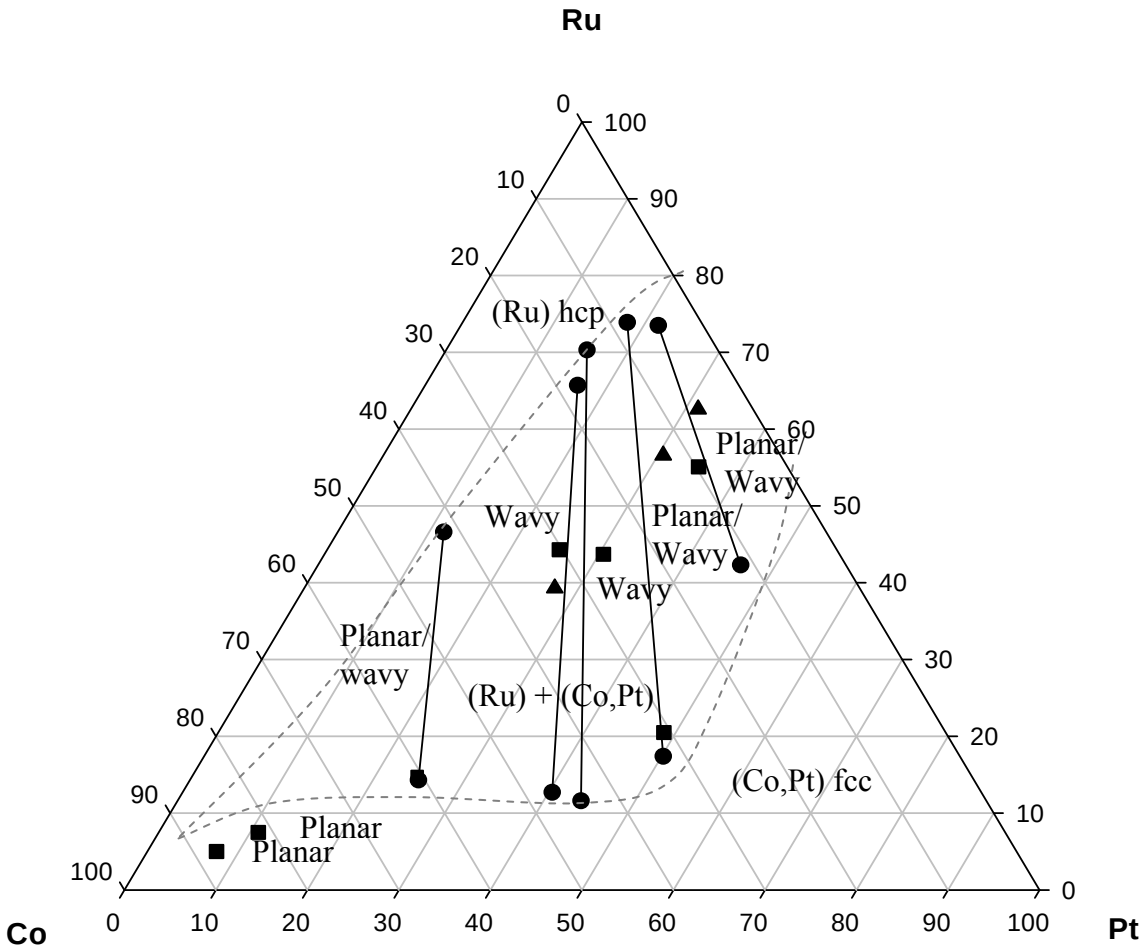


Figure 4.155. Slip modes for the heat treated Co-Pt-Ru alloys superposed on the 1000°C isothermal section (at.%).

A comparison of the as-cast and heat treated hardness values and slip modes is shown in Table 4.60. The hardness values for alloys LG 13 and LG 14 changed slightly after heat treatment, while the slip modes stayed the same. The microstructure of Alloy LG 15 coarsened after heat treatment, which could have lead to the large drop in hardness, whilst the slip mode was the same.

Alloy LG 16 changed after heat treatment from a single phase alloy to a two-phased alloy. This could explain the increase in hardness, while the slip mode stayed unchanged.

Alloys LG17, LG18 and LG19 stayed two-phased after heat treatment. The only difference was that there was a very prominent dark needle-like (Ru) structure afterwards. This might be the cause of the increase in hardness. No change in slip mode was observed.

Table 4.60. Hardness values of the as-cast Co-Pt-Ru alloys.

Alloy	**Hardness (HV_{10}), As-cast**	**Phase**	**Slip Mode**	**Hardness (HV_{10}), Heat treated**	**Phase**	**Slip Mode**
LG 11	153 ± 12	(Co,Pt)	Planar/wavy	420 ± 43	CoPt	Planar/wavy
LG 12	168 ± 5	(Co,Pt)	Planar/wavy	179 ± 23	(Co,Pt)	Planar/wavy
LG 13	303 ± 43	(Ni,Pt)	Planar	260 ± 40	(Co,Pt)	Planar
LG 14	264 ± 48	(Co,Pt))	Planar	294 ± 14	(Co,Pt))	Planar
LG 15	552 ± 16	(Co,Pt), (Ru)	Wavy	290 ± 36	(Co,Pt), (Ru)	Wavy
LG 16	375 ± 29	(Co,Pt)	Planar/wavy	406 ± 9	(Co,Pt), (Ru)	Planar/wavy
LG 17	456 ± 65	(Co,Pt), (Ru)	Planar/wavy	528 ± 15	(Co,Pt), (Ru)	Planar/wavy
LG 18	457 ± 25	(Co,Pt), (Ru)	Wavy	547 ± 11	(Co,Pt), (Ru)	Wavy
LG 19	434 ± 12	(Co,Pt)	Wavy	537 ± 41	(Co,Pt), (Ru)	Wavy

5. Discussion

5.1 Solidification Projection of the Ni-Pt-Ru System

Figure 5.1 shows the solidification projection for the Ni-Pt-Ru system, i.e. the phase compositions in the as-cast alloys. Both (Ru) and (Ni) phase boundaries show deflections and the directions are consistent with each other. Alloys LG 3 and LG 7 were mainly single-phase fcc (Ni,Pt), but also contained small amounts of (Ru). Alloy LG 8 consisted of a cored (Ni,Pt) matrix and also contained a small amount of (Ru). The (Ru) was formed on solidification, at the edges of the dendrites. This shows that the liquidus surface tilts towards the Ru corner. Whenever (Ru) is formed where it is not expected, it shows that the (Ni,Pt) solvus moves back towards the Pt corner in the ternary. This is in agreement with the Pt-Ru binary [1990Mas], where the solvus retreats ~8 at.% Pt after solidification, and especially with the Ni-Ru binary [1990Mas] where the solvus retreats ~30 at.%.

In Alloys LG 2, LG 3, LG 8, LG 9 (minimally) and LG 10 all showed overall composition analyses which were not on the tie-lines between the analysed phases as well as minor XRD peaks for (Ru). Thus, (Ru) was present in small amounts, and these samples must lie in the (Ni,Pt) + (Ru) two-phase field, and the projection is drawn showing this, with the boundary very close to LG 8, LG 9 and LG 10.

5.2 Isothermal section of the Ni-Pt-Ru system at 1000°C

The 1000°C isothermal section for the Ni-Pt-Ru system is shown in Figure 5.2. This was established by heat treating Alloys LG 2 – LG 10 at 1000°C at 1000 hours and water quenching. Alloys LG 2 – LG 3 and LG 7 – LG 9 were all single-phased in the as-cast condition and became two-phased after heat treatment. Alloys LG 4 – LG 6 stayed two-phased despite the heat treatment. LG 10 did not change after heat treatment and stayed single-phase and retained some of the coring. Some of the previously single-phase as-cast alloys showed the presence of a third phase after heat treatment. An explanation for this third phase could be a local change in microstructure caused by the precipitation of (Ru) with a high Ru content or pure Ru needles in regions with higher Ru content. These needles were very fine, and so beyond the capability of EDX to analyse accurately, which would have lowered the Ru content since X-rays were also collected from the surrounding matrix. This would have given values intermediate between (Ru) and (Ni,Pt), which could explain the analyses around ~Ni_{20}: Pt_{30}: Ru_{50} to ~Ni_{10}: Pt_{50}: Ru_{40}. However, all the XRD spectra showed

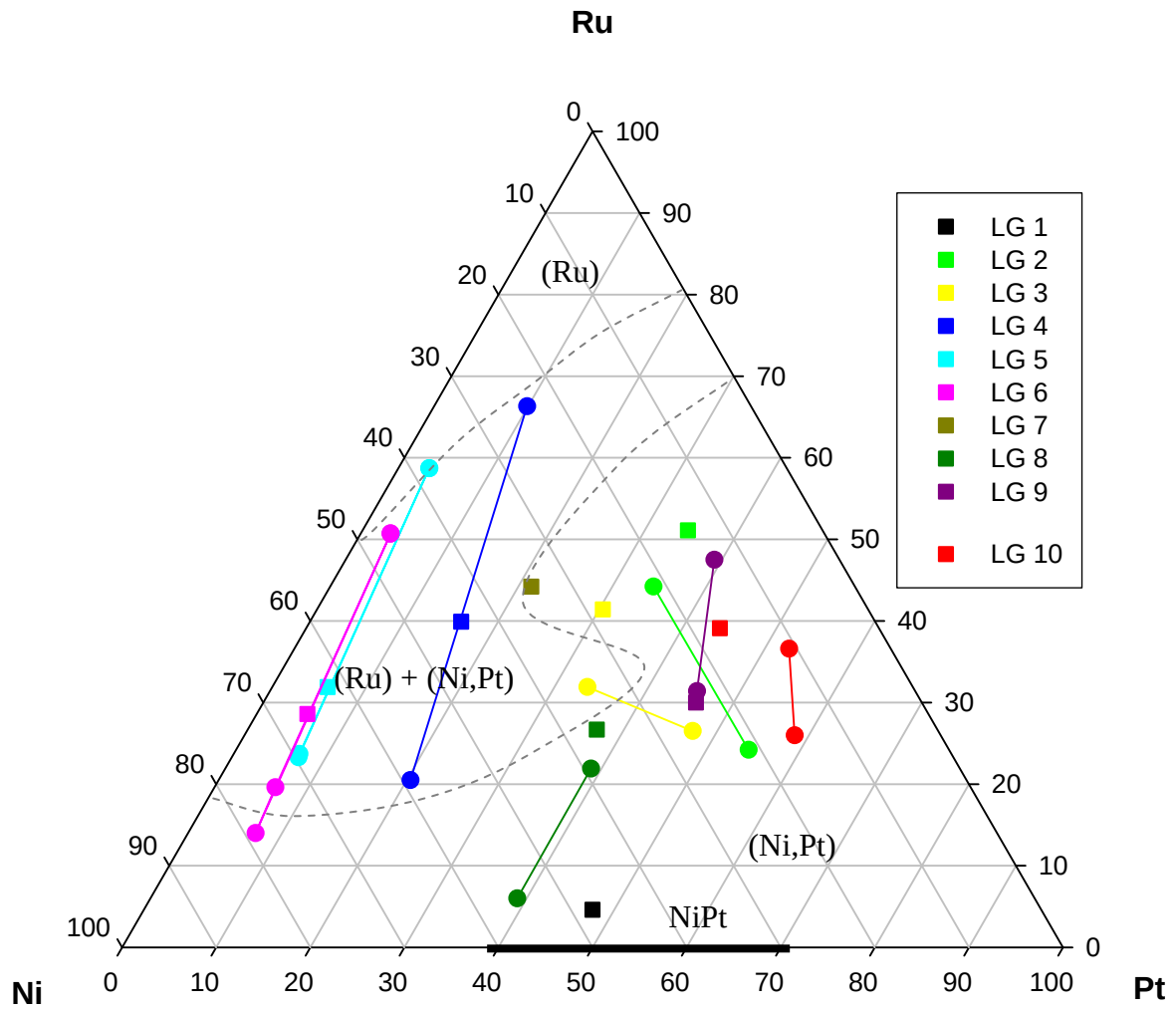


Figure 5.1. Solidification projection for the Ni-Pt-Ru system (at.%), where filled circles are phases and filled squares are overall alloy compositions.

extra peaks which did not match up with any of the phases from the component binaries, thus showing that a new phase was present. The EDX spectrum showed small peaks for oxygen and so it was deduced that the peaks were related to NiO since this would be the most easiest oxide to form (Pt being more unreactive, and Ru having only a volatile oxide), even though the matches to the XRD peaks were not perfect. One analysis of a larger dark phase needle in LG 8 showed that it was (Ru), but this does not necessarily mean that the fine needles were (Ru).

Currently, it is accepted that the fine needles are probably an oxide related to Ni, although this does not explain why the analyses lie between (Ni,Pt) and (Ru). One explanation could be that the fine needles are (Ru), which explains their similar contrast to the larger (Ru) needles, and that the analyses lie between (Ru) and (Ni,Pt). However, this does not explain why the sample overalls do not lie on the tie-lines between the phase analyses. An explanation of this could be that the Ni oxide lies on the surface of the (Ni,Pt) phase, and so would compromise the overall analyses and those of

the (Ni,Pt) phases where the oxide is present. This would explain why the sample overall analyses do not always lie on the tie-lines between the phases.

Alternatively, since the third phase analyses lie on the locus from ~Ni_{20}: Pt_{30}: Ru_{50} to ~Ni_{10}: Pt_{50}: $Ru_{40,}$ this implies that a third phase is actually present here, although the analyses could arise from a fine mixture of (Ru) and (Ni,Pt) (due to the fine structure as described above). Another indication of a third phase is that it only appears in the samples with phase compositions crossing the locus. If the phase was a Ni oxide, it should be more apparent at high Ni contents, e.g. LG 6, but it was not. The microstructure of LG 9 should have been coarse enough to analyse accurately, but this gave the darker phase as being within the locus of the third apparent phase. Interestingly, the light (Ni,Pt) phase had larger errors (up to 4 at.%) than the dark phase (just over 1 at.%). One interpretation is that a miscibility gap is present in (Ni,Pt).

LG 9 has the extra peaks, while LG 10, which has a similar and coarse microstructure, has only fcc peaks, although they are fairly broad. The errors on the phase analyses of LG 10 are large, up to 6.3 at.%. This sample suggests that there is a miscibility gap in (Pt), so that two different phase compositions are found, with only one fcc structure. If this was the case, then there would be a three-phase field between the two fcc compositions and (Ru) at a higher Ni content, for example as seen in LG 9. This would mean that the locus of the third phase would be: ~Ni_{20}: Pt_{30}: Ru_{50} to ~Ni_{18}: Pt_{39}: Ru_{43}, and the three phase field between the two fcc and (Ru) would lie immediately to the right of this in Figure 5.2. This is the interpretation given in Figure 5.2.

With the current alloys, the problem of the third phase cannot be solved, and it also appears that the Ni oxide does only forms at intermediate Ni,Pt values and not at either high or low Ni contents. Ideally, a sample within the apparent third phase composition range needs to be manufactured, and studied to resolve this issue.

After annealing at 500°C, there was ordering in the ternary up to 5.2 at.% Ru. More alloys of higher Ru contents would be needed to ascertain the limiting Ru content for ordering.

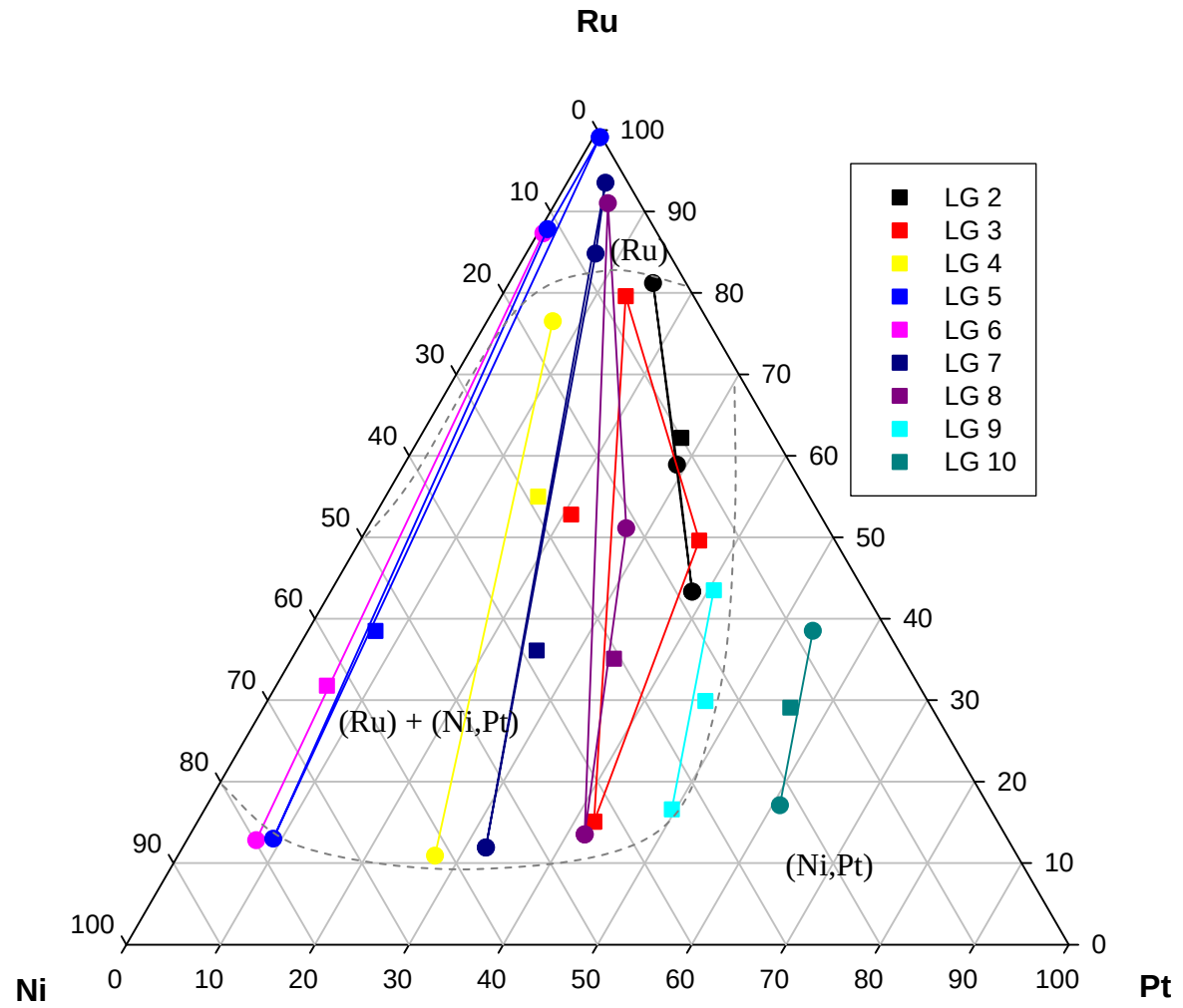


Figure 5.2. 1000°C isothermal section of the Ni-Pt-Ru system (at.%), where filled circles are phases and filled squares are overall alloy compositions.

5.3 Solidification Projection of the Co-Pt-Ru System

The solidification projection for the Co-Pt-Ru system is shown in Figure 5.3. Alloys LG 15, LG 17, LG 18 and LG 19 are lying in the two-phase region (Ru) + (Co,Pt). The phase boundaries of the two phases show curving which enlarges the two-phase area. The rest of the alloys (LG 11, LG 12, LG 13, LG 14 and LG 16) are single phase alloys.

Alloys LG 13, LG 14, LG 16 and LG 19 consisted of the (εCo,Pt) phase since the XRD peaks for the εCo (hexagonal) phase were a good fit to the measured XRD patterns. Both the Co-Pt and Co-Ru show a transformation from α→ε (Figures 2.4 and 2.5 [1990Mas]). In the Co-Ru system at ~90 at.% Co, the transformation takes place at ~800°C [1990Mas], and in the Co-Pt system at ~90 at.%

Co, there is a magnetic transformation α→ε at ~1100°C [1990Mas]. In Co-Pt, the hcp/fcc (ε→α) phase transformation takes place at ~650°C, and is a direct transformation, whereas in Co-Ru, the phase change occurs as a peritectic reaction [1990Mas].

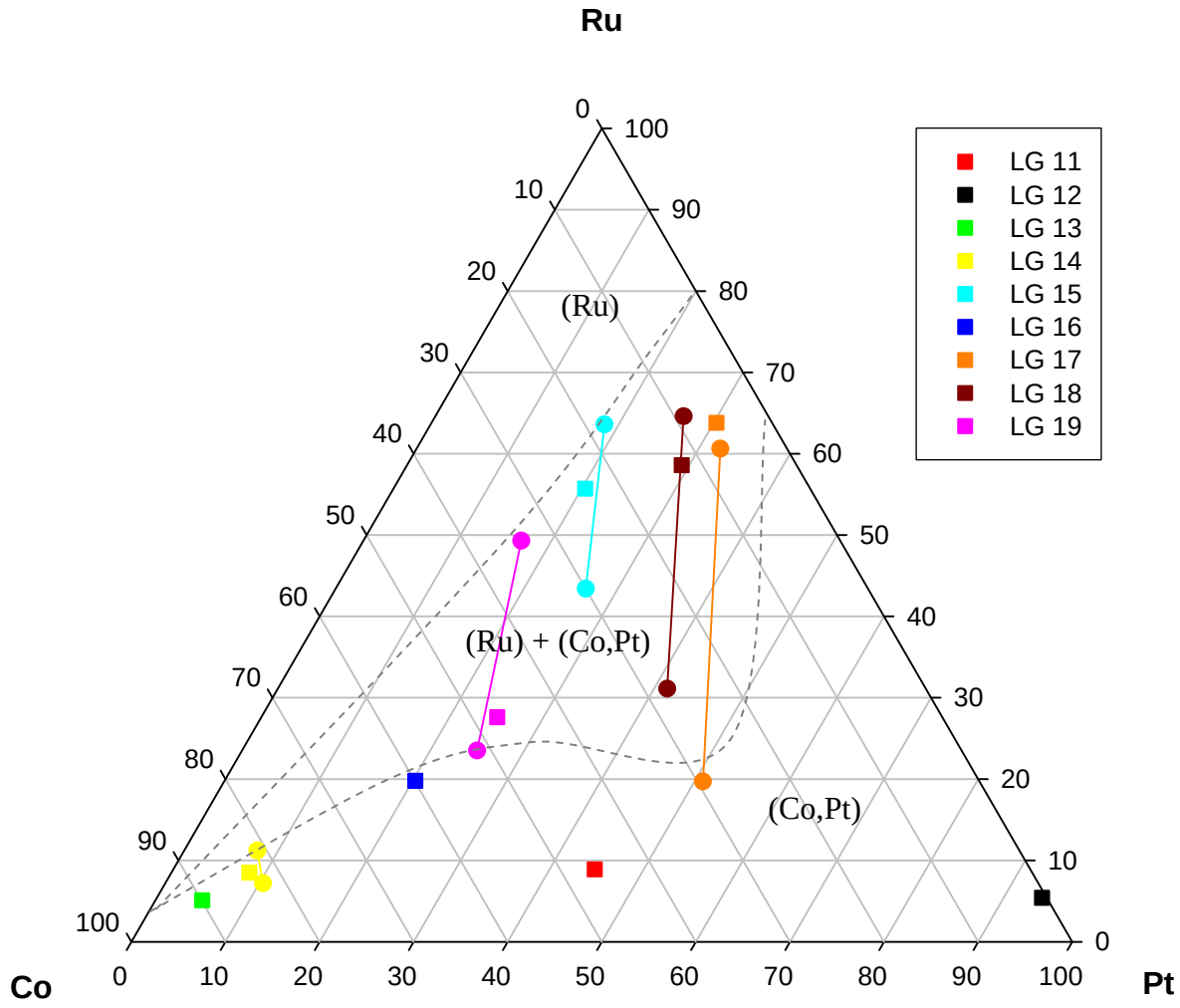


Figure 5.3. Solidification projection of the Co-Pt-Ru system (at.%), where filled circles are phases and filled squares are overall alloy compositions.

The XRD data indicating the presence of ε(Co) shows that the ε(Co) phase is stabilised in the ternary system. Many alloys showed two-phase structures, and Alloys LG 14, LG 15, LG 17 and LG 19 had microstructures demonstrating the L + (Ru) → fcc(Co,Pt) peritectic reaction.

5.4 1000°C Isothermal Section of the Co-Pt-Ru System

The 1000°C isothermal section for the Co-Pt-Ru system in shown in Figure 5.4. The apparent data point of Alloys LG 15, LG 17, LG 18 and LG 19 from fine needles in a two-phase region. Alloys

LG 13 and LG 14 appeared single-phase after heat treatment but still consisted of ε(Co) and fcc (Co,Pt). LG 16 changed from a single-phase Co-rich (Co,Pt) alloy to a two-phase alloy consisting of dark (Ru) needles in a light (Co,Pt) matrix. As-cast alloys LG 15, LG 17, LG 18 and LG 19 consisted of (Ru) and (Co,Pt), whereas in the heat treated condition, the dark (Ru) phase became more prominent in the form of a needle-like structure, ranging greatly in size. The two-phase area on the isothermal section became larger with the phase extent of the fcc (Co,Pt) becoming less. The deflection in the phase boundary between the two-phase area and the (Ru) straightened out and the (Ru) region became slightly smaller.

LG 11 was manufactured to verify the extent of the CoPt ordering. Comparison to database [2005ICD] showed that the peaks were similar to disordered fcc, although the positions were different, showing a larger lattice parameter. The lack of extra peaks in an ordered structure compared to the random or disordered structure might be considered unusual, because these superlattice peaks result from the atoms occupying set positions and thus changing the structure factor for the unit cell [1978Cul]. However, this can be explained because the structure of CoPt was given as *tP*4 *P*4/*mmm with the* AuCu prototype [1990Mas], which has different atoms in the two different positions, thus giving no change in the structure factor, and only changing the structure from cubic to tetragonal. This is achieved by the different element atoms forming alternating layers.

The structure of LG 19 was quite different from the other alloys in that the needles appeared light in contrast, whereas the other needles precipitated on heat treatment were dark (Ru). Comparison to the ordered sample, LG 11, showed that although no extra peaks were given in the XRD database [2005ICD], the lattice parameter for CoPt was different from (Co,Pt) so that ordering could be recognized in both samples. The CoPt for LG 19 had lower intensities, indicating that the CoPt phase was a minor component. Apart from the peak at 2θ = ~13°, which was derived from plasticene, the CoPt phase accounted for all the otherwise unidentified XRD peaks in LG 19.

The LG 12 sample had been made to ascertain the extent of the $CoPt_3$ ordered phase into the ternary. However, the sample had lost (or never had) all Co, and so could not be utilised for this purpose. The microstructure was apparently single phase, but there were extra peaks to (Pt), which could not be identified. Since heat treatment caused precipitation of (Ru) precipitates, this demonstrated that the fcc (Co,Pt) solvus was sloping, and retreated to lower Ru contents at lower temperatures.

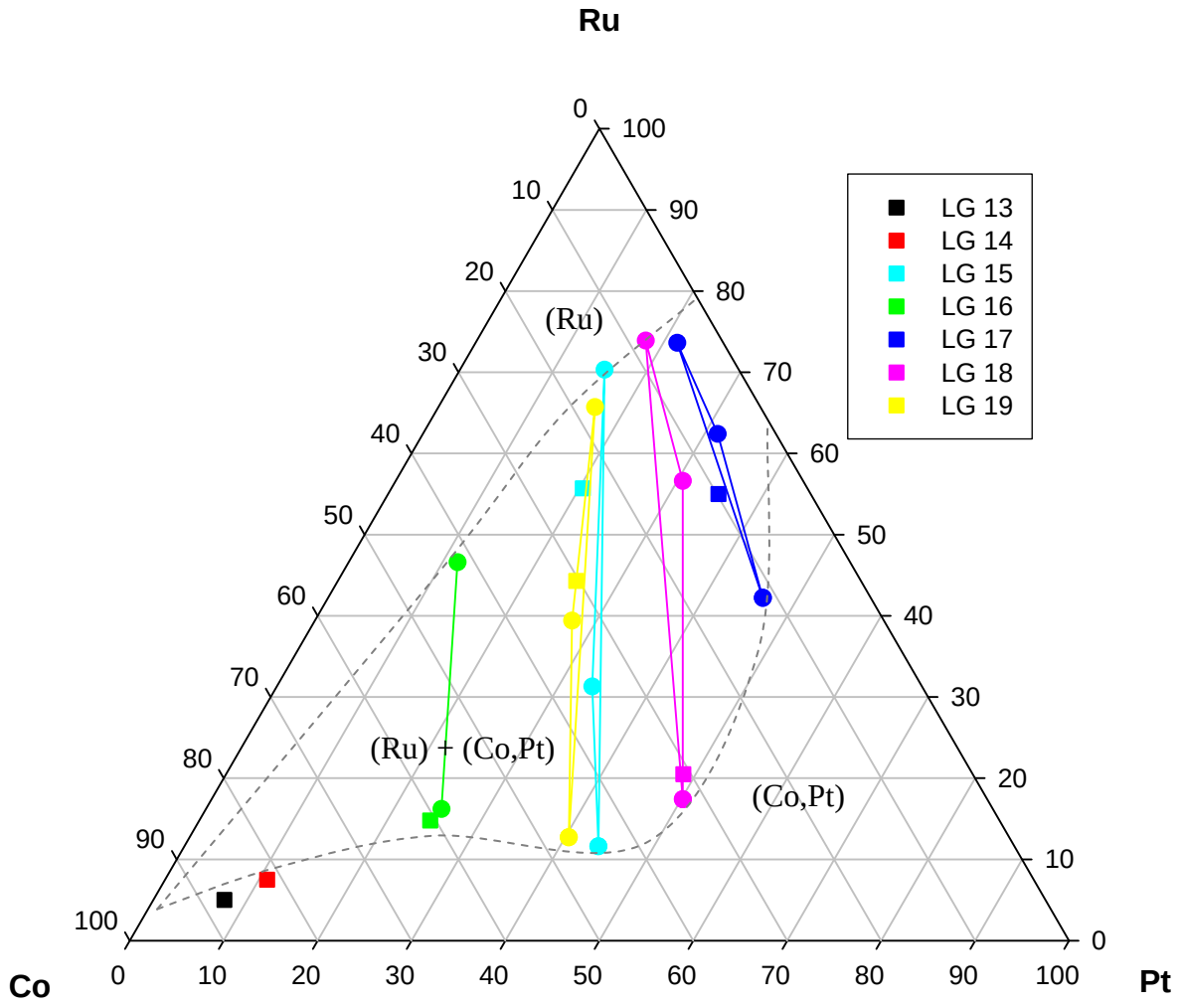


Figure 5.4. 1000°C Isothermal section for the Co-Pt-Ru system (at.%), where filled circles are phases and filled squares are overall alloy compositions.

5.5 Mechanical Properties of the Ni-Pt-Ru System

The hardness of the alloys in the Ni-Pt-Ru system shows that softening mostly occurs during heat treatment. This is true even for the alloys that became two-phased after annealing. Nearly all the hardnesses decreased after annealing except LG 1. However, LG 8 showed a slight increase that is probably within experimental error. The reduced hardnesses could be attributed to the fact that coring is being removed, and any strain associated with fast cooling (due to the arc-melting manufacture) in the phases is also reduced or removed. In addition, grain growth might have taken place. The drop in hardness in the two-phased alloys could be explained by the coarsening of the different phases during annealing.

Alloys LG 7 and LG 8 had material pile-up at the edges and were lying right in the middle of the two-phase region. The reason for not seeing any slip in most of the alloys is that there are no intermetallic compounds in the alloys. All the alloys have the fcc phase that allowed for easy deformation as well as reasonable toughness. The irregular hardness indentations are due to the nature of the two-phase alloys. The two phases deform in different ways.

5.6 Mechanical Properties for the Co-Pt-Ru System

The hardness of Alloy LG 11 increased significantly after annealing from 153 HV_{10} to 420 HV_{10} and according to the XRD spectrum in Figure 4.139 the fcc ordered phase CoPt formed. The hardnesses for Alloys LG 12, LG 13, LG 14 and LG 16 did change a little, but the changes were within the experimental errors.

There was a significant drop in hardness for Alloy LG 15 after annealing. Although the microstructure stayed two-phase, there was a significant change in the size and distribution of the (Ru) needles after annealing. Larger agglomerated (Ru) formed with small needles that precipitated within the (Co,Pt) matrix. The decrease in hardness can be attributed to coarsening of the microstructure after heat treatment. The hardnesses for Alloys LG 17, LG 18 and LG 19 appeared to have increased, but some of these increases were within the experimental errors. The slip modes for all the alloys stayed the same and since all of the alloys contained the fcc (Co,Pt) phase the toughness are reasonable.

6. Conclusions

Ni-Pt-Ru System

The solidification projection for Ni-Pt-Ru show that both (Ru) and (Ni,Pt) phase boundaries have deflections and their directions are consistent with each other. In the samples where (Ru) is formed where it is not expected, it shows that the (Ni,Pt) solvus moves back towards the Pt corner in the ternary.

After heat treatment of the as-cast alloy, some of the previously single-phase as-cast alloys showed the presence of a third phase after heat treatment. This third phase appears to lie on the locus from ~Ni_{20}: Pt_{30}: Ru_{50} to ~Ni_{10}: Pt_{50}: Ru_{40}. Alloy LG 10 has a coarse two-phase structure with large experimental errors. This suggests that there is a miscibility gap in the (Pt) with two different phase compounds but with only one fcc structure.

After the heat treatment at 500°C, Alloy LG 1 became ordered and the hardness increased. The hardness of the other alloys in the Ni-Pt-Ru system shows that softening mostly occurs during heat treatment. This is the result of coring and strain being reduced, coarsening of the two-phase structure and possible grain growth. The alloys are also reasonably tough because of the fcc phase that occurs in all of them.

Co-Pt-Ru System

The XRD data indicating the presence of ε(Co) shows that it is stabilised in the ternary system, both in the as-cast and annealed alloys. Many of the as-cast alloys showed two-phase structures demonstrating the L + (Ru) $\rightarrow$ fcc(Co,Pt) peritectic reaction.

Ordering took place after annealing at 500°C in Alloy LG 11 and to some extent in Alloy LG 19. Since heat treatment caused precipitation of (Ru) precipitates in many of the alloys, this demonstrated that the fcc (Co,Pt) solvus was sloping, and retreated to lower Ru contents at lower temperatures.

The hardness of the alloys appeared to have not changed significantly after heat treatment, with the exception of Alloys LG 11 and LG 15. Alloy LG 11 had a large increase due to the ordering that

took place. In the case of Alloy LG 15 there was a decrease due to a significant change in the size and distribution of the two phases in the sample. The toughness remained reasonable for al the alloys as a result of the presence of the fcc phase in all of them.

7. Recommendations

- There is a possible third phase in the Ni-Pt-Ru system that needs to be explored. A sample needs to be made up on the locus of this third phase at ~Ni_{20}: Pt_{30}: Ru_{50} to ~Ni_{18}: Pt_{39}: Ru_{43}.
- More alloys of higher Ru contents in the Ni-Pt-Ru system would be needed to ascertain the limiting Ru content for ordering.
- The annealing of the Ni-Pt-Ru alloys should be done under an argon atmosphere to avoid oxidization of the surfaces.

8. References

[1931Kur] N.S. Kurnakow and V.A. Nemilov, *Z. anorg. Chem., 210,1933, 13-20; Izvest. Inst. Platiny U.S.S.R.* 8, 17-24, 1931.

[1932Nem] W.A. Nemilow, *Z. anorg. Chem.*, 213, 1933, 283-291, *Invest. Inst. Platiny U.S.S.R.*, 9, 23 -30, 1932.

[1937Mar] V. Marian, *Ann. Phys.*, 7, 459-527, 1937.

[1940Ger] E. Gerhardt and W. Köster, *Z.Metallkunde*, 32, 253-261, 1940.

[1951New] J.B. Newkirk, R. Smoluchowski, A.H. Geisler, D.L. Martin, *J. Appl. Phys.*, 22, 290-298, 1951.

[1952Kos] W. Koster, *Z. Metallkunde,* 43, 444-449, 1952.

[1952Gei] A.H. Geisler, D.L. Martin, *J. Appl. Phys.*, 23, 375, 1952.

[1953Ori] R.A. Oriani and T.S. Jones, *Acta Metall*., vol. 1, 243, 1953.

[1958Han] M. Hansen., Constitution of Binary Alloys, 1958.

[1961Rau] E. Raub and D. Menzel, *Z. Metallkd.*, 52, 891-893, 1961.

[1964Kor] I.I. Kornilov and K.P. Myasnikova, *Izv. Akad,Nauk USSR, Met.Govn.Delo,* (4) 1964.

[1965Sch] K. Schwerdtfeger and A. Muan, *Acta Metall*., vol13, 503-515, 1965.

[1965Sel] G.L. Selman, M.R. Spender and A.S. Darling, *Plat. Met. Rev*., 9(4), 130-135, 1965.

[1970Wal] R.A. Walker and J.B. Darby, *Acta Metall*., vol 18, 1261-1266, 1970.

[1972Hut] J. M. Hutchinson Jr, *Plat. Met. Rev*., 16, 88-90 1972.

[1975Loe] K.L. Loewenstein, *Plat. Met. Rev*., 19(3), 82-87, 1975.

[1978Sav] Savitsky, V. Polyakova, N. Gorina and N. Roshan, Physical Metallurgy Of Platinum Metals E, Moscow, MIR Publications, 1978.

[1978Ste] G.T. Stevens, M. Hatherly and J.S. Bowles, *J. Mater. Sci*., vol13, 499-504, 1978.

[1978Cul] B.D. Cullity, Elements of X-ray Diffraction, Addison-Wesley Publishing Company, Inc., Reading Massachusetts, USA, 1978.

[1979Var] N.I. Varich, A.N. Petrunina, *Russ. Metall.*, 90-91, 1979.

[1981Usi] M.P. Usikov, G.S. Stepanova and E.I. Rytvin, Influence of alloying (with Pd, Rh, Ir, Ru) on the dislocation structure and high temperature creep of Platinum. *Russ. Metall*. USSR, 5, 114-116, 1981.

[1981Diw] A.F. Diwell and B. Harrison, *Plat. Met. Rev*., 25(4), 142-151, 1981.

[1985Don] J.D. Donaldson, S.J. Clark, Cobalt in Superalloys, Cobalt Development Institute, UK, 1985.

[1985Sun] B. Sundman, B. Jansson and J.O. Andersson, *CALPHAD, 9*, 153-190, 1985.

[1985Dah] C.E. Dahmani, M.C. Cadeville, J.M. Sanchez, J.L. Morán-López, "Ni-Pt Phase Diagram: Experiment and Theory", Phys. Rev. Let., 55, 11, 1208-1211, 1985.

[1987Sim] C.T. Sims, N.S. Stoloff and W.C. Hagel, Superalloys II: High Temperature Materials for Aerospace and Industrial Power, Wiley-Interscience, USA, 1987.

[1988Sea] R.A. Searles, *Plat. Met. Rev*., 32(3).quantit 123-129, 1988.

[1988Exn] H. E. Exner, H. P. Hougardy, Quantitative Image Analysis of Microstructures, DCM Informationsgesellschaft Verlag, Germany, 1988.

[1990ASM] Properties and Selection: Nonferrous alloys and Special-purpose materials, Metals Handbook, ASM International, 1990.

[1990Mas] T.B. Massalski, 5th ed., Binary Alloy Phase diagrams, USA, ASTM int., Metals Park, 1990.

[1991Nas1] P. Nash, M.F. Singleton, "Ni-Pt (Nickel-Platinum)", "Phase Diagrams of Binary Nickel Alloys", *Institution of Metallurgists and London,*1991.

[1991Nas2] P. Nash, "Ni-Ru (Nickel-Ruthenium)", "Phase Diagrams of Binary Nickel Alloys", *Institution of Metallurgists and London,* 1991.

[1991Fle] R.L. Fleisher, C.L. Briant and R.D. Field, *Mat Res. Soc. Symp. Proc*., 213, 463-475, 1991.

[1991Din] A.T. Dinsdale, *CALPHAD, 15*, 317-425, 1991.

[1993Lei] Y. Lei, *Plat. Met. Rev*., 37(3), 146-150, 1993.

[1996New] S.B. and W.M. Stobbs, Elevated Temperature Coatings: Science and Technology 2, California, 265-274, 1996.

[1997Mil] A. Mills, *Plat. Met. Rev*., 41(3), 115-127, 1997.

[1999Cle] W.J. Clegg, A. Kelly and J.E. Pitchford, *Key Engineering Matrials*, 161-163, 315-320,1999.

[1999Zha] J.-C.Zhao, *Z.Metallkd.*, vol 90, (3), pp 223-232, 1999.

[2000Wol] I.M. Wolff and P.J. Hill, Platinum metals-based intermetallics for high temperature service, *Plat. Met. Rev.*, 44, (4), 158-166, 2000.

[2000Hil] P.J. Hill, L.A. Cornish, M.J. Witcomb and P. Ellis, The (Pt)/Pt_3Al relationship in the Pt-Al-Cr and Pt-Al-Ti systems, *Proc. Microscopy Soc. South Afr.*, Vol. 30, p.13, 2000.

[2001Hil] P.J. Hill, PhD Thesis: Superalloy Analogues Based on Platinum for Ultra-High Temperature Applications, University of Witwatersrand, 2001.

[2001Süs] R. Süss, P.J. Hill, P. Ellis and L.A.Cornish, The oxidation resistance of Pt-base superalloy Pt_{80}:Al_{14}:Cr_3:Ru_3 compared to that of Pt_{86}:Al_{10}:Cr_4, *Proc. Microsc. Soc. South. Afr.* Vol. 31, p. 21, 5th-7th December 2001.

[2001Oik] K. Oikawa, G.W. Qin, T. Ikeshoji, O. Kitakami, Y. Shimada, K. Ishida, K. Fukamichi, *J of Magnetism and Magnetic Material*, 236, 220-233, 2001.

[2002Süs1] R. Süss, L.A.Cornish, P.J. Hill. and J. Hohls, *Proc. Conference on Advanced Materials and Processes for Gas Turbines*, Copper Mountain, Colorado, USA, 22-26 September, 301-308, 2002.

[2002Süs2] R. Süss, R. Völkl, D. Freund, B. Fischer, P.J. Hill, P. Ellis and I.M. Wolff, Mater. *Sci. Eng. A*, Vol. 338, pp. 133-141, 2002.

[2002Süs3] R. Süss, L.A.Cornish, P.J. Hill. and J. Hohls, Proc. Conference on Advanced Materials and Processes for Gas Turbines, Copper Mountain, Colorado, USA, 22-26 September, 301-308, 2002.

[2002Cor] L.A. Cornish, J. Hohls, P.J. Hill, S. Prins, R. Süss, D.N. Compton, *Journal of Mining and Metallurgy*, Vol. 28, No.3-4 B, pp. 197-204, 2002.

[2002Hil] P.J. Hill, G.B. Fairbank and L.A. Cornish, New Developments in High-Temperature Platinum Alloys, *J. of Metals*, 53, 10, 19-20, 2001.

[2003Gla] L. Glaner and L.A. Cornish, The Effect of Nickel Additions to the Pt-Al-Cr-Ru System, Proc. *Microsc. Soc. South. Afr.*, Volume 33, p17, Cape Town, 3rd – 5th December 2003.

[2003Twi] M.V. Twigg, *Plat. Met. Rev*., 47(4), 157-162, 2003.

[2003Cho] L.H. Chown and L.A. Cornish, *Proc. 2nd African Materials Research Society Conference*, p.136-137, Johannesburg, 8-11 December 2004.

[2004nml] www.nml.csir.co.za/News/200408/, accessed August 2004.

[2004key] www.key-to-metals.com/Article54.htm, accessed August 2004.

[2004Hyu] S. Hyun, O. Kraft and R.P. Vinci, *Acta Materialia* 52, 4199-4211, 2004.

[2004Cor] L.A. Cornish, R Süss, L.H. Chown, S. Taylor, L. Glaner, A. Douglas and S.N. Prins, Platinum-based Alloys for High Temperature and Special Applications, *International Conference Platinum Adding Value*, 329-336, The Southern African Institute of Mining and Metallurgy, Sun City, South Africa, 3rd - 7th October 2004.

[2005ICD] ICDD, International Centre for Diffraction Data (ICDD), Powder diffraction file (PDF-2), 12 Campus Boulevard, Newtown Square, Pennsylvania, USA, 2005.

[2006Cor] L.A. Cornish, R. Süss, L.H. Chown, A. Douglas, M. Matema, L. Glaner and G. Williams, New Pt-based alloys for high temperature application in aggressive environments: The next stage, *International Platinum Conference "Platinum Surges Ahead"*, 57-66, The Southern African Institute of Mining and Metallurgy, Sun City, South Africa, 8 – 12 October 2006.

[2006Mal] N.B. Maledi, J.H. Potgieter, M. Stephton, L.A. Cornish, L. Chown and R Süss, Hot corrosion behaviour of Pt-Alloys for application in the next generation of gas turbines, *International Platinum Conference "Platinum Surges Ahead"*, p81-90, The Southern African Institute of Mining and Metallurgy, Sun City, South Africa, 8 – 12 October 2006.

[2007Wat] A. Watson, R. Süss and L.A. Cornish, *Plat. Met. Rev.*, 51, (4), 189-198, 2007.

[2008Sho] M.B. Shongwe, L.A. Cornish and R. Süss, Optimisation of Compositions and Heat Treatments of Pt-Based Superalloys, *Proc. Microsc. Soc. South. Afr.*, Volume 38, p27, Botswana, July 2008.

9. Appendix: Papers published during the course of this study.

INVESTIGATION OF THE Ni-Pt-Ru PHASE DIAGRAM

L. Glaner[1, 3], L.A. Cornish[1] and B. Joja[2]

[1]Physical Metallurgy Division and [2]Mineralogy Division, Mintek, Private Bag X3015, Randburg, 2125
[3]School of Process and Materials Engineering, University of the Witwatersrand, Johannesburg, South Africa

Platinum and ruthenium additions are being used in protective coatings for nickel-based superalloys. Their diffusion rates have been studied in order to understand their beneficial effect on the coating's stability[1]. As part of a programme to identify and implement improvements for these coatings, phase relationships between the different components are being modelled. In order to glean input for the computer modelling, the phase diagrams of various systems have to be obtained. To date, no phase diagram for Ni-Pt-Ru has been published in the available literature, and so a study has been initiated.

The Ni-Pt binary phase diagram is a complete solid solution with two ordering phenomena below 700°C and a magnetic transformation on the Ni-rich side[2]. It would be of interest to determine how far the ordering extended into the ternary. Both the Ni-Ru and Pt-Ru phase diagrams comprise peritectic reactions between the terminal solid solution phases, and the former has very temperature dependent solubility ranges of the two phases[2]. Information regarding the position of the peritectic loci and the phase boundaries for both systems within the ternary is needed. The ternary phase diagram is expected to be a simple peritectic system, with some ordering on the Ni-Pt side.

Five ternary alloy compositions were selected to lie in the two-phase (Ru) + (Ni,Pt) region and one was chosen to be near the NiPt ordered region. Six alloys were manufactured from raw materials of at least 99% purity. The Pt and Ni were in bulk form, but the Ru was in compacted powder form. The samples were melted under argon in a button arc furnace, then sectioned and prepared for metallography. The samples were studied in the as-cast condition in a Jeol 840 SEM using Tracor Northern EDS. X-ray diffraction was also performed.

There were problems in fully melting the components of the first alloy, but ignoring the unmelted lumps of Ru and Pt, the overall composition was 47.7at% Pt (±0.3), 4.5at% Ru (±0.2) and 47.7 at% Ni (±0.3). The next two alloys ($Pt_{37.9}$:$Ru_{57.2}$:$Ni_{4.9}$ and Pt_{35}:$Ru_{54.5}$:$Ni_{10.5}$) had a central region, which was more Ru-rich and less Pt-rich in than the outer rim. However, all the compositions would be expected to lie within the (albeit Pt-rich) Ni,Pt solid solution. None of the compositions were unfortunately near the binary ordered regions and thus these samples cannot be used (after suitable heat treatment) to ascertain the extension of the ordering. However, they do show that Ni loss can occur in the manufacture of the samples, although such losses were negligible in the remaining samples

The next three samples ($Pt_{25.8}$:$Ru_{53.4}$:$Ni_{20.8}$, $Pt_{11.5}$:$Ru_{53.8}$:$Ni_{34.7}$ and $Pt_{12.2}$:Ru_{44}:$Ni_{43.8}$) were clearly two-phase. Two had very similar microstructures, but with different phase proportions, showing (Ni, Pt) dendrites in a cored (Ru) matrix, (Fig. 1). There was a sudden change on the solubility of (Ru) for Ni at about 25 at.% Ni, 8 at.% Pt and 67 at.% Ru. The last sample appeared very different, having (Ru) dendrites in a (Ni,Pt) matrix and there was much less contrast between the phases. Comparing overall alloy compositions and the reported binary liquid composition of the peritectic reactions, showed that the locus of the ternary peritectic reaction most likely progressed from the Pt-Ru side to the Ni-Pt in a regular fashion, agreeing with the primary phases. The compositions for (Ru) are consistent with the binary values and show more agreement with the higher temperature values for the Ni-Ru binary. On the other hand, the compositions of the (Ni, Pt) phase shows much less solubility than would be expected from extrapolating the boundaries from the binaries. Thus the trend of limited solubility which originates from the Ni-Ru binary penetrates at least to 50 at. % Pt within the ternary. No other phases were found than those already reported, namely (Ru) and (Ni,Pt).

Future work will comprise more samples to check the kink in the (Ru) boundary and making samples near the expected ordered region. Heat treatments will be undertaken, probably at 1150°C, and at low temperatures to check for ordering.

The financial assistance of Mintek, NRF/DST and the PDI are gratefully acknowledged.

References

1. Karunaratne, M.S.A. and Reed, R.C. (2003) Acta Materialia 51, 2905.
2. Massalski, T.B. (1990) Binary Alloy Phase Diagrams. Metals Park, Ohio, ASM International.

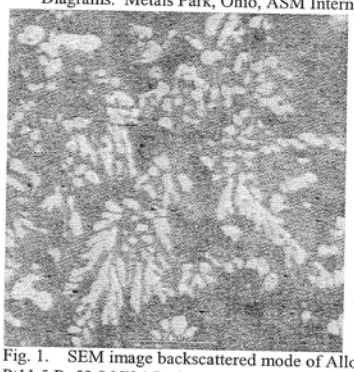


Fig. 1. SEM image backscattered mode of Alloy Pt11.5:Ru53.8:Ni34.7 showing (Ru) dendrites (light) in (Ni, Pt) matrix. (Scale bar = 24μm).

[3]e-mail: lizelleg@mintek.co.za

THE 1000°C ISOTHERMAL SECTION OF THE Ni-Pt-Ru PHASE DIAGRAM

L. Glaner[1,3], L.A. Cornish[1,3] and B. Joja[2]

[1]Advanced Materials and [2]Mineralogy Division, Mintek, Private Bag X3015, Randburg, 2125
[3]DST/NRF Centre of Excellence for Strong Materials, Private Bag 3, WITS, 2050

Pt-modified aluminide coatings (with ruthenium additions) on nickel-based superalloys have been used for over a decade[1]. The mechanism of how platinum and ruthenium benefits the properties of the coatings and the degradation mechanism of these coatings is not yet fully understood. Diffusion rates of Pt and Ru have been studied to understand their beneficial effect on the coating's stability[2]. The Pt-Ni-Ru system is one system that has been studied to understand and optimise the coatings with both Pt and Ru additions. The binary systems are well known[3], but nothing was found in the literature on the ternary system.

As-cast studies showed the ternary system to be a simple peritectic, with ordering near the Ni-Pt binary. Here, the 1000°C isothermal section of this ternary was established by annealing nine alloys at 1000°C for 1000 hours. The alloys were prepared from elements of at least 99% purity and melted in an arc furnace under an argon atmosphere. The samples were examined in a JEOL 840 SEM using a Tracor Northern EDS. XRD studies were done on a Siemens D500 XRD with Diffrac Plus software, with Mo Kα radiation to identify the phases.

Nine alloy compositions were chosen. Alloys 2-6 were chosen to lie in the two-phase area between the (Ru) and (Ni,Pt) solid solutions. In the as-cast condition, Alloys 2 (Ni_{10}:Pt_{23}:Ru_{67}) and 3 (Ni_{20}:Pt_{20}:Ru_{60}) were single phase (Ni,Pt), while Alloys 4 (Ni_{35}:Pt_{13}:Ru_{52}), 5 (Ni_{50}:Pt_5:Ru_{45}) and 6 (Ni_{60}:Pt_5:Ru_{35}) had two phases: (Ru) and (Ni,Pt). After annealing, Alloy 2 (Ni_{10}:Pt_{23}:Ru_{67}) and 3 (Ni_{20}:Pt_{20}:Ru_{60}) also became two-phase: (Ru) and (Ni,Pt). Alloy 1 was chosen to check the extent of ordering from the Ni-Pt into the ternary system. It is not shown here because ordering only takes place at ~ 500°C and is removed by annealing at 1000°C.

The initial results showed an inflection in the (Ni,Pt) boundary and this was checked with four more alloys. They were all single phase (Ni,Pt) with coring. After annealing, Alloy 7s (Ni_{45}:Pt_{25}:Ru_{30}) and 8 (Ni_{35}:Pt_{35}:Ru_{30}) showed three phases (Fig. 1a and 1b). The (Ru) and (Ni,Pt) phases were identified by EDS, and there was a black needle-like structure that was too small to analyse accurately. However, analysis of the XRD spectra is ongoing. The microstructure of Alloys 9 (Ni_{25}:Pt_{45}:Ru_{30}) and 10 (Ni_{15}:Pt_{55}:Ru_{30}) were cored (Fig. 2a and 2b), with XRD analyses confirming only the (Ni,Pt) phase. The 1000°C isothermal section using the data of all the alloys annealed at 1000°C at 1000 hours is shown in Fig. 3. It can be seen that Alloys 7 – 10 confirmed the inflections in the (Ru) and (Ni,Pt) phase boundaries.

The financial assistance of Mintek, NRF/DST and the PDI is gratefully acknowledged.

References

1. Newcomb, S.B. and Stobbs, W.M. (1996) Elevated Temperature Coatings: Science and Technology 2, California, 265-274.
2. Karunaratne, M.S.A. and Reed, R.C. (2003) Acta Materialia 51, 2905.
3. Massalski, T.B. (1990) Binary Alloy Phase Diagrams. Metals Park, Ohio, ASM International.

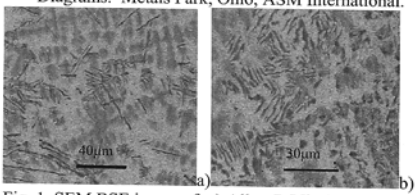


Fig. 1. SEM BSE image of: a) Alloy 7 (Ni_{45}:Pt_{25}:Ru_{30}) and b) Alloy 8 (Ni_{35}:Pt_{35}:Ru_{30}): both showing (Ru) dendrites (medium), (Ni,Pt) matrix (light) and black needles.

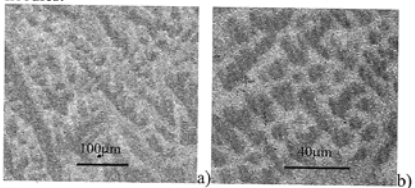


Fig. 2. SEM BSE image of : a) alloy 9 (Ni_{25}:Pt_{45}:Ru_{30}) and b) alloy 10 (Ni_{15}:Pt_{55}:Ru_{30}): both showing cored (Ni,Pt)

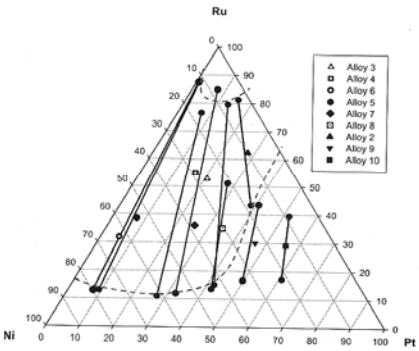


Fig. 3. 1000°C isothermal section of the Ni-Pt-Ru phase diagram.

Corresponding author: *lizelleg@mintek.co.za*